Modelling of Mass Transfer Phenomena in Chemical and Biochemical Reactor Systems using Computational Fluid Dynamics

Larsson, Hilde Kristina; Krühne, Ulrich; Gernaey, Krist V.; Skov, Anne Ladegaard

Publication date:
2015

Document Version
Publisher's PDF, also known as Version of record

Modelling of Mass Transfer Phenomena in Chemical and Biochemical Reactor Systems using Computational Fluid Dynamics

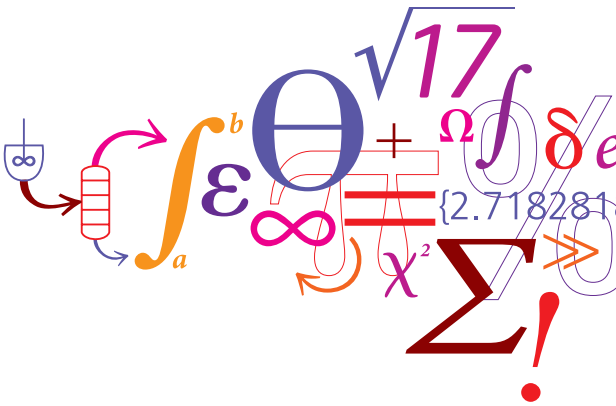

Hilde Kristina Larsson

PhD Thesis

November 2015

DTU Chemical Engineering
Department of Chemical and Biochemical Engineering

Modelling of Mass Transfer Phenomena in Chemical and Biochemical Reactor Systems using Computational Fluid Dynamics

Hilde Kristina Larsson

November 30, 2015

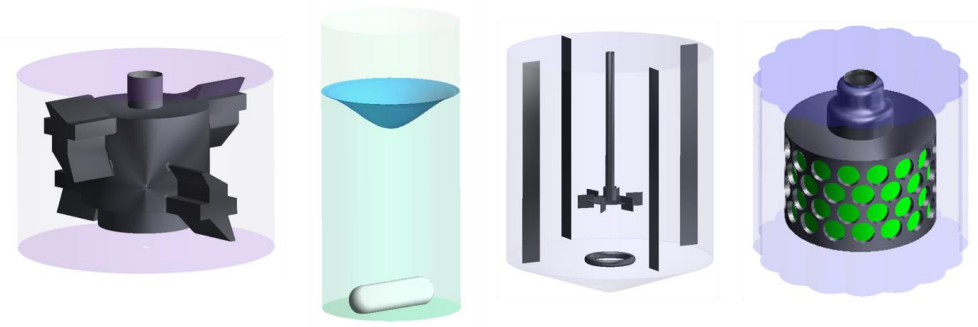

DTU Chemical Engineering
Department of Chemical and Biochemical Engineering

Address: CAPEC-PROCESS Research Center

Department of Chemical and Biochemical Engineering

Technical University of Denmark

Building 229

Dk-2800 Kgs. Lyngby

Denmark

Phone: +45 4525 2800

Web: www.capec-process.kt.dtu.dk/

Print: GraphicCo.

DTU Chemical Engineering
Department of Chemical and Biochemical Engineering

Preface

The work presented in this PhD thesis was carried out at the Department of Chemical and Biochemical Engineering at the Technical University of Denmark (DTU) in the period December 2012 to November 2015. It was performed in the CAPEC-PROCESS Research Center under the main supervision of Associate Professor Ulrich Krühne and co-supervision by Professor Krist Gernaey and Associate Professor Anne Ladegaard Skov.

This project was founded by the Novo Nordisk Foundation under the grant "Exploring biochemical process performance limits through topology optimization".

The microbioreactor case study was performed in collaboration with PhD student Andrijana Bolic, and the pilot plant reactor work was performed in collaboration with PhD student Christian Bach and PhD student Anders Nørregaard.

The rotating bed reactor case study was performed in collaboration with master thesis student Patrick Alexander Schjøtt Andersen, and Emil Byström and Henrik Scherman from SpinChem AB, Umeå, Sweden.

Special thanks go to master thesis student Jifeng Yang for rewarding discussions on modelling of dispersed flow, CFX Berlin Software GmbH for two highly valuable courses, DTU Computing Center for support on the HPC cluster, and ANSYS Sweden AB and Associate Professor Alan Burns at the University of Leeds for useful and friendly advice.

Thanks also to my family, friends and former and current colleagues for support throughout this project and beyond.

Abstract English

Computational fluid dynamics (CFD) is the application of numerical methods to solve systems of partial differential equations related to fluid dynamics. The continuity and the momentum equations are the most commonly applied equations within CFD, and together they can be used to calculate the velocity and pressure distributions in a fluid. CFD also enables the modelling of several fluids simultaneously, e.g. gas bubbles in a liquid, as well as the presence of turbulence and dissolved chemicals in a fluid, and many other phenomena. This makes CFD an appreciated tool for studying flow structures, mixing, and other mass transfer phenomena in chemical and biochemical reactor systems.

In this project, four selected case studies are investigated in order to explore the capabilities of CFD. The selected cases are a 1 ml stirred microbioreactor, an 8 ml magnetically stirred reactor, a Rushton impeller stirred pilot plant reactor, and a rotating bed reactor filled with catalytic porous material. A selection of the simulated phenomena includes the velocities and turbulent quantities in the reactors, as well as the distribution of the gas and liquid phases in them. Mixing times, oxygen transfer rates and an ion-exchange reaction are also modelled and compared to experimental data.

The thesis includes a comprehensive overview of the fundamentals behind a CFD software, as well as a more detailed review of the fluid dynamic phenomena investigated in this project. The momentum and continuity equations are presented as well as the theory behind the SST and the k-ε turbulence models. Modelling of additional variables, porous materials and two-phase flows are also introduced. The two-phase flows are modelled using the Euler-Euler method, and both dispersed and free-surface flows are simulated.

The importance of mass transfer with a focus on mixing, gas-liquid transfer of oxygen, and heterogeneous reactor systems is reviewed and mathematical models for these applications are presented. A review of how these mass transfer phenomena have been modelled in the scientific literature is also included.

The models are subsequently evaluated based on their applicability in the four case studies. The evaluations especially focus on the impact of the choice of turbulence model and other modelling decisions made by the user. The conclusion is that CFD is a highly valuable tool for modelling several important parameters in chemical and biochemical reactors but that the user must be well aware of the shortcomings with the applied models.

Abstract Danish

Computational Fluid Dynamics (CFD) er anvendelsen af numeriske metoder til at løse systemer af partielle differentialligninger relateret til strømningslæren. Ligningerne for kontinuitet og impulsbevarelse er de mest almindeligt anvendte ligninger indenfor CFD, og sammen kan de bruges til at beregne hastigheder og tryk i en fluid. CFD giver også mulighed for samtidig modellering af flere fluider, f.eks. af gasbobler i en væske, samt modellering af turbulens og transport af kemikalier i en væske og mange andre fænomener. Dette gør CFD til et værdsat værktøj til at studere hastighedsvektorer, blandingstider og andre masseoverførsels-fænomener i kemiske og biokemiske reaktorsystemer.

I dette projekt er fire udvalgte casestudier blevet undersøgt for at udforske mulighederne af CFD. De udvalgte casestudier er en 1 ml omrørt mikrobioreaktor, en 8 ml magnetisk omrørt reaktor, en *pilot plant reactor* med en Rushton turbine som rørelement og en *rotating bed reactor* fyldt med katalytisk porøst materiale. De udvalgte simulerede egenskaber inkluderer hastighederne og turbulente mængder i reaktorerne, samt fordelingen af gas- og væskefaser i dem. Blandingstider, iltoverførselshastigheder og ionbytningsreaktioner modelleres også og sammenlignes med eksperimentelle data.

Afhandlingen omfatter et samlet overblik over de grundlæggende elementer bag CFD-software, samt en detaljeret gennemgang af de fluid-dynamiske fænomener undersøgt i dette projekt. Ligningerne for momentum og kontinuitet præsenteres, lige så vel som teorien bag de SST og k-ε turbulensmodeller det er blevet brugt. Modellering af skalare tilstandsvariabler *(additional variables)*, porøse materialer og tofasede strømninger er også præsenteret. De tofasede strømme er modelleret ved hjælp af Euler-Euler-metoden, og både *dispersed* og *free-surface* modellerne er revideret.

Betydningen af massetransport med fokus på blandingstider, gas-væske overførsel af ilt, og heterogene reaktorsystemer er revideret og matematiske modeller for disse applikationer er præsenteret. En gennemgang af hvordan disse fænomener er blevet anvendt i den videnskabelige litteratur er også inkluderet.

Modellerne er efterfølgende evalueret baseret på deres anvendelighed i de fire casestudier. Evalueringerne fokuserer især på konsekvenserne af valg af turbulensmodel og andre modelleringsafgørelser truffet af brugeren. Konklusionen er, at CFD er et meget værdifuldt værktøj til modellering af flere vigtige parametre i kemiske og biokemiske reaktorer, men at brugeren skal være klar over manglerne ved de anvendte modeller.

List of Symbols

α	Phase in two-phase flow
β	Phase in two-phase flow
γ, γ_2	Volume fraction in porous modelling
δ_{ij}	The Kronecker delta
E	Turbulent energy dissipation rate
μ	Molecular (dynamic) viscosity
μ_{eff}	Effective (dynamic) viscosity
μ_t	Turbulent (dynamic) viscosity
Y	Kinematic viscosity
P	Density
$\sigma_A, \sigma_B, \sigma_C$	Constants used in the SST model
τ_{ij}	Viscous stress
τ_w	Wall shear stress
Φ	Scalar/Additional variable
Ω	Turbulent frequency
$\boldsymbol{\Omega}$	Rotational velocity vector
$\boldsymbol{a}$	Acceleration vector
$A_{\alpha\beta}$	Specific interfacial area between phase α and β
$A_{interface}$	Interfacial area between phases
A_S	Specific interfacial area of porous particles
C_1	Linear loss coefficient
C_2	Quadratic loss coefficients
C_{Drag}	Drag coefficient
C_P	Proportionality constant
$d_{\alpha\beta}$	User specified constant for the mixture model
d_B	Bubble diameter
d_P	Particle diameter
D	Diameter of pipe/Diameter of impeller
D_φ	Mass diffusion coefficient
$\boldsymbol{F}$	Force vector
F_1	Blending factor for the SST turbulence model
$\boldsymbol{g}$	Gravitational acceleration vector
k	Turbulent kinetic energy
k_L	Mass transfer coefficient
k_La	Volumetric mass transfer coefficient/Mass transfer rate
m	Mass
$\boldsymbol{M}_\alpha$	Sum of interfacial forces
M_{global}	Local mixing quality
M_{local}	Global mixing quality
N	Rotational speed
p	Pressure
P_k	Production term for turbulence models
$\boldsymbol{r}$	Location vector
r_i	Volume fraction of phase i
Re_{Pipe}	Reynolds number for flow in pipe
$Re_{Impeller}$	Reynolds impeller number

Re_{Wall}	Reynolds number for wall flow
$\boldsymbol{S_M}$	Momentum source vector
S_φ	Scalar source
S_i	Momentum source in the i direction
T	Time
u_i	Time fluctuating flow
$\boldsymbol{U}$	Velocity vector
$\boldsymbol{U}_\alpha$	Vector field of phase α
$\boldsymbol{U}_\beta$	Vector field of phase β
u^+	Dimensioless velocity
U_i	Velocity component in the *i* direction
U_s	Superficial velocity
U_{slip}	Slip velocity (of bubbles)
$\overline{U}_i$	Time mean flow
v	Averaged linear velocity
V_i	Volume in phase i
y^+	Dimensioless distance to wall

List of Publications and Presentations

Poster presentations:

- **Larsson, H.**, Ladegaard Skov, A., Gernaey, K. V., Krühne, U., 2013. CFD-based modeling of dissolved oxygen in microbioreactors. At CAPEC-PROCESS Industrial Consortium Annual Meeting 2013, June 3-5 in Snekkersten, Denmark.
- **Larsson, H.**, Ladegaard Skov, A., Gernaey, K. V., Krühne, U., 2014. Modeling oxygen transfer in small scale reactors using CFD. At BIOPRO World Talent Campus, October 19-27 in Sorø, Denmark.
- **Larsson, H.**, Ladegaard Skov, A., Gernaey, K. V., Krühne, U., 2014. Modeling and optimizing oxygen transfer in small scale reactors using computational fluid dynamics. At 13th International Conferences on MicroReaction Technology, June 23-25 in Budapest, Hungary.
- **Larsson, H.**, Gernaey, K. V., Krühne, U., 2015. Modeling Mass Transfer in Small Scale Reactors using Computational Fluid Dynamics. At Scale-up and scale-down of bioprocesses, May 11-13 in Hamburg, Germany.

Oral presentations:

- **Larsson, H.,** 2014. Modeling and optimizing oxygen transfer in small scale reactors using computational fluid dynamics. At CAPEC-PROCESS Industrial Consortium Annual Meeting, June 11, Copenhagen, Denmark.
- **Larsson, H.,** 2015. Modeling of Mass Transfer Phenomena in Small Scale Reactor Systems using Computational Fluid Dynamics. At DANSIS research seminar 2015, May 20, Kgs. Lyngby, Denmark.

Journal articles:

- Lormenti, L.R., Nørregaard, A., Bolic, A., Quintanilla Hernandez, D., Hagemann, T., Heins, A.L., **Larsson, H.**, Mears, L., Mauricio-Iglesias, M., Krühne, U., Gernaey, K.V., 2014. Challenges in industrial fermentation technology research. *Biotechnology journal*, 9(6), pp. 727-738.
- Krühne, U., **Larsson, H.**, Heintz, S., Ringborg, R. H., Rosinha, I. P., Bodla, V. K., Santacoloma, P. A., Tufvesson, P., Woodley, J. M., Gernaey, K. V., 2014. Systematic Development of Miniaturized (Bio) Processes using Process Systems Engineering (PSE) Methods and Tools. *Chemical and Biochemical Engineering Quarterly* 28(2), pp. 203-214.

Table of Contents

1. Introduction

Mass transfer in chemical and biochemical reactor systems is very important in order to achieve good and effective processes. In heterogeneous reactor systems good mixing and mass transfer is for example important to bring the reacting species close to the reactive sites. Mass transfer is also of critical importance in fermentations in order to provide high enough substrate and oxygen concentrations for the growing organisms.

With its ability to model fluid flow and chemical reactions, computational fluid dynamics (CFD) is a valuable tool for studying flow structures, mixing, and other mass transfer phenomena in chemical and biochemical reactor systems. The use and importance of CFD is also growing constantly with increased computational power, software development, and disseminated knowledge about its possibilities.

Using CFD modelling to understand fluid dynamic phenomena better has many of the same benefits as other kinds of modelling. It is for example often cheaper, faster and safer to perform simulations rather than experiments, but the used models must also be reliable and preferably validated in order to give meaning and confidence.

There are also many misconceptions regarding CFD and its applicability. Examples of this range from an over-belief that the results from a CFD simulation always represent reality regardless of the models included, to the conception that CFD software is so automated that the key steps in a simulation are to import a geometry, press a start button and wait for colourful flow diagrams to appear.

The aim of this thesis is therefore to investigate how CFD can be used to model mass transfer phenomena in four selected reactor systems, and to both explore the possibilities and drawbacks associated with it. The four case studies have been selected in order to represent a range of volumes and mass transfer phenomena and focus mainly on mixing, interfacial mass transfer and mass transfer around catalytic particles. The applied models are evaluated based on their abilities to model the studied mass transfer phenomena, and their sensitivity to common user-defined variables is also investigated.

The four case studies are shortly presented in the next section together with an introduction of which mass transfer phenomena are modelled in each case study. The section follows an overview about the thesis arrangement.

1.1.1. Presentation of case studies

Four case studies are examined in this thesis in order to cover a range of volumetric scales and different mass transfer phenomena. The selected cases are a microbioreactor, a magnetically stirred reactor, a pilot plant reactor and a rotating bed reactor. The microbioreactor is displayed in Figure 1 and it was developed by PhD student Andrijana Bolic at the Department of Chemical and Biochemical Engineering, DTU. It is previously presented at Bolic et al. (2012) where also the experimental oxygen transfer rates and mixing times simulated in this project origin from.

The microbioreactor is developed for surface and bubble aeration, one and bi-directional stirring and a working volume range of 0.5-2 ml Bolic et al. (2012). In this project, 1 ml filling volume, constant rotational speed and surface aeration is modelled, and two-phase,

free-surface simulations have therefore been performed. A free-surface simulation indicates that the gas and the liquid phase are not dispersed in each other but have a distinct interface, or free surface.

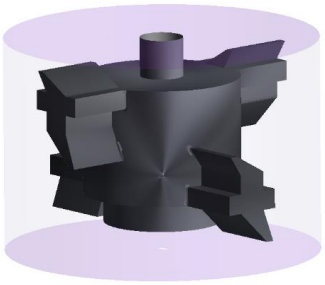

Figure 1. The microbioreactor.

The magnetically stirred reactor, i.e. the second case study, contains 8 ml water and is displayed in Figure 2. The flow in the reactor is also modelled as two-phase flow with a free surface, and the simulated oxygen transfer rates are compared to experimental data.

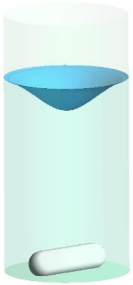

Figure 2. The magnetically stirred reactor.

The pilot plant reactor is presented in Figure 3 and is physically located in the pilot plant hall at the Department of Chemical and Biochemical Engineering, DTU. The volume of the geometry in Figure 3 is 680 L and it contains a gas sparger, a Rushton turbine impeller and four baffles. One and two-phase simulations have been performed for the pilot scale reactor with the purpose to model mixing time, gas holdup and oxygen transfer rates.

Figure 3. The pilot plant reactor.

The fourth case study in this project is a rotating bed reactor (RBR) developed by SpinChem AB (former Nordic ChemQuest AB), Umeå, Sweden. The simulated RBR is placed in a baffled vessel holding 160 ml liquid and is displayed in Figure 4. The RBR has a hole in the bottom and holds four compartments that can be filled with for example porous ion-exchange resins. When the RBR rotates the fluid in the porous material (displayed with green colour in the figure) is forced out of the reactor through the small outer holes and new fluid enters through the bottom hole. In this case study, simulated and experimental ion-exchange data are compared.

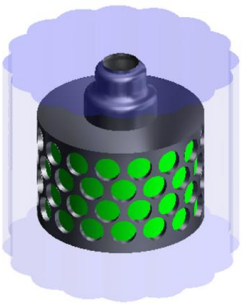

Figure 4. The rotating bed reactor placed in a baffled vessel.

1.1.2. Thesis disposition

The structure of this thesis is arranged around the four chapters theoretical background, material and methods, results and discussion, and conclusion and outlook. The theoretical background is divided into four subsections and starts with an introduction to CFD summarizing the most important concepts of how to set up and run the simulations. The mathematical models and theoretical concepts of fluid dynamics used in this project are thereafter presented. This follows by an introduction to mass transfer from a chemical and biochemical engineering point of view and highlights for example the importance of mixing, interfacial mass transport of oxygen and heterogeneous chemical reactions. A literature review describing the work of others in relation to the four case studies is thereafter presented.

The materials and methods chapter starts with a description of the experimental methods followed by the general computational fluid dynamics methods applied in this project. The four case studies have thereafter one subchapter each describing the specific mesh and geometry, simulation and evaluation setups applied in each case. The results and discussion chapter has the same arrangement with one subchapter per case study and the results are discussed in the sections in which they are presented. The general conclusions from the case studies are however summarized in the last chapter where also suggestions for future work are presented.

2. Theoretical Background

2.1. Introduction to computational fluid dynamics

2.1.1. Introduction to CFD software

Computational fluid dynamics (CFD) is the use of numerical methods to solve systems of partial differential equations from the field of fluid dynamics. The use of numerical methods is essential to solve these, since the system of equations most often is very complicated and otherwise only possible to solve analytically for very simple flow problems.

The fluid dynamics field is based on conservational laws, i.e. the laws of conservation of mass, linear momentum and energy in a system. Starting from those principles, systems of partial differential equations have been derived, that for example describe velocities and pressures in a fluid and the behaviour of chemicals in it.

There is a range of CFD simulation software packages available, both open source and commercial ones and in this project the commercial software ANSYS CFX 15.0 has been used for the fluid dynamic simulations, while ICEM CFD 14.0 and 15.0 have been used for the creation of the computational meshes needed for the simulations. The exact solution method differs between different programs, but most software goes through the same principal steps geometry and mesh generation, problem setup, numerical solution stage and finally post processing of the results. These steps will be shortly presented in this section from a CFX/ICEM CFD perspective, and the details of the used models and equations will be presented in section 2.2.

2.1.2. Geometry and mesh generation

The first step in performing a CFD simulation is to define the geometry of the flow problem, which is the same as the volume of the fluid that is going to be simulated. For example, when simulating the flow pattern around a car it is the air around the vehicle that is the geometry or volume of interest, while the car itself is just represented by its outer surfaces. The geometry can consist of one or several domains, i.e. sub-parts, and different phenomena can be modelled in different domains.

After the geometry has been defined, it needs to be transformed into a computational mesh, which is the representation of the geometry the solver can use. A computational mesh consists of mesh elements and nodes, which connect the edges of the elements. ANSYS CFX has a node based solver, which means that each node in a simulated mesh will be assigned an own value for each flow variable, e.g. a velocity vector, a pressure value and a temperature. The numerical methods implemented in the solver will then act on each node individually and in an iterative manner gradually solve the flow equations in the entire geometry.

Several different element shapes are possible in a three-dimensional space, for example four-sided tetrahedron volumes, six-sided hexahedra volumes and five-sided pyramid shaped volumes. Triangular prism elements are also commonly used in order to create fine element layers close to wall boundaries. The quality of a mesh can be defined in many different ways, but a good mesh is generally characterized by compact elements with relatively large angles between its edges, and that neighbouring elements have approximately the same volume.

An example of two different meshes created on the same geometry can be seen in Figure 5, which shows one tetrahedron and one hexahedral mesh. With ICEM CFD, it is also possible to combine different element types in one single mesh.

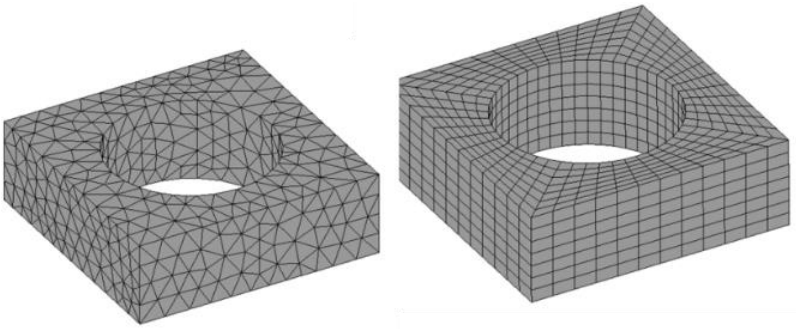

Figure 5. One mesh with four-sided tetrahedron elements (left) and one with six-sided hexahedral mesh elements (right).

The largest advantage using tetrahedron shaped mesh elements is that they can be created more or less automatically by ICEM CFD or similar programs, which is often preferred when more complicated geometries are involved. Using the automatic tool, parts of the tetrahedral elements can subsequently be merged into hexahedral elements. The resulting mesh can however be of quite poor quality once automatically generated, and it can be hard to control the distribution of elements.

The available method in ICEM CFD to create hexahedral meshes is called blocking. Using blocking it is possible to create structured meshes, i.e. meshes where each element has a fixed and user defined position in the volume. This increase in user control over the mesh generation process often leads to meshes of higher quality, but it requires much more time and experience. The difficulty of creating good hexahedral meshes also increases fast with the complexity of a geometry.

Once generating a mesh, it is important to make sure that it has most elements per volume where many fluid dynamic phenomena are expected to take place within the geometry. When simulating a car, it is for example a very good idea to have a finer mesh region in the wake just behind the car, while it is not so important far away from it.

A high quality mesh will increase the chance for a simulation to run smoothly towards a solution that satisfies the partial differential equations everywhere in the geometry. It is therefore advisable to invest time in generating a good mesh, and to remember that the mesh-generating step is most often the most work intense part of a CFD project.

2.1.3. Setup of the flow problem

After the mesh generating step, the user needs to decide which partial differential equations have to be solved, i.e. which flow phenomena to model. The user also needs to declare certain model parameters, e.g. the viscosity and the density of the simulated fluids, and to state the boundary conditions for the flow problem. For a transient simulation, i.e. a simulation that considers the time derivative and therefore can model flow phenomena over time, the user

also needs to state initial conditions for the simulation. A time-step size must then also be defined, as well as a simulation end time, i.e. for how long the system should be simulated. The contrary to a transient simulation is a steady-state simulation, which only models static flow phenomena, e.g. velocities that are not expected to change over time.

Boundary conditions must be stated for each boundary, i.e. surface, on a geometry and the most common options are inlet, outlet, opening, wall, symmetry or periodicity. For inlets and outlets, velocities or pressures are stated. Openings work in a similar manner, but fluids are allowed to both enter and exit the geometry through them.

For walls, the two most used boundary conditions are *free slip wall* and *no slip wall*. At *no slip walls* the velocity is zero in all directions, which makes them a regular wall. At *free slip walls*, the tangential velocities are not necessarily zero, but the velocity gradient normal to the surface is. This means that a fluid cannot enter or exit through a *free slip wall*, but also that it cannot be accelerated or decelerated by it in the tangential direction.

This also means that the shear stresses at *free slip walls* are zero by default, which can be interpreted as if a fluid moving parallel to a wall does not "feel" the presence of it. For a *no slip wall* on the other hand, a fluid moving close to the wall will "feel" a force acting on it.

Free slip walls are often a good choice at non-physical boundaries present just to close a geometry. For example, when simulating an object that moves freely in a fluid, such as a submarine in an ocean, it is far from reasonable to simulate the entire sea around it. The boundaries around the submarine can then be modelled as *free slip walls*, since there are no actual walls there in reality. *Free slip walls* can also be used to model gas-liquid interfaces in simulations where it is only desired to model the liquid, and where the physical appearance of the interface is known in advance.

An example of which boundary conditions that should be used in the submarine case is shown in Figure 6, where the inlet and outlet velocity should be the same as the velocity of the simulated submarine. The outer walls of the submarine should be ordinary *no slip walls*.

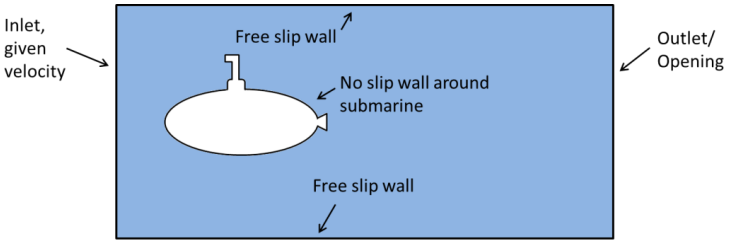

Figure 6. An example of how the boundary conditions inlet, free slip wall, no slip wall, opening and outlet can be used.

A *no slip wall* can be either stationary or moving while the *free slip walls* have no velocity by definition. It can also be important to have a fine mesh close to *no slip walls* since high velocity gradients can be expected once increasing from zero velocity by the wall to the velocity of the bulk fluid further away.

The two last boundary conditions mentioned, i.e. symmetry and periodicity, can both be used in order to decrease the computational time for a simulation by decreasing the number of nodes in a simulated geometry. The symmetry boundary condition works as an imaginary mirror as shown in Figure 7, and rotational periodicity can be used to simulate a system with rotational symmetry around an axis as exemplified in Figure 8.

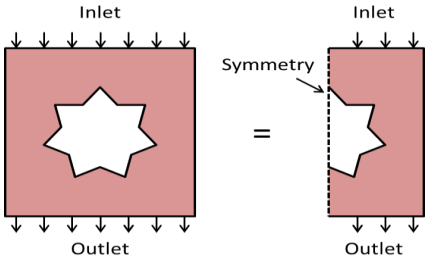

Figure 7. An example of how the symmetry boundary condition can be used to half the size of a simulated geometry, and thus decrease the simulation time.

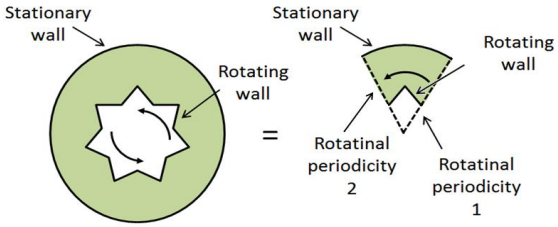

Figure 8. An example of how the boundary condition rotational periodicity can be used to decrease the size of a simulated geometry.

2.1.4. Running the solver

This is the actual solution step where the solver applies the numerical methods to the mesh in order to find solutions to the selected equation systems. Normally this step requires least user input, but it is also the step that can require the most time in a CFD project. How long a simulation takes is highly dependent on the complexity of the problem (e.g. the number of equations to be solved), the number of nodes in the mesh and the computer power available for the task. If the solver is provided with a good initial guess of the solution and a high quality mesh, it also increases the chances to reach a solution faster.

Once the solver is running, it is possible for the user to see how the solution is developing by tracking the residuals from the solution iterations. One residual is available per modelled variable (e.g. velocity in the x-direction, pressure, temperature) and node and the residual is a measurement of the imbalances for that variable in the current solution step. The smaller the imbalance, the better does a variable value match the differential equations the solver is trying to fit it to. The values of the residuals are also normalized by the actual values of the variable they represent. This means that an imbalance of 10 g in a node representing 100 g gives rise to a larger residual than an equally big imbalance in a node representing 1 kg (ANSYS® Academic Research (2013)).

The residuals for a variable are presented either as their root mean square (RMS) value or as their maximum (MAX) value, and these values are one of the solver outputs the user can use in order to evaluate the convergence of a simulation. During the course of a simulation, the residuals should decrease towards zero and a common practice is to stop the simulations at a certain threshold value. Convergence can also be defined as when the values of certain key parameters, e.g. the torque around a stirrer or the flow in a point, has stabilized and do not change anymore.

If the residuals in a simulation are not decreasing but are fluctuating around a relatively high value, it means that the solver cannot find a solution with the current model setup. Possible reasons for this are many, for example pure errors in the simulation setup or a too low quality of the mesh. It can also occur once a steady solution is not possible to find, i.e. when the flow is actually transient.

2.1.5. Post processing

When the solver is finished, it creates a result file containing all the values of the system variables in each node. These results can then be used as an initial guess for later simulations, or post-processed and interpreted by the user. In the post-processing module available in ANSYS CFX 15.0, it is for example possible to visualise the value of all system variables on user-defined lines, planes and volumes. The post processing also allows several calculations on the system variables, such as computing their mean values.

One important part of the post-processing is to judge the mesh independence of a simulation. Mesh independence means that important characteristics in the result of a simulation do not change significantly for a different mesh, so in order to investigate this, simulations should be repeated several times with different meshes. Important features of the simulation, for example the total torque around a shaft or the flow pattern in an area, should then be calculated for the different meshes and compared.

2.2. Fluid dynamics and its modelling

2.2.1. Introduction to computational fluid dynamics

Computational fluid dynamics is, as its name suggests, the computer aided simulation of fluids and is the application of numerical methods to solve selected partial differential equations from the field of fluid dynamics. These equations describe for example the balances of momentum, energy, turbulence or reacting chemicals in fluids and with the aid of numerical methods CFD makes it possible to find solutions for them even in complex geometries.

The background to how CFD software can operate was presented in section 2.1, and in this section the flow models and equations used in this project will be presented. All fluids modelled within this project are considered incompressible and Newtonian, so modelling of compressible and non-Newtonian flow has therefore been omitted in the following section.

A Newtonian fluid, e.g. water and air, is a fluid that has a constant viscosity regardless of what strain forces it is encountering. The opposite is a non-Newtonian fluid, which for example can be shear thinning such as ketchup, blood and fermentation broths or shear thickening such as potato starch in water and silly putty.

An incompressible fluid has a constant density, while the density of a compressible fluid can change dependent on what pressures it experiences. All fluids are in reality compressible, some (e.g. air) more and some (e.g. water) less, but for the pressures considered in this project they can all be considered incompressible. Temperature variations are not considered within this project either, so temperature dependence on the density has also been omitted.

First, the continuity and momentum equations, i.e. the fundamental balances of the fluid dynamics, will be presented followed by a section about dimensionless numbers. One of the most known dimensionless numbers within the field of fluid dynamics is the Reynolds number, which for example can be used to judge if a flow is turbulent or not. Thereafter a section will follow about the fundamental differences between laminar and turbulent flow and the modeling of these.

In simulations involving mixing phenomena or chemical reactions so-called additional variables or scalars are often used to represent colour dyes or chemicals, so the modelling of this is presented in section 2.2.6. After that follows a section about modelling of flow through porous materials since that is included in the rotating bed reactor case study. Finally, the flow equations associated with multi-phase flow will be presented with a focus on the two-phase flows modelled within this project.

The theory about the continuous and momentum equations, the turbulent modelling, the additional variables and flow through porous material is written as how it is applied for a one-phase flow, but the theory can also be adapted to multi-phase flow. However, for simplicity reasons two-phase flow is only considered in the multi-phase section.

2.2.2. The continuity and the momentum equations

The most fundamental equations in the fluid dynamics are the continuity equation together with the momentum equation. The continuity equation for incompressible flows is shown in equation 1 and the momentum equation for an incompressible Newtonian flow is presented in

equation 2. In equation 1 and equation 2 $\boldsymbol{U}$ is a velocity vector, p the pressure, ρ the density, μ the molecular viscosity and $\boldsymbol{S_M}$ a momentum source.

$$\nabla \cdot \boldsymbol{U} = \frac{\partial U_x}{\partial x} + \frac{\partial U_y}{\partial y} + \frac{\partial U_z}{\partial z} = 0 \tag{1}$$

$$\rho \frac{D\boldsymbol{U}}{Dt} = \rho \left(\frac{\partial \boldsymbol{U}}{\partial t} + (\boldsymbol{U} \cdot \nabla)\boldsymbol{U} \right) = -\nabla p + \mu \nabla^2 \boldsymbol{U} + \boldsymbol{S_M} \tag{2}$$

The continuity equation (equation 1) is derived based on mass conservation, and it can be interpreted such that the sum of all flows entering and leaving a volume or point in space must cancel out if the flow is incompressible.

The momentum equation (equation 2) consist of three equations in a three-dimensional space and its components are formulated in equations 3. The momentum source $\boldsymbol{S_M}$ is the sum of all external forces acting on a fluid and one of the most common momentum sources in a fluid is gravity. If the gravity is the only momentum source considered $\boldsymbol{S_M}$ is replaced with $\rho \boldsymbol{g}$ where $\boldsymbol{g}$ is the gravitational acceleration vector.

$$\begin{aligned}
\rho \left(\frac{\partial U_x}{\partial t} + U_x \frac{\partial U_x}{\partial x} + U_y \frac{\partial U_x}{\partial y} + U_z \frac{\partial U_x}{\partial z} \right) &= -\frac{\partial p}{\partial x} + \mu \left(\frac{\partial^2 U_x}{\partial x^2} + \frac{\partial^2 U_x}{\partial y^2} + \frac{\partial^2 U_x}{\partial z^2} \right) + S_x \\
\rho \left(\frac{\partial U_y}{\partial t} + U_x \frac{\partial U_y}{\partial x} + U_y \frac{\partial U_y}{\partial y} + U_z \frac{\partial U_y}{\partial z} \right) &= -\frac{\partial p}{\partial y} + \mu \left(\frac{\partial^2 U_y}{\partial x^2} + \frac{\partial^2 U_y}{\partial y^2} + \frac{\partial^2 U_y}{\partial z^2} \right) + S_y \\
\rho \left(\frac{\partial U_z}{\partial t} + U_x \frac{\partial U_z}{\partial x} + U_y \frac{\partial U_z}{\partial y} + U_z \frac{\partial U_z}{\partial z} \right) &= -\frac{\partial p}{\partial z} + \mu \left(\frac{\partial^2 U_z}{\partial x^2} + \frac{\partial^2 U_z}{\partial y^2} + \frac{\partial^2 U_z}{\partial z^2} \right) + S_z
\end{aligned} \tag{3}$$

The derivation of the x-component in equation 3 will be presented in the following. It is based on Newton's second law, which states that the sum of external forces ($\boldsymbol{F}$) acting on an object must equal the mass (m) of that object times its acceleration ($\boldsymbol{a}$). This general form of Newton's second law is formulated in equation 4, and in equation 5 it is written in the form describing the rate of change of momentum in the x-component per volume unit of a control volume. In equation 5, $\sum F_x$ is the sum of forces per volume that act on the element in the x-direction, such as gravity, pressure and viscous forces. The total effect of the surface forces pressure and viscosity are shown in equation 6, where τ_{xx}, τ_{yx} and τ_{yx} are the viscous stresses acting on the fluid.

$$m\boldsymbol{a} = m \frac{D\boldsymbol{U}}{Dt} = \Sigma \boldsymbol{F} \tag{4}$$

$$\rho \frac{DU_x}{Dt} = \Sigma F_x \tag{5}$$

$$\Sigma F_{x,Viscous+Pressure} = \frac{\partial(-p + \tau_{xx})}{\partial x} + \frac{\partial \tau_{yx}}{\partial y} + \frac{\partial \tau_{zx}}{\partial z} \tag{6}$$

The viscous stresses τ acting on an incompressible Newtonian fluid are proportional to the fluids rate of deformation and the molecular viscosity μ, and they are defined according to equation 7.

$$\begin{bmatrix} \tau_{xx} & \tau_{xy} & \tau_{xz} \\ \tau_{yx} & \tau_{yy} & \tau_{yz} \\ \tau_{zx} & \tau_{zy} & \tau_{zz} \end{bmatrix} = 2\mu \begin{bmatrix} \frac{\partial U_x}{\partial x} & \frac{1}{2}\left(\frac{\partial U_x}{\partial y} + \frac{\partial U_y}{\partial x}\right) & \frac{1}{2}\left(\frac{\partial U_x}{\partial z} + \frac{\partial U_z}{\partial x}\right) \\ \frac{1}{2}\left(\frac{\partial U_x}{\partial y} + \frac{\partial U_y}{\partial x}\right) & \frac{\partial U_y}{\partial y} & \frac{1}{2}\left(\frac{\partial U_y}{\partial z} + \frac{\partial U_z}{\partial y}\right) \\ \frac{1}{2}\left(\frac{\partial U_x}{\partial z} + \frac{\partial U_z}{\partial x}\right) & \frac{1}{2}\left(\frac{\partial U_y}{\partial z} + \frac{\partial U_z}{\partial y}\right) & \frac{\partial U_z}{\partial z} \end{bmatrix} \quad (7)$$

When $\sum F_x$ in equation 5 is replaced with the forces from the pressure and the viscosity from equation 6, the general additional force S_x accounting for gravity etc. is added, and τ_{xx}, τ_{yx} and τ_{yx} are replaced with their expressions from equation 7. The x-component formulation of the incompressible Navier-Stokes equation (equation 8) is then reached. Equation 8 is equivalent to the x-component in equation 3, and the additional components (y and z) can be derived in a very similar manner.

$$\rho \frac{DU_x}{Dt} = \frac{\partial(-p + \tau_{xx})}{\partial x} + \frac{\partial \tau_{yx}}{\partial y} + \frac{\partial \tau_{zx}}{\partial z} + S_x \Rightarrow$$

$$\rho \frac{DU_x}{Dt} = -\frac{\partial p}{\partial x} + \mu\left(2\frac{\partial}{\partial x}\frac{\partial U_x}{\partial x} + \frac{\partial}{\partial y}\left(\frac{\partial U_x}{\partial y} + \frac{\partial U_y}{\partial x}\right) + \frac{\partial}{\partial z}\left(\frac{\partial U_x}{\partial z} + \frac{\partial U_z}{\partial x}\right)\right) + S_x \Leftrightarrow$$

$$\rho \frac{DU_x}{Dt} = -\frac{\partial p}{\partial x} + \mu\left(\frac{\partial^2 U_x}{\partial x^2} + \frac{\partial^2 U_x}{\partial y^2} + \frac{\partial^2 U_x}{\partial z^2} + \frac{\partial}{\partial x}\left(\frac{\partial U_x}{\partial x} + \frac{\partial U_y}{\partial x} + \frac{\partial U_z}{\partial x}\right)\right) + S_x \Leftrightarrow$$

$$\rho\left(\frac{\partial U_x}{\partial t} + U_x\frac{\partial U_x}{\partial x} + U_y\frac{\partial U_x}{\partial y} + U_z\frac{\partial U_x}{\partial z}\right) = -\frac{\partial p}{\partial x} + \mu\left(\frac{\partial^2 U_x}{\partial x^2} + \frac{\partial^2 U_x}{\partial y^2} + \frac{\partial^2 U_x}{\partial z^2}\right) + S_x \quad (8)$$

When analyzing the momentum equation for an incompressible, Newtonian fluid (equation 2 and 3) it can be seen that the first term on the left hand side represents the change of velocity over time inside a control volume. The remaining terms on the left hand side account for the change in velocity, or momentum to be precise, due to convection. The first term on the right hand side in the momentum equations is the change in pressure, which is nothing but a force pushing fluid from regions with higher pressures to regions with lower pressures.

The middle term on the right hand side in equation 8, i.e. the parenthesis that is multiplied with the viscosity, is the change in velocity due to viscous effects. Viscous effects should be thought of as diffusion of momentum, e.g. by the fact that momentum is more easily spread in a fluid with a high viscosity than in a fluid with lower viscosity. The source term S_x is as mentioned above an additional term accounting for additional forces that might be modelled such as gravity, centrifugal forces, electromagnetic forces or the pressure loss a fluid experience once moving through a porous material.

The continuity and momentum equations are, given the necessary boundary conditions, everything that is needed to describe a Newtonian, single-phase and laminar flow and its

corresponding pressure field in a three-dimensional space. In order to model fluid problems involving turbulent flows, multi-phase flow or flows through porous materials additional models (i.e. equations) must however be added to the continuity and momentum equations.

2.2.3. Dimensionless numbers in fluid flow

There are several dimensionless numbers related to flow phenomena and mass transfer that are all used in order to compare different kinds of flow and mass transfer situations to each other. One of the most known from the field of fluid dynamics is the Reynolds number, which for example is used to determine if a flow is expected to behave laminar or turbulent.

The Schmidt number and the Sherwood number are both related to mass transfer in terms of transfer of chemicals in a liquid, and they will both be presented in this section in order to keep the theory regarding dimensionless numbers together in one place. Subsequently the focus will return to the use of the Reynolds number and turbulent and laminar modelling.

2.2.3.1. The Reynolds number

The Reynolds number is a dimensionless quantity that can be calculated for a flow by multiplying a characteristic length and a characteristic velocity related to the flow, and dividing it with the kinematic viscosity (dynamic viscosity/density) of the fluid.

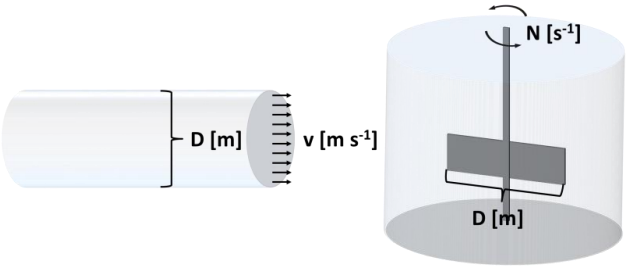

Figure 9. The definitions of the diameter *D*, the velocity v and the rotational speed *N* for flow in a tube (left) and for a stirred liquid (right).

The Reynolds number for a pipe flow is shown in equation 9 and the Reynolds number for a liquid stirred with an impeller is shown in equation 10. As can be most clearly seen in equation 9 the Reynolds number is the ratio between the inertial and viscous forces in a flow.

The definitions of *N*, υ and *D* are shown in Figure 9, and it can be seen that *D* is the diameter of the pipe associated with equation 9, but the diameter of the impeller for the case with the stirred liquid and equation 10. In equation 9 the velocity υ is also the averaged linear velocity, while *N* in equation 10 is defined as the rotational speed of the impeller. However, since the diameter *D* is squared in equation 10, the numerator has the same unit for both equation 9 and 10.

$$Re_{Pipe} = \frac{\upsilon D}{\upsilon} = \frac{\rho \upsilon D}{\mu} \tag{9}$$

$$Re_{Impeller} = \frac{ND^2}{\upsilon} = \frac{\rho ND^2}{\mu} \tag{10}$$

Important to note is also that the impeller Reynolds number does not take the radius of the reactor or other geometrical parameters than the impeller diameter into account, and therefore equation 10 is more representing the maximum Reynolds number in the liquid than the average value in it.

The Reynolds number is a very important measure of the characteristics of a flow and it arises from the non-dimensional analysis of the momentum equation. For showing this the x-component of the incompressible momentum equation (equation 8, with S_x set to zero) is scaled with the dimensionless variables introduced in equation 11, and the result is shown in equation 12. As can be seen equation 12 is very similar to equation 8, with the difference that it is now dimensionless and that the diffusion, or viscosity, term is scaled with the reciprocal Reynolds number. This means that for a large Reynolds number the impact of the viscosity term on the flow will be small, but for small Reynolds numbers it will be large.

$$\bar{x} = \frac{x}{L}, \bar{y} = \frac{y}{L}, \bar{z} = \frac{z}{L}, \bar{t} = \frac{tv_0}{L}, \overline{U_x} = \frac{U_x}{v_0}, \bar{p} = \frac{p}{\rho v_0^2} \tag{11}$$

$$\left(\frac{\partial \overline{U_x}}{\partial \bar{t}} + \overline{U_x}\frac{\partial \overline{U_x}}{\partial \bar{x}} + \overline{U_y}\frac{\partial \overline{U_x}}{\partial \bar{y}} + \overline{U_z}\frac{\partial \overline{U_x}}{\partial \bar{z}}\right) = -\frac{\partial \bar{p}}{\partial \bar{x}} + \frac{\mu}{v_0 L\rho}\left(\frac{\partial^2 \overline{U_x}}{\partial \bar{x}^2} + \frac{\partial^2 \overline{U_x}}{\partial \bar{y}^2} + \frac{\partial^2 \overline{U_x}}{\partial \bar{z}^2}\right) \tag{12}$$

This means that for a flow with a low Reynolds number the viscous forces will be dominant, while for a flow with a higher Reynolds number the inertial forces, i.e. those involving the inertia or momentum of the flow, will be the most important.

This makes the Reynolds number an important indicator when a flow is characterized as laminar or turbulent, since laminar flows are characterised by dominating viscous forces (i.e. low Reynolds numbers) and turbulent flows are characterized by dominating inertial forces (i.e. high Reynolds numbers). Exactly where a flow changes from laminar to turbulent is however different for different kinds of flows, and there is a large transient regime between laminar and fully turbulent flow. Empirical investigations are therefore often performed in order to determine if a flow is turbulent or not.

In pipes it is sometimes considered that laminar flows occur at Reynolds numbers smaller than 2100 and that the flow is turbulent for Reynolds numbers above 4000, leaving the regime $2100 < Re < 4000$ for transient flows. For stirred liquids on the other hand, laminar conditions are occasionally assumed for Reynolds numbers smaller than 10 and with a transient regime covering the Reynolds numbers 10-1000, after which turbulent flow is assumed to be fully developed (Doran (1995)).

The Reynolds number range for which a flow can be considered transient is not only different for different flows and geometries, there is also no consistent rule for how to define the Reynolds number for more complex flow and geometries. It is for example not always obvious which length and velocity scale to use for its calculation.

One example of a Reynolds number calculated for a rather complex geometry is presented in Eibl, Werner, and Eibl (2009), where the Reynolds number for a wave-type bioreactor is

derived. The critical Reynolds number, i.e. the Reynolds number where the flow could be considered turbulent, was then determined to lie between 200 and 1000 for different reactor types on the basis of visual observations (Eibl, Werner, and Eibl (2009)).

A third way to define the Reynolds number (other than equation 9 and equation 10) is to calculate it as the wall-bound Reynolds number, which will be further discussed in section 2.2.5.7. The Reynolds number can also be defined for the flow around a porous particle, which is presented in section 2.3.4.

2.2.3.2. The Schmidt number

The Schmidt number, defined in equation 13, can be used to estimate how thick a boundary layer is relative to mass diffusion and is calculated by the dynamic viscosity, the density and the diffusivity D_φ. The Schmidt number is for example important once studying mass transfer through film layers formed at solid surfaces. High viscosities induce thicker boundary layers at solid walls, meaning that a larger part of the mass transfer between the bulk flow and the solid surface will take place by mass diffusion. A higher viscosity gives a higher Schmidt number, which indicates that transport through a thick boundary layer takes longer than through a thin one. An increase in mass diffusion on the other hand decreases the Schmidt number, i.e. the diffusion through a boundary layer is faster the higher the mass diffusion coefficient.

$$Sc = \frac{Viscous\ diffusion\ rate}{Mass\ diffusion\ rate} = \frac{\mu}{\rho D_\varphi} \tag{13}$$

2.2.3.3. The Sherwood number

The Sherwood number can be used to estimate how important mass diffusion is relative to the total mass transfer in a system. The Sherwood number is defined in equation 14 where k_S is the mass transfer coefficient and l_0 a characteristic length. In this project, the Sherwood number has been used to calculate the value of k_S around solid particles and therefore l_0 has been defined as the diameter of the particles.

A small Sherwood number means that the impact of diffusion is important relative to the total mass transfer, and if it is very big it means the opposite, i.e. that diffusion is insignificant. An example of systems with low Sherwood numbers are laminar systems, since the diffusion there is dependent on molecular diffusion due to a lack of turbulent eddies. In systems with a lot of turbulent mixing the impact of molecular diffusion relative to the contribution of the turbulent eddies is low. The Sherwood numbers are therefore high in such systems.

$$Sh = \frac{Total\ mass\ transfer\ rate}{Mass\ diffusion\ rate} = \frac{k_s l_0}{D_\varphi} \tag{14}$$

The Sherwood number can be modelled by various empirical equations and is often written as a function of the Schmidt and the Reynolds number of a system as shown in equation 15. In equation 15 a, b, α and β are constants that are differently defined in different applications, but the general trend shows that the Sherwood number increases both with increasing values of the Schmidt number and the Reynolds number.

$$Sh = a + bRe^{\alpha}Sc^{\beta} \quad (15)$$

In equation 15 the Sherwood number is a function of the Reynolds number. This can be interpreted as follows: the higher the Reynolds number is in a system, the higher is the tendency for turbulence and the more turbulence the smaller the impact of molecular diffusion.

2.2.4. Laminar and turbulent flows

As stated above laminar flow occurs at small Reynolds numbers, i.e. when the inertial forces in a fluid are relatively small compared to the viscous forces. When considering a steady flow in a pipe, a laminar flow is characterized by all velocity vectors or streamlines moving along the length of the pipe and parallel to each other. This parallel and constant flow pattern has the consequence that the spread of molecules or momentum along the radial axis of the pipe is very low since it is caused by diffusion only.

With an increasing Reynolds number, the flow will become more and more unstable. The streamlines will for example no longer be all parallel to the length of the pipe but they will oscillate and become unstable, even in a constant geometry with a constant inlet velocity. At even higher Reynolds number, a fully turbulent flow will develop and the flow will consist of a wide range of turbulent and chaotic motions in all directions of the flow, even if the main flow in average is still moving in the axial direction.

A higher viscosity will decrease the Reynolds number of an otherwise equal flow and will therefore decrease the turbulence in it. The reason why a more viscous fluid has a larger ability to maintain a laminar flow is that viscosity per definition is the ability of a fluid to transport momentum and equilibrate velocity gradients. This means that a more viscous fluid will have smaller gradients in its velocity field, which decreases the chance of developing instabilities and turbulent behavior in the flow.

A fully developed turbulent flow consist of so called eddies, which are rotating units of flow with different length and time scales. These eddies move in all three dimensions in space and they are not steady over time, not even under static flow conditions. They also interact with each other, and will split into smaller and smaller eddies until they are so small that their kinetic energy is absorbed by the viscous forces of the liquid.

An illustration of the difference between laminar and turbulent flow is provided in Figure 10. As already stated, the spread of momentum or molecules is low in the perpendicular direction of a laminar flow, since there are no streamlines or velocities in that direction which can help to spread the molecules or the momentum. In a turbulent flow field on the other hand, both momentum and mass (molecules) can easily spread perpendicular to the main flow assisted by the motions of the turbulent eddies that act in all directions.

There are several important differences to note between laminar and turbulent flow. First, mass transfer and mixing is more effective in turbulent systems. In addition, since the turbulent eddies carry momentum with them in all directions in space, it also increases the apparent viscosity of the flow, since it has the same effect (momentum being more effectively spread) as an increased molecular viscosity term. Finally, the presence of turbulence will increase the energy losses in a moving liquid, since the viscous interactions in it increase.

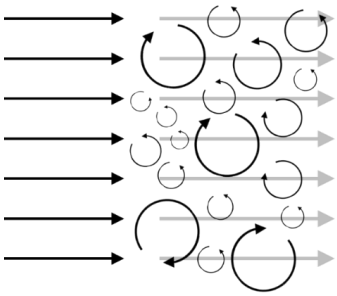

Figure 10. An illustration of the flow patterns in laminar (left) and turbulent (right) flow.

2.2.5. Simulating turbulent flow using CFD

2.2.5.1. Modelling turbulent flows in CFD

Simulating turbulence directly using CFD is very challenging due to its chaotic nature and the wide range of time and length scales the turbulent eddies consist of. There are methods available for direct modelling of turbulent flow, based on transient simulations of the continuity and the momentum equations, but such simulations are very computationally demanding. They are demanding since they are transient by definition, and since they require both very small time-steps and very fine computational meshes in order to model the behavior of the turbulent eddies correctly.

Fortunately, direct modelling of turbulence is not always necessary, since it in many applications are more important to model the general characteristics of a flow than to know exactly how eddies are expected to behave. Turbulence models are then often applied which are able to model the general outcomes of a turbulent flow (e.g. higher apparent viscosities and improved mixing) without actually modelling the turbulent eddies.

The turbulence models used in this projects all belongs to the RANS (Reynolds Averaged Navier-Stokes)-family and the sub-group *two-equation models*. This means that they all model the expected increase of viscosity in a turbulent fluid by adding two extra equations to the flow equations, i.e. to the momentum and continuity equations, which are slightly re-formulated. The RANS equations are also time averaged, which means that they can model a turbulent flow (that is transient by nature) in a time independent (steady-state) manner.

Time averaging changes the appearance of the momentum equations and adds a term accounting for turbulent viscosity to them. The theory behind this and the different turbulence models used to model the turbulent viscosity will be presented in the following sections. The boundary conditions for turbulent flow will also be discussed shortly.

2.2.5.2. The Reynolds Averaged Navier Stokes (RANS) equations

The most common kind of turbulence model is the RANS (Reynolds Averaged Navier-Stokes) based class of models, which assume that turbulent flow consists of a mean time flow value $\overline{U}_i$ and a fluctuating component u_i according to equation 16. By definition, the mean flow $\overline{U}_i$ is steady over time for a steady flow, while U_i and u_i vary over time. This means that the mean value of U_i over time is equal to the value of $\overline{U}_i$, since the time averaged value of u_i

also is zero per definition. The index *i* (and in further equations *j*) in equation 16 can be either x, y or z to represent all three dimensions.

$$U_i = \overline{U}_i + u_i \tag{16}$$

Once re-rewriting the continuity equation (1) with this notation and performing a time averaging it results in equation 17, which is equivalent to equation 1. The reason for this is that the divergence of the time averaged velocity vector $\overline{\boldsymbol{U}}$ becomes equal to the not time-averaged vector $\boldsymbol{U}$.

$$\nabla \cdot \overline{\boldsymbol{U}} = \nabla \cdot \boldsymbol{U} = \frac{\partial U_x}{\partial x} + \frac{\partial U_y}{\partial y} + \frac{\partial U_z}{\partial z} = 0 \tag{17}$$

The momentum equation on the other hand becomes slightly different, where inserting the notation from equation 16 into the x-component of equation 2 and time averaging results in equation 18.

$$\rho \frac{DU_x}{Dt} = -\frac{\partial p}{\partial x} + \mu \left(\frac{\partial^2 U_x}{\partial x^2} + \frac{\partial^2 U_x}{\partial y^2} + \frac{\partial^2 U_x}{\partial z^2} \right) + S_x - \rho \left[\frac{\partial \overline{u_x u_x}}{\partial x} + \frac{\partial \overline{u_x u_y}}{\partial y} + \frac{\partial \overline{u_x u_z}}{\partial z} \right] \tag{18}$$

In equation 18 the newly appeared terms $\rho \overline{u_i u_j}$ are called Reynolds stresses, and they are the time-averaged values of the fluctuating velocity components multiplied with the density. The main challenge with the Reynolds stresses is that they cannot be derived from the flow directly, which means that they must be modelled. The most common way to model the Reynolds stresses used in CFD software is presented in the next section.

2.2.5.3. The eddy viscosity turbulence models

One way to describe the unknown Reynolds stresses is to use the eddy viscosity model proposed by Boussinesq in 1877. The idea behind the eddy viscosity model is that there is a correlation between the Reynolds stresses and the rate of deformation of a fluid. This correlation is, for an incompressible fluid, shown in equation 19, where δ_{ij} is the Kronecker delta. The Kronecker delta is by definition one when *i* and *j* are equal and is otherwise zero. Turbulence models modelling the Reynolds stresses according to equation 19 are classified as eddy viscosity turbulence models.

$$-\rho \overline{u_i u_j} = \mu_t \left(\frac{\partial U_i}{\partial x_j} + \frac{\partial U_j}{\partial x_i} \right) - \frac{2}{3} \delta_{ij} \rho k \tag{19}$$

In equation 19 *k* is the turbulent kinetic energy, i.e. the kinetic energy of the fluctuating components and it has the SI unit m^2/s^2. The definition of *k* is shown in equation 20. The newly introduced μ_t is the turbulent viscosity and will be further explained below.

$$k = \frac{1}{2} u_i^2 \tag{20}$$

Inserting equation 19 into equation 18, rearranging, and repeating the same procedure for the y and z components, results in equation 21.

$$\rho \frac{D\boldsymbol{U}}{Dt} = \rho \left(\frac{\partial \boldsymbol{U}}{\partial t} + (\boldsymbol{U} \cdot \nabla)\boldsymbol{U} \right) = -\nabla p - \frac{2}{3}\rho \nabla k + \nabla \cdot (\mu + \mu_t)\nabla \boldsymbol{U} + \boldsymbol{S_M} \quad (21)$$

Equation 21 is very similar to equation 2 and they only differ by the addition of the turbulent kinetic energy term and the addition of μ_t. The term with the sum of μ_t and μ is now also positioned after the first nabla symbol (∇) since there is no guarantee that μ_t is constant.

The kinetic energy and the turbulent viscosity appearing in equation 19 are unknown and need to be modelled. This is also the purpose of the eddy viscosity model, i.e. trading three unknown Reynolds stresses per dimension to two unknown variables, i.e. the eddy viscosity and the kinetic energy. The default setting in ANSYS CFX 15.0 is however disregarding the term containing the turbulent kinetic energy in equation 19 and 21, which has the effect that nine Reynolds stresses (for three dimensions) are replaced with one new variable, i.e. the turbulent viscosity. The momentum equation that is used for turbulent modelling in CFX 15.0 is shown in equation 22, where p' represents a slightly modified pressure accounting for the fact that the term involving the turbulent kinetic energy has been omitted. The effective viscosity μ_{eff} in equation 22 is the sum of the molecular dynamic viscosity μ and the eddy viscosity μ_t.

$$\rho \frac{D\boldsymbol{U}}{Dt} = \rho \left(\frac{\partial \boldsymbol{U}}{\partial t} + (\boldsymbol{U} \cdot \nabla)\boldsymbol{U} \right) = -\nabla p' + \nabla \cdot \mu_{eff} \nabla \boldsymbol{U} + \boldsymbol{S_M} \quad (22)$$

There are several eddy viscosity turbulence models available and a common feature for them is that they all aim to model the eddy viscosity μ_t for direct insertion into equation 22. One common class of the eddy viscosity turbulence models is the two-equation models, which add two additional equations to the system to be solved. Three examples of these are the k-ε, k-ω and SST models. They will be explained in the next section and it will be shown how they all model the turbulent viscosity μ_t in slightly different manners.

Before explaining these turbulence models, a few more variables related to turbulent flow must however be introduced. First, there is the turbulent energy dissipation rate ε, which is the rate at which turbulent kinetic energy is absorbed by the liquid from the smallest eddies. The turbulent energy dissipation rate is defined according to equation 23 and has the unit m^2/s^3.

$$\varepsilon = \frac{\rho}{\mu} \left(\frac{\partial u_i}{\partial x_j} \right)^2 \quad (23)$$

From ε (equation 23) and k (equation 20) a turbulent frequency ω (equation 24) with the unit the unit s^{-1} can be defined.

$$\omega = \frac{\varepsilon}{k} \quad (24)$$

The correlation in equation 24 means that if two of the variables ε, k or ω are known, the third one can always be calculated. Two commonly used two-equation models are the k-ε and the k-ω model that both add two variables and two equations to the continuity and momentum equations. As strongly suggested by their names the k-ε turbulence model is modelling k and ε, while the k-ω model models k and ω. It is however straightforward to

calculate the turbulent energy dissipation rate ε in a simulation that uses the k-ω turbulence model by applying equation 24.

2.2.5.4. The k-ε and the k-ω turbulence model

As explained above the eddy viscosity turbulence models are used to calculate the eddy viscosities for direct insertion into the time averaged momentum equations (equation 22) in order to model the effect of the turbulence on the mean flow. The turbulent viscosity term is calculated according to equation 25 for the k-ε turbulence model and according to equation 26 for the k-ω model.

$$\mu_t = 0.09\rho\frac{k^2}{\varepsilon} \tag{25}$$

$$\mu_t = \rho\frac{k}{\omega} \tag{26}$$

The k-ε and the k-ω models also add two equations each for the modelling of their respectively newly introduced turbulent variables. Equation 27 and 28 show the equations for the standard k-ε model with the default values for the modelling parameters as implemented in ANSYS CFX 15.0. In the format written here the turbulence equations are neither accounting for compressible flows nor the effect of buoyancy since that was not modelled within this PhD project.

From the appearance of the equations 27 and 28, it can be seen that they are both similar to the momentum equation (equation 2). They both relate the change of k or ε over time to its spread due to convection (second term, left hand side) and due to diffusive effects (first term, right hand side) based on both the turbulent and the dynamic viscosity. Both equations also contain a production term (second term, right hand side) and a dissipation term (third term, right hand side) each. The production and dissipation terms are analogous to the source terms in the momentum equations.

$$\frac{\partial(\rho k)}{\partial t} + \nabla\cdot(\rho k\boldsymbol{U}) = \nabla\cdot[(\mu+\mu_t)\nabla k] + P_k - \rho\varepsilon \tag{27}$$

$$\frac{\partial(\rho\varepsilon)}{\partial t} + \nabla\cdot(\rho\varepsilon\boldsymbol{U}) = \nabla\cdot\left[(\mu+\frac{\mu_t}{1.3})\nabla\varepsilon\right] + \frac{1.44P_k\varepsilon}{k} - \frac{1.92\rho\varepsilon^2}{k} \tag{28}$$

The production term P_k in equations 27 and 28 is defined in equation 29 and is the scalar product of the tensor describing the rate of deformation (equation 30) of an element. The full expansion of equation 29 (divided by μ) can be seen in equation 7. The fact that the production of turbulence is dependent on the rates of deformation of an element is logical, since more turbulence is expected to be created in regions with high velocity or momentum gradients. Likewise, less turbulence is expected to be formed in regions with a more uniform flow.

$$P_k = \frac{1}{2}\mu_t S_{ij}S_{ij} \tag{29}$$

$$S_{ij} = \frac{\partial U_j}{\partial x_i} + \frac{\partial U_i}{\partial x_j} \tag{30}$$

In the Wilcox k-ω model, which is the standard k-ω model applied in ANSYS CFX 15.0, the two additional equations are shown in equation 31 and equation 32. The production term P_k is the same in the k-ω model as in the k-ε model, i.e. the expression in equation 29.

$$\frac{\partial(\rho k)}{\partial t} + \nabla \cdot (\rho k \boldsymbol{U}) = \nabla \cdot \left[(\mu + \frac{\mu_t}{2})\nabla k\right] + P_k - 0.09\rho k\omega \tag{31}$$

$$\frac{\partial(\rho \omega)}{\partial t} + \nabla \cdot (\rho \omega \boldsymbol{U}) = \nabla \cdot \left[(\mu + \frac{\mu_t}{2})\nabla \omega\right] + \frac{5}{9}\frac{\omega}{k}P_k - 0.075\rho\omega^2 \tag{32}$$

When the equations for the k-ε model (27 and 28) are compared to the ones for the k-ω model (31 and 32) *k* it can be seen that they are very similar and have the same structure, except the change of ε to ω and the division by k in the production and dissipation terms in the k-ω model. The values of a few of the numerical constants are also different between the equations.

There are a few different versions of the k-ε and the k-ω model. Two that are mentioned in the literature review part of this thesis are the realizable k-ε and the RNG k-ε model. The RNG k-ε model differs from the standard model by having a few different constants in the equations, i.e. in equation 27 and equation 28 (ANSYS® Academic Research (2013)). The realizable k-ε model has an alternative way to model the eddy viscosity, and it has a slightly modified equation for ε equation 27 (ANSYS® Academic Research (2013)).

2.2.5.5. The shear stress transport (SST) turbulence model

The third two-equation turbulence model involved in this project, i.e. the shear stress transport (SST) model, will be introduced now. It can be interpreted as a combination of the k-ω and the k-ε models and it is developed to behave like the k-ω model close to surfaces/walls in the simulation and to act as the k-ε model in the free stream further away from any walls.

In the derivation of the SST model, the ε term in the k-ε equation (equation 28) was rewritten in order to describe the spread of ω instead of ε. The equations describing k in both models (27 and 31) were then combined into a new equation (33) describing the spread of k. In equation 33 σ_A is a linear combination of the corresponding coefficients in equation 27 and equation 31, i.e. a linear combination of the values 1 and 2 that are the constants the eddy viscosity is divided by in the respective equations.

$$\frac{\partial(\rho k)}{\partial t} + \nabla \cdot (\rho k \boldsymbol{U}) = \nabla \cdot \left[(\mu + \frac{\mu_t}{\sigma_A})\nabla k\right] + P_k - 0.09\rho k\omega \tag{33}$$

The rewritten ε-equation of the k-ε model (not shown) was then combined with the ω-part of the k-ω equation (equation 32) and the result is displayed in equation 34. The constants $\sigma_{B,}\sigma_C$ and σ_D are also linear combinations of the constants in the original equations. The linear combination is performed using the blending factor F_1, and this blending factor is involved in one of the terms in equation 34.

The blending factor takes the value 1 at the boundaries defined as walls in a geometry, and its value decreases further away from any boundary. Far away from any walls, i.e. in the free stream or in the bulk fluid, it takes the value 0. The exact equation used to calculate the blending factor F_1 can be found in the ANSYS CFX 15.0 manual.

$$\frac{\partial(\rho\omega)}{\partial t} + \nabla \cdot (\rho\omega \boldsymbol{U}) = \nabla \cdot \left[\left(\mu + \frac{\mu_t}{\sigma_B}\right)\nabla\omega\right] + \sigma_C \frac{\omega}{k} P_k - \sigma_D \rho\omega^2 + (1 - F_1) 2\rho \frac{0.856}{\omega} \nabla k \nabla \omega \quad (34)$$

How the linear combination is performed for σ_A based on the contributions from the k-ε and the k-ω models is shown in equation 35, which is also applicable for σ_B and σ_C. It is clear that once F_1 is one, i.e. at the walls, the equations 33 and 34 will take the same constant values as the k-ω model uses. For smaller values of F_1, the constants used in the k-ε model will become more influential.

$$\sigma_A = (1 - F_1)\sigma_{A,k\varepsilon} + F_1 \sigma_{A,k\omega} \quad (35)$$

One important difference between the SST, the k-ω and the k-ε model in ANSYS CFX 15.0 is that the default settings for the SST and k-ω models include a product limiter that controls the maximum value of the turbulence production term P_k, (equation 29). This product limiter has the effect that the production of turbulence in a point cannot become too big, which can be an advantage in order to avoid build-up of turbulence in regions with high rates of deformation as calculated in equation 29. The SST model in ANSYS CFX 15.0 also uses a limiter for the eddy viscosity (equation 26) to prevent it from becoming too large.

2.2.5.6. The dispersed phase zero equation

The dispersed phase zero equation is an optional turbulence model to use once modelling multi-phase and dispersed flows. Modelling of multi-phase and dispersed flows is presented in section 2.2.9, where also the terms continuous and dispersed are further explained. In multi-phase flow modelling, it is possible to use the standard k-ε or SST turbulence model for the continuous phase and using the dispersed phase zero equation for the dispersed phase. Doing this, no additional turbulent model equations are actually solved for the dispersed phase, but the turbulent viscosity of it is calculated based on the value of the turbulent viscosity in the continuous phase. For a dispersed phase β in the continuous phase α, the eddy viscosity of phase β is calculated according to equation 36 once applying the dispersed phase zero equation.

$$\mu_\beta = \frac{\rho_\beta}{\rho_\alpha} \frac{\mu_\alpha}{\sigma} \quad (36)$$

In equation 36 σ is said to be the Turbulent Prandtl number and in ANSYS CFX 15.0, it is set to unity.

2.2.5.7. Wall functions associated with turbulent flow

As briefly mentioned in section 2.1.3 boundary conditions must be defined for all surfaces in a geometry. Velocities or pressure must for example be defined at inlets and outlets, and for solid walls it must be defined if they are so-called *free slip walls* or *no slip walls*. At *no slip walls* the tangential velocity is set to zero for a stationary wall or to a constant value if the wall is moving.

Fluid in the nodes closest to a *free slip wall* will "feel" the presence of the wall by the shear stresses it induces on it. The wall shear stress τ_w is defined in equation 37, where U is the velocity parallel to the wall and y is the distance perpendicular to the wall. The numerical values of the shear stresses at a *no slip wall* must be calculated by the solver and the impact of it is added to the momentum equations as slightly altered source terms. At a *free slip wall*-condition on the other hand the shear stresses are zero by definition, and the velocities in the nodes closest to the surface are calculated based on the overall flow in the geometry.

$$\tau_w = \mu \left(\frac{\partial U}{\partial y} \right)_{y=0} \tag{37}$$

If the k-ε or the k-ω turbulence models are being used, two extra variables (k and ε or k and ω) have been added to the system as described above, and this means that additional information also must be added to complete the boundary conditions. For an inlet boundary in a laminar simulation it is for example enough to specify only the velocities or pressures of the entering fluid, but once the flow is turbulent its content of k and ε (or k and ω) must also be defined at all inlets.

The values of the turbulent variables at solid walls must also be defined, and they cannot be set to zero. One reason for this is that equation 25 is undefined if ε is zero, i.e. if it is defined that no energy is dissipated close to the walls. Instead, the values of the turbulent quantities at the walls must be modelled. The shear stresses τ_w at the walls must also be modelled in a turbulent system, since they cannot always be calculated using the same method as they are at laminar walls. At laminar walls, the shear stresses are estimated based on equation 37.

However, in order to understand the behavior of a turbulent flow at a solid wall a few new concepts and variables must first be defined. First there is the wall-bounded Reynolds number Re_{Wall} that is defined in equation 38, where U is still the velocity parallel to the wall, y the distance to the wall and υ and μ the kinematic and the dynamic viscosity respectively.

$$Re_{Wall} = \frac{Uy}{\upsilon} = \frac{\rho U y}{\mu} \tag{38}$$

Closest to a wall, i.e. where the values of y and therefore the wall-bound Reynolds number is small, the turbulent eddies are not expected to have any effect on the flow, which means that the flow is only dependent on the viscous forces present. Farther away from the wall the inertial forces of the main flow are expected to have a larger impact on the flow profile, which makes it different compared to the profile closest to the wall.

The dimensionless distance to a wall used to determine if a point of evaluation is "close" or "far away" from its closest wall is called y^+ and is defined in equation 39.

$$y^+ = \frac{\rho u_\tau y}{\mu} \tag{39}$$

Equation 39 is very similar to equation 38, but the velocity has been replaced with u_τ that is the friction (or shear) velocity defined in equation 40.

$$u_\tau = \sqrt{\frac{\tau_w}{\rho}} \tag{40}$$

Based on the friction velocity also the dimensionless velocity u^+, shown in equation 41, can be defined.

$$u^+ = \frac{U}{u_\tau} \tag{41}$$

Closest to the wall (where y^+<5) the dimensionless velocity u^+ can be assumed to be linear to y^+ and this region is therefore referred to as the viscous or the linear sub-layer. Further out from the wall (30 < y^+ <500) is the so-called log-law layer where the dimensionless velocity is a logarithmic function of the distance to y^+ as shown in equation 42. The constants used in equation 42 (0.41 and 5.2) are those used in ANSYS CFX 15.0 for smooth walls.

$$u^+ = \frac{ln(y^+)}{0.41} + 5.2 \tag{42}$$

The region between the viscous and the low-law region (i.e. where 5 < y^+ <30) is assumed to be a combination of these, but has no equation on its own. The appearance of how the dimensionless velocities vary with y^+ is shown in Figure 11 where also the intersection between the two lines at 11.06 is pointed out. Before this limit, i.e. where y^+ < 11.06, the viscous red flow profile is assumed, and for higher values of y^+ the blue logarithmic appearance of u^+ is expected.

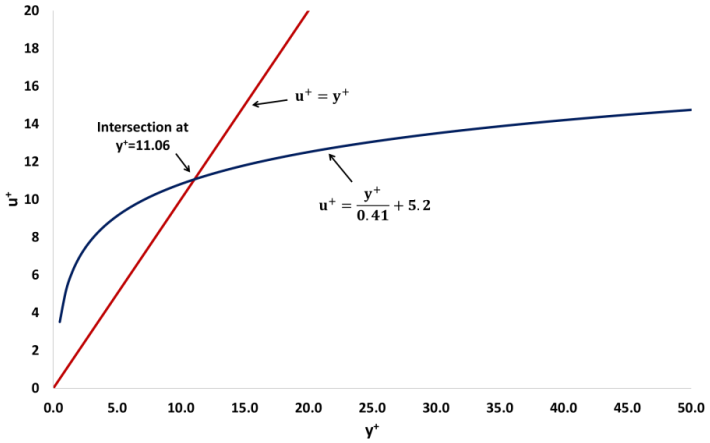

Figure 11. The dimensionless velocity u^+ as a function of the dimensionless wall distance y^+ for the linear (red) and the logarithmic correlation (blue).

Choosing the correct value of u^+ is important since it is one of the variables used when the solver calculates the wall stresses and the turbulent quantities at the walls. Exactly how the solver calculates these values is alternating for different turbulence models and solvers, but by default ANSYS CFX 15.0 uses the *scalable wall function* for the k-ε turbulence model and the *automatic wall function* for the k-ω and the SST model.

These wall functions however are no single functions, but rather concepts on how to handle wall treatment for the different turbulence models. One feature the wall functions have in common is that they both calculate the value of y^+ at each node adjacent to a *no slip wall* and use this value for further calculations. The value of y^+ is directly proportional to the physical distance each node has to the wall, which means that mesh refinement at a boundary will move the boundary nodes closeser to the wall and therefore decrease the values of y^+.

The scalable wall function, i.e. the one associated with the k-ε model, always assumes that the y^+ value is located in the log-law region, which means that equation 42 is always used to calculate the values of u^+ and the resulting values of τ_w, k and ε. One interesting detail to note is also that ε is calculated as function of k in the scalable wall function. If the calculated value of y^+ in a node is smaller than 11.06, the scalable wall function will round it up to 11.06. This means that the viscous boundary layer is never modelled using the k-ε model, since the values of τ_w, k and ε at the walls is always calculated as if they were located in the log-law region.

The automatic wall function (used for the k-ω and the SST model) can however simulate nodes located within the viscous sublayer, i.e. where $y^+ < 11.06$. This is achieved by using different equations for the calculations of ω at the walls dependent on whether y^+ is larger or smaller than 11.06. The value of k at the walls is set to zero for all values of y^+. The shear stress τ_w is calculated as well using a blend function based on the distance to the wall. This means that for very low values of y^+ τ_w is calculated very similarly to as it is in laminar, flows but for higher values it is calculated more and more based on the log-law profile in equation 42.

To summarize, both the automatic and the scalable wall functions evaluate the values of y^+ and use it to calculate the shear stresses and turbulent variables. The automatic wall function is however more flexible since it can model wall flow both in the viscous sublayer and in the log-law region, i.e. it can model wall-bound flow both in the low and high Reynolds number regime. For low wall-bound Reynolds numbers, e.g. if the mesh is very fine and the wall-bound node is very close to the wall, it can set up boundary conditions very similar to those of a laminar flow. For high values of y^+, the automatic wall function can adapt and provide boundary conditions adapted for a more turbulent wall flow.

The scalable wall function is however only suitable for higher wall-bound Reynolds numbers since it always assumes that the flow by the boundary is located in the y^+ regime.

2.2.6. Additional variables

Additional variables are user-defined scalars or vectors that can be simulated using ANSYS CFX 15.0. An example of a vector quantity already defined in the software is the velocity vector $\boldsymbol{U}$ and examples of already defined scalars are temperature, pressure or the turbulent energy dissipation rate. Scalar additional variables are commonly used to represent chemicals or colour dyes and they can then be used to model mixing phenomena or chemical reactions.

Scalar additional variables will from now on be referred to as additional variables since their vector counterparts have not been used within this project.

The general equation for a scalar φ spread in the velocity field $\boldsymbol{U}$ can be seen in equation 43. The first term on the left hand side represents the change in the scalar over time and the second the spread of the scalar due to convection. The first term on the right side is the diffusion term, which includes the gradient of the scalar itself accounting for the fact that the apparent diffusion is higher once higher gradients are present. The second term on the right hand side is the source coefficient. Sources can for example be used for modelling chemical reactions in order to simulate consumption or production of the additional variables.

In equation 43 D_φ is the diffusivity coefficient and since it varies from case to case, the user must specify its value to the software.

The diffusion term also includes the turbulent viscosity μ_t as defined in equation 25 or 26 if a turbulence model is activated. If no turbulence model is used, i.e. if the system is modelled as laminar, the turbulent viscosity is set to zero. The turbulent viscosity is divided by the turbulent Schmidt number Sc_t, which has the default value 0.9 in ANSYS CFX 15.0.

$$\frac{\partial(\rho\varphi)}{\partial t} + \nabla \cdot (\rho \boldsymbol{U} \varphi) = \nabla \cdot \left(\left(\rho D_\varphi + \frac{\mu_t}{Sc_t} \right) \nabla \varphi \right) + S_\varphi \tag{43}$$

Two different additional variable scalar types are available in ANSYS CFX 15.0: Volumetric and Specific. According to the documentation the solver does always model the specific variable, but can transform it to its volumetric counterpart in the post-processing by multiplication with the fluid density (ANSYS® Academic Research (2013)).

In ANSYS CFX 15.0, it is also possible to use additional variables for storage of variable values or numerical data not modelled in equation 43, or even present in the fluid. The term additional variable is however used in this project to refer to the fluid-bound scalar described above unless explicitly stated otherwise.

2.2.7. Modelling of porous material

One way to model porous material using ANSYS CFX 15.0 is to use to the so-called full porous model. In this model, altered versions of the continuity and the momentum equations are applied. For an incompressible and Newtonian fluid with the constant volume fraction γ (i.e. where the porous material takes up a fraction 1-γ of the space) the altered momentum equations are shown in equation 44. For an incompressible and Newtonian fluid with a constant value of γ, the continuity equation is the same as shown in equation 1, i.e. the ordinary one.

$$\rho\gamma \left(\frac{\partial \boldsymbol{U}}{\partial t} + (\boldsymbol{U} \cdot \nabla)\boldsymbol{U} \right) = -\gamma \nabla p + \nabla \cdot \gamma\mu \nabla \boldsymbol{U} + \gamma \boldsymbol{S_M} \tag{44}$$

In equation 44 μ is still the viscosity, either the molecular viscosity once a laminar flow is modelled or the effective viscosity (μ+μ_t) if the flow is modelled as turbulent. The momentum source $\mathbf{S_M}$ has also received an extra term for porous flow modelling, which is caused by the extra resistance of the porous material that is expected to interact with the fluid.

If the porous material is assumed isotropic, i.e. if the pressure losses in it are equal in all directions, the resistances added to the momentum sources are modelled according to equation 45, where C_1 and C_2 are the linear and quadratic loss coefficients.

$$\begin{aligned} S_{M,x} &= C_1 U_x - C_2 |\boldsymbol{U}| U_x \\ S_{M,y} &= C_1 U_y - C_2 |\boldsymbol{U}| U_y \\ S_{M,z} &= C_1 U_z - C_2 |\boldsymbol{U}| U_z \end{aligned} \tag{45}$$

2.2.8. Modelling of rotating geometries

2.2.8.1. Modelling of rotational domains

When rotating systems such as impellers are simulated, it is often necessary to use rotating domains in order to model their motions correctly. An example is shown in Figure 12, where on the left hand side it is desired to model a rotation of the star-like rotor in the middle of the figure, while the outer walls should be standing still.

Using moving wall boundary conditions is not possible here, and instead two different domains must be defined. The orange fluid domain in the picture to the left should therefore be separated into one rotating and one stationary domain. The results are presented in the picture to the right, where the pink geometry closest to the impeller has been defined as a rotating domain. The wall velocity of the star structure should be set to zero in the rotating domain, since that corresponds to a rotation in the stationary domain. The rotational speed of the rotating domain can be set arbitrary by the user.

A domain interface arises between the two domains, and handling of such an interface will be discussed in the next section.

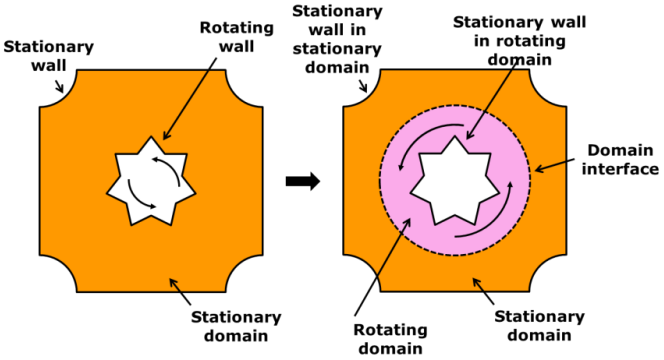

Figure 12. Modelling of a rotating system using one rotational (pink) and one static (orange) domain.

For the rotating domains, extra forces are added to the momentum source, namely the actions of the Coriolis and the centrifugal forces. These extra forces are added to the momentum source $\mathbf{S_M}$ in the momentum equations (e.g. to equation 2). The extra contribution to the momentum sources caused by the Coriolis and the centrifugal force in the rotating domains are show in equation 46 and in equation 47. In equation 46 and 47 $\boldsymbol{\Omega}$ is the rotational velocity vector of the rotational domain and $\boldsymbol{r}$ the location vector. The directions of the forces in a rotating domain are visualized in Figure 13.

$$\boldsymbol{S_{Coriolis}} = -2\rho\boldsymbol{\Omega} \times \boldsymbol{U} \tag{46}$$

$$\boldsymbol{S_{Centrifugal}} = -\rho\boldsymbol{\Omega} \times (\boldsymbol{\Omega} \times \boldsymbol{r}) \tag{47}$$

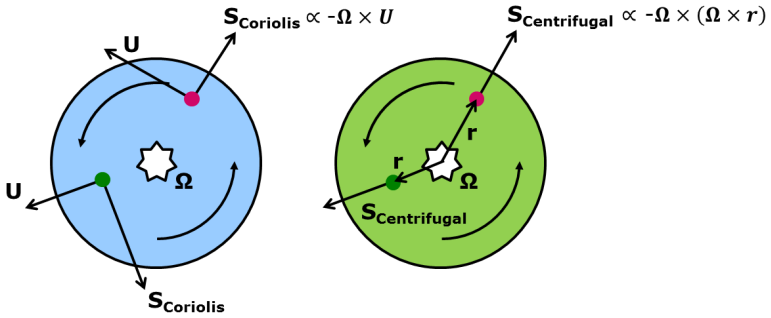

Figure 13. The direction of the Coriolis and the centrifugal forces on two particles located in a rotating domain. The Coriolis force is dependent on the particles own velocity **U** while the centrifugal force also affects static particles.

2.2.8.2. Modelling of rotational interfaces

Once modelling two domains with different relative rotations, such as the rotating and stationary domain in Figure 12, the interface between the two domains must be modelled in order to simulate the transfer of mass, momentum and additional variables etc. between the domains correctly.

There are three different methods available in ANSYS CFX 15.0 for modelling of such interface and two of those will be introduced here. The most advanced and accurate method is a transient method that actually rotates the rotating domain in each time step. This means that the geometry changes throughout the simulation as it does in reality, which for example can be important in geometries where both domains contain baffles. Transient simulations are however required for this type of interface, which is a drawback since they are much more computationally demanding than steady-state simulations. This method is occasionally referred to as a sliding interface.

An easier way to simulate the interface is to use the *Frozen rotor* approach. It means that the domains are frozen with respect to each other, e.g. that the position of baffles etc. in the geometry has a constant and locked in position. The drawback of this method is however just that the geometries are fixed and that transient behaviour caused by interacting baffles etc. cannot be captured by the model. Both transient and steady-state simulations can however be done using a *frozen rotor* interface so other kinds of transient simulations, e.g. mixing simulations, can still be performed. The *frozen rotor* approach is also referred to as the *Multiple Reference Frame* (MRF) model.

2.2.9. Multi-phase flow

2.2.9.1. Introduction to modelling of multi-phase flows

Many interesting flow situations within the field of bioprocessing and fermentation technology involve multi-phase flow, i.e. flows including two or more phases. In CFD, a multi-phase case is defined by the simulation of two or more phases that do not mix with each other on a microscopic scale such as air and water or water and oil. Water and ethanol is however not an example of a multi-phase system according to this definition, since water and ethanol do mix with each other on a molecular level. The water and oil example also points out that two fluids can have the same state of matter, i.e. both being liquids, and still be defined as a multi-phase system.

The simplest multi-phase flow situation is naturally a flow consisting of only two phases, and two-phase flow is the only multi-phase flow that is considered in this project. The theory presented will therefore only focus on two-phase flow, even if the software is capable of more. In addition, no phase-changes (e.g. evaporation or condensation) have been considered throughout this project, and such theoretical details have therefore been omitted from the following sections as well.

2.2.9.2. Continuous versus dispersed flow

According to the theory applied in ANSYS CFX 15.0 a two-phase flow can consist of either two continuous phases or one continuous phase and one dispersed phase. This means that when water and air is simulated the fluids can be considered either to be two continuous phases (e.g. water flowing through a semi-filled tank) or one dispersed phase in a continuous one. Both the water and the air can be simulated to be the dispersed phase, i.e. both water droplets in air and air bubbles in water are possible to model. Two dispersed phases can however not exist without a third, carrying, continuous phase.

2.2.9.3. The Euler-Euler versus the Euler-Lagrangian method in multi-phase modelling

There are two fundamentally different ways to model multi-phase flows in ANSYS CFX 15.0, the Euler-Lagrangian method and the Euler-Euler method. If considering a liquid with dispersed air bubbles, the Euler-Lagrangian method is based on simulating the water as a continuous phase and the bubbles as particles in it. The particles, or bubbles, follow then the velocities of the continuous phase but the continuity and the momentum equations are not solved for them. The particles have, however, the ability to affect the liquid phase, for example by momentum transfer. The particles in an Euler-Lagrangian simulation can also be modelled to interact with each other, for example by collisions.

One of the most characteristic features of the Euler-Lagrangian method is that the particles follow the streamlines in the continuous phase and that each individual particle, or group of particles, has a given position in the continuous phase in which they are defined. This means that Euler-Lagrangian simulations can become very computationally demanding with a large number of simulated particles, but also that the simulation does not become much heavier than a single-phase simulation if only a few particles are present.

In a two-phase Euler-Lagrangian simulation, it is also only possible to define one continuous phase and one dispersed phase, i.e. two continuous phases are not allowed. When the Euler-

Euler method is used, it is however possible to both model two phases as continuous and to model one of them as dispersed.

With the Euler-Euler method, all phases are accounted for in all locations in a geometry, compared to the Euler-Lagrangian where they are only accounted for exactly at the positions they have been transported to by the continuous flow. This makes the Euler-Euler method similar to one-phase simulations, where the equation variables (pressure, velocity) should be balanced in every single node in a geometry in order to satisfy the continuity and momentum equations etc.

This means that both fluids in a two-phase flow are accounted for everywhere in the geometry in an Euler-Euler simulation, i.e. that every node contains a volume fraction for each phase and that all relevant flow equations are solved everywhere.

The fact that all flow equations, e.g. the continuity and the momentum equations, are solved for both phases everywhere in the geometry regardless of how small volume fraction they may represent in certain regions, makes the method equally computationally demanding regardless of the distribution of the two fluids.

The Euler-Euler method is the only multi-phase modelling approach that has been considered within this project, which makes it the only method on which the following theory in this multi-phase section will focus.

2.2.9.4. Two-phase modelling using the Euler-Euler approach

In the derivations behind the two-phase Euler-Euler flow equations, a phase averaging was performed on the single-phase continuity and momentum equations. The phase averaging means that for a flow consisting of the two phases α and β every node is assigned a volume fraction of phase α (denoted r_α) and a volume fraction of phase β (denoted r_β). The information on where exactly α or β is supposed to be located within each point has therefore been lost. This has the consequence that there is no information in the two-phase continuity and momentum equations regarding whether one of the two phases is dispersed in the other or not, or if they are both continuous. Such information must therefore be provided by the user.

As stated above both phases in a two-phase simulation are present everywhere at all times, even if the volume fraction of one of the phases can be very small in certain regions. An additional demand for the volume fractions is that they must sum up to unity. For a two-phase system, this can be written as the constraint in equation 48.

$$r_\alpha + r_\beta = 1 \tag{48}$$

The continuity or mass conservation equation for each phase in a multi-phase system is shown in equation 49. In equation 49 α is interchangeable with β to describe the second phase, and any mass transfer between the phases (e.g. evaporation, condensation) has been disregarded. S_α is a mass source of a phase that can be implemented in special cases, but is zero by default.

One difference between the multi-phase continuity equation (equation 49) and the single-phase continuity equation (equation 1) is that the term including the density multiplied with the volume fraction term is present in the multi-phase case. This term is also indirectly present in the single-phase case, but since the volume fraction r_α is one for a single-phase flow, this term disappears in an incompressible single-phase fluid. For a two-phase fluid simulation, the volume fractions in a point are however allowed to vary, which also makes the total mass in a point variable given that the involved fluids have different densities.

$$\frac{\partial r_\alpha \rho_\alpha}{\partial t} + \nabla \cdot (r_\alpha \rho_\alpha \boldsymbol{U}) = \boldsymbol{S}_{M,\alpha} \tag{49}$$

There are two sub-groups of the Euler-Euler method available in ANSYS CFX 15.0, the homogenous and the inhomogeneous model. Both models apply the continuity equation shown in equation 49, but they differ in how they apply the momentum equations to the multi-phase flow. The main difference between the models is that the homogenous model uses a single velocity field for all participating fluids, while each fluid has its own velocity field in the inhomogeneous model. Both models will be presented below.

2.2.9.5. The inhomogeneous multi-phase model

The inhomogeneous model uses as stated above one vector field for each participating phase (e.g. $\boldsymbol{U}_\alpha$ and $\boldsymbol{U}_\beta$), but the scalar pressure field is shared between all phases. The momentum equations for the incompressible and Newtonian phase α involved in a two-phase simulation using the inhomogeneous approach are shown in equation 50. An important observation in equation 50 is that the velocity field, viscosity and density are phase dependent while the pressure field is not, which means that the second phase β shares its pressure field with the phase α but has an individual density etc.

$$\frac{\partial r_\alpha \rho_\alpha \boldsymbol{U}_\alpha}{\partial t} + (\boldsymbol{U}_\alpha \cdot \nabla) r_\alpha \rho_\alpha \boldsymbol{U}_\alpha = -r_\alpha \nabla p + \nabla \cdot r_\alpha \mu_\alpha \nabla \boldsymbol{U}_\alpha + \boldsymbol{S}_{M,\alpha} + \boldsymbol{M}_\alpha \tag{50}$$

The new term $\boldsymbol{M}_\alpha$ in equation 50 is the sum of the interfacial forces between the phases α and β. The interfacial forces act to equalize the momentum balances between the participating fluids in a flow. They are for example responsible for the fact that gas bubbles in a liquid stream tend to follow their carrier phase (to a certain extent) and they also explain why bubbles traveling through a liquid can induce movements in it. Several sub-models may be included in the interfacial force term $\boldsymbol{M}_\alpha$, and these will be discussed later in further detail.

One interesting aspect to note is that if a single-phase constraint is applied to equation 50, i.e. if r_α is set to unity everywhere and $\boldsymbol{M}_\alpha$ is set to zero, it becomes identical to the momentum equation for the single-phase flow displayed in equation 2.

When two phases are simulated using the inhomogeneous method, an entire new velocity field must be defined for the second phase. This means that three extra momentum equations are added if a three-dimensional flow is simulated, one for each vector component in space. In addition to this, one extra continuity equation is added and the two-phase equation system becomes even more complex once starting to account for the interfacial forces $\boldsymbol{M}_\alpha$. The homogenous model is however less computationally demanding than the inhomogeneous one, and it will be described in the next section.

2.2.9.6. The homogeneous multi-phase model

The homogenous multi-phase model uses the continuity equations shown in equation 49 and the same momentum equation as for single-phase flow, i.e. equation 2. The momentum equation is however slightly altered, since the viscosity and density terms in it are weighted based on the volume fraction of each phase. For a two-phase system with the phases α and β the densities and viscosities in each node are calculated as shown in equation 51 and 52.

$$\rho = \rho_\alpha r_\alpha + \rho_\beta r_\beta \tag{51}$$

$$\mu = \mu_\alpha r_\alpha + \mu_\beta r_\beta \tag{52}$$

Using equation 2, i.e. a single momentum equation, means that all participating phases share the same velocity (and pressure) field. One advantage with the homogenous model is that it is much less computationally demanding than the inhomogeneous one, since fewer equations are involved, but it has however severe disadvantages. One disadvantage is that it cannot model two-phase flow where the participating phases are expected to behave differently, for example if it is desired to model bubbles rising in a flowing liquid stream moving against the gravity.

2.2.9.7. Modelling of interfacial transfer phenomena

There is, as mentioned earlier, nothing in the two-phase momentum or continuity equations that states if the system consists of one continuous and one dispersed phase or if two continuous phases are considered, and that information must be provided by the user. The information is important for the simulations, since it for example affects the size of the interface between the phases.

In Figure 10 three areas are shown that each have a 50:50 distribution of the two phases orange and purple. In the first case both phases are illustrated as continuous and in the second and third case the orange phase is dispersed. It can clearly be seen that the choice between a continuous or dispersed second fluid, and the diameter of the dispersed fluid, has a direct impact on the size of the interface between the phases.

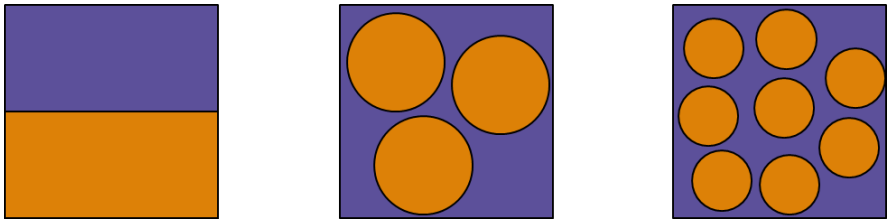

Figure 14. Two phases (orange and purple) either defined as two continuous phases or with the orange phase dispersed in the purple one. It can be clearly seen that the specific interfacial area between the phases varies between the three cases.

The relative size of the interface, i.e. the specific interfacial area, is important for the calculation of the interfacial transfer of momentum, mass and dissolved chemicals. One

example of mass transfer between the phases is evaporation of water droplets in air, a process that is faster the smaller the droplets are.

An example of interfacial transfer of chemicals is the transport of gaseous oxygen into the dissolved state in a liquid, which is also one of the most discussed mass transport processes in this project. However, transport of dissolved chemicals between two phases is often not regarded as mass transfer from a fluid dynamic point of view. The reason for this is that dissolved chemicals are often modelled as additional variables without any defined mass.

Interfacial transfer of mass and chemicals can be included both in the homogenous and in the inhomogeneous model, but transfer of momentum can only occur in the inhomogeneous model. The reason for this is that transfer of momentum per definition takes place between two separate velocity vector fields, and therefore cannot be applied on the homogenous model that only has one single velocity field.

In the inhomogeneous model, and in reality, the interfacial transfer of momentum is the reason explaining why dissolved bubbles in a stream somewhat follow the behavior of their carrying phase, and why bubble columns can have a non-zero velocity in their liquid phase.

The most commonly modelled interfacial force contributing to $\boldsymbol{M}_{\alpha}$ in equation 50 is the drag force that aims to equalize the velocities between the participating phases by transferring momentum from the faster to the slower liquid.

The drag force is available both when the second fluid is dispersed and when it is continuous, but again per definition only for inhomogeneous flows. The drag force vector between two fluids is defined in equation 53, where C_{Drag} is a constant or a function, ρ is the weighted density as calculated in equation 51 and $A_{\alpha\beta}$ is the specific interfacial area between the phases. Note that the contribution from phase α to phase β is negative if the velocity of β is higher than the velocity of α, and that the sum of the drag forces between α and β and β and α always balances out.

$$\boldsymbol{Drag\ force}_{\alpha\beta} = C_{Drag}\rho A_{\alpha\beta}\left|\boldsymbol{U}_{\alpha} - \boldsymbol{U}_{\beta}\right|\left(\boldsymbol{U}_{\beta} - \boldsymbol{U}_{\alpha}\right) \tag{53}$$

When modelling two continuous phases C_{Drag} is defined by the user and is then usually a constant referred to as the drag coefficient. For dispersed flows C_{Drag} can however be modelled, and there are several different options for this in ANSYS CFX 15.0. The recommended model for C_{Drag} in bubbly flows is the so-called Grace model, and a mathematical description of it can be found in the ANSYS CFX 15.0 manual.

In equation 53 $A_{\alpha\beta}$ is the specific interfacial area and how it is modelled is presented in the next section.

2.2.9.8. Modelling of specific interfacial areas

The specific interfacial area $A_{\alpha\beta}$ can be simulated in two different ways for two continuous phases in ANSYS CFX 15.0 and the options are using either the *mixture model* or the *free-surface model*.

In the *free-surface model*, $A_{\alpha\beta}$ is calculated according to equation 54, i.e. it is the absolute value of the gradients of the volume fractions in all involved directions. In the mixture model, $A_{\alpha\beta}$ is calculated according to equation 55, where $d_{\alpha\beta}$ is a user specified constant.

$$A_{\alpha\beta} = |\nabla r_\alpha| \tag{54}$$

$$A_{\alpha\beta} = \frac{r_\alpha r_\beta}{d_{\alpha\beta}} \tag{55}$$

For a dispersed phase, the specific interfacial area is theoretically calculated as shown in equation 56, where d_B is the bubble diameter and N the number of bubbles in a given volume. In ANSYS CFX 15.0, the value of r_α is however slightly altered before it is inserted in equation 56 in order to prevent the largest values of r_α to give overestimated values of $A_{\alpha\beta}$. The default version of the recalculation of r_α applied in ANSYS CFX 15.0 is shown in equation 57, and it ensures that the value of r_α decreases steadily towards 10^{-7} after reaching 0.8.

$$A_{\alpha\beta} = \frac{A_{interface}}{V_{\alpha+\beta}} = \frac{A_{interface}}{V_\alpha}\frac{V_\alpha}{V_{\alpha+\beta}} = \frac{\pi d_B^2 N}{\left(\frac{\pi d_B^3 N}{6}\right)} r_\alpha = \frac{6 r_\alpha}{d_B} \tag{56}$$

$$r_{\alpha,Altered} = \begin{cases} max(r_\alpha, 10^{-7}) & r_\alpha < 0.8 \\ max(4(1-r_\alpha), 10^{-7}) & r_\alpha > 0.8 \end{cases} \tag{57}$$

2.3. Mass transfer

2.3.1. Introduction to mass transfer in chemical and biological reactor systems

Sufficient mass transfer in chemical and biological reactor systems is crucial in order to achieve effective and reliable processes. The reason for this can be simplified to the fact that chemical or biological species must be physically extremely close to each other in order to enable a reaction to occur between them.

Mass transfer is however a very broad term and includes for example transport of fluids and chemicals through advection, diffusion or turbulent eddies. Mass transfer can also occur within or between different phases. The previous sections in this chapter have concentrated on how CFD can be used to model mass transfer phenomena, and this section will focus on mass transfer from a chemical and biological point of view.

This project has mainly focused on the different mass transfer phenomena mixing, interfacial transfer of oxygen and mass transfer at reactive surfaces and those three processes are therefore shortly introduced in the following sections. The derivation of the eddy cell model is also explained since it is commonly applied but seldom discussed.

2.3.2. The importance of mixing

Mixing capacity can be defined as the ability of a system to eliminate concentration gradients and it is important in chemical and biological systems for many reasons. Insufficient mixing in a chemical reactor can for example lead to longer reaction times if the involved chemicals do not have an optimal chance to come in close proximity.

Many experimentally determined reaction rates also assume perfect mixing, which can make reaction modelling and control of an unmixed system problematic. Experimental kinetic data might likewise be misleading if the reaction rates in the setup are influenced by the mixing process. Good mixing is also preferred when measurements, for example monitoring of the pH in a reactor, are performed since is then it desirable that the measured values are representative for the entire fluid.

Mixing in bioreactors is also essential in order to avoid regions of too low or too high concentrations of reactants or produced chemicals. Organisms in a fermenter (e.g. yeast cells, bacteria or fungi) must for example have specific environmental conditions with access to substrates in order to survive and grow. Many enzymes are also product inhibited, which means that they will not work properly if the concentration of the chemical they produce is too high.

Mixing can be achieved, as described in section 2.2.6, through advection or molecular or turbulent diffusion. This means that a stirred system is often better mixed the more it is agitated due to increased velocities and more turbulence, but there are no guarantees and too much stirring can also cause disadvantages ranging from high energy costs to damaged cells or equipment.

2.3.3. Interfacial mass transfer of oxygen

The interfacial mass transfer capability is, together with mixing, the most central parameter for comparing and characterizing different bioreactors and fermentation systems. Transfer of

gaseous oxygen into fermentation broths is highly important since oxygen often is the growth limiting substrate for the organisms suspended in the broth. The reason for this is that oxygen has a very low solubility in water compared to other substrates such as glucose. A growing cell culture will therefore rapidly consume all available oxygen leading do oxygen depletion. This makes it important to design bioreactors in a way in which they fast can provide new oxygen to the fermentation broth (Lee (2014)).

In small-scale reactor systems (e.g. shake flasks, microbioreactors, and microtiter plates) oxygen is often provided from the air by surface aeration. In larger systems, this transfer is however often not enough, and gas is therefore added to the reactor by sparging. In two of the presented case studies of this project (the microbioreactor and the magnetically stirred reactor) surface aeration has been assumed and in one (the pilot plant reactor) gas sparging has been considered.

The most common way to report the oxygen transfer in a bioreactor is via the oxygen transfer coefficient, k_La, which is defined in equation 58. As can be seen in equation 58, k_La is the proportionality constant that correlates the rate of change of the oxygen concentration (C) in the liquid phase in the bioreactor to its concentration at full saturation (C_{sat}). The concentration at full saturation is when the concentration of oxygen in the liquid is in equilibrium with the oxygen concentration in the gas phase.

$$\frac{dC}{dt} = k_L a(C_{sat} - C) \tag{58}$$

In equation 58 perfect mixing is assumed both in the liquid and in the gas phase. The transfer rate is therefore only expected to depend on the transfer rate over the gas-liquid interface and it is therefore proportional to the mass transfer coefficient k_L at the interface and the specific interfacial area a between the phases. Determining the two parameters k_L and a separately is however often very hard in most practical applications and their product k_La is therefore most often used instead.

One method to determine k_La experimentally for a bioreactor is to first lower the concentration of dissolved oxygen in it, for example by sparging with nitrogen, and then to measure the oxygen concentration over time as it recovers. The k_La can then therewith be directly calculated from the transient oxygen recovery profile.

In CFD simulations, the common practice is however to model k_L and a separately and multiply them in order to model the oxygen transfer coefficient. Within the field of simulating reactors for fermentation or living cell purposes, the most common way to model k_L is by using the correlation shown in equation 59.

$$k_L \propto \left(\frac{D_\varphi}{\upsilon}\right)^{0.5} (\varepsilon\upsilon)^{0.25} \tag{59}$$

This model, referred to as the eddy cell model, was derived by Lamont and Scott (1970) and describes the mass transfer coefficient for a chemical with the diffusivity D_φ in a liquid with the kinematic viscosity υ and the turbulent energy dissipation rate ε. The eddy cell model only accounts for the mass transfer on the liquid side of the gas-liquid interface since the transfer at the gas side is higher and therefore assumed negligible.

Details on how the eddy cell model was derived are explained in section 2.3.5, and a literature review on how it has been applied by others in relation to CFD simulations is presented in section 2.3.5 and 2.4.

2.3.4. Heterogeneous reactor systems

Mass transfer is also important in heterogeneous systems, which can be defined as chemical systems where the chemical reactions are not expected to take place evenly throughout the fluid. Catalytic reactions are often heterogeneous since they by definition are expected to be faster where the catalyst is present and since the catalyst often is located at solid surfaces or particles.

The case study in this project that involves catalytic reactions is the rotating bed reactor where ion-exchange has been considered at the catalytic sites. Ion-exchange takes place when an ion (in this case a positively charged sodium ion) approaches a surface (here a porous particle) and changes place with another ion with the same electrical charge (in this case a hydrogen ion). This means that there is no chemical reaction happening at the surface in this case, but the theory presented here can nevertheless be applied to surface catalyzed chemical reactions. A molecule can for example diffuse to a surface where enzymes are immobilized, react, and then diffuse back to the bulk fluid as another molecule.

Independently of how good the mixing in a fluid is a molecule in it must always diffuse the last distance through a virtual film layer in order to reach a solid surface. This film layer is always present, but its thickness varies with the flow conditions (e.g. viscosity, levels of turbulence) in the fluid. Turbulent eddies in the main flow contributes for example to a thinner film virtual layer, i.e. a shorter distance to diffuse through.

The reaction modelled in this project is shown in equation 60 and 61. Equation 60 shows the reaction occurring at the negatively charged surface (S^-), i.e. on the inside of the film layer, where the sodium ion is exchanged with hydrogen. If it can be assumed that the reaction in equation 60 is instantaneously fast it can also be assumed that the concentrations of Na^+ at the solid surfaces are zero. Equation 61 shows the overall reaction, where fully dissociated NaOH in the bulk liquid is replaced with neutral H_20 due to the ion-exchange at the surfaces.

$$S^-H^+ + Na^+ \rightarrow S^-Na^+ + H^+ \tag{60}$$

$$S^-H^+ + OH^- + Na^+ \rightarrow S^-Na^+ + H_2O \tag{61}$$

If perfect mixing in the outer surroundings of the particles is assumed, the concentrations of Na^+ outside of the film layer can be assumed representative for the entire bulk. The rate at which the concentration of Na^+ changes in the bulk can then be modelled through the pseudo-first-order expression in equation 62.

$$\frac{dC_{Na^+}}{dt} = KC_{Na^+} \tag{62}$$

In equation 62 K is a general mass transfer coefficient, which can be calculated through experimental monitoring of the entire reaction. The general mass transfer rate however is a function of many contributing factors. Factors that contribute to K are the rate of mixing in

the bulk fluid (i.e. if the concentration outside of the film layer actually is representative for the bulk concentrations), the rate of reaction at the surface, film diffusion and intra-particle diffusion.

Film diffusion is a measurement of how fast a molecule travels through the virtual film layer assuming it has a constant thickness. Intra-particle diffusion is caused by the fact that all catalytic particles are not solid spheres but can contain pores that makes the diffusion path from the outside of the film layer to the solid surface longer.

The dependence of K on all these factors (i.e. mixing k_m, film diffusion k_f, intra-particle diffusion k_i, and reaction rate k_r) is shown in equation 63 and illustrated in Figure 15.

$$\frac{1}{K} = \frac{1}{k_m} + \frac{1}{k_f} + \frac{1}{k_i} + \frac{1}{k_r} \tag{63}$$

The dependence on mixing in this project is automatically modelled since the reacting chemicals will be defined as additional variables as described in section 2.2.6. The reaction, i.e. the ion-exchange at the surface, will be assumed instantaneous. The effect of intra-porous diffusion will not be explicitly modelled, even if its impact is not necessarily negligible.

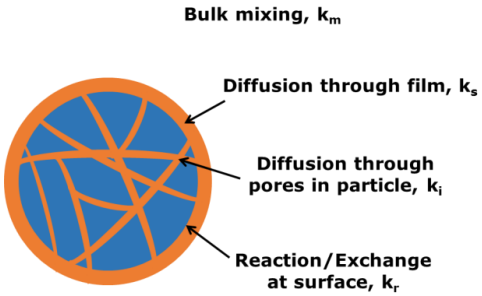

Figure 15. Visualisation of the regions around a catalytic particle where bulk mixing, film diffusion, pore diffusion and catalytic reactions occur.

If all factors other than k_f are ignored in equation 63, then the rate of reaction in equation 62 is only dependent on the film diffusion. The film diffusion coefficient k_f can be written as a product of the mass transfer velocity k_s and the specific transfer area A_s according to equation 64. The mass transfer coefficient k_s is the same in equation 64 as in equation 14, and it is often calculated in equation 14 for insertion in equation 64.

$$k_f = k_s A_s \tag{64}$$

The Sherwood number in equation 14 however is modelled by various different empirical correlations, and these correlations successively are often based on the Schmidt and the Reynolds number as seen in equation 15. The characteristic length l_0 in equation 14 is then often defined as the diameter of the particles. As explained in section 2.2.3.3, different values of the constants a, b, α and β in equation 15 are used in different literature sources. A few options of these are reviewed in section 2.4.6, and a more detailed analysis of the different options is presented in Schjøtt Andersen (2015).

The Reynolds number around a particle is often defined as shown in equation 65 or equation 66. In equation 65 and equation 66 U_s is the superficial velocity, i.e. the actual velocity multiplied with the volume fraction γ previously presented in section 2.2.7. The characteristic length is also often defined as the particle diameter, i.e. d_p.

$$Re_{Particle1} = \frac{\rho U_S d_p}{\mu} \tag{65}$$

$$Re_{Particle2} = \frac{\rho U_S d_p}{\mu \gamma} \tag{66}$$

The specific interfacial area A_s in equation 64 is here the interfacial area between the particles and the fluid divided by the total volume, i.e. the volume of the fluid plus the particles. It is defined and derived in equation 67 where γ_2 also is the porosity.

$$A_s = \frac{A_P}{V_{Total}} = (1-\gamma_2)\frac{A_P}{V_P} = (1-\gamma_2)\frac{\pi d_P^2}{\pi d_P^3/6} = \frac{6(1-\gamma_2)}{d_P} \tag{67}$$

2.3.5. The eddy cell model and its derivation

The eddy cell model in equation 59 is derived in Lamont and Scott (1970) and Lamont (1966), where also all details of the following summary can be found. The eddy cell model is based on the surface renewal theory which is stated to origin from Higbie (1935) The surface renewal theory states that the rate of transport between two phases is dependent on how fast the interface between them is renewed. In Lamont and Scott (1970) the smallest turbulent eddies in a flow are assumed to be most important for this renewal, and the model is based on the flow pattern assumed for an ideal two-dimensional eddy located in the liquid phase at a free-surface. Such an eddy is illustrated in Figure 16.

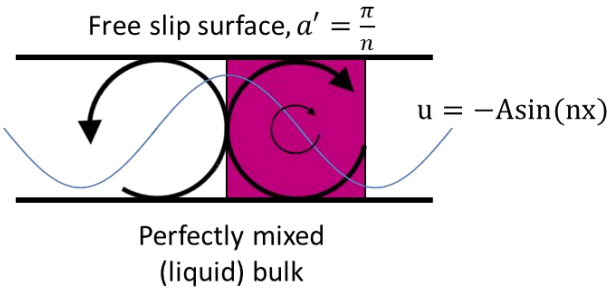

Figure 16. The two-phase ideal turbulent eddy from which the eddy cell model is derived.

From this flow pattern equation 68 is derived, which correlates k_L to the eddy/interface size length a', the eddy velocity amplitude A for the idealized eddy and the diffusivity of the transported chemical D_φ.

$$\frac{k'_L a'}{D_\varphi} = 0.445\left(\frac{a'A}{D_\varphi}\right)^{0.5} \tag{68}$$

The amplitude (A) for a given wave number (n) is then correlated to the energy quantity $E(n)$ according to equation 69.

$$A \propto \sqrt{nE(n)} \tag{69}$$

The energy spectrum chosen for $E(n)$ in Lamont and Scott (1970) is the Kovasznay spectrum presented in Hinze (1959) and displayed in equation 70. This energy spectrum is inserted into equation 68 via equation 69 and the result is integrated over the wavenumbers from zero up to the wavenumber where $E(n)$ is zero. The integral and its solution are displayed in equation 71. This result is the same as the correlation shown in equation 59, i.e. the proportionality expression that is applied in many CFD simulations.

$$E(n) = 0.45\varepsilon^{2/3}n^{-5/3}\left[1 - \frac{0.6\upsilon}{\varepsilon^{1/3}}n^{4/3}\right]^2 \tag{70}$$

$$k_L(n) \propto \int_0^{\frac{\varepsilon^{1/4}}{0.6^{3/4}\upsilon^{3/4}}} D_\varphi^{\frac{1}{2}} n^{-\frac{2}{3}} \varepsilon^{\frac{1}{6}} \left[1 - \frac{0.6\upsilon}{\varepsilon^{\frac{1}{3}}}n^{\frac{4}{3}}\right]^2 dn \propto \left(\frac{D_\varphi}{\upsilon}\right)^{0.5} (\varepsilon\upsilon)^{0.25} \tag{71}$$

For the validation of the model ε was defined according to equation 72, where D is the diameter of the pipe in which the experiments in Lamont and Scott (1966) were performed. Equation 72 is based on the assumption that all energy lost in a pipe under turbulent conditions is dissipated in the form of ε, and a correlation between the pressure drop and the Reynolds number is applied to describe this energy loss.

$$\varepsilon = 0.16 Re_{Pipe}^{2.75} \frac{\upsilon^3}{D^4} \tag{72}$$

As it can be seen in equation 59 and equation 71 the mass transfer is only expressed as proportionality, and no constant of proportionality is given. According to Lamont and Scott (1970) the value of the constant of proportionality is 0.4 based on the mathematical derivation of equation 71. It is also pointed out in Lamont and Scott (1970) that this theoretical value gives a quite good agreement for one piece of experimental data (k_L = 4.5 cm/min vs. k_L = 2.8 cm/min for carbon dioxide).

Once assuming a constant value for D_φ and υ, equation 59 is only proportional to the energy dissipation rate ε. Once replacing the expression for the energy dissipation rate in equation 59 with the Reynolds number dependent expression in equation 72, k_L is proportional to $Re^{0.69}$ as shown in equation 73. It is however pointed out in Lamont (1966) that the exponent 0.69 is too high and that 0.52 correlates better to experimental data. In Lamont and Scott (1966) the correlations $k_L \propto Re^{0.45}$ and $k_L \propto Re^{0.49}$ are instead suggested based on experimental data.

$$k_L \propto (\varepsilon)^{0.25} \propto (Re^{2.75})^{0.25} = Re^{0.69} \tag{73}$$

In the theory presented in Lamont and Scott (1970) the surface area a' is assumed to be inversely proportional to the wave number for an idealized eddy. This is also seen in Figure 16. The surface area a' is therefore replaced with n^{-1} before the derivation of the integral in

equation 71. The result of this is that the expression shown in equation 59 only correlates k_L to the eddy dissipation rate, and does not involve the specific interfacial area.

The experimental data referred to in Lamont and Scott (1970) is published in Lamont and Scott (1966), and the interfacial areas in the experiments are not expected to be a function of the Reynolds number either. The gas bubbles in the experiments are instead expected to have perfect spherical shapes. It is however suggested in Lamont and Scott (1966) that a more intense flow, i.e. a higher Reynolds number, would increase the interfacial area since the perfect sphere shaped bubbles might no longer exist.

2.4. Literature review

2.4.1. Introduction to CFD modelling of bioreactors

As presented in section 2.2.9 there are two main alternatives for modelling two-phase flow, i.e. the Euler-Euler method and the Euler-Lagrangian approach. The Euler-Lagrangian approach is not considered in this project, but it is an alternative for modelling of bioreactors as shown for example in Wutz et al. (2015).

For the Euler-Euler two-phase method, the gas phase can be considered either dispersed or continuous. The difference between these modelling approaches is how the specific interfacial area is calculated between the phases. For a free-surface flow (i.e. two continuous phases) it is calculated using equation 54 and for a dispersed gas flow it is calculated with equation 56 in combination with equation 57 in ANSYS CFX 15.0. The free-surface model has also, according to ANSYS® Academic Research (2013), a few special features to ensure that the interface between the phases is sharply defined between the models. This means that a free-surface simulation aims to keep the volume fractions as close to one or zero as possible, while the dispersed model allows intermediate values.

The eddy cell model has been applied both for cases where the gas phase is dispersed and continuous, and an introduction on how the mass transfer coefficient k_L is modelled is presented in section 2.4.2. Flow and mass transfer modelling of a free-surface flow is presented in section 2.4.3 and section 2.4.4 reviews the modelling work performed for dispersed phases. For a dispersed flow either a constant bubble diameter can be assumed or can a population balance model be applied. Population balance models are not considered in this project and are therefore not presented in the theory section. Population balance models can however be used to simulate a range of gas bubble diameters, and the models can also be used to simulate break-up and coalescence phenomena between the bubbles. This means that the models adapt the bubble sizes dependent on the hydrodynamic conditions in the reactor.

Section 2.4.5 presents how mixing modelling can be achieved with CFD and section 2.4.6 presents a summary of the scientific literature for CFD modelling of rotating bed reactors.

2.4.2. Modelling of the mass transfer coefficient k_L

There are two main alternatives within the CFD community for how the gas-liquid mass transfer coefficient k_L is modelled. The first is to apply the proportionality expression displayed in equation 59. This equation was derived in Lamont and Scott (1970) and is there referred to as the eddy cell model. An overview of the derivation is presented in section 2.3.5. The same equation, but with the proportionality constant 0.301 is presented in Kawase, Halard, and Moo-Young (1992). This correlation is also stated to be based on the surface renewal model just as in Lamont and Scott (1970) but through another derivation pathway. Kawase, Halard, and Moo-Young (1992) also states that their equation is based on the Higbie penetration theory shown in equation 74.

$$k_L = 2\left(\frac{D_\varphi}{\pi t}\right)^{0.5} \tag{74}$$

In equation 74 t represents the contact time between the two phases the mass transfer takes place and D_φ is the mass diffusion coefficient. The contact time between the two phases is however seldom known and must therefore be modelled according to Kawase, Halard, and

Moo-Young (1992). Kawase, Halard, and Moo-Young (1992) describe how k_L is derived for a non-Newtonian fluid, and this expression is thereafter simplified to equation 75 considering that the fluid is of Newtonian nature. Kawase, Halard, and Moo-Young (1992) is referring to Lamont and Scott (1970) and confirms that their models are the same besides the different values for the proportionality constant. Knowing the similarities between these models is important, since published literature sometimes refers to Kawase, Halard, and Moo-Young (1992) and sometimes to Lamont and Scott (1970).

$$k_L = 0.301\left(\frac{D_\varphi}{\upsilon}\right)^{0.5}(\varepsilon\upsilon)^{0.25} \tag{75}$$

Ranganathan and Sivaraman (2011) confirm that equation 74 is published in Higbie (1935) and state also that it, in combination with theory presented in Kolmogorov (1941), results in equation 76. Equation 76 is identical with equation 75 despite the change of proportionality constant to $2/\sqrt{\pi} \approx 1.13$.

$$k_L = \frac{2}{\sqrt{\pi}}\left(\frac{D_\varphi}{\upsilon}\right)^{0.5}(\varepsilon\upsilon)^{0.25} \tag{76}$$

The second commonly used model, equation 77, is also applied in Ranganathan and Sivaraman (2011) and it is claimed that equation 77 is based on concepts from Danckwerts (1951). U_{slip} is the bubble slip velocity, i.e. the velocity difference between a gas bubble and its carrying liquid phase. The parameter d_B is the gas bubble diameter.

$$k_L = \frac{2}{\sqrt{\pi}}\sqrt{\frac{D_\varphi U_{slip}}{d_B}} \tag{77}$$

Gimbun, Rielly, and Nagy (2009) claim however that equation 77 is based on the Higbie penetration theory while equation 75, with the exception of the proportionality constant being 0.4 instead of 0.301, is based on the application of the theory from Danckwerts (1951) in Lamont and Scott (1970).

The above are only examples of many inconsistencies in the use of the models, and it is therefore advisable to carefully examine which equation that is used in a publication of interest. The two models are nevertheless summarized in equation 78 and equation 79 with the proportionality constants C_{P1} and C_{P2}.

$$k_L = C_{P1}\left(\frac{D_\varphi}{\upsilon}\right)^{0.5}(\varepsilon\upsilon)^{0.25} \tag{78}$$

$$k_L = C_{P2}\sqrt{\frac{D_\varphi U_{slip}}{d_B}} \tag{79}$$

The theory behind the eddy cell model is however seldom discussed in articles which are applying it. One exception is the publication of Hung, Garbe, and Tsai (2010) who rises selected theoretical concerns about the derivation in Lamont and Scott (1970) and highlights that the applied energy spectrum in Lamont and Scott (1970), i.e. equation 70, only is

applicable for fully developed turbulent flow. Hung, Garbe, and Tsai (2010) comment also on the wavenumber selection which the expression in equation 71 is integrated between, and questions finally the use of the model in their field of application, which is mass transfer processes at an air-sea interface.

2.4.3. Modelling of flow and mass transfer in free-surface reactor systems

There are only few examples published in the scientific literature where oxygen transfer for a free-surface is modelled. The work most similar to the microbioreactor and magnetically stirred reactor in this project is presented in Brüning (2012) and Brüning and Weuster-Botz (2014). In Brüning and Weuster-Botz (2014) a 10 ml unbaffled and paddle stirred bioreactor is modelled and the Reynolds numbers are in the range 2356 to 6281 for the water phase. Equation 78 is used to model the mass transfer coefficient with C_{P1} set to 0.167 since this coefficient provides the best fit for the experimental data. The simulated k_L values are in the range $1.1\text{-}2.7 \cdot 10^{-4}$ m s^{-1}. The specific interfacial areas are also simulated in Brüning and Weuster-Botz (2014) but it is not stated exactly how.

According to Brüning and Weuster-Botz (2014) others (Kawase, Halard, and Moo-Young (1992), Laakkonen, Alopaeus, and Aittamaa (2006), Laakkonen et al. (2007), Lamont and Scott (1970) and Talvy, Cockx, and Line (2007)) have found empirical constants for the proportionality constant in equation 78 in the range between 0.3 and 0.46. The lower constant of proportionality value found (0.167) is explained in Brüning and Weuster-Botz (2014) by the different flow models, i.e. that a free-surface flow is simulated in Brüning and Weuster-Botz (2014) while the listed references model dispersed flows (Brüning and Weuster-Botz (2014)).

In Brüning and Weuster-Botz (2014) the shear stress transport (SST) turbulence model is applied as well as the free-surface interface model. Brüning (2012) also reveals that the inhomogeneous momentum model is used.

Another free-surface mass transfer work is presented in Li et al. (2013) where baffled and unbaffled shake flasks with filling volumes of 50-150 ml are simulated. The RNG k-ε turbulence model is applied, and two versions of equation 78 are evaluated to simulate k_L, one with the proportionality constant 0.4 as given in Lamont and Scott (1970) and one with the proportionality constant $2/\sqrt{\pi}$ which is claimed to be based on Higbie's penetration model.

Li et al. (2013) show that the simulated k_La value is up to 100% higher once the liquid volume averaged energy dissipation rate (ε) is considered rather than the gas-liquid interface averaged value. This is interesting since the theory behind the eddy cell model (equation 78) is based on uniform turbulence and no alternative to this is discussed in Lamont and Scott (1970). In Lamont and Scott (1966) ε is namely calculated as a single value for an experimental setup based on the pressure drop in it while CFD calculates a value of ε in each node of a mesh.

A third free-surface mass transfer example is presented in Kaiser (2014) where equation 78 is applied with the proportionality constant 0.36. In Kaiser (2014) a toroidal shaped traveling wave bioreactor is simulated and the proportionality constant is found by correlating experimental and simulated data and the simulated gas-liquid interface averaged value of ε is the value applied.

One alternative modelling approach is presented in Zhang et al. (2005) where gas-liquid mass transfer in shake flasks is modelled. The filling volumes of the shake-flasks are 25-100 ml and no turbulence model is explicitly mentioned. Equation 74 is used to calculate k_L, and the gas-liquid contact time t is stated to be calculated based on the local velocity of the gas phase and the position of the gas-liquid interface. Exactly how this is calculated is unclear, but Zhang et al. (2005) declare that the methodology is similar to the one presented in Taniguchi, Kawaguchi, and Kikuchi (2002).

In Taniguchi, Kawaguchi, and Kikuchi (2002) mass transfer is modelled in a dispersed system in a sparged vessel. No free-surface model is therefore applied, but the mass transfer contribution at the top of the vessel is still calculated and it is referred to as the free-surface. At this surface k_L is simulated using equation 74, and the contact time is defined as the fraction between the radius of the vessel and the average radial velocity at the free-surface (Taniguchi, Kawaguchi, and Kikuchi (2002)).

The mass transfer model in Zhang et al. (2008) is similar to Zhang et al. (2005) and mass transfer in microtiter plates is simulated. Equation 74 is once again applied to model k_L, but details on how the contact time is calculated are once again not given exactly. It is nevertheless clearly defined in Zhang et al. (2008) that the specific interfacial area is calculated as the fraction between the area of the isosurface where the liquid volume fraction is 0.5 and the total liquid volume (Zhang et al. (2008)).

Free-surface simulations investigating the velocities and gas-liquid interfaces without considering interfacial mass transfer are also rare in the scientific literature. This is supported by Torré et al. (2007) who state that there are only few studies published considering free-surface deformation in combination with turbulent flow. This is also stated in Haque et al. (2006), who also claim that modelling of free-surface turbulent flow in unbaffled vessels is challenging because of the complexity of the flow. In Haque et al. (2006) a free-surface flow is simulated in an unbaffled system with a Rushton turbine and the resulting gas-interfaces and velocities are investigated.

A more recent study is presented in Mahmud et al. (2009) where flow induced by a magnetic stirrer is modelled. This article claims also that modelling of unbaffled reactors is rare. The homogenous momentum model is applied in Mahmud et al. (2009) and this choice is motivated by the argument that the inhomogeneous model would be unnecessary since no air was trapped in the liquid during the experimental investigations. The free-surface profiles are displayed and discussed in Mahmud et al. (2009) and the simulated velocity profiles are compared to experimental data. The study is followed up by Haque et al. (2011) where both simulated velocities and turbulent kinetic energies are compared to experimental data.

2.4.4. Modelling of flow and mass transfer in dispersed reactor systems

There are considerably more publications describing CFD modelling of mass transfer phenomena in dispersed systems than in free-surface systems. This is understandable considering that most bioreactors use sparger equipment in order to achieve high oxygen transfer rates. In a dispersed system the specific interfacial area is most often calculated using equation 56. In the derivation of equation 56 however the entire volume, i.e. the sum of the gas and the liquid phase, is considered. It should be more correct to consider only the liquid volume, i.e. to calculate the specific interfacial area as the fraction between the gas-liquid interfacial area and the liquid volume. Support for this opinion has however only been found

in one publication, i.e. in Kaiser (2014) who present equation 80 for the specific area per liquid volume. Kaiser (2014) point out, however, that the specific interfacial area $A_{\alpha\beta}$ becomes very large once the gas volume fraction r_α approaches one. For small values of r_α equation 56 and equation 80 are however very similar.

$$A_{\alpha\beta} = \frac{A_{interface}}{V_\beta} = \frac{A_{interface}}{V_{\alpha+\beta}} \frac{V_{\alpha+\beta}}{V_\beta} = \frac{6r_\alpha}{d_r} \frac{1}{r_\beta} = \frac{6r_\alpha}{d_r(1-r_\alpha)} \tag{80}$$

Gimbun, Rielly, and Nagy (2009) state that most modelling studies in recent years have considered a uniform bubble diameter and list Khopkar and Ranade (2006), Sun, Mao, and Yu (2006), Wang, Mao, and Yang (2006) Deen, Solberg, and Hjertager (2002) and Scargiali et al. (2007) as examples. These publications however do not consider mass transfer, i.e. they do not model $k_L a$.

In Kaiser et al. (2011) a 2 L bioreactor is modelled with a constant bubble diameter of 1 mm, and equation 78 is used with the proportionality constant $2/\sqrt{\pi}$. The specific interfacial area is also calculated using equation 56. Appa, Deglon, and Meyer (2013) simulate $k_L a$ in a sparged autoclave and compare the use of a population model and a fixed bubble diameter. For calculation of k_L equation 78 is used with the proportionality constant 0.7 which is selected since it provides the best fit to experimental data. Elqotbi et al. (2013) present an impeller stirred, baffled bioreactor with a 5 L working volume. A constant bubble diameter, 2 mm, is assumed and a kinetic model is also included in the simulation. Equation 56 is used for the specific interfacial area and equation 78 for k_L. The value of the proportionality constant C_{P1} is however not described.

Xia et al. (2009) model a shear thinning flow in 35 L working volume bioreactors with various impeller types. The impeller Reynolds number is calculated to Re = 1156 and the conclusion is that this flow is turbulent. The k-ε turbulence-model is used and the bubble diameter is set to 4 mm. The specific interfacial area is calculated via equation 56 and the mass transfer coefficient is modelled by equation 81. Equation 81 is claimed to be proposed by Garcia-Ochoa and Gomez (2004) and K and n are the consistency coefficient and the flow index, respectively. These values should be experimentally determined for a non-Newtonian fluid. For a Newtonian fluid K is equal to the dynamic viscosity and n to unity. A Newtonian fluid reduces then equation 81 to equation 78, which is similar to the derivation performed in Kawase, Halard, and Moo-Young (1992).

$$k_L = \frac{2}{\sqrt{\pi}} \left(D_\varphi\right)^{0.5} \left(\frac{\varepsilon\rho}{K}\right)^{1/2(1+n)} \tag{81}$$

Moilanen, Laakkonen, and Aittamaa (2006) model mass transfer in non-Newtonian liquids as well but use a different model for the calculation of the non-Newtonian viscosity than Xia et al. (2009). The applied mass transfer coefficient is also not described in detail by Moilanen, Laakkonen, and Aittamaa (2006), but it is stated to originate from Kawase, Halard, and Moo-Young (1992).

An example of a dispersed system for a milliliter scaled reactor is described in Lamping et al. (2003), where a 6 ml stirred system is simulated using the k-ε turbulence model. In Lamping et al. (2003) the average bubble size is set to an unknown constant and the local specific surface area is calculated according to equation 56. Equation 78 with the proportionality constant $2/\sqrt{\pi}$ is used to model k_L. The product of a and k_L is then integrated for the working

volume in order to calculate an average k_La for the full reactor. The local energy dissipation rates (ε) are also integrated over the volume in order to calculate the average power input.

Gimbun, Rielly, and Nagy (2009) use a population balance model in the modelling of two different stirred reactors and models k_L via equation 78 with the proportionality constant 0.4 and equation 79 with the constant $2/\sqrt{\pi}$. Gimbun, Rielly, and Nagy (2009) calculates the local interfacial area per unit volume according to equation 82 where $d_{b,i}$ is the bubble diameter for each bubble size considered and n_i is the number of bubbles of this size per unit volume. It is concluded in Gimbun, Rielly, and Nagy (2009) that equation 78 produces the highest values of k_La around the impeller region due to the high dissipation rates (ε) at this location.

$$a = \sum_i \pi d_{b,i}^2 \, n_i \tag{82}$$

In Ranganathan and Sivaraman (2011), as stated previously, equation 78 and 79 are compared with the proportionality constants 0.4 and $2/\sqrt{\pi}$ respectively. In addition another k_L correlation is used which is originally presented in Alves, Maia, and Vasconcelos (2004). The correlation from Alves, Maia, and Vasconcelos (2004) is a function of the diffusion coefficient, the bubble diameter, the kinematic viscosity of the liquid, the bubble slip velocity and a constant. Contour plots of k_L are provided in Ranganathan and Sivaraman (2011), and it is also shown that the correlation based on equation 78 has the highest k_L values around the impellers.

Another example of a publication using a population balance model is Kerdouss et al. (2008) which presents a 5 L stirred bioreactor. The k-ε turbulence model is used and k_L is modelled using equation 78 with the proportionality constant $2/\sqrt{\pi}$. The specific interfacial area is calculated using equation 56, but d_B is defined as the Sauter diameter, or the mean diameter of the bubbles of varying size.

Wang and Wang (2007) model oxygen transfer in a bubble column and evaluate both equation 78 and equation 79 for the modelling of k_L. The proportionality constant 0.27 is concluded to provide the best fit to experimental data for equation 78. Wang and Wang (2007) state that Sheng, Meng, and Fox (2000) claim that the reasons for inconsistencies in the determination of the proportionality constant between different cases is that it is difficult to correctly determine the turbulent energy dissipation rates. The specific interfacial area in Wang and Wang (2007) is calculated as in equation 82.

In Moilanen et al. (2008) a Rushton turbine is simulated together with two other impeller designs in a 200 L reactor. The SST model is applied with the motivation that Hartmann et al. (2004) claim that it combines the best of the k-ε and k-ω model. Two different population balance models are also compared. Equation 78 is used to model k_L with the C_{P1} set to 0.3. The value 0.3 is said to be based on a multi-block simulation performed in Laakkonen et al. (2006).

Moilanen et al. (2008) also compare the sliding interface and the multi-phase reference frame approach for modelling of the interface between the rotating and the stationary domain. The conclusion is that the difference in the simulated k_La values between these methods is less than 1%.

2.4.5. Mixing modelling

Mixing time simulations with CFD are often performed by simulating the spread of a scalar, i.e. additional variable as described by equation 43 in section 2.2.6, in a frozen velocity and (one applicable) turbulence field. This means that the momentum and turbulence equations often are solved separately in a steady-state simulation, and that the scalars then are simulated in a transient simulation where these equations are not solved. The velocity, pressure and turbulence field in the transient simulations are then "frozen" and equal to the initial values, i.e. to the steady-state result file, provided.

Equation 43 however is defined slightly differently in different software packages since the default value of the turbulent Schmidt number, Sc_t, tends to vary. It is for example set to 0.9 in ANSYS CFX 15.0 while e.g. Coroneo et al. (2011) state that the conventional value for the turbulent Schmidt number is 0.7. This is important, since Coroneo et al. (2011) also state that lowering the turbulent Schmidt number to around 0.1-0.2 is a used method to fit simulated mixing times to experimental data. Coroneo et al. (2011) comments on this as an arbitrary way to compensate for low eddy viscosities, i.e. for low estimations of μ_t in equation 43.

How to initialize the additional variables varies from case to case, but the two most common approaches are either to initialize it to a limited region of the fluid (e.g. the bottommost part of a reactor) or to add it from a virtual source point for a finite number of time steps, e.g. for the first second in a transient simulation. How to define the mixing times varies also, and in many publications it is furthermore not clearly stated how the mixing time has been defined. A few examples of CFD mixing simulations will be presented here to demonstrate the variety.

Allonneau et al. (2015) model the mixing in a 10 ml reactor agitated by a triangular shaped magnet. The Reynolds numbers are in the range 747-1644 (Allonneau et al. (2015)) and the laminar, SST and the k-ε models are compared. One monitoring point is used to measure the concentrations of an additional variable in the simulated fluid, and the mixing time is defined as the time needed for the concentration in the monitoring point to settle within the ±5% interval from the final value. It is also stated in Allonneau et al. (2015) that this is the most common mixing time definition. The resulting mixing times are displayed in Allonneau et al. (2015), but there is no consistency regarding which turbulence model is the fastest. Elsewhere (Yeoh, Papadakis, and Yianneskis (2005)) the mixing time is defined based on the time it takes for 95% of the finite volumes in a reactor to reach within the ±5% interval of the final additional variable value.

Another mixing time definition is found in Kumaresan and Joshi (2006) where stirred reactors are simulated. The mixing time is there defined as the time needed for the fraction between the lowest and highest values of the additional variable in the fluid to reach the value 0.985.

Brüning (2012) defines the mixing time as the time when the global mixing quality M_{global} in a reactor (equation 84) reaches the value 0.97. The global mixing quality is calculated based on the local mixing quality M_{local} in the reactor, i.e. on equation 83. Equation 83 is defined as the fraction between the time dependent concentration of the scalar/additional variable and the additional variable concentration at steady-state. The method is stated to origin from Hennig, Grän-Heedfeld, and Deerberg (2007).

$$M_{local}(t) = \frac{c(t)}{\bar{c}} \tag{83}$$

$$M_{global}(t) = 1 - \sqrt{\frac{1}{V_L}\iiint_{V_L}\left(\frac{c(t)}{\bar{c}} - 1\right)^2 dV} \tag{84}$$

In Johnson, Natarajan, and Antoniou (2014) mixing is modelled in 315 and 15000 L reactors by adding an additional variable at the top of the reactors. Johnson, Natarajan, and Antoniou (2014) use monitoring surfaces instead of monitoring points to virtually measure the additional variable concentrations in selected regions in the reactor. Mixing time is then defined as the time needed for the surface concentrations to reach within the ±5% interval of their final value following a pulse addition of a tracer compound. The simulated and experimental mixing times are in good agreement which is interpreted as a validation of the CFD model according to Johnson, Natarajan, and Antoniou (2014).

One last mixing time example is Thompson et al. (2014) where mixing in a stirred vessel is modelled. An additional variable is added to the system in Thompson et al. (2014) and the concentration is monitored through monitoring points. The mixing times are then determined through manual inspection of the results files, searching for unmixed regions by visualising the dynamics of the additional variable over time.

2.4.6. Modelling of stationary and rotating catalytic basket setups

The concept of using rotating catalyst baskets was introduced more than 50 years ago by Carberry (1964) who developed a setup consisting of four rotating cages filled with catalytic material aiming to catalyze gaseous reactions (Svendsen (2013)). Since then many alternative catalytic basket reactors have been developed, both designs with rotating catalytic baskets and setups with rotating impellers transporting the fluid through a static catalytic basket.

Only a limited amount of CFD studies have however been performed on basket reactors according to Santos-Moreau, Brunet-Errard, and Rolland (2012), who refer to Warna et al. (2002) and Magnico and Fongarland (2006) as two of few examples available. These three articles will be presented in this section, together with a review of the work presented in Svendsen (2013). Three additional publications about modelling of rotating bed setups are Martínez et al. (2012), Yang et al. (2010) and Shi et al. (2013), but since these do not consider calculations of mass transfer rates they will not be further reviewed in this section. The rotating bed reactor investigated in this project has also been described in Schjøtt Andersen (2015) which is not included in this literature review but is referred to throughout the methodology and result sections.

In Svendsen (2013) the performance of a rotating bed reactor (RBR) is evaluated in relation to the production of biodiesel. The RBR used in Svendsen (2013) is very similar to the RBR investigated in this project since they are both developed by SpinChem AB (former Nordic ChemQuest AB). The RBR in Svendsen (2013) has however a slightly different design and it is simulated to be located in a different vessel. Svendsen (2013) is furthermore not considering any pressure drop in the porous material, i.e. C_1 and C_2 in equation 45 were set to zero.

The k-ε turbulence model is used in Svendsen (2013) and the resulting flow patterns are visualized. Mixing simulations are performed using an additional variable, and an optimization study investigating the vertical position of the RBR in the reactor is presented. For the mixing simulations it is concluded that the simulated mixing times are similar to the experimental mixing times in the system, i.e. around 2.5 seconds. It is however not possible to conclude on any optimal position for the RBR based on the performed simulations, which is stated to be in accordance with previous experimental experience from Nordic ChemQuest AB (Svendsen (2013)).

In Warna et al. (2002) two catalytic rotating basket reactor designs are compared. One cylindrical basket design and one annular is simulated and the pressure drop is modelled as a body force linear to the velocity in the porous domain. The k-ε turbulence model is applied in the non-porous parts of the geometry and the laminar model is applied in the porous material. A chemical reaction occurring over time is also modelled in Warna et al. (2002), but it is not stated how this is implemented.

The mass transfer rates are modelled in Warna et al. (2002) using the correlation displayed in equation 85, which is a combination of the previously presented equation 14 and equation 15. In Warna et al. (2002) a is set to 2, but the values of b, α and β are not directly stated. The Reynolds numbers in the catalytic region are stated to be in the range 100-1500 (Warna et al. (2002)).

$$Sh = \frac{k_s d_p}{D} = a + bRe^{\alpha}Sc^{\beta} \tag{85}$$

In Magnico and Fongarland (2006) two different stationary basket reactors are simulated. Both designs have an annular shape with rotating impellers and stationary baffles placed in the middle of the annular space. The pressure drop in the porous material is modelled with a pressure loss term involving both a linear and quadratic term, i.e. both C_1 and C_2 in equation 45. As in Warna et al. (2002), the k-ε turbulence model is applied outside of the catalytic baskets in Magnico and Fongarland (2006) while no turbulence model is used in the porous material. Magnico and Fongarland (2006) however state that well established turbulence cannot be assumed outside of the stationary basket, and that it should therefore be relevant to use a turbulence model designated for lower Reynolds numbers. The RNG k-ε model is also evaluated for one rotational speed in Magnico and Fongarland (2006). It is stated that this turbulence model does not give rise to a different flow pattern compared to the standard k-ε model, but that the simulated and averaged values for the kinetic energy and eddy dissipation are decreased by a factor of 2.2 and 3.2, respectively, in the inner part of the volume.

The mass transfer coefficients k_s are calculated in Magnico and Fongarland (2006) using the same equation as Warna et al. (2002), i.e. equation 85. The values of the parameters a, b, α, and β are reported to be 0, 1.1, 0.41 and 0.4 respectively. The simulated values of k_s are shown and compared to experimental values along an axial profile in the porous material. No direct chemical reactions are however modelled. The Reynolds numbers around the porous particles are in the range 2-55 (Magnico and Fongarland (2006)).

Another example of a simulated stationary basket reactor is Santos-Moreau, Brunet-Errard, and Rolland (2012) where an annular catalytic case with an impeller placed inside is presented. The catalytic basket is modelled as a porous domain and the values of C_1 and C_2 are stated. The MRF approach is used to model the interface between the rotating and the

stationary domain in Santos-Moreau, Brunet-Errard, and Rolland (2012) and the position of this interface is also investigated. It is declared that the position of the stator-rotor interface does not have a large impact on the results. The impeller Reynolds numbers are in the range $1\text{-}2\cdot10^4$ which is considered fully turbulent, and the realizable k-ε model is chosen for modelling of the liquid outside of the catalytic basket. Inside of the porous domain no turbulence model is mentioned suggesting that it is modelled as laminar.

The mass transfer coefficients k_s in Santos-Moreau, Brunet-Errard, and Rolland (2012) are calculated using equation 85 with the constants 2, 1.8, 0.5 and 0.33 for a, b, α and β, respectively. It is however stated that this correlation might not be applicable for such a short catalyst bed (Santos-Moreau, Brunet-Errard, and Rolland (2012)). The simulated values of k_s are calculated at two positions in the catalytic material.

3. Materials and Methods

The experimental methods used in relation to this project are presented in section 3.1. The experiments with the magnetically stirred reactor was performed at DTU and ion-exchange experiments for the rotating bed reactor were performed by SpinChem AB. Experimental data previously presented at Bolic et al. (2012) are also modelled in this project but were performed separately.

Section 3.2 describes the general computational methods used in this project, i.e. the methods applicable for more than one case study. Section 3.3 to 3.6 describes then the mesh and geometries, simulation setups and the evaluation procedures for each case study.

3.1. Experimental methods

3.1.1. The magnetically stirred reactor

8 ml nitrogen-sparged distilled water was transferred into a small glass vial and the liquid was then stirred using a rotating magnet. The concentrations of dissolved oxygen in the liquid were then recorded over time using an optical needle-type probe (PyroScience, GmbH, Germany) that was submerged in it.

The rotational speeds 300, 600 and 900 rpm were selected for the experiment since the position of the formed vortex was still stable at those rotational speeds. The magnet was also located on the bottom of the reactor for the investigated rotational speeds, and it gave the visual impression to be rotating with a constant speed along a fixed axis.

The oxygen recovery data was plotted according to equation 86, which is a solution to equation 58, and the k_La values were evaluated through linear regression. The k_La values were evaluated from data where the oxygen saturation concentrations in the water were in the range between 28% and 95% of full saturation.

$$In\frac{C - C_{sat}}{C_0 - C_{sat}} = -k_L a * t \tag{86}$$

3.1.2. The rotating bed reactor

Experimental reaction (ion-exchange) data for the rotating bed reactor case study was provided by SpinChem AB who also performed the experiments at their facilities. The experiments were performed using the rotating bed reactor SpinChem ® RBR S221 that was placed in a baffled cylindrical glass reactor with 18 petals.

Experimental procedure

Before the experiments the four compartments in the RBR were filled with the cation exchange resin beads AMBERLITE™ IRN99 after which the RBR was assembled. The RBR was then mounted to rotate in the glass reactor that was pre-filled with a basic solution. The neutralization of the basic solution caused by the acid beads was monitored by the addition of the indicator phenolphthalein, and the time from start of each experiment until the visual disappearance of the indicator was measured. Different rotational speeds ranging from 70 to 900 rpm were evaluated, and the experiments with 500 rpm were performed repeatedly in order to assure that the performance of the ion-exchange resin had not changed.

Experimental details

A basic water solution was prepared by dissolving 4.2 g sodium hydroxide (NaOH) in 100 ml distilled water, and from this basic solution 0.5 ml was used to dissolve 22.5 mg of the indicator phenolphthalein. The basic indicator solution was then added to the glass reactor together with 160 ml distilled water. The final concentration of hydroxide was $3.27 \cdot 10^{-3}$ mol/l, which corresponds to pH 11.5, assuming complete dissociation of the sodium hydroxide. Phenolphthalein is pink under basic conditions and shifts to colourless around pH 8.2, which corresponds to a concentration of sodium hydroxide of approximately $1.6 \cdot 10^{-6}$ mol/l.

3.2. Computational methods

The overall computational methods are described in this section, and section 3.3, 3.4, 3.5, and 3.6 describe further how the methods were implemented in the respective case studies.

3.2.1. Software

The CFD simulation software ANSYS CFX 15.0 was used for all simulations and post processing of the results. The computational meshes used were created using ANSYS ICEM CFD 14.0 and 15.0.

3.2.2. Setup of flow the problems

3.2.2.1. One-phase steady-state simulation setup

All one-phase simulations were performed with water only which means that a density of 997 kg m^{-3} and a dynamic viscosity of $9.899 \cdot 10^{-4}$ kg m^{-1} s^{-1} was used. More details on how the one-phase simulations were performed are found in the respective sections.

3.2.2.2. Two-phase steady-state simulation setup for free-surface flow

For the free-surface, two-phase steady-state simulations the two simulated phases were both defined as continuous and they were given the fluid properties of water and air. The water had the density of 997 kg m^{-3} and the dynamic viscosity of $9.899 \cdot 10^{-4}$ kg m^{-1} s^{-1}, and the air had the density of 1.185 kg m^{-3} and the dynamic viscosity of $1.831 \cdot 10^{-5}$ kg m^{-1} s^{-1}.

The inhomogeneous Euler-Euler modelling approach described in section 2.2.9 was used, and buoyancy was activated in the model in order to simulate gravity. The buoyancy reference density was set to 1.185 kg/m^3, i.e. the same as the density of the gas phase after a recommendation in ANSYS® Academic Research (2013) regarding free-surface calculations.

For the simulations applying a turbulence model the homogenous turbulence model was used, i.e. the gas and the liquid phase were set to share the same turbulent variables ε, ω and k.

The free-surface model was chosen for the interphase momentum transfer and the drag coefficient 0.44 was used. The volume separation of the water and the gas phases was initiated by using a step function and in this way the total liquid volumes in the simulations could be defined.

3.2.2.3. Two-phase steady-state simulation setup for dispersed flow

The only case study involving dispersed flow was the pilot plant bioreactor and due to the sparging, it was the only one with defined inlets and outlets. The two fluids were set to consist of water and air with the same physical properties as in the free-surface flow, but the air phase was set to be dispersed in the continuous water phase. The dispersed air bubbles were set to have constant and user-defined diameters.

The drag force model Grace was used, as well as the turbulence transfer option *Sato Enhanced Eddy Viscosity*. The turbulence transfer option was used since it was applied in a

very similar system (ANSYS® Academic Research (2013)), but it is however not described in detail in the program documentation.

Gravity (buoyancy) was also activated in the simulation, and the buoyancy reference density was set to 997 kg/m^3, i.e. the same density as the liquid phase after yet another recommendation in the documentation ANSYS® Academic Research (2013) regarding dispersed multi-phase flow.

3.2.2.4. Transient mixing time simulation setup for one and two-phase simulations

For the mixing simulations, dimensionless specific additional variables (scalars) were defined in all domains of the simulations and their standard diffusion coefficient was set to $2 \cdot 10^{-9}$ m^2 s^{-1}. The additional variables were set to be only present in the liquid phase, i.e. the air phases in the microbioreactor and the pilot plant reactor did not contain any additional variable. The additional variables were modelled by equation 43 with the turbulent Schmidt number kept at 0.9.

The additional variables were added to the transient simulations through step functions defined either in time or in space. Once initiated to be space bound, specified regions were selected to contain unity concentration of the additional variable in the beginning of the simulation. For the time dependent addition of additional variables source points were defined, which specified the coordinates where the additional variables should enter into the domain via the source term in equation 43. The source points were defined such that they included a time dependent step function, which added additional variables for a user-defined moment of simulated time.

All mixing simulations were performed as transient, i.e. time dependent, and the initial conditions for the simulations were provided by the corresponding steady-state simulation. In the transient mixing simulations only the additional variables/scalars were simulated, i.e. the continuity, momentum or turbulent equations were not solved. This means that the velocity and turbulence fields were "frozen" since they were not allowed to change during the course of the transient simulations i.e. the initial values from the steady-state simulations were retained.

The additional variables were monitored in different ways during the simulations. Its direct values at certain defined monitoring points were reported, as well as their maximum and minimum values in the entire geometry.

3.2.3. Transformation from the Cartesian to the cylindrical coordinate system

In the results files created by ANSYS CFX 15.0 all velocities are reported in the Cartesian coordinate system, but the post-processing module includes the possibility to transform the velocities to the cylindrical coordinate system. All velocity results in this project were transformed to the cylindrical coordinate system, since all investigated case studies (the microbioreactor, the magnetically stirred beaker, the pilot plant reactor, and the rotating bed reactor) involved in this project consider rotating stirrers of some kind.

When velocity vectors (scalars are not affected) are transformed to the cylindrical coordinate system their x, y and z velocities are translated into their radial, axial and circumferential

counterparts. An example of this is shown in Figure 17 where the z-axis in the Cartesian coordinate system has been chosen as the axis of rotation.

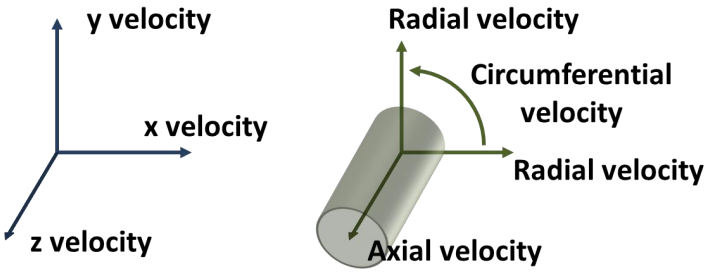

Figure 17. The velocity vectors in the Cartesian coordinate system (left) and their counterparts in the cylindrical system (right) once the z-axis is defined as the axis of rotation.

3.2.4. Evaluation of simulations

3.2.4.1. Two-phase steady-state result evaluation for free-surface flow

For the processing of results for the free-surface flow simulations, i.e. mainly for the microbioreactor and the magnetically stirred beaker case studies, first all velocity vectors were transformed to their cylindrical counterparts as described above.

Lines and planes were then defined inside of the geometry and the exact location of those can be seen in the respective method sections. For each line 50 user defined values (e.g. water velocity in the radial direction, eddy viscosity) were reported and exported to Excel. The values of the step function shown in equation 87 were also exported for each line. The purpose of this was to be able to remove the water velocity values in regions that were dominated by the air phase.

$$H(Water\ volume\ fraction) = \begin{cases} 0\ if\ Water\ volum\ fraction < 0.5 \\ 1\ if\ Water\ volum\ fraction > 0.5 \end{cases} \qquad (87)$$

An isovolume was also defined with the boundary conditions shown in equation 87. This means that only elements in the result file with a water volume fraction larger than 0.5 were included in the volume, and the other elements were not. This isovolume then represented the liquid dominated parts or the liquid volume.

An isosurface representing the gas-liquid interface was defined in a very similar manner, i.e. as an isosurface defined by the water volume fraction being 0.5. The area of this interface was then calculated by the post-processing unit of ANSYS CX 15.0.

The maximum and averaged values of the turbulent energy dissipation ε in the results files were also calculated in the liquid volume and at the gas-liquid interface.

3.2.4.2. Two-phase steady-state result evaluation for dispersed flow

For the two-phase simulation with dispersed flow (i.e. the pilot plant reactor), the velocities were transformed and exported similar as described for the free-surface flow but with the exception that the step-function in equation 87 was never used to remove any data.

The gas holdup fraction in the volume was calculated by integrating the volume fractions of gas in the entire reactor and dividing it with the total volume of the reactor. Likewise, the total liquid volume was calculated by integrating the liquid volume fractions.

The average and maximum values of the turbulent energy dissipation rates ε in the liquid were also reported in the entire volumes. For visualisation of the results various isovolumes were created, for example those containing a volume fraction higher than 0.1. No isovolumes or isosurfaces were however used in the numerical evaluation of the results.

The averaged specific interfacial areas were calculated for the volumes using either equation 56 (referred to as *Theory*) or equation 56 in combination with the modification shown in equation 57 (referred to as *CFX*).

3.2.4.3. Oxygen transfer evaluation for free-surface flow

The eddy cell model shown in equation 88 was used for modelling the mass transfer coefficient k_L in this project. A constant specific interfacial area was however assumed in the derivation of the eddy cell model, and equation 88 was therefore rewritten into equation 89 in order to account for varying sizes of the gas-liquid interface. Equation 89 is in this project referred to as the extended eddy cell model.

For the free-surface simulations, the simulated specific interfacial areas a_{sim} were calculated as the fraction between the gas-liquid isosurface and the liquid volumes as defined in section 3.2.4.1. The proportionality constant C_P was then computed by plotting the experimental k_La values against the simulated values and by evaluating the slope of the linear trend lines in Microsoft Excel 2010.

$$k_L = C_P \left(\frac{D_\varphi}{\upsilon}\right)^{0.5} (\varepsilon\upsilon)^{0.25} \tag{88}$$

$$(k_La)_{Exp.} = C_P(k_La)_{Sim.} = C_P \left(\frac{D_\varphi}{\upsilon}\right)^{0.5} (\varepsilon_{Sim.}\upsilon)^{0.25} a_{Sim.} \tag{89}$$

The molecular diffusion D_φ in equation 89 was set to $1.98 \cdot 10^{-9}$ m^2s^{-1}, which is the diffusivity of oxygen in water at 20 °C (Werner et al. (2014)). The kinematic viscosity of water, i.e. $8.926 \cdot 10^{-7}$ m^{-2} s^{-1} was used for υ.

Three different methods to determine a representative value of ε for use in equation 88 and equation 89 were evaluated, i.e. the maximum value of ε in the liquid, the average value of ε in the liquid and the average value of ε at the interface.

The Reynolds numbers, experimental k_La values and the simulated specific interfacial areas and volume averaged energy dissipation rates were also related to each other via the correlations displayed in equation 90 to 95. The exponents in these correlations were evaluated using Microsoft Excel 2010.

$$k_L a_{Exp.} \propto Re_{Impeller}^{X} \quad (90)$$

$$\varepsilon_{Sim.\ Volume\ Ave.} \propto Re_{Impeller}^{X} \quad (91)$$

$$a_{Sim.} \propto Re_{Impeller}^{X} \quad (92)$$

$$k_L a_{Exp.} \propto a_{Sim.}^{X} \quad (93)$$

$$k_L a_{Exp.} \propto a_{Sim.}^{1} \varepsilon_{Sim.\ Volume\ Ave.}^{X} \quad (94)$$

$$k_L a_{Exp.} \propto a_{Sim.}^{X} \varepsilon_{Sim.}^{0.25} \quad (95)$$

3.2.4.4. Oxygen transfer evaluation for dispersed flow

The oxygen transfer rates were evaluated similarly for the dispersed flow as for the free-surface simulations, i.e. using equation 89, and likewise the mass transfer coefficients were evaluated via equation 88. One important difference was however that the simulated $k_L a$ values were evaluated in each node, instead of globally, for the dispersed simulations. The reason for this difference was that the specific interfacial surfaces could only be calculated once per free-surface simulation while it could be evaluated in each node for the dispersed flows. The specific interfacial areas were thereby evaluated using equation 56 in combination with equation 57.

3.2.4.5. Transient mixing time simulation evaluation for one and two-phase flows

During mixing simulations, abundances of the additional variables in the pre-defined monitoring points as well as their maximum and minimum value in the reactor domains were observed over time. Mixing time was then defined as the time when the concentrations entered within the ± 5, 10 or 15% interval of their final value. The final values were defined as the concentration of the additional variables once homogenously distributed in the fluid. Two examples of how the mixing time is defined are shown in Figure 18 where the concentrations 'red' and 'blue' are plotted over time. Both concentrations will eventually stabilize at the value 1, and a ± 10% interval around this value has therefore been plotted in the figure as well. The last time the concentrations enter within this region are defined as the 10% mixing time, and the corresponding time values are pointed out on the time axis.

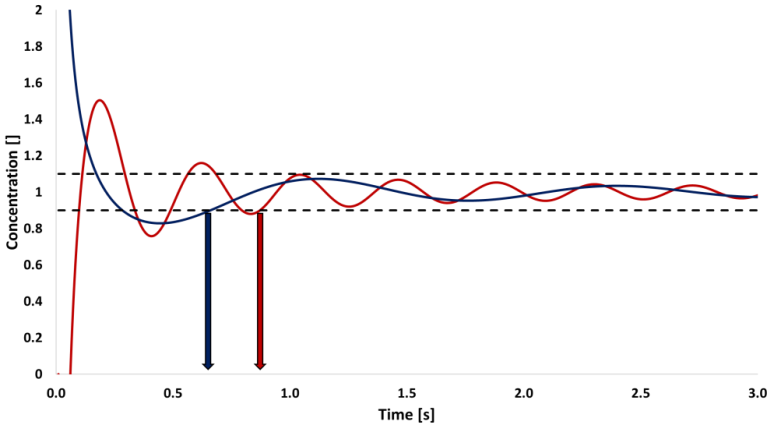

Figure 18. The mixing time definition used in this project.

3.3. Simulation setup for the microbioreactor

3.3.1. Mesh and geometry setup

The full geometry of the microbioreactor used in Bolic et al. (2012) was kindly provided by Andrijana Bolic as a STEP file. The geometry of the microbioreactor was split in two in order to take advantage of the 180° rotational symmetry around the shaft, and the design of the paddles were slightly simplified from the original design. This means that the simulated stirring element only had two paddles, one upper and one lower one, instead of four as in the original geometry. The paddles were also made to be fully attached to the rotating element in order to simplify the geometry. The simulated geometry is shown in Figure 19.

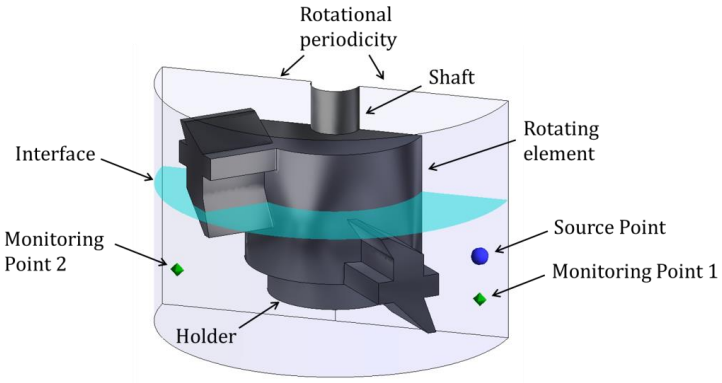

Figure 19. The simulated microbioreactor geometry.

Three different tetrahedral dominant meshes were created for the geometry with a decreasing maximum allowed size for the tetrahedral elements. The number of nodes and elements in the respective meshes can be seen in Table 1, and the full appearance of the coarsest mesh (i.e. Mesh 1) can be seen in Figure 20.

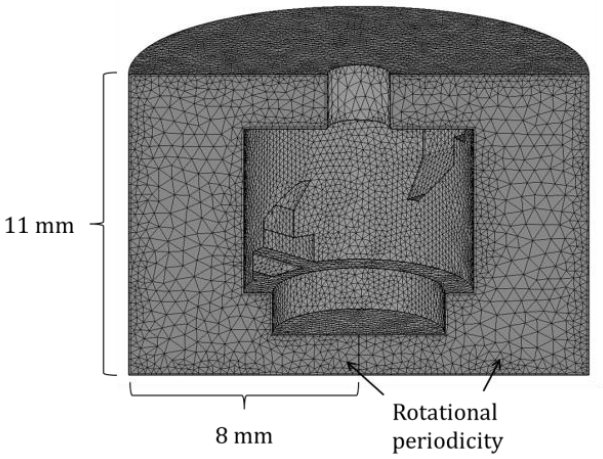

Figure 20. The dimensions of the geometry and the appearance of Mesh 1.

Table 1. Number of nodes and elements in the three meshes associated with the microbioreactor geometry.

Mesh	Number of Elements	Number of Nodes
Mesh 1	282 716	65 170
Mesh 2	807 930	152 378
Mesh 3	1 579 301	291 989

The meshes had a single layer of prism elements on the majority of their boundaries. The reason for not implementing prism layers at all surfaces is that elements with very low quality appeared when it was tested. The surfaces for which prism element generation was not activated are highlighted in Figure 21. Prism elements were not created on the orange paddles since it was not possible to create good quality mesh elements there, and they were not generated on the green rotational periodicity surfaces since no wall boundary condition was applied on them.

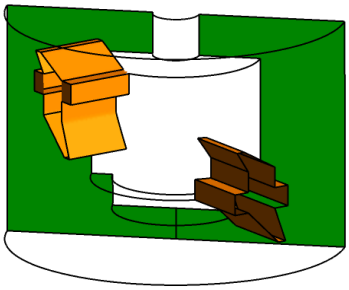

Figure 21. The surfaces not covered with prism mesh elements for the microbioreactor geometry. The surfaces on the stirring element are displayed as orange and the two rotational symmetry planes are green.

3.3.2. Simulation setup

The general simulation setup for modelling of free-surface flow described in section 3.2.2.2 was implemented on the geometry shown in Figure 19. The boundary condition *rotational periodicity* was applied on the indicated planes and the entire geometry was set to be a rotating domain. The top, bottom and the outer reactor wall as well as the shaft and the surface indicated *holder* in Figure 19 were defined to be counter rotating walls. This resulted in simulations where the *rotating element* had the rotational speed chosen, while the counter rotating parts were stationary in the stationary frame.

The light blue interface in Figure 19 indicates the position of the liquid-gas interface when no rotation was applied, and is the height at which the gas-liquid interface was initialized. The liquid volume in the geometry shown, i.e. the volume of the liquid phase under the interface in Figure 19, was 0.5 ml which means that the volume of the full reactor was modelled to be 1 ml.

The rotational speeds 200, 400, 600, 800 and 1000 rotations per minute (rpm) were simulated for the microbioreactor and the k-ε, k-ω and the SST turbulence models were evaluated as well as the laminar model.

For the transient simulations, additional variables (with diffusivity $2 \cdot 10^{-9}$ m^2 s^{-1}) were added to the system into the source point shown in Figure 19. The additional variables were added

for the first 0.01 seconds using the time dependent step function. The values of the additional variables were observed in the two monitoring points M.P.1 and M.P.2 also indicated in Figure 19, and the maximum and minimum concentrations of the additional variable over time were recorded.

3.3.3. Simulation evaluation

Three standard (straight) lines and two polylines (curved) were defined in the geometry and their positions are shown in Figure 22. From these lines data describing the water velocities, energy dissipation rates and viscosities were exported as explained in section 3.2.4.1. The abundances of energy dissipation rates in the liquid volume and at the interface were also evaluated, as well as the size of the interface as described in section 3.2.4.1.

The oxygen transfer rates were evaluated as explained in section 3.2.4.3 and the mixing time was evaluated according to section 3.2.4.5. The Reynolds number for the two phases was calculated using equation 10 and the impeller diameter 14 mm.

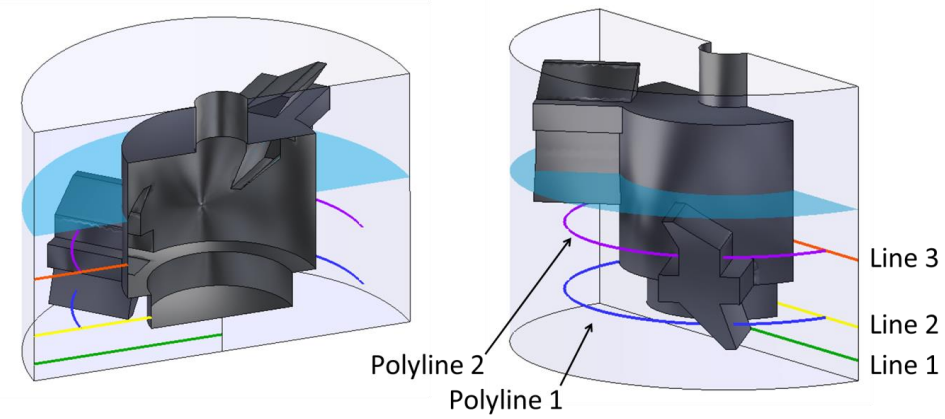

Figure 22. The positions of the monitoring lines.

3.4. Simulation setup for the magnetically stirred reactor

3.4.1. Mesh and geometry setup

An overview of the simulated geometry for the magnetically stirred reactor can be seen in Figure 23 and the geometry was built based on measurements on the experimental setup. The turquoise interface indicates the surface between the gas and the liquid phase for a resting system, and the rotating magnet is located on the bottom of the reactor. Rotational periodicity was used for this geometry similar to the microbioreactor case study, and the two faces for where it was applied are indicated in Figure 23. A detailed view on the appearance of the surface mesh in the bottom part of the geometry and on the magnet is shown in Figure 24. The magnet was slightly lowered into the bottom of the reactor in order to facilitate the mesh generation.

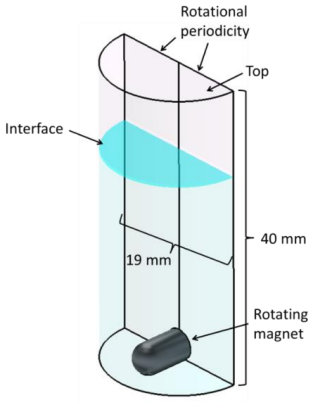

Figure 23. The simulated geometry for the magnetically stirred reactor.

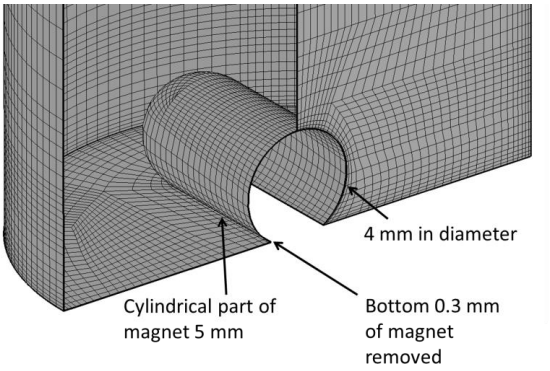

Figure 24. A detailed view of the magnet and the surface meshes in the lower part of the magnetically stirred reactor.

Six different structured (hexahedral) meshes were created for the geometry. One of them was defined as the original geometry, and the other meshes were created by alternating details of it. The appearance of the original mesh is shown most towards the left in Figure 25 followed by four of the alternative meshes.

The original mesh was altered in three ways: Either the interface region was refined or coarsened in the height direction, or the middle region of the mesh was refined or coarsened. The fifth alternation was the addition of a refined boundary at the outer cylindrical wall.

The alternations in the height direction are shown in Figure 25 and the appearance of the refined boundary layer from above is compared to standard boundaries in Figure 26. All meshes shown in Figure 25 have the standard boundaries shown in Figure 26, and the mesh with the refined boundaries looked like the original mesh from the perspective in Figure 25. The number of nodes and elements in the respective meshes can be seen in Table 2.

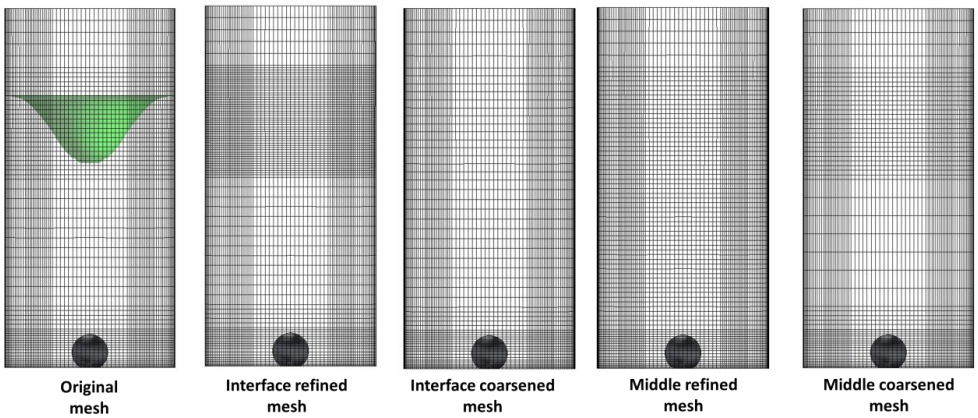

Figure 25. The appearance of the original mesh and four of the altered meshes. The green interface in the original mesh visualized the position of the gas-liquid interface at 900 rpm.

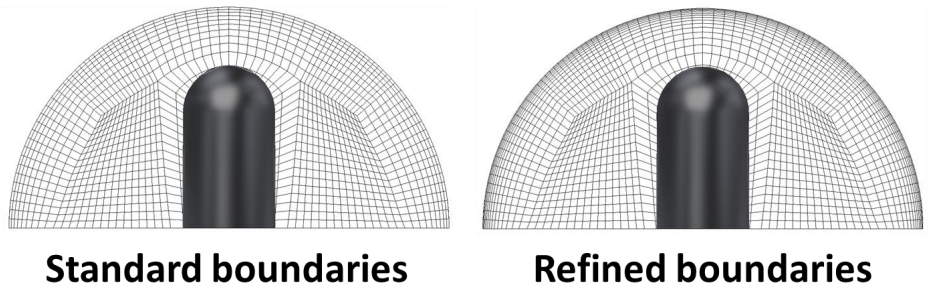

Figure 26. The top-view of the standard meshes and the boundary refined mesh.

Table 2. Number of nodes and elements in the six meshes associated with the magnetically stirred reactor geometry.

Mesh	Number of Elements	Number of Nodes
Original mesh	101 712	108 792
Interface refined mesh	140 562	149 517
Interface coarsened mesh	86 172	92 502
Boundary refined mesh	142 458	150 965
Middle refined mesh	92 388	99 018
Middle coarsened mesh	123 468	131 598

3.4.2. Simulation setup

The rotational speeds 300, 600 and 900 rpm were simulated using the free-surface, two-phase settings presented in section 3.2.2.2 and both the SST and the k-ε turbulence models were evaluated. The top surface indicated in Figure 23 was simulated as a *free slip wall* for both the liquid and the gas phase in all simulations except one. Two variants where then simulated: In the one exception the opening option *entrainment* was used instead of the free-slip wall at the top, and in a few simulations the homogenous Euler-Euler method was used.

The entire reactor geometry was defined to be a rotating domain and the outer cylindrical walls and the bottom wall in the reactor were modelled to have counter-rotating velocities. The top boundary was defined to be a *free slip wall*.

The location of the initial gas-liquid interface was set to create a liquid volume close to 4 ml in the half geometry, and the position of the initial gas-liquid interface is pointed out in Figure 23.

3.4.3. Simulation evaluation

Three straight lines and six curved polylines were defined at the positions shown in Figure 27. From these lines the numerical values for the water velocities, the energy dissipation rates and the viscosities were exported as explained in section 3.2.4.1. The averaged value of the energy dissipation rate in the liquid volume as well as its average at the gas-liquid interface and its maximum value in the liquid volume were also evaluated in accordance with section 3.2.4.3.

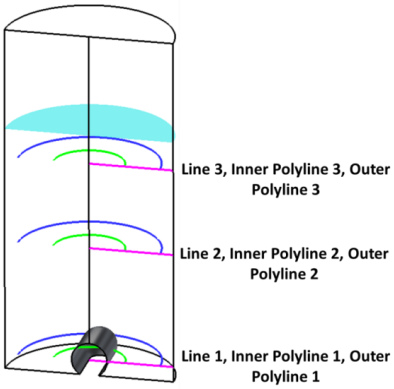

Figure 27. The positioning of the evaluation lines for the magnetically stirred reactor.

The oxygen transfer rates were evaluated for the steady-state results as explained in section 3.2.4.3. No transient mixing simulations were performed for the magnetically stirred reactor. The Reynolds number for the water phase was calculated using equation 10 and the impeller diameter 12 mm. The Reynolds number for the air phase was not evaluated for this setup since the air phase did not have any contact with the rotating magnet.

3.5. Simulation setup for the pilot plant reactor

3.5.1. Mesh and geometry setup

The geometry setup for the pilot plant reactor is shown in Figure 28 and the geometry was initially drawn by PhD student Christian Bach based on measurements on the experimental setup. As in the microbioreactor and the magnetically stirred reactor case studies, only half of the geometry was simulated and the boundary condition rotational periodicity was used.

The simulated geometry contained two baffles, one impeller connected to a rotating shaft and a ring sparger. Details of the sparger and the impeller are displayed in Figure 29. The geometry was split in one (green) rotating domain containing the impeller and the ring sparger and one (pink) stationary domain holding the baffles and most of the impeller shaft. The total volume of the half reactor in Figure 25 was 340 L.

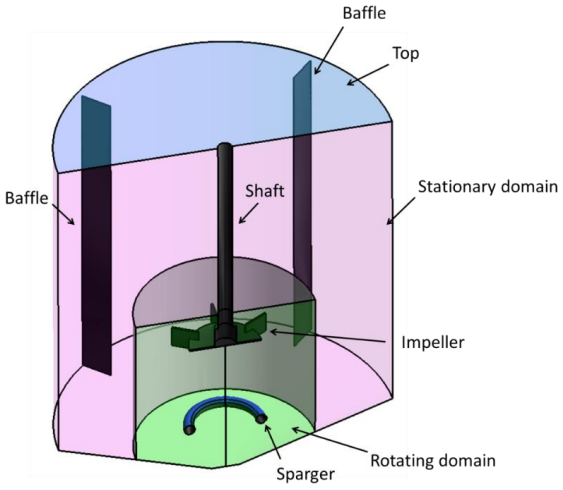

Figure 28. The simulated geometry for the pilot plant reactor.

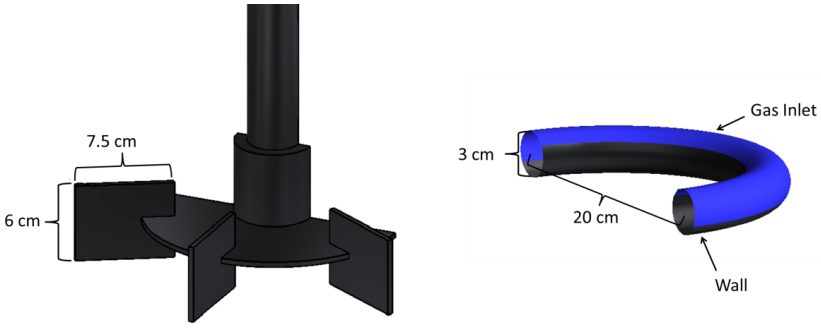

Figure 29. The impeller and the sparger used for the pilot plant reactor.

Two different hexahedral meshes were created, one original and one boundary refined mesh. An overview of the appearance of some of the surface meshes in the original mesh can be seen in Figure 30.

For the boundary-refined mesh the elements closest to the surfaces were refined by splitting the elements closest to the walls into three elements. This was performed by creating a so-called o-grid around the relevant surfaces in ICEM CFD 15.0. The region above the ring sparger was also refined, i.e. the number of nodes was increased, for the refined mesh.

Two pictures illustrating the differences between the original and the refined mesh are shown in Figure 31. The purple pictures in Figure 31 are shown from the bottom corner of the reactor and the green ones from the area around the impeller. The number of elements and nodes in each mesh is reported in Table 3.

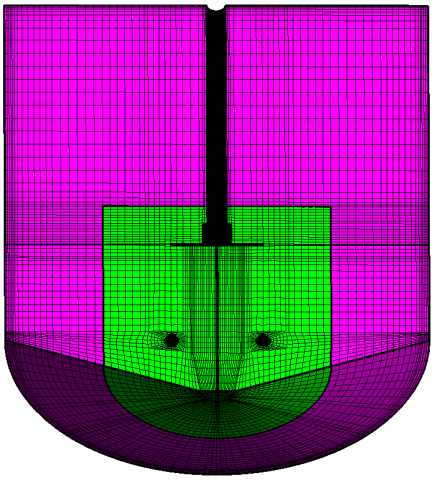

Figure 30. The surface meshes of the original mesh viewed from underneath.

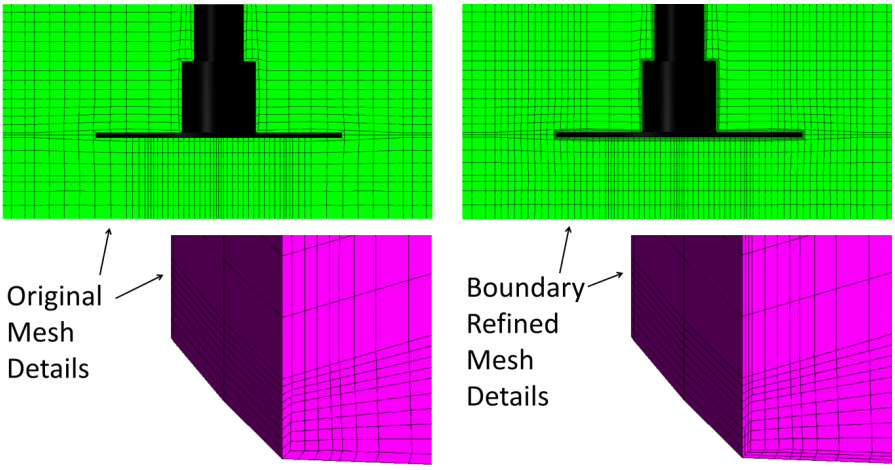

Figure 31. Two details of the original mesh compared to the boundary refined mesh.

Table 3. Number of nodes and elements in the two meshes associated with the pilot plant reactor geometry.

Mesh	Number of Elements	Number of Nodes
Original Mesh	148 094	164 660
Boundary Refined Mesh	209 998	230 800

3.5.2. Simulation setup

Both one-phase and two-phase simulations were performed for the pilot plant bioreactor. In both cases the pink volume in Figure 28 was defined as a stationary domain while the green volume was defined to be a rotating domain. Between the domains two domain interfaces were defined, one with a circular shape and one shaped like half a cylinder. Both interfaces were modelled using the frame change option *frozen rotor*.

The bottom wall in the rotating domain was defined to be a counter-rotating wall in order to make it static in the stationary domain. The same was applied for the grey part of the sparger in Figure 26, so that it was also standing still. In the one-phase simulations this was also true for the blue part of the sparger.

In the one-phase simulations water was selected as the simulated fluid and for the two-phase simulations the fluid consisted of water with dispersed air as described in section 3.2.2.3. For the one-phase simulations the top boundary condition shown in Figure 28 was defined to be a free slip surface and for the two-phase simulations it was defined as the outlet option *degassing condition*.

For the one-phase simulation the shaft was modelled to be static in the rotating frame. In the two-phase simulations, it was set to have the same rotational speeds as the impeller for the water phase. For the air-phase, the shaft as well as the baffles and the additional walls in the stator domain were defined to be *free slip walls*.

The SST and the k-ε turbulence models were both evaluated for the one-phase simulations, and the SST model was applied for the two-phase flow. The rotational speeds 174, 230 and 286 rpm were investigated for all rotational rates and turbulence models.

For the two-phase simulations, air was injected into the system from the blue part of the sparger shown in Figure 29. The air injection rates corresponded to 500 L/min, 250 L/min and 125 L/m for the full reactor, which correlated to $4.94 \cdot 10^{-3}$, $2.47 \cdot 10^{-3}$ and $1.23 \cdot 10^{-3}$ kg s^{-1} for the simulated geometry. The flow direction was set to be normal to the boundary conditions and was defined to consist of 100% air.

Different bubble size diameters were evaluated for the two-phase simulations, namely 1, 2, 4, 8 and 16 mm. Most simulations were however performed with 4 mm bubbles.

Mixing simulations were performed both on the one-phase and two-phase cases and were initiated as presented in section 3.2.2.4. The additional variables were added from the source point shown in Figure 32 for varying time length. The values of the additional variables were evaluated in the top and bottom monitoring point indicated in the same picture. The maximum and minimum values of the additional variable were monitored as well.

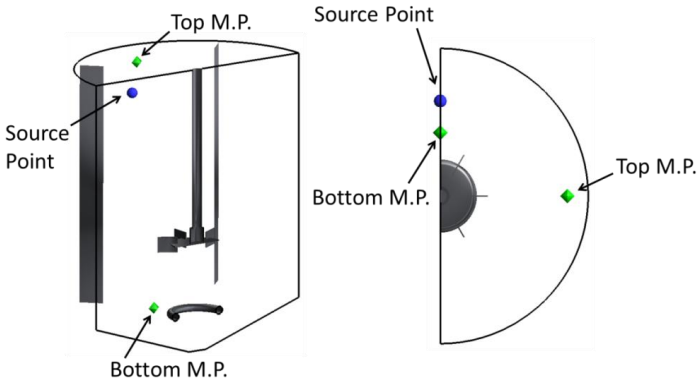

Figure 32. The positions of the source point and monitoring points (M.P.) for the mixing simulations in the pilot plant reactor.

3.5.3. Simulation evaluation

The steady-state results were evaluated according to section 3.2.4.2 for the two-phase flow, and the one-phase flow was evaluated in a very similar manner. The used lines and polylines are displayed in Figure 33. The mass transfer coefficient and oxygen transfer rates were evaluated according to section 3.2.4.4 using the C_P constant 1.

The mixing simulations were evaluated according to section 3.2.4.5 using the transient additional variable measurements from the top and bottom monitoring points displayed in Figure 32 as well as the maximum and minimum concentrations.

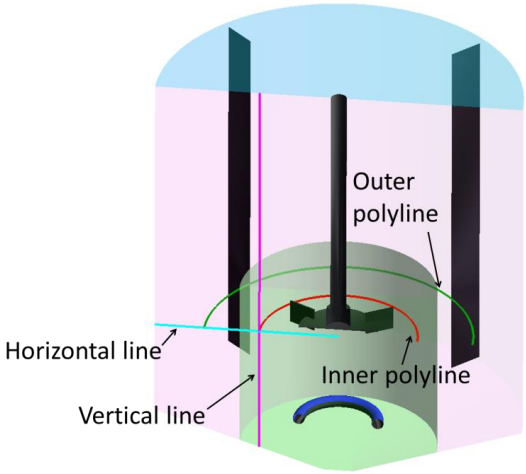

Figure 33. The position of the monitoring lines and polylines used in the pilot plant reactor.

3.6. Simulation setup for the rotating bed reactor

3.6.1. Mesh and geometry setup

Three fundamentally different geometries were created in order to describe the rotating bed reactor (RBR). One geometry was based on a STEP-file provided by SpinChem AB, and a simplified version of this geometry was also evaluated. The third geometry consisted of only the porous part of the simplified geometry. The simplified geometry was also altered for the sake of optimization studies.

3.6.1.1. The original geometry

The provided original geometry was slightly simplified in order to facilitate mesh generation on it. For example, the two top holes on the shaft were removed since their purpose mainly was to avoid capture of air bubbles inside of it during practical use. In addition to this were a couple of additional minor alternations performed on the geometry where a few thin gaps and cavities were sealed.

The RBR geometry was then virtually placed in a flower-shaped vessel with 16 petals, which was drawn around it. The vessel the experiments were performed in had 18 petals, or baffles, but it was simplified to 16 in order to be able to use the symmetry of the system to simulate only one fourth of the geometry. The main dimensions of the geometry are displayed in Figure 34.

The fluid volume in this 360° setup was 164.5 ml including the volume taken up by the porous material. The geometry shown in Figure 34 will from now on be referred to as the original RBR geometry or just the original geometry.

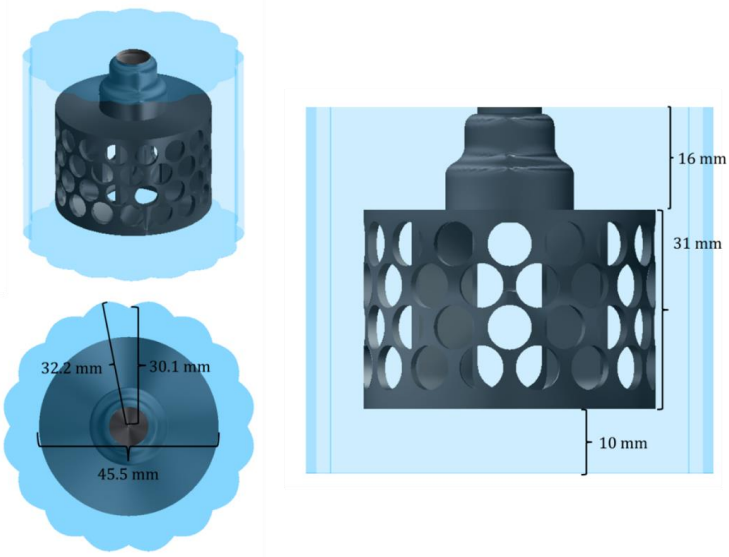

Figure 34. The simulated geometry for the rotating bed reactor.

The original geometry was spilt into one 90° section to facilitate mesh generation and decrease the computational costs. The geometry was then separated into one rotating and one

stationary part. The rotating part was furthermore split into one porous domain and one standard fluid domain. The location of the different domains together with the interfaces connecting them is shown in Figure 35.

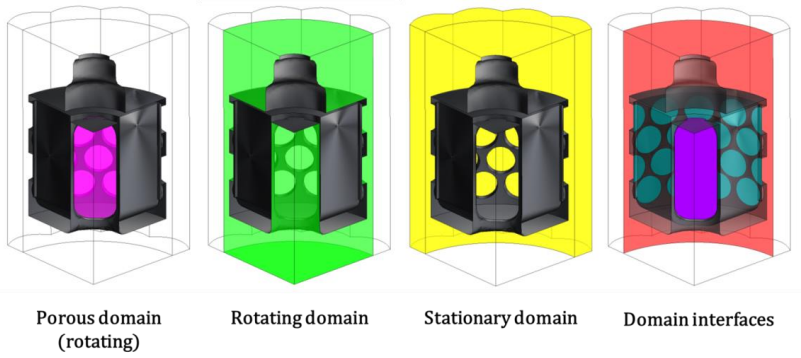

Figure 35. The tree different domains *porous*, *rotating* and *stationary* as well as the interfaces between them.

Four different unstructured meshes were created and the settings in ICEM CFD 15.0 allowed the creation of hex-core elements in all of the meshes. Two different maximum sizes for the mesh elements were selected, and the meshes were created with or without a prism layer. In the cases where prism layers were activated they were allowed to be generated at all actual surfaces in the mesh, i.e. everywhere except at the symmetry planes and at the domain interfaces.

The appearance of the original meshes is displayed in in Figure 36. In the top row in the figure, the hexahedral elements are displayed as grey and the great majority of the mesh elements not displayed in the figure were tetrahedral. The purple surfaces in the figure also show the details of the mesh structures at this plane, and the total number of nodes and elements in the four meshes are stated in Table 4.

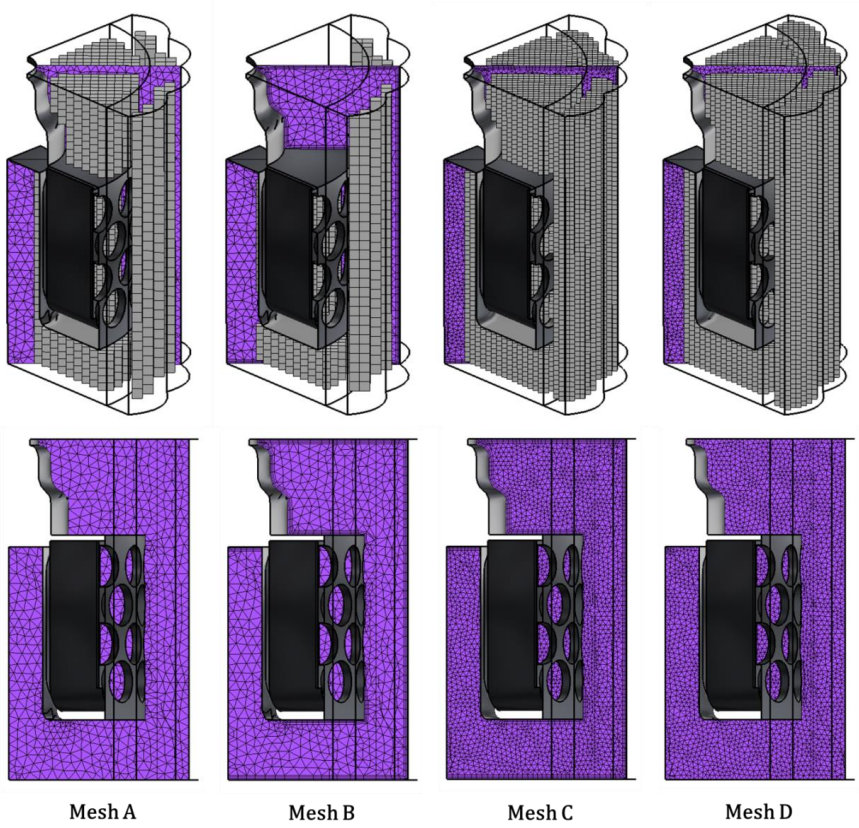

Figure 36. The four meshes used for the original rotating bed reactor geometry. The hexahedral mesh elements are displayed in grey.

Table 4. Number of nodes and elements in the four meshes associated with the original rotating bed reactor geometry.

Mesh	Number of Elements	Number of Nodes
Mesh A	127 508	35 700
Mesh B	165 418	52 099
Mesh C	458 232	149 303
Mesh D	353 006	103 944

3.6.1.2. The simplified geometry

The simplified reactor design was very similar to the original one with the same dimensions, but it was as its name suggests once again simplified in order to facilitate mesh generation. For example, the inner and outer holes (purple and turquoise in Figure 35) were removed which means that the material surrounding them was removed and they were replaced by just two large openings. The effect of this is clarified in Figure 37.

The shape of the shaft was also simplified such that it got a constant radius. The four internal walls inside of the porous material were also removed, which made it possible to simplify the

geometry to a piece of 22.5°. A smaller geometry than 22.5° was not possible to achieve due to the existence of the 16 baffles petals.

The geometrical setup of the simplified geometry was very similar to the original one, and the shape and position of the different domains are shown in Figure 37 where the general geometry of the setup can be seen as well. The liquid volume in the simplified 22.5° geometry was 10.7 ml, which corresponds to about 172 ml for the analogous full 360° geometry.

Due to the significantly less complex shape of the simplified geometry, it was possible to create hexahedral meshes associated with it. The two meshes shown in Figure 38 were created for the simplified geometry and the number of nodes and elements in them are displayed in Table 5.

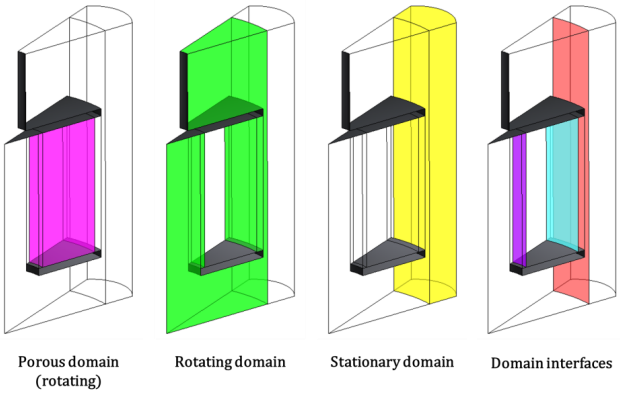

Figure 37. The porous, rotating and stationary domain as well as the domain interfaces for the simplified reactor design.

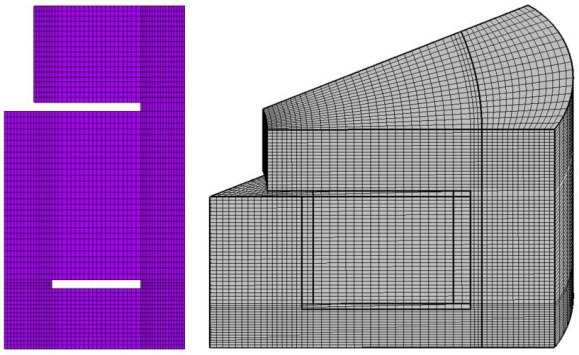

Figure 38. The coarsest of the two used meshes (Mesh α) for the simplified rotating bed reactor geometry. All mesh elements are hexahedral.

Table 5. Number of nodes and elements in the two meshes associated with the simplified rotating bed reactor geometry.

Mesh	Number of Elements	Number of Nodes
Mesh α	56 439	64 992
Mesh β	306 880	332 792

A set of alternative geometries and meshes were also created for shape alteration studies of the glass beaker. The new geometries were based on Mesh α and their shapes are summarized in Figure 39, Figure 40 and Figure 41. The number of nodes and elements in the meshes are displayed in Table 6, Table 7 and Table 8.

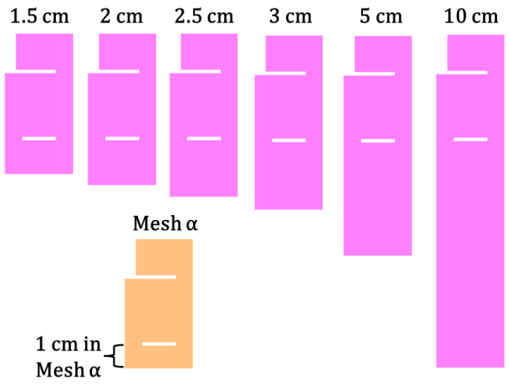

Figure 39. Side-view of the altered geometries investigating changes in the distance from the bottom of the rotating bed reactor to the bottom of the beaker. Mesh α is displayed for comparison.

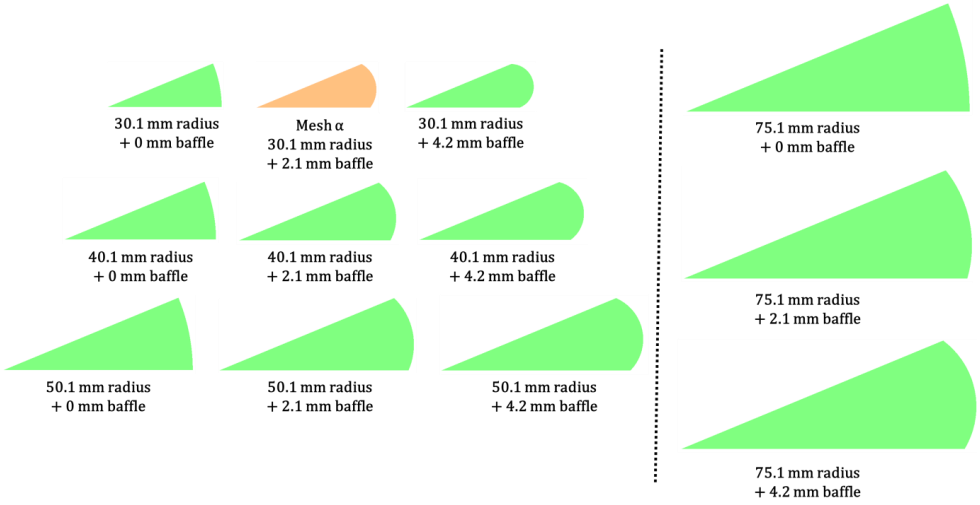

Figure 40. Top-view of the altered geometries investigating changes in the beaker radius and baffle depth. Mesh α is displayed for comparison.

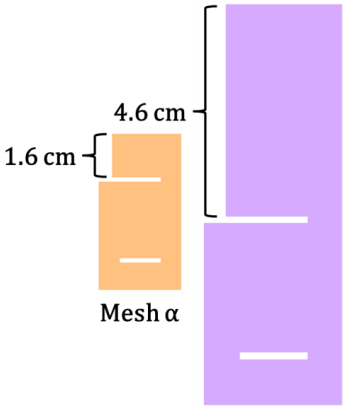

Figure 41. Side-view of the altered geometry used for the two-phase simulations, which was only changed in the height direction. Two of these geometries were created: One with the baffle depth 0 and one with the baffle depth 2.1 mm. Mesh α is displayed for comparison.

Table 6. Number of nodes and elements in the meshes associated with the geometries presented in Figure 39.

Mesh/Depth	Number of Elements	Number of Nodes
1.5 cm	62 676	71 810
2 cm	69 804	79 602
2.5 cm	76 932	87 394
3 cm	83 169	94 212
5 cm	109 899	123 432
10 cm	176 724	196 482

Table 7. Number of nodes and elements in the meshes associated with the geometries presented in Figure 40.

Mesh/Baffle dimension	Number of Elements	Number of Nodes
30.1 mm radius, 0 mm baffle	56 439	64 992
30.1 mm radius, 4.2 mm baffle	56 439	64 992
40.1 mm radius, 0 mm baffle	66 087	75 328
40.1 mm radius, 2.1 mm baffle	66 087	75 328
40.1 mm radius, 4.2 mm baffle	66 087	75 328
50.1 mm radius, 0 mm baffle	75 735	85 664
50.1 mm radius, 2.1 mm baffle	75 735	85 664
50.1 mm radius, 4.2 mm baffle	75 735	85 664
75.1 mm radius, 0 mm baffle	101 061	112 796
75.1 mm radius, 2.1 mm baffle	101 061	112 796
75.1 mm radius, 4.2 mm baffle	101 061	112 796

Table 8. Number of nodes and elements in the meshes associated with the geometries presented in Figure 41.

Mesh/Baffle dimension	Number of Elements	Number of Nodes
0 mm baffle	88 029	99 819
2.1 mm baffle	88 029	99 819

3.6.1.3. The isolated porous geometry

The porous domain of the simplified reactor design was isolated and treated as an own geometry for a set of simulations. The geometry of the used porous piece is shown in Figure 42 and the three hexahedral meshes created for it are displayed in Figure 43. The number of nodes and elements in the meshes are stated in Table 9.

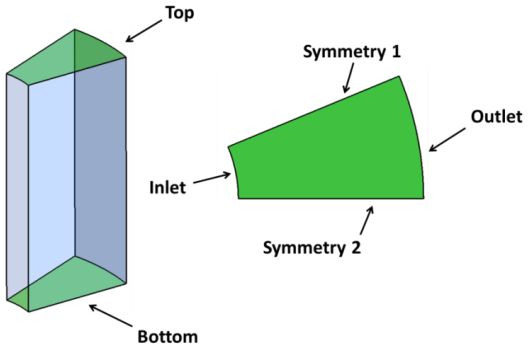

Figure 42. Side and top view of the porous geometry.

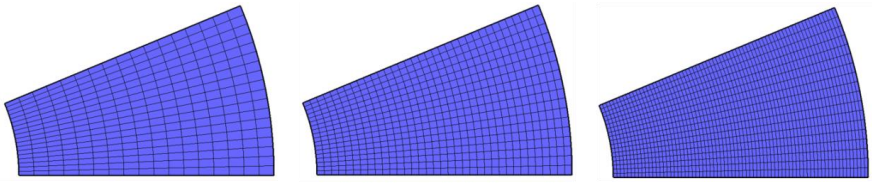

Figure 43. The three meshes created for the separated porous material shown in Figure 42.

Table 9. Number of nodes and elements in the meshes displayed in Figure 43

Mesh	Number of Elements	Number of Nodes
Mesh i	8 874	10 260
Mesh ii	18 270	20 520
Mesh iii	37 062	41 040

3.6.2. Simulation setup

3.6.2.1. Simulation setup for the original and simplified geometry

The RBR was simulated with the one-phase model in all cases except one. For the original and simplified reactor design, as explained above, the rotating and the porous domains in Figure 35 and Figure 37 were modelled to be rotating domains while the stationary domain was set to be stationary in the stationary frame of reference.

The inner and outer interfaces (purple and turquoise in the figures) between the porous and rotating domains were set to be a general connection while the interface between the rotating and stationary domain (red) was set to be a *frozen rotor* interface.

All solid walls in the reactor were set to be *no slip walls* except the top surface. The top surface was instead set to be a *free slip wall* in order to simulate a gas-liquid interface. The part of the bottom surface located within the rotating domain was set to be a counter rotating wall in order to keep it static relative to the stationary frame.

The porous rotating domain was set to be a porous domain associated with an isotropic linear loss coefficient. The superficial linear resistance coefficient (C_1 in equation 45) was determined to be $5.4 \cdot 10^6$ kg m^{-3} s^{-1} based on pressure drop data. The pressure drop data was taken from the product data sheet (The Dow Chemical Company) of the resin used in the experiments described in section 3.1.2. Simulations were also performed where variations of C_1 were investigated.

The volume porosity coefficient in the porous domain (γ in equation 44) was set to 1 for the simulations as a basis, but the impact of using the values 0.5 and 0 was also investigated. Both the SST and the k-ε turbulence models were also investigated for the reactors. For the original reactor design the rotational speeds 70, 500 and 900 rpm were simulated and for the simplified design the rotational speeds 70, 100, 300, 500, 700 and 900 rpm were simulated.

Most of the simulations were performed for the original Mesh A, B, C and D and the simplified Mesh α and Mesh β presented in Figure 36 and Figure 38, but shape improvement studies of the glass vessels were also performed. The impact of the distance from the bottom of the RBR to the bottom of the reactor vessel was investigated by simulating the geometries presented in Figure 39. The impact of the radial distance to the baffled wall as well as the depth of the baffles was investigated based on the geometries displayed in Figure 40.

Two two-phase free-surface simulations were also performed for the simplified reactor. For this two new meshes were created, both with an extended height. The difference between the extra high meshes and the ordinary Mesh α is displayed in Figure 41. One of the two-phase adapted meshes had no baffles (i.e. it had a cylindrical outer wall) and the other one had 2.1 mm deep baffles. The top-view of this difference is shown in Figure 40. The two-phase simulations were performed with the settings presented in section 3.2.2.2 and the location of the gas-liquid interface was initiated at the same height as the top wall in Mesh α in order to keep the liquid volume constant.

3.6.2.2. Simulations of the isolated porous geometry

Separate simulations were performed for the isolated porous geometry and for this the geometry and meshes presented in section 3.6.1.3 were used. The geometry was still modelled as a porous domain with the loss coefficient C_1 in equation 45 set to $5.4 \cdot 10^6$ kg m^{-3} s^{-1}.

One-phase simulations were performed, and the wall boundary condition *symmetry* was used at the indicated walls in Figure 42. The top and the bottom walls were set to be *no slip walls*.

The inlet and outlet walls were set to have positive and negative mass flow rates based on the results from the simplified reactor design. This means that for the simulations of the isolated porous material the mass flow rates were taken from the calculated flow through the porous material in the simulations based on Mesh α, i.e. in the simplified geometry. Different inflow (and outflow) rates were therefore used to simulate different rotational speeds.

Additional variables were used to model the chemical reactions (ion-exchange phenomena) taking place in the porous materials. The additional variables were defined as volumetric and given the diffusion coefficient $2 \cdot 10^{-9}$ m^2 s^{-1}. Both the laminar and the SST turbulence model were evaluated. Simulations were also performed where the eddy viscosity μ_t was set to different constant values instead of being calculated via equation 26.

For the first kind of transient simulations, the concentration of the additional variable in the porous volume was initialized to zero and mixing-like experiments were performed where the inlet concentration of the additional variable was set to unity. In these simulations the momentum equations were solved first, and further on the scalar equation based on a frozen velocity field as described in section 3.2.2.4. Steady-state and transient simulations were then performed where the ion-exchange phenomena were modelled.

The ion-exchange rate was modelled based on the pseudo-first-order reaction presented in section 2.3.4. This means that the source term shown in equation 96 was added to equation 43 in the entire porous domain. The step function in equation 96 was implemented in order to avoid any reaction to occur if the values of the additional variable φ decreased below zero. The particle Reynolds number used is defined in equation 65, and the specific interfacial area A_s was calculated using equation 67.

$$S_\varphi = \frac{Sh \cdot D_\varphi \cdot A_s \cdot \varphi \cdot Step(\varphi)}{d_P} \tag{96}$$

Four different Sherwood numbers were evaluated for insertion into equation 96, two constant Sherwood number values, and two correlations obtained from the literature. They are summarized in equation 97, and the two literature correlations used were found in Magnico and Fongarland (2006) and Santos-Moreau, Brunet-Errard, and Rolland (2012) respectively.

$$\begin{gathered} Sh_5 = 5 \\ Sh_{50} = 50 \\ Sh_{Magnico} = 1.1 Re^{0.41} Sc^{0.40} \\ Sh_{Santos-Moreau} = 2 + 1.8 Re^{0.50} Sc^{0.33} \end{gathered} \tag{97}$$

The four investigated Sherwood correlations, as well as the relation used in Schjøtt Andersen (2015), i.e. *Dwivedi*, are displayed in Figure 44.

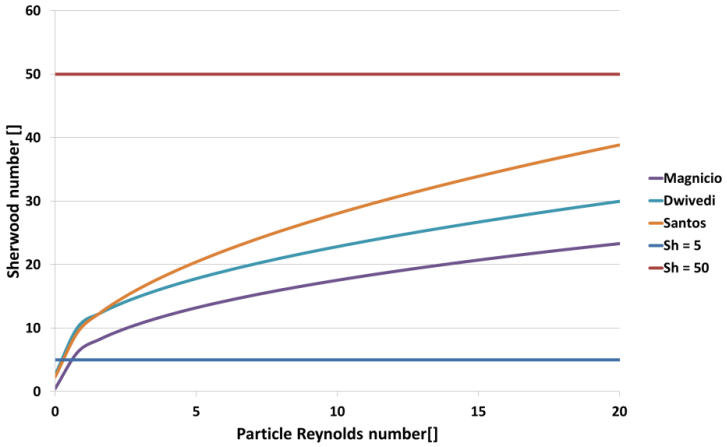

Figure 44. The Sherwood numbers as a function of the particle Reynolds number. The three literature correlations are from Magnico and Fongarland (2006), Dwivedi and Upadhyay (1977) cited in Schjøtt Andersen (2015), and Santos-Moreau, Brunet-Errard, and Rolland (2012).

The diffusion coefficient D_φ in equation 96 was set to $9.3 \cdot 10^{-9}$ m^2 s^{-1}, i.e. the same as for H^+ in Serowy et al. (2003). The constant γ_2 (used in equation 67) was set to 0.35 as in Schjøtt Andersen (2015) and the particle diameter (d_P) was set to 0.5 mm. The particle diameter was estimated based on the resin material data sheet (The Dow Chemical Company), which states that less than 0.1% of the particles were smaller than 0.3 mm and that less than 1% was larger than 0.85 mm.

In the steady-state ion-exchange simulations, the inlet concentration of the additional variable was set to unity and both the momentum and scalar equations were solved until reaching a steady-state solution.

The purpose of the transient ion-exchange simulations was to model how the entire RBR performed over time by only modelling the isolated porous domain. Instantaneous mixing in the liquid outside of the porous regions was therefore assumed, and a mass balance was set up to calculate the inlet concentrations, which varied over time. The concentrations of the additional variable inside of the porous material as well as the inlet concentrations were initiated to unity.

The concentrations outside of the porous material in the fluid were assigned the variable *CF* and the mass of the volume in this region, i.e. outside of the porous material, was calculated to $8.69 \cdot 10^{-3}$ kg based on Mesh α. The value of *CF* was initated to 1 and for each time-step could the concentration in the outer liquid (CF_{New}) then be calculated based on the concentration from the previous time-step (CF_{Old}). The correlation implemented is shown in equation 98, where Q is the mass flow rate in and out of the porous domain, Δt is the time step size and C_{Outlet} is the average concentration of the additional variable at the outlet.

$$CF_{New} = CF_{Old} - \frac{\Delta t \cdot Q \cdot (C_{Outlet} - CF_{Old})}{8.69 \cdot 10^{-3}} \tag{98}$$

The concentrations of the additional variable in the inlet of the porous domain were then set to CF_{New}. Equation 98 is based on recursion where the concentration in the fluid is calculated

as a function of its value in the previous time-step. No officially supported solution of how to implement this in ANSYS CFX 15.0 was however found, but a solution based on manually adding the command 'Update Loop = TRAN_LOOP' to an additional variable describing CF_{New} was found online and implemented. A manual for this was originally published in (ANSYS-bloggen) but this site has been removed. It was nevertheless possible to retrieve a backed up version of it via the online tool https://archive.org/web/.

3.6.3. Simulation evaluation

The flows in the rotating bed reactor were evaluated by exporting the velocities, eddy viscosities and turbulent energy dissipation rates from the lines visualised in Figure 45. Contour plots and vectors were also created on the purple plane displayed in the same figure. Figure 45 only shows the original geometry setup, but the lines and planes were located in the corresponding positions in the simplified geometry.

The volumetric flow through the porous material was determined in the post-processing unit of ANSYS CFX 15.0 by determining the flow through the inner boundary interface shown in purple in Figure 35. In a similar manner were the flows of additional variables at the inlet and outlet of the porous material evaluated.

For the isolated porous material contour plots were created on the two planes indicated in Figure 46 and the mixing times in the isolated porous material were evaluated at the two monitoring points shown. The levels of the additional variables were monitored in two monitoring points and the mixing times were evaluated according to section 3.2.4.5.

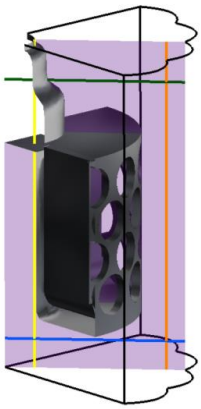

Figure 45. The position of the monitoring lines and the visualisation plane in the original reactor.

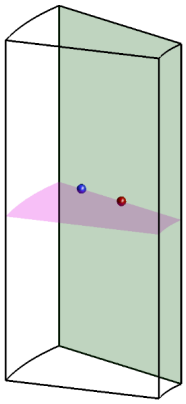

Figure 46. The two monitoring points 'Middle M.P.' (red) and 'End M.P.' (blue) and the two visualisation planes in the isolated porous domain.

4. Results and Discussion

4.1. The microbioreactor

4.1.1. Experimental results

No experiments on the microbioreactor were performed within the scope of this PhD project. The experimental data used was previously presented at Bolic et al. (2012). The mixing times were determined using a colorimetric method and the gassing-out method was used to determine the k_La values of the reactor.

The experimental mixing times and k_La values for the rotational speeds 200, 400, 600, 800 and 1000 rpm from Bolic et al. (2012) are shown in Table 10.

Table 10. Experimental mixing time and k_La values for the microbioreactor previously published in Bolic et al. (2012)

Rotational speed	Mixing time [s]	k_La [h^-1]	k_La [s^-1]
200 rpm	2	70	$1.94 \cdot 10^{-2}$
400 rpm	1.7	120	$3.33 \cdot 10^{-2}$
600 rpm	1.17	150	$4.17 \cdot 10^{-2}$
800 rpm	0.73	180	$5.00 \cdot 10^{-2}$
1000 rpm	0.4	230	$6.39 \cdot 10^{-2}$

4.1.2. Reynolds number and the choice of turbulence model

The Reynolds numbers for the water and the air phase in the microbioreactor calculated using equation 10 and the impeller diameter 14 mm are shown in Table 11.

Table 11. The Reynolds number for the microbioreactor

Fluid	200 rpm	400 rpm	600 rpm	800 rpm	1000 rpm
Water	732	1 464	2 196	2 928	3 660
Air	42	85	127	169	211

As can be seen, the Reynolds numbers are in the range 42 to 3660. It is difficult to choose an appropriate turbulence model based on these values, since they suggest that the flow in the microbioreactor most likely is somewhere in the transient regime. As described in section 2.2.3.1, the transient flow regime for an impeller is in between the Reynolds numbers 10 and 10 000, after which the flow can be assumed to be fully turbulent (Doran (1995)). The definition for flow in a pipe would however define the flow as laminar for most of the cases of Table 11 (i.e. in the air phase for all rotational speeds and in the water phase for less than 600 rpm).

According to the definition in Eibl, Werner, and Eibl (2009), it could be interpreted as if the flow is turbulent in the water phase for all rotational speeds. It is however important to note that a different way of defining the Reynolds number was used in Eibl, Werner, and Eibl (2009). The above discussion highlights however the difficulty of classifying a flow in a non-obvious flow regime and in a complex geometry. An easier case to judge would for example be an obvious laminar flow in a pipe with a Reynolds number smaller than 10, or a flow with a Reynolds number much higher than 10 000.

Knowing if the flow is turbulent or not is nevertheless important, since the k-ε model for example is only valid for fully turbulent flows according to ANSYS® Academic Research (2013). Using an incorrect turbulence model for a flow that is close to a laminar regime might result in too high values for the eddy viscosity, which makes the fluid appear more viscous than it actually is. Using no turbulence model where it should be applied can on the other hand easily lead to the problem that a simulation does not converge since the molecular viscosity alone is too low to stabilize the flow.

An additional disadvantage related to not using a turbulence model is that no ε is calculated in laminar simulations, which makes the eddy cell model impossible to use. This would also be the consequence even if a very fine time step and mesh were used and the turbulent eddies actually were captured correctly in the simulation. Once using an incorrect turbulence model the risk of having the wrong model is still present, but a simulated value for ε is at least provided by the model.

As presented in the literature study in section 2.4 the eddy cell model has also been used for similar systems where fully developed turbulence is questionable. Most similar to the microbioreactor is the system presented in Brüning and Weuster-Botz (2014) where the SST model is used for a miniaturized reactor system with the lowest Reynolds number 2356. The SST model should also be theoretically better for flows with a lower Reynolds number since it can adapt its wall treatment to behave as the laminar model as discussed in section 2.2.5.7.

Since there was no obvious correct turbulence model to use for the microbioreactor, neither based on the Reynolds number nor the literature study, it was decided to evaluate three different turbulence models for the microbioreactor, i.e. the k-ε, k-ω and the SST model. They were chosen since they are the most common turbulence models according to the scientific literature and based on the description in the ANSYS CFX 15.0 manual. The laminar model, i.e. no turbulence model, was also evaluated for comparison purposes.

The general outcome from the simulations was that only the k-ε model managed to converge properly for the higher rotational speeds 800 and 1000 rpm. The k-ω, SST and laminar model also only accomplished to converge for the coarsest mesh, i.e. Mesh 1. Trials were performed with several different solver settings and a fully hexahedral mesh (not shown) was also created and evaluated, but none of the efforts led to convergence for 800 and 1000 rpm. Transient simulations (i.e. time dependent, not steady-state) were also attempted for the higher rotational flows but once again without success.

Another general observation was that the k-ω model behaved very much like the SST model. As explained in section 2.2.5.5 the SST model is a combination of the k-ω model and the k-ε model, where it should behave as k-ω closest to the walls and as k-ε in the middle of a free stream. A plausible explanation for the fact that the SST and k-ω approaches gave so similar results is therefore that the solver considered the entire fluid to be located close to the walls. The results from the k-ω model will however not be discussed further, since they were so similar compared with the SST results.

The lack of convergence for the laminar and SST models was defined by the fact that the residuals did not decrease towards zero, and that the velocities in the monitoring points did not stabilize around a steady value. Oscillations of a monitoring point value in a steady-state simulation must however not always be a problem, but rather an indication of small regions of instability according to LEAP CFD Team (2012). This happened for example in the 600

rpm laminar and SST simulations, but was considered not to be problematic since the oscillations were so small. For the simulations that were not converging the instabilities in the monitoring points were however very large and no periodicity could be seen in them.

The conclusion from the simulations with the different turbulence models was that the k-ε model was the only one that worked properly for all rotational speeds and meshes. That conclusion is however a bit troublesome, since the k-ε model should only be valid for fully turbulent flow. According to Versteeg (2007) the k-ε model has also a poor performance for curved boundary layers and rotating flows. These three statements make the k-ε model a very bad theoretical choice for the microbioreactor with its most likely transient regime and for certain rotating flows, in combination with the curved boundary layers of the outer walls.

This means that the SST model should be better in theory, while the k-ε model worked better in practice. It is also important to remember that the proper convergence of the k-ε model is not equal to stating that the flows predicted by it are correct. Convergence only means that the solver manages to find a solution for the set of differential equations, and has often very little to do with whether the differential equations describe the modelled system are correct or not.

The majority of the presented results in the following sections will be based on the k-ε model, once again since that was the only evaluated turbulence model that provided stable results. The results can also be physically valid even if achieved with a turbulence model not optimized for the system. The results for the laminar and the SST model for the rotational speeds up to 600 rpm are also presented.

4.1.3. Steady-state results for the microbioreactor

4.1.3.1. Appearance and size of the gas-liquid interfaces

The gas-liquid interface and the liquid volumes defined in section 3.2.4.1 were visualised in order to compare the size and appearance of them between different meshes, turbulence models and rotational speeds.

For the k-ε turbulence model the visual result confirmed that the appearances of the interfaces for Mesh 2 and Mesh 3 were very similar for all investigated rotational speeds. The interfaces from Mesh 1 have however a different appearance for higher rotational speeds. The conclusion from the visual inspections was therefore that Mesh 2 was sufficiently fine to model the appearance for all rotational speeds.

The appearances of the interfaces for the k-ε model at 1000 rpm for the three different meshes are shown in Figure 47. The sizes of the resulting specific interfacial areas are also indicated.

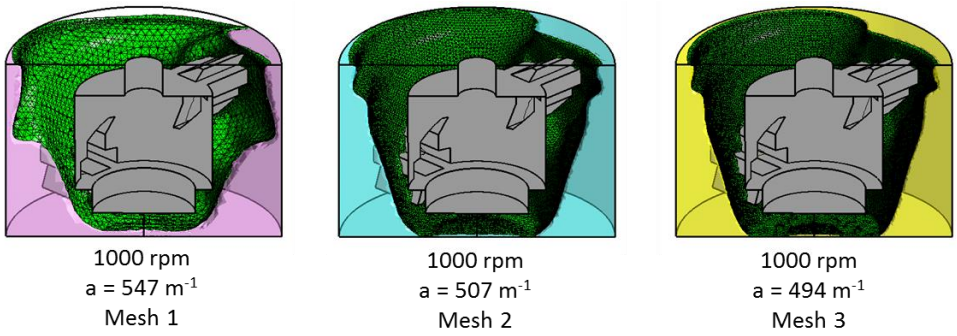

Figure 47. The appearance of the interfaces using the k-ε turbulence model and different meshes for 1000 rpm.

The appearances and specific areas of the interfaces for all simulated rotational speeds using Mesh 2 are shown in Figure 48 and this figure is important in order to understand where the model predicts the liquid interface for the different rotational speeds.

Figure 48 suggests for example that there is almost no liquid located under the stirrer holder for 800 and 1000 rpm, which might be important information for the correct positioning of sensors in the reactor or the selection of the rotational speed to use for a specific experiment. Investigating if there is actually liquid present under the holder for the higher rotational speeds or not is also a reasonable approach to validate the CFD model.

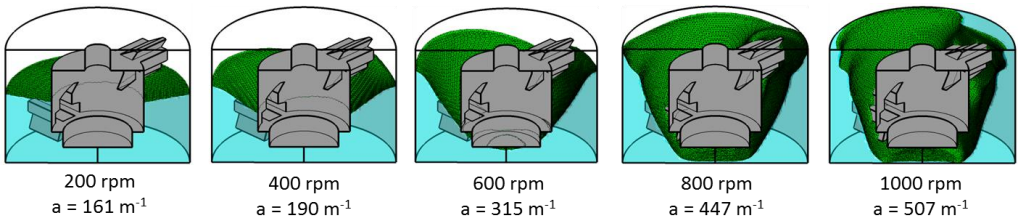

Figure 48. The appearance of the interfaces using the k-ε turbulence model, Mesh 2 and varying rotational speeds.

According to the theory, the oxygen transfer rate k_La is linearly proportional to the size of the specific interfacial area, and once looking at Figure 48 it is clear how a higher rotational speed can give rise to a larger interfacial area. If the distribution of water in Figure 48 is fairly close to the actual distribution of water in the experimental setup, there is however the possibility that the green areas under the holders for 800 and 1000 are only present in the simulation and not in reality.

The reason for this is that the liquid layer just under the green interface below the holder should be very thin in reality, and therefore may not even be present. It is nevertheless present in the simulations since it cannot evaporate or be transported out to the thicker fluid layer by means of surface forces. The consequence of this might be that the prediction of the interfacial area by the model is over-predicting reality.

As mentioned in the previous section the laminar and the SST model did only work for Mesh 1 and for 200, 400 and 600 rpm. The appearances of the 600 rpm interfaces for the laminar,

SST and k-ε model are shown in Figure 49. Interesting observations are that the laminar and the SST model look very similar to each other, and that they are not completely different from the prediction of the k-ε model.

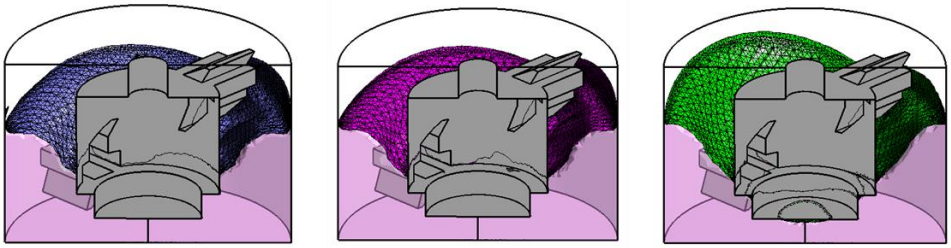

600 rpm
a = 279 m^{-1}
Laminar

600 rpm
a = 279 m^{-1}
SST

600 rpm
a = 314 m^{-1}
k-ε

Figure 49. The appearance of the interfaces using Mesh 1, 600 rpm and the laminar, SST or the k-ε turbulence model.

The specific interfacial area sizes for the different meshes and rotational speeds are shown in Figure 50. One trend is that the size of the interface decreases with an increasing number of nodes for the k-ε model. A possible explanation is that the interface, which is an isosurface created by the post-processing program, might be smoother the smaller the distances between the nodes are. The largest relative size difference between Mesh 2 and Mesh 3 was achieved for 1000 rpm, but since it was less than 3% in combination with their similarities shown in Figure 48 it was decided that Mesh 2 was of sufficient quality to also numerically represent the specific interfacial mesh size. The SST and laminar model achieved also a relatively good performance for the converging cases.

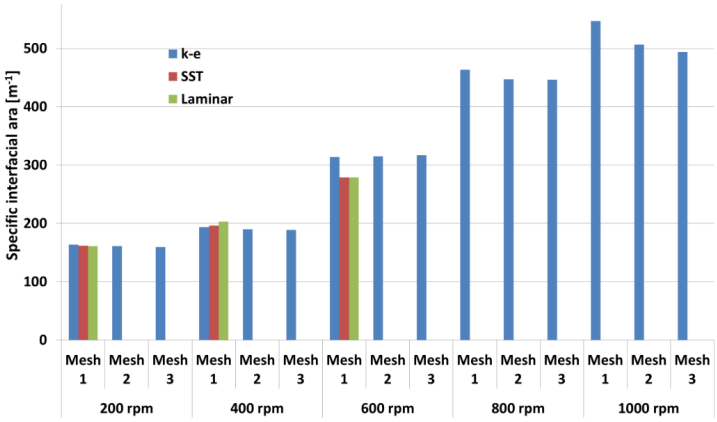

Figure 50. The specific interfacial areas for the different turbulence models, meshes and rotational speeds for the microbioreactor.

4.1.3.2. Velocity profiles for the k-ε turbulence model

The simulated velocities and eddy viscosities for the polylines and lines shown in Figure 22 were compared for the different rotational speeds and meshes. The k-ε model was however the only turbulence model for which the mesh dependence of the solution could be evaluated, since the other models only converged for one of the meshes.

Again, a general trend was that Mesh 1 differed slightly from the results simulated with Mesh 2 and Mesh 3 for the higher rotational speeds. It was therefore decided to use the results from Mesh 2 when comparing the results from different rotational speeds. Two examples of the mesh investigation are shown in Figure 51 and Figure 52. The results for 200 rpm are only shown once in the figures since no difference between the three meshes could be observed. The discontinuities of the velocity lines occur, when the air phase was larger than 0.5. Furthermore, no data is shown inside of the lower impeller blades around 140° in Figure 52.

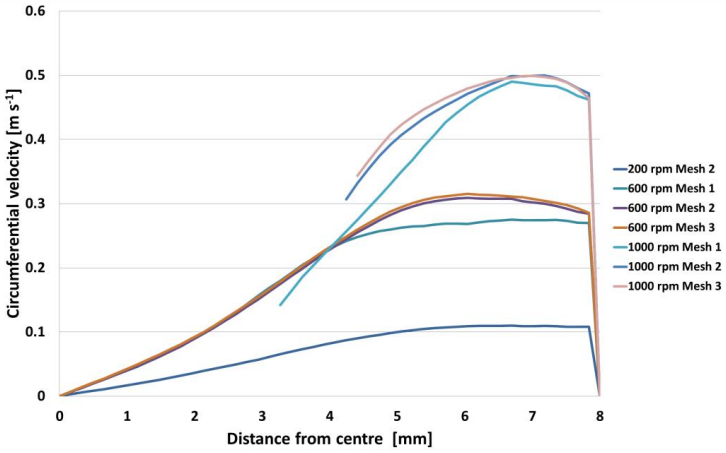

Figure 51. The circumferential velocities on Line 1 (Figure 22) for different meshes at 200, 600 and 1000 rpm. The k-ε turbulence model was used.

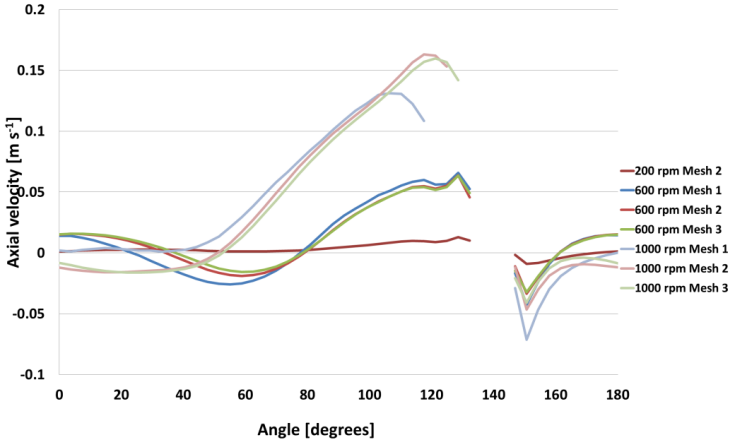

Figure 52. The axial velocities for Polyline 1 (Figure 22) for different meshes and 200, 600 and 1000 rpm. The k-ε turbulence model was used.

The circumferential velocities at Line 1 (Figure 22) for all rotational speeds using Mesh 2 are displayed in Figure 53. It can be seen that all velocities at the outer wall, i.e. 8 mm from the centre, are zero but that the velocities increase rapidly to the velocity of the bulk fluid.

The curves corresponding to 800 and 1000 rpm are not defined closest to the centre, which means that the water is not present there, i.e. that the volume fractions of air is larger than 0.5 where the curves are absent. This observation is also confirmed by Figure 48.

However, for the simulations with fluid present under the holder (i.e. 200, 400 and 600 rpm) Figure 53 shows that the circumferential velocities are very low in this region. This is also true for the corresponding plots of the axial and radial velocities (not shown), i.e. they all have velocities close to zero under the holder.

This is a reasonable outcome once inspecting the design of the reactor, since both the holder and the bottom of the reactor are not moving. All motions of the liquid under the rotor element are therefore caused by viscous forces, i.e. the momentum is transferred to the fluid under the holder by viscous forces from the rotating liquid farther out. The liquid farther away has in turn gained its velocity from the rotating paddles and to a certain extent from the rotating inner cylindrical wall.

Low velocities in the fluid under the holder might be responsible for bad mixing in that region. The low velocities in the radial direction for the liquid under the holder are especially troublesome. Turbulence or instabilities in the actual fluid could however compensate for this to a certain extent. The mixing in the reactor is also further investigated in section 4.1.5.

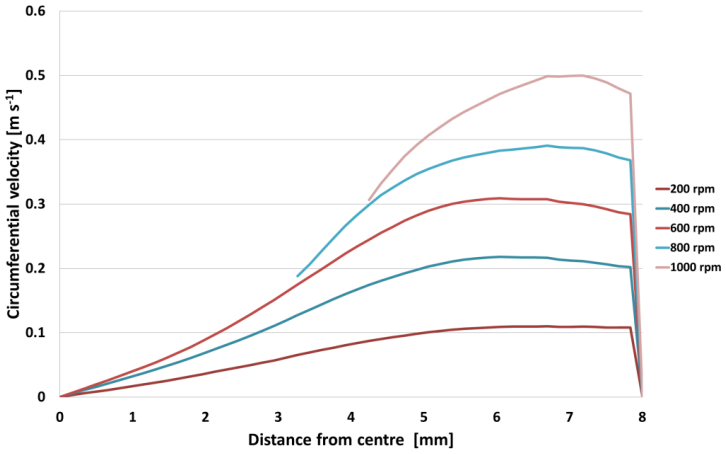

Figure 53. The circumferential velocities for Line 1 (Figure 22) for all rotational speeds using Mesh 2 and the k-ε turbulence model.

The axial, radial and circumferential velocities for Polyline 1 are shown in Figure 54, Figure 55 and Figure 56 respectively. The absence of curves in the region around 140° is as well representing the solid of the lower paddle shown in Figure 22. The curve corresponding to 1000 rpm ends slightly before the other curves, which is a consequence of the liquid being more accelerated to the walls at 1000 rpm.

Several characteristics of the flow can be revealed from studying the pictures. In Figure 56 it is observed that the circumferential velocities are quite constant around the circular path of the polyline, and that the velocities are very similar to the velocity of the paddle. This suggests a bulk movement, i.e. that the liquid is moving as one unit transported by the motions of the paddles.

Figure 55 shows the velocities in the radial direction. One detail to note about the velocities in the radial direction is that they are only one tenth in magnitude from the velocities in the circumferential direction. It can also be seen that the fluids have a tendency to be pushed outwards just before the paddle (i.e. after the 140°-gap) and slightly inwards just after it.

The axial velocities revealed in Figure 54 suggest that liquid is pushed under the paddle when interacting with the paddle and that is it being slightly transported upwards behind it. This can be seen for negative axial velocities after the 140°-gap and the positive direction just in front of it. The magnitudes for the axial flow are also larger than the radial velocities but smaller than the circumferential ones.

The flow velocities are all fully reasonable considering the appearance of the lower paddle in Figure 22. When the paddle moves in the counter-clockwise direction, the velocities at the right hand side of the polyline have nowhere to go. Going upwards is not an option due to the design of the paddle and the fluid cannot move inwards since it would then be stuck between the paddle and the rotating wall. After the paddle the flow has however the room to move both upwards and inwards for Polyline 1.

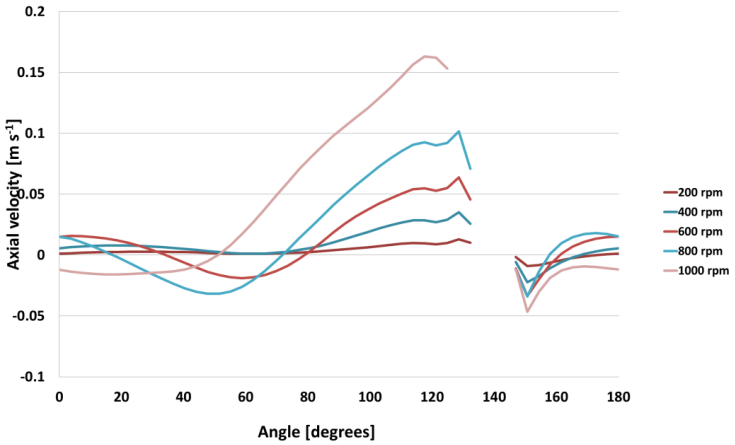

Figure 54. The axial velocities at Polyline 1 (Figure 22) for all rotational speeds using Mesh 2 and the k-ε turbulence model.

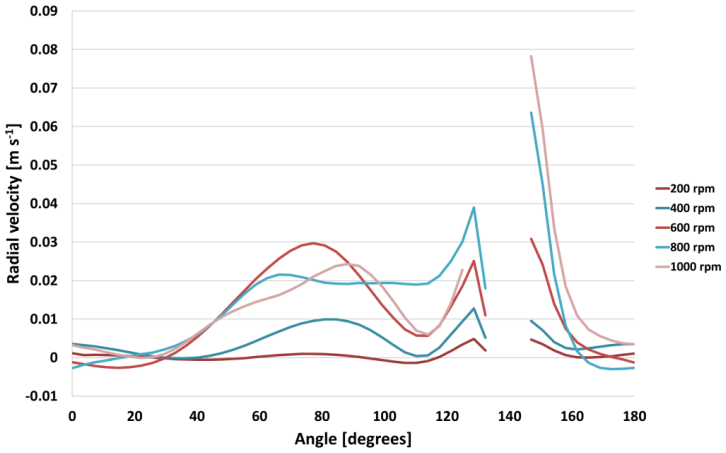

Figure 55. The radial velocities at Polyline 1 (Figure 22) for all rotational speeds using Mesh 2 and the k-ε turbulence model.

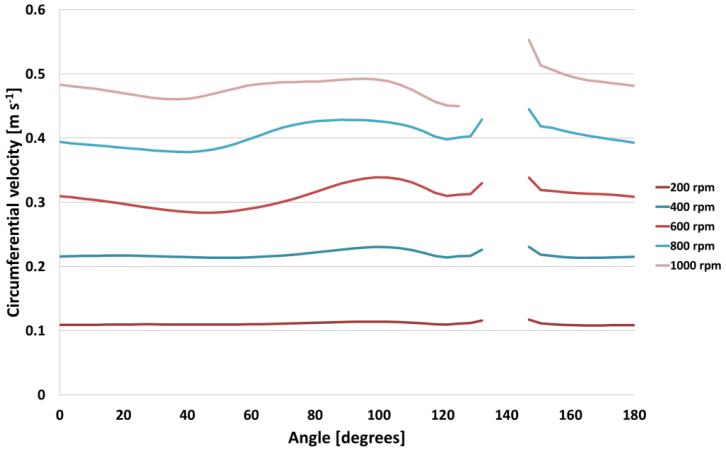

Figure 56. The circumferential velocities at Polyline 1 (Figure 22) for all rotational speeds using Mesh 2 and the k-ε turbulence model.

4.1.3.3. Velocity profile comparisons for the laminar, k-ε and the SST turbulence model

The laminar and the SST model only converged for Mesh 1 at 200, 400 and 600 rpm as mentioned above. These velocity profiles are therefore compared with the corresponding profiles achieved with the k-ε model, even if it was known that the results for Mesh 1 were not fully mesh independent.

The comparison of the circumferential velocities for Line 3 is shown in Figure 57. It is remarkable that there is a clear difference in the flow profiles at the fixed wall (8 mm) between the k-ε model, and the laminar and SST model, which both perform similarly. Another observation is that the k-ε model has a more plug flow like flow profile, while the laminar and the SST model have more a classical laminar flow profile.

The different velocity values at the 8 mm wall for the circumferential velocity shown in Figure 57 can possibly be explained by different wall treatments and different calculations of the wall shear stresses between the turbulence models. The shear stress is, as explained in section 2.2.5.7 a quantification of how much the fluid is influenced by retracting forces of the wall.

It can however not be seen in Figure 57 if the higher velocities for the k-ε model closest to the 8 mm wall are caused by the fact that the k-ε model is less affected by the retracting forces at the wall or not. It can namely also be that the k-ε model results in higher eddy viscosity values, which cause the velocities created by the paddles to spread more across the radial direction of Line 3.

Another interesting observation for Figure 57 is that there is no abrupt change in the velocities close to the rotating wall at 4 mm. This is because the paddles are connected to the 4 mm wall, which forces the flow to adapt to their velocity. The velocity at the wall at 4 mm is also exactly twice as high for 400 rpm as for 200 rpm, which is also expected for the system.

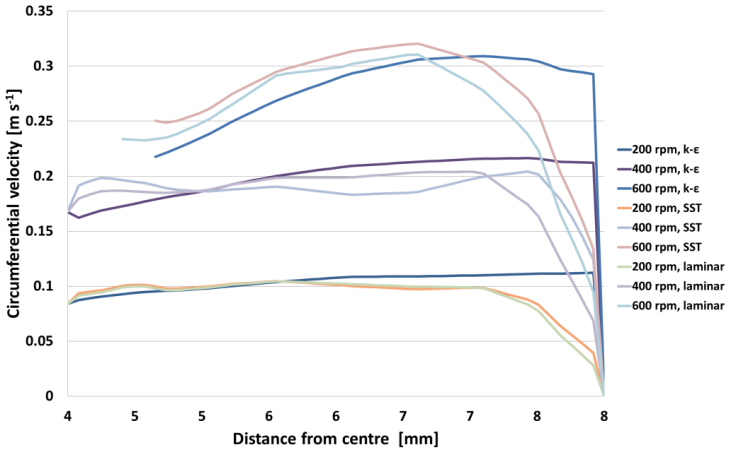

Figure 57. The circumferential velocities at Line 3 (Figure 22) for 200, 600 and 1000 rpm using the laminar, k-ε and the SST model.

The radial velocities for Polyline 2 are shown in Figure 58 for 200 and 600 rpm. Once again, it can be seen that the behaviour of the laminar model is very similar to the behaviour of the SST model, especially for 200 rpm. One reason for the larger difference at 600 rpm may be that the solutions were not fully stable at 600 rpm for the laminar and the SST model and that the velocities instead oscillated slightly around a fixed value. Another explanation is that the impact of the SST model might have been larger for the 600 rpm flow than for 200 rpm.

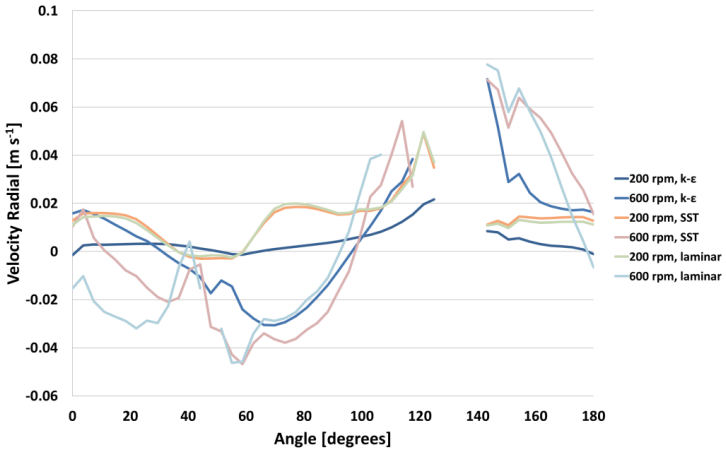

Figure 58. The radial velocities at Polyline 2 (Figure 22) for 200, 600 and 1000 rpm using the laminar, k-ε and the SST model.

The reasons for the different velocity profiles when comparing the different turbulence models can however not be explained by visual analysis. Based on the background about turbulence modelling presented in Section 2.2.5 it is very likely that the difference is caused by different values of the eddy viscosities. The eddy viscosity profiles will therefore be investigated in more detail in the next section.

4.1.3.4. Eddy viscosity profiles for the k-ε and the SST model

The eddy viscosities followed the same trend for the k-ε model with respect to the mesh sensitivity, i.e. the results from Mesh 1 differed slightly for the highest rotational speeds. The results from Mesh 2 were therefore chosen for display.

The eddy viscosity distributions at Line 3 using Mesh 2 and the k-ε model are shown in Figure 59. One interesting detail with this figure is that the wall at 4 mm is moving while the wall at 8 mm is stationary, but the boundary values for the eddy viscosity at the walls are the same, i.e. $4.04 \cdot 10^{-3}$ kg m^{-1} s^{-1}. This means that the eddy viscosities at the boundaries are approximately four times larger than the dynamic viscosity ($9.899 \cdot 10^{-4}$ kg m^{-1} s^{-1}) at the walls for the k-ε model, and even higher in the middle of the flow.

The CFX software manual ANSYS® Academic Research (2013) states however that the eddy viscosity should be about 1000 times larger for the eddy viscosity compared with the molecular viscosity for a fully developed turbulent flow. This suggests once again that the turbulence is not fully developed in the microbioreactor, which should be yet another indication that the k-ε model should not really be used for this case study from a theoretical perspective.

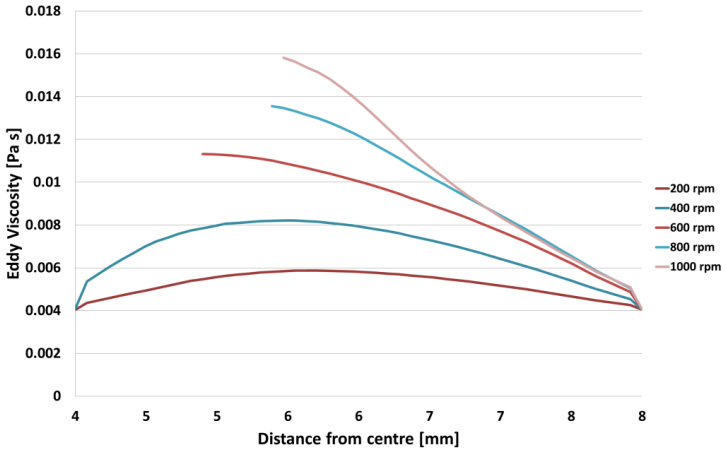

Figure 59. The eddy viscosities for Line 3 (Figure 22) using Mesh 2 and the k-ε model for different rotational speeds.

The SST model did not result in the same consistency in the eddy viscosity values at the boundary walls as the k-ε model did. The boundary values for the SST model were also in the range of 10^{-8}-10^{-10} kg m^{-1} s^{-1}, i.e. much smaller than the molecular viscosity. The SST model also produced consistently lower values than $9.899 \cdot 10^{-4}$ kg m^{-1} s^{-1} at Line 3. That means that the SST model had basically the same effective viscosity as the laminar model, which explains why they had so similar velocity profiles for example in Figure 57 and in Figure 58.

The fact that the eddy viscosities were the same at all boundary conditions for the k-ε model and not the same for the SST model can be explained by considering how the wall functions are defined and how the eddy viscosities are calculated.

As explained in section 2.2.5.4 the eddy viscosity for the k-ε model (equation 25) is proportional to k^2/ε and for the SST model (equation 26) it is proportional to k/ε. The interesting details are therefore how k and ε are defined at the surface using the turbulent wall treatment functions. The scalable wall function, by default associated with the k-ε model in ANSYS CFX 15.0, always calculates ε as a function of k and the correlation between them is quadratic, i.e. ε is proportional to k^2. Other variables, such as the solver y^+ value, are also included in the function for calculating the boundary condition value of ε.

However, once investigating the resulting values of k and ε at the wall boundaries for the k-ε model it was seen that both values were different for the different rotational speeds. This is a clear indication that the scalable wall function calculated a value of k at the boundaries, which was then used for the determination of the values of ε. Since the fraction k^2/ε became the same for all rotational speeds, it indicates that ε is only a function of k and that the solver y^+ value and other factors affecting ε were kept constant.

The automatic wall function, i.e. the one activated for the SST turbulence model, on the other hand sets the production of k at the walls to zero. This means that k is allowed to be transported out to the walls, but that it is not produced there. A low value of k should also give a low value for the eddy viscosity according to equation 26, unless the value of ε is even lower.

Low values for the eddy viscosity are a serious problem for the turbulence models, since the eddy viscosity is a factor in the turbulence production term displayed in equation 29. If this production term is low it also means that no new k is added to the equations for simulating the kinetic energy k, i.e. equation 27 for the k-ε model and equation 33 for the SST model. Indications of this phenomenon were also seen. For example, the monitored values of both k and eddy viscosity decreased towards zero during the course of the SST simulations.

It is however difficult to decide if this was an error of the boundary condition or not. More specifically if a general lack of k produced by the walls leads to a lack of eddy viscosity in the entire domain and therefore that no new k could be produced, or if this would have happened regardless of whether the boundary conditions had contributed to k or not.

The above explanation about the eddy viscosities also clarifies the failures of the SST simulations: For some reason the SST model did not manage to produce significant eddy viscosities to stabilize the flow in the reactor so that a steady-state solution could be found for higher rotational speeds. It can however not be stated if this problem was caused in the bulk or at the boundary without further investigations.

However, it is still uncertain if the failing result of the SST model was actually a correct description of the flow in the microbioreactor or not. For example, if the flow in the microbioreactor is unstable at higher rotational speed the SST model was correctly not converging into a steady-state solution. Likewise, would the k-ε model then have been wrong when it created an exaggerated eddy viscosity that managed to stabilize a system that in fact should not be stable at all.

It is however very hard to know the answer to the above questions without detailed and complicated experiments performed for the investigated system. A reasonable approach to investigate the simulations is nevertheless to investigate the y^+ values of the system, which is presented in the following section.

4.1.3.5. Investigation of the y^+ values at the walls for the k-ε and the SST model

The y^+ values must be evaluated in order to know how the wall functions operate at solid and no slip surfaces. The y^+ values for the highest and lowest rotational speeds investigated, i.e. 200 and 1000 rpm, are therefore shown in Figure 60. It is clear that the y^+ values are smaller than 11.06 for all rotational speeds and meshes, which means that they were all rounded up to 11.06 in accordance with the theory presented in section 2.2.5.7. This contributes therefore to the explanation for why the eddy viscosities are constant at all solid boundaries for the k-ε model as discussed in the previous section. I.e. no matter the values of k was y^+ constant (i.e. 11.06) and contributed therefore only with a constant value to the calculations of ε and finally the eddy viscosity at the walls.

The above discussion highlights once again that the k-ε model is unsuitable for flow modelling close to refined walls since it all the time models them as if the closest node is located in the logarithmic sublayer, even if it is not. But this is on the other hand the strength of the scalable wall function as well, i.e. that it is not so sensitive to varying small values of y^+, since it always assumes y^+ to be at least 11.06. Without this, the flow results for the k-ε model would maybe have been much more mesh dependent. However, this also includes the risk that the wall function consistently influences the simulations with a systematic error.

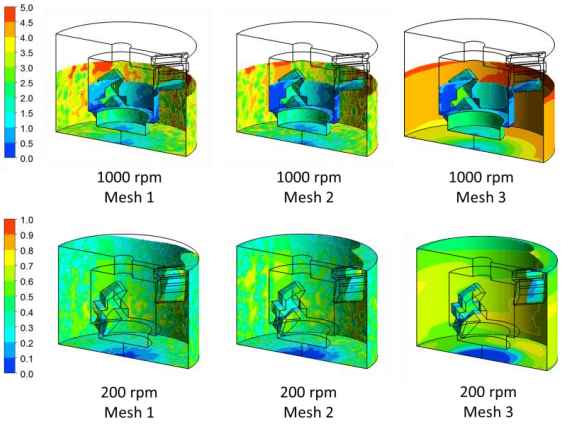

Figure 60. The y^+ values for the k-ε model for all the investigated meshes for 200 and 1000 rpm.

For the SST results, i.e. 200, 400, 600 rpm for Mesh 1 the y^+ values (not shown) were also less than 5. They were also slightly different from each other and since the automatic model uses the y^+ values directly without modification it is also a good explanation why the eddy viscosities were not identical at the walls for the SST model.

4.1.3.6. Distribution of turbulence energy dissipation ε for the k-ε model

As described earlier the values of the turbulence energy dissipation ε are at the walls determined by the wall functions. In the bulk the value of it is however dependent on the production, dissipation and transport through the liquid according to equation 28 for the k-ε model and equation 34 for the SST model. Equation 34 simulates the values of ω, but the modelled ω is easily transformed to ε via equation 24.

Once considering the data plots of ε for the k-ε model at the monitoring lines in Figure 22 (not shown) it appears that the highest values of ε are located closets to the fixed wall at 8 mm from the centre and around the paddles. This suggests either that the boundary conditions calculated higher values of ε than supposed for the k-ε model, or that the production of the energy dissipation rate actually was highest in the regions closest to the outer surface.

The high velocity gradients close to the 8 mm wall in Figure 57 suggest that ε could actually be induced by the wall, since the velocity gradients are much higher there than at the rotating wall at 4 mm.

The energy dissipation rate in the fluid can be determined in several different ways. Li et al. (2013) calculated both the averaged value at the gas-liquid interface and the average in the liquid volume, and others have taken the maximum values of ε into account as well. The theory presented in Lamont and Scott (1970) assumed an even distribution of ε in the liquid phase, which was calculated based on the total energy input to the fluid. Based on the theory, i.e. the theory behind the eddy cell model, it is however the value of ε at the liquid side of the interface that matters. It was therefore decided to calculate ε in three ways, i.e. as the maximum value in the liquid, the average value in the liquid and the average value at the gas-liquid interface and to compare the results.

The liquid averaged and the gas-liquid interface averaged values of the energy dissipation for the k-ε model are shown in Figure 61. The corresponding maximum values in the liquid domain are displayed in Figure 62. Showing them in the same diagram would be unsuitable, since they have very different scales of magnitude. That is also an interesting point in itself, i.e. that the two different averaged values are fairly similar to each other while the maximum values are about ten times higher in magnitude.

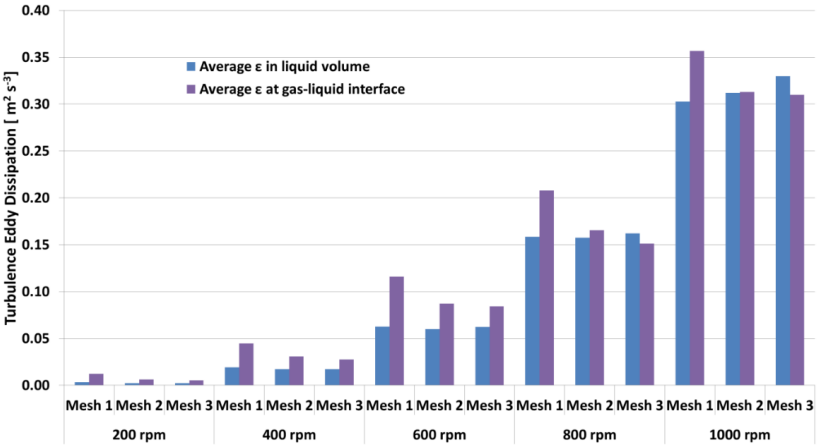

Figure 61. The liquid volume and gas-liquid interface averaged values of ϵ for the k-ε model.

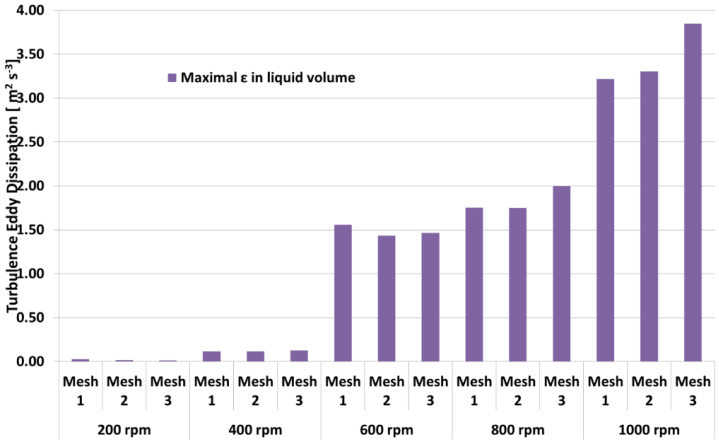

Figure 62. The maximum values of ϵ in the liquid volume for the k-ε model.

In Figure 61 the general trend is that the surface averaged energy dissipation rates are decreasing with increasing number of nodes in the meshes. The volume-averaged values do not show that tendency and they are less mesh sensitive.

Comparing Figure 61 and Figure 62, it can be seen that the relation between the different values for the varying rotational speeds are quite similar in most of the cases. For 600 and 800 rpm on the other hand the volume averaged values are more than twice as large for 800

compared to 600 rpm, while their maximum values are almost of the same order of magnitude.

This raises the question of how much influence the maximum values actually have on the volume-averaged values. For example, if only few nodes are involved in an averaging procedure a single outlier could raise a calculated average to a value non-representative for the sample. The example for 600 and 800 rpm above shows however that this should not be a concern in this case, possibly since the number of nodes in Mesh 1 was already large enough to dampen the effect of a few very high values.

Another risk in the attempt to find a representative value of ε in the domain is if most of the turbulent dissipation in a volume is produced at solid surfaces, e.g. the 8 mm wall, far from the gas-liquid interface. Figure 61 indicates however that this is no major concern in this case study, since the volume averaged and surface averaged values are quite similar. The experiences from Li et al. (2013) show however that it could be a problem, so the risk should not be disregarded.

The distributions of ε were visualised in order to get a more thorough understanding where the highest values were located in the domain. The visual results for the different meshes are shown in Figure 63 for 200 and 1000 rpm. The legends show the levels of ε at the surfaces, and they have different scales in order to display the differences properly. The golden volumes show the regions of the liquid volumes where the concentrations of epsilon are the highest in the respective cases. For the 1000 rpm cases in Figure 63 the golden volumes have levels of ε over 0.6 $m^2\ s^{-3}$. For the 200 rpm cases, the highlighted volumes represent ε larger than $7.5 \cdot 10^{-3}\ m^2\ s^{-3}$.

For 1000 rpm, the parts of the volumes with the highest values of ε are located around the two paddles and between the paddles and the outer cylindrical wall. This is fully reasonable, since the wall and the paddles have different relative velocities. High velocity gradients are therefore expected in these regions. There should also be relatively large velocity gradients around the paddle on the surfaces normal to the rotational direction, which explains the development of ε in these regions as well.

For 200 rpm the highest values of ε are however located just below the gas-liquid interface. One explanation for this phenomenon is that the relative velocity between the paddles and the outer cylindrical wall is five times lower for 200 rpm than for 1000 rpm, which leads to smaller velocity gradients and therefore lower production of ε in those regions.

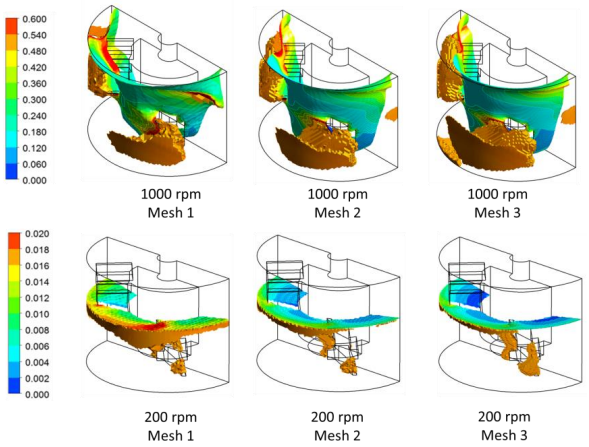

Figure 63. The distribution of ε at the surfaces, and the volumes with the highest levels of ε in the liquid volumes for 200 and 1000 rpm and the k-ε turbulence model. The legend describing the contour plots at the surfaces has the unit $m^2\ s^{-3}$ and the highest ε are golden.

A potential modelling problem is also highlighted in the 200 rpm figures in Figure 63, which is that the turbulence was modelled homogenously in the entire reactor even if the velocities were modelled as inhomogeneous. A shared turbulent field introduces for example the risk that turbulent quantities of k and ε can be produced in the air phase and then have the possibility to diffuse over to the liquid side without having to take the existence of the interface into consideration. Gradients can also arise in the gas-liquid interface that give raise to production of turbulence.

The reason why the energy dissipation rate can be both produced and dissipated lies in the construction of its governing equation, i.e. equation 28 for the k-ε turbulence model. According to equation 28 it is reasonable that the energy dissipation rate ε can both be produced and dissipated in a node as well as it can be transported by both velocities and diffusion-like phenomena to the surrounding nodes.

These concepts can however be difficult to understand from a physical point of view, and it might be even more complicated to visualise the diffusion of the frequency ω that is involved in equation 32. However, it is nevertheless important to know that this is what the transport equations for turbulent quantities do in order to be able to understand possible shortcoming of the models. One example of this is how the failure of the SST model was explained by discussing the production term of k in section 4.1.3.4.

4.1.4. Oxygen transfer simulation results

The simulated oxygen transfer rates in this project were modelled as a function of the specific interfacial area and the modelled energy dissipation rate in accordance with equation 89. Equation 89 is an extension of the eddy cell model, i.e. equation 88, since the eddy cell model alone only correlates the energy dissipation rate to the mass transfer coefficient k_L, while equation 89 correlates both the specific interfacial area and the energy dissipation rate to the volumetric mass transfer coefficient k_La. All k_L and k_La values in this project are also reported in the unit m s^{-1} and s^{-1} despite the common practice within the fermentation community to use the unit h^{-1} for k_La.

4.1.4.1. Analysis of the experimental k_La values

The experimental data for the oxygen transfer rates in the microbioreactor were previously presented at Bolic et al. (2012), and are shown in Table 12 together with the liquid phase Reynolds numbers from Table 11.

Table 12. The experimental k_La values and the Reynolds numbers for the liquid phase in the microbioreactor.

	200 rpm	400 rpm	600 rpm	800 rpm	1000 rpm
Experimental k_La [s^{-1}]	$1.94 \cdot 10^{-2}$	$3.33 \cdot 10^{-2}$	$4.17 \cdot 10^{-2}$	$5.00 \cdot 10^{-2}$	$6.39 \cdot 10^{-2}$
Reynolds number	732	1464	2196	2928	3660

The correlation in equation 90 was fitted to the data in data in Table 12 and the result was $k_La \propto Re^{0.71}$, which is very close to the theoretical correlation $k_L \propto Re^{0.69}$ previously presented in Lamont and Scott (1970). The striking similarities between the correlations must however only have been a coincidence since the Reynolds numbers were defined differently in the two systems, and since a specific interfacial area was assumed in Lamont and Scott (1970). The method of applying equation 90 is nevertheless useful for comparisons between different more similar reactor systems such as the microbioreactor and the magnetically stirred reactor.

4.1.4.2. The simulated a, k_L and k_La values

The specific interfacial areas for the k-ε turbulence model in combination with all investigated rotational speeds and meshes are shown in Table 13 for the microbioreactor. The conclusion regarding the mesh dependence in Table 13 is consistent with section 4.1.3.1, i.e. that there is a noticeable difference in specific interfacial areas for 1000 and 800 rpm between Mesh 1 and Mesh 2 (and Mesh 3) while the results for the other rotational speeds can be considered relatively mesh independent.

Table 13. Specific interfacial areas [m^{-1}] for microbioreactor and the k-ε turbulence model in combination with all evaluated meshes and rotational speeds.

Mesh	200 rpm	400 rpm	600 rpm	800 rpm	1000 rpm
Mesh 1	$1.64 \cdot 10^2$	$1.94 \cdot 10^2$	$3.14 \cdot 10^2$	$4.63 \cdot 10^2$	$5.47 \cdot 10^2$
Mesh 2	$1.61 \cdot 10^2$	$1.90 \cdot 10^2$	$3.15 \cdot 10^2$	$4.47 \cdot 10^2$	$5.07 \cdot 10^2$
Mesh 3	$1.60 \cdot 10^2$	$1.89 \cdot 10^2$	$3.17 \cdot 10^2$	$4.47 \cdot 10^2$	$4.94 \cdot 10^2$

The energy dissipation rates ε in Lamont and Scott (1970) were calculated based on the Reynolds number according to equation 72, while they in this and many other CFD projects are based on the distribution of the scalar ε in accordance with the theory in section 2.2.5.4 and 2.2.5.5. This means that only a single value of ε was calculated in Lamont and Scott (1970) per experiment while there are many different ways to find a representative value of ε in a CFD simulation. As shown in section 4.1.3.6 ε could for example be defined as the liquid volume average, the gas-liquid interface averaged or the liquid maximum value. However the results presented in Figure 61 and Figure 62 indicate that the choice of definitions had a major impact on the resulting representative value.

The largest relative difference for the simulated ε values was about 14% and occurred for the maximum values, i.e. in Figure 62, between Mesh 2 and Mesh 3 at 1000 rpm. Once transforming these values into their k_L counterparts via equation 88 their relative difference was however smaller than 4%. A maximum error of 4% was considered acceptable, and therefore the use of Mesh 2 for the k_La calculations was considered to be acceptable.

The numerical values of ε from Mesh 2 are shown in Table 14 and their corresponding simulated values of k_L are presented in Table 15. The values in Table 15 are calculated with equation 88 and the proportionality constant C_P set to one, but alternative values of C_P are discussed later in this section.

Table 14. Energy dissipation rate data for the k-ε model and Mesh 2.

	200 rpm	400 rpm	600 rpm	800 rpm	1000 rpm
Average ε in liquid volume [m^2s^{-3}]	$2.44 \cdot 10^{-3}$	$1.72 \cdot 10^{-2}$	$5.98 \cdot 10^{-2}$	$1.57 \cdot 10^{-1}$	$3.12 \cdot 10^{-1}$
Maximum ε in liquid volume [m^2s^{-3}]	$1.59 \cdot 10^{-2}$	$1.14 \cdot 10^{-1}$	$1.43 \cdot 10^{0}$	$1.75 \cdot 10^{0}$	$3.30 \cdot 10^{0}$
Average ε at gas-liquid interface [m^2s^{-3}]	$6.35 \cdot 10^{-3}$	$3.06 \cdot 10^{-2}$	$8.72 \cdot 10^{-2}$	$1.65 \cdot 10^{-1}$	$3.13 \cdot 10^{-1}$

Table 15. Simulated k_L values based on the ε data in Table 14.

	200 rpm	400 rpm	600 rpm	800 rpm	1000 rpm
Average k_L in liquid volume [m s^{-1}]	$3.22 \cdot 10^{-4}$	$5.24 \cdot 10^{-4}$	$7.16 \cdot 10^{-4}$	$9.12 \cdot 10^{-4}$	$1.08 \cdot 10^{-3}$
Maximum k_L in liquid volume [m s^{-1}]	$5.14 \cdot 10^{-4}$	$8.42 \cdot 10^{-4}$	$1.58 \cdot 10^{-3}$	$1.66 \cdot 10^{-3}$	$1.95 \cdot 10^{-3}$
Average k_L at gas-liquid interface [m s^{-1}]	$4.09 \cdot 10^{-4}$	$6.06 \cdot 10^{-4}$	$7.87 \cdot 10^{-4}$	$9.23 \cdot 10^{-4}$	$1.08 \cdot 10^{-3}$

The relative differences in between the data in Table 14 are much larger than the ones in Table 15. This again can be understood by equation 88 where the fourth root of the only modelled variable ε is calculated. The practical outcome of this can for example be noted as the magnitude of difference between the highest and the lowest value for the volume averaged values of ε (i.e. for 200 versus 1000 rpm) which is 130 in Table 14 while the corresponding difference in Table 15 is 3.4.

The same phenomena appear also for the different methods of defining ε. This means that the choice between a volume and surface averaged approach becomes less critical comparing its impact on k_L rather than on ε. Using this observation either against or in favour of using the eddy cell model in combination with CFD modelling is difficult but it should nevertheless be discussed.

The dampening of variances between different meshes could for example be considered a strength of the model, but from another aspect, it is highly questionable to use a model in which the single input variable contributes very little to the output. This criticism however has nothing to do with the eddy cell model but is more a comment on how it has been applied within the CFD community. The eddy cell model has in its expression two additional variables, the dynamic viscosity and molecular diffusivity, which are normally not varied in the simulations.

The simulated k_L values in Table 15 are in the same order of magnitude as those presented in Brüning and Weuster-Botz (2014). The k_L values in Brüning and Weuster-Botz (2014) are in the range $1.1 \cdot 10^{-4}$ to $2.7 \cdot 10^{-4}$ but k_L are then calculated using equation 88 with the proportionality constant 0.167. With C_P set to one, they should therefore have been in the range $6.6 \cdot 10^{-4}$ to $1.6 \cdot 10^{-3}$, which is very close to the values in Table 15. These similarities are

especially positive since the SST turbulence model was applied in Brüning and Weuster-Botz (2014), which indicates that the SST model actually has the ability to produce averaged values of ε in the same range as the k-ε model even if it was not accomplished for the microbioreactor.

The product of the values in Table 13 and Table 15 are shown in Table 16 and corresponds to the simulated k_La values for Mesh 2 according to equation 89 with C_P set to one. Using a set of corresponding experimental and simulated k_La values, i.e. Table 12 and Table 16, it could then be considered easy to find the best-fit parameter C_P. This turned however out to be more complicated than expected after the discovery that the data was not linearly correlated. This is further discussed in the following section.

Table 16. Simulated k_La values based on the products of the Mesh 2 data in Table 13 and Table 15.

	200 rpm	400 rpm	600 rpm	800 rpm	1000 rpm
Average k_La in liquid volume [s^{-1}]	$5.17 \cdot 10^{-2}$	$9.95 \cdot 10^{-2}$	$2.25 \cdot 10^{-1}$	$4.08 \cdot 10^{-1}$	$5.48 \cdot 10^{-1}$
Maximum k_La in liquid volume [s^{-1}]	$8.27 \cdot 10^{-2}$	$1.60 \cdot 10^{-1}$	$4.99 \cdot 10^{-1}$	$7.44 \cdot 10^{-1}$	$9.89 \cdot 10^{-1}$
Average k_La at gas-liquid interface [s^{-1}]	$6.57 \cdot 10^{-2}$	$1.15 \cdot 10^{-1}$	$2.48 \cdot 10^{-1}$	$4.13 \cdot 10^{-1}$	$5.48 \cdot 10^{-1}$

4.1.4.3. Correlation studies between experimental k_La and simulated ε and a

As mentioned in section 4.1.4.1 the Reynolds numbers were fitted to the experimental k_La data according to equation 90, which resulted in equation 99. The high R^2 value (i.e. close to 1) in equation 99 indicates that the model (i.e. equation 90) fitted well with the data. Equation 99 should therefore be interpreted such that if the Reynolds number would be doubled the experimental k_La value should increase with $2^{0.71} \approx 1.64$.

$$k_L a_{Exp.} \propto {Re_{Impeller}}^{0.71} \qquad R^2 \approx 0.99 \tag{99}$$

Likewise, the results from the evaluations of equation 91 and 92 are displayed in equation 100 and 101. Equation 100 shows that the Reynolds number, i.e. the rotational speed, has a very large impact on the simulated volume averaged ε and likewise equation 101 shows that its effect on the simulated specific interfacial area is smaller but evident.

$$\varepsilon_{Sim,Volume\ Ave.} \propto {Re_{Impeller}}^{3.02} \qquad R^2 \approx 1.00 \tag{100}$$

$$a_{Sim.} \propto {Re_{Impeller}}^{0.77} \qquad R^2 \approx 0.92 \tag{101}$$

The result of fitting the simulated specific interfacial areas to the experimental k_La values according to equation 93 is displayed in equation 102. In equation 102 it can be seen that the proposed model has a good fit to the data, and more interesting is that the exponent on the specific area is 0.84 and not one as theoretically expected. This is an important insight since it means that the simulated specific interfacial areas, the experimental k_La values or the theory stating that the area is linearly proportional to k_La is somehow incorrect.

$$k_L a_{Exp.} \propto {a_{Sim.}}^{0.84} \qquad R^2 \approx 0.89 \tag{102}$$

It was never expected that either the CFD model or the experimental methods would provide fully correct and consistent k_La data but it is still important to recognise this shortcoming. A consequence of it can for example be seen once trying to calculate a set of pseudo-experimental k_L values by dividing the experimental k_La with the simulated specific interfacial areas and correlating them to the simulated volume averaged values of ε according to equation 94.

$$\frac{k_L a_{Exp.}}{a^1_{Sim.}} \propto \varepsilon^{-0.021}_{Sim.Volume\ Ave.} \qquad R^2 \approx 0.06 \tag{103}$$

Theoretically, this correlation should be $k_L \propto \varepsilon^{0.25}$, but as can be seen in equation 103 the result is both an insufficient fit for the proposed model as well as it is a non-physical solution since it suggests that an increased value of ε should decrease the oxygen transfer rates in the liquid. The explanation can be found in Table 17 where the pseudo-experimental k_L values do not increase for an increased rotational speed. In Table 14 it is nevertheless shown that the volume averaged ε increases for increased stirring rates, which suggests not to relate these data with a power law correlation.

Table 17. Pseudo-experimental k_L based on the experimental k_La divided with the simulated specific interfacial areas.

	200 rpm	400 rpm	600 rpm	800 rpm	1000 rpm
Pseudo-experimental k_L [m s^{-1}]	$1.21 \cdot 10^{-4}$	$1.76 \cdot 10^{-4}$	$1.32 \cdot 10^{-4}$	$1.12 \cdot 10^{-4}$	$1.26 \cdot 10^{-4}$

The opposite procedure, i.e. assuming that ε had the exponent 0.25 and searching for the exponent for the specific interfacial area according to equation 95 was in a similar way unsuccessful as displayed in equation 104.

$$\frac{k_L a_{Exp.}}{\varepsilon^{0.25}_{Sim,Volume\ Ave.}} \propto a^{-0.076}_{Sim.} \qquad R^2 \approx 0.5108 \tag{104}$$

If the proposed theory, i.e. equation 89, is entirely correct and the simulations would provide correct data for both the specific interfacial area and ε the power constants in equation 103 and in equation 104 would have been 0.25 and 1 respectively.

There are many reasons for why the CFD models most likely did not provide entirely accurate data. First, it is important to remember that ε is modelled using the relatively complex equation 28 when the k-ε turbulence model is used. Equation 28 is certainly mechanistic regarding the transport of ε, but its equation constants (1.3, 1.44 and 1.92) are not guaranteed to be applicable for all kinds of flow, and especially not for rotating flows with curved boundary layers in the transient flow regime as discussed earlier.

The specific interfacial area can also have varied between the experiments and the simulations as discussed in section 4.1.3.1. It is also reasonable to believe that small gas bubbles were present in the experiments which was not considered in the CFD model.

4.1.4.4. *Correlation studies between experimental and simulated k_La*

Despite the discussion in the previous section, the simulated k_La values are correlated to the experimental values in Figure 64. The linear trend lines and corresponding equations for the maximum and volume averaged k_La values are also included in the figure. The trend lines for the interface-averaged values were excluded since they were very similar to the ones for the volume-averaged values.

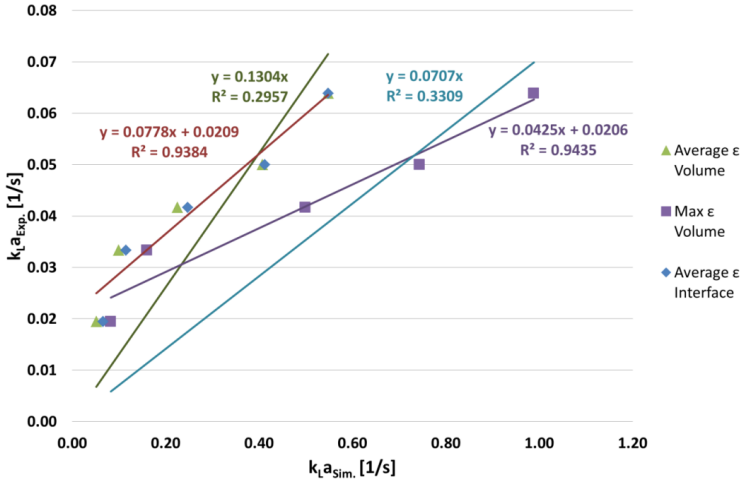

Figure 64. The simulated k_La data based on the liquid and surface averaged values as well as the maximum ε plotted against the experimental values. The trend lines and the corresponding equations are also displayed for four of the data sets.

Figure 64 shows that the trend lines not forced through the origin fit the data better, i.e. they have considerably higher R^2 values. The problems with these directly proportional lines is however that they are not based on equation 89, i.e. that they do not represent the eddy cell model. Instead, they represent the model proposed in equation 105.

$$(k_La)_{Exp.} = C_{P1}(k_La)_{Sim.} + C_{P2} \tag{105}$$

Equation 105 however has a few serious shortcomings even though it correlates the experimental and simulated data very well. It suggests that mass transfer between two phases is not dependent solely on the existence of an interfacial area since the model includes the constant C_{P2}. Likewise, it suggests that oxygen transfer can exist even when k_L is zero. Equation 105 should therefore be regarded as a good example of how data fitting can suggest well correlated but non-physical models.

The lack of direct proportionality between the data in Figure 64 suggests however that the eddy cell model could be applied in a better way than in equation 89. Equation 106 is therefore proposed as an alternative where the simulated k_L is the sum of the eddy cell model contribution from equation 89 and the constant C_{P4}.

$$k_La = \left(C_{P3}\left(\frac{D_\varphi}{\upsilon}\right)^{0.5}(\varepsilon\upsilon)^{0.25} + C_{P4}\right)a_{Sim.} \tag{106}$$

Equation 106 has many theoretical prospects, it can for example also be applied for laminar flow conditions where ε is zero. The mass transfer coefficient contribution becomes then constant and equal to C_{P4}. This idea is inspired by equation 15 where the Sherwood number (later used to calculate k_L for the mass transfer at solid surfaces) is close to constant for very low Reynolds or Schmidt numbers. According to equation 106 the oxygen transfer rate is also proportional to both k_L and the specific interfacial area, which is fully consistent with the established theory. Parameter estimation of the model proposed in equation 106 was however not performed in this project but left for future work. Instead, equation 89 was used for consistency with the work by others.

The direct proportional trend lines in Figure 64 state that C_P (in equation 89) is 0.1304 for the volume averaged ε and 0.0707 for the maximum value of ε. Figure 65 presents the results for inserting these values of C_P into equation 89 by displaying the simulated and experimental data.

The volume averaged value of C_P in Figure 64, i.e. 0.1304, is relatively close to the value 0.167 found in Brüning and Weuster-Botz (2014). Figure 65 shows also that the stated proportionality constants provide a reasonably good fit between the simulated and the experimental values. It must however be stressed that the constant values of C_P per definition are the values which provide the best fit between the experimental and simulated data.

This is also the strongest criticism towards the use of the eddy cell model found in this project, i.e. that two parameters that cannot be experimentally verified individually (i.e. the specific interfacial area and the mass transfer coefficient) are simulated separately and that their product is correlated with a single and case specific proportionality constant.

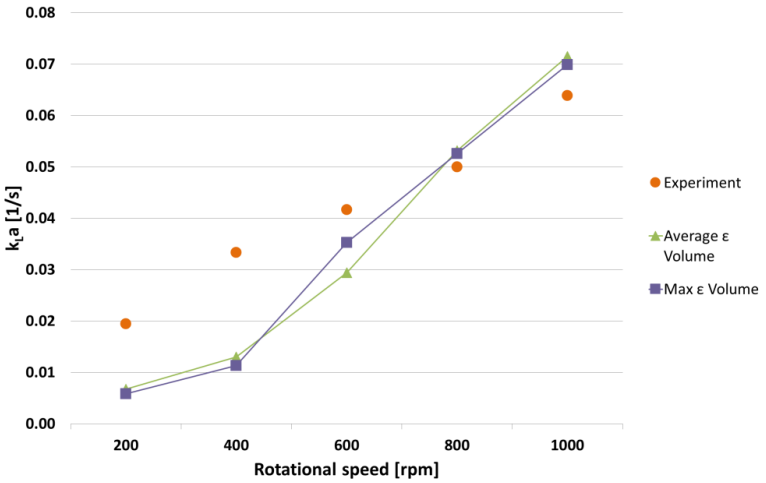

Figure 65. The experimental and simulated volume averaged and maximum k_La values. The two simulated data sets are correlated with the proportionality constants C_P shown in Figure 64.

4.1.5. Mixing time results for the microbioreactor

Mixing simulations for the microbioreactor were performed with a focus on the k-ε turbulence model. The time step and mesh sensitivity for the mixing time with the k-ε model is first evaluated in section 4.1.5.1, and the overall results for the different rotational speeds

follows in section 4.1.5.2. The mixing times for the few converging laminar and the SST model simulations are presented in section 4.1.5.5.

4.1.5.1. Mesh and time step and sensitivity for the k-ε turbulence model

A sensitivity analysis was performed to determine the mesh and time step dependence of the mixing times. The mixing times, evaluated as described in section 3.2.4.5, were investigated for the k-ε turbulence model and for the rotational speeds 200 and 1000 rpm. The results are displayed in Figure 66 and Figure 67.

The figures reveal that the monitoring method chosen for the mixing time definition is much more critical for 200 rpm than for 1000 rpm. For 1000 rpm, the mixing time results between the two monitoring points are for example almost identical, and the mixing times are much higher once based on the maximum value. For the 200 rpm simulations there are larger differences depending on if the mixing time is defined based on the maximum value or on the monitoring point values. The longer mixing times for the maximum values for 200 rpm compared to 1000 rpm can be explained by higher eddy viscosities and velocities in the later.

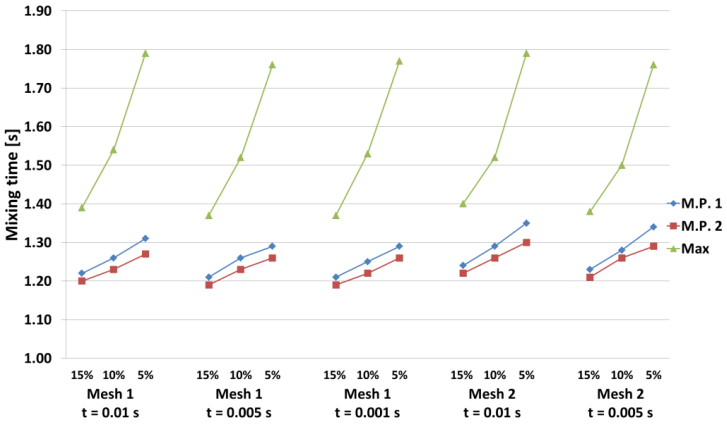

Figure 66. Mixing times using the k-ε turbulence model at 200 rpm for Mesh 1 and Mesh 2.

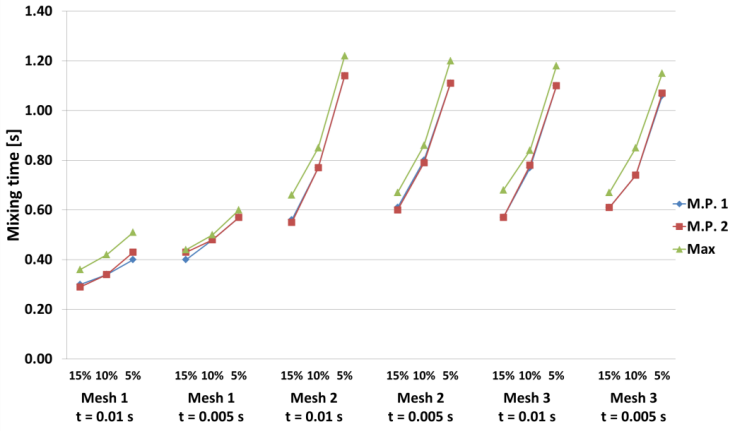

Figure 67. Mixing times using the k-ε turbulence model at 1000 rpm for Mesh 1, Mesh 2 and Mesh 3.

Figure 66 and Figure 67 also show that the definition of the mixing time has a large effect on the result. In Figure 67 the mixing times in some cases, e.g. Mesh 2 with the time step 0.01 s, is almost twice as high using the 15% compared to the 5% definition.

Comparing the meshes and time steps it is also noted that the results are very similar for 200 rpm, and that Mesh 1 performs rather different for 1000 rpm compared with Mesh 2 and Mesh 3. The time step choice is also not critical for 200 rpm but for 1000 rpm, it has a large relative importance for Mesh 1. The conclusion is that Mesh 1 should be avoided for mixing simulations. Mesh 2 in combination with the time step 0.01 second was instead selected for all results further displayed in this section.

4.1.5.2. Mixing time results for the k-ε model

The mixing results for Mesh 2, the time step 0.01 s, and the k-ε model are shown in Figure 68 together with the experimental data for all investigated rotational speeds. The mixing time values from monitoring point 2 are omitted.

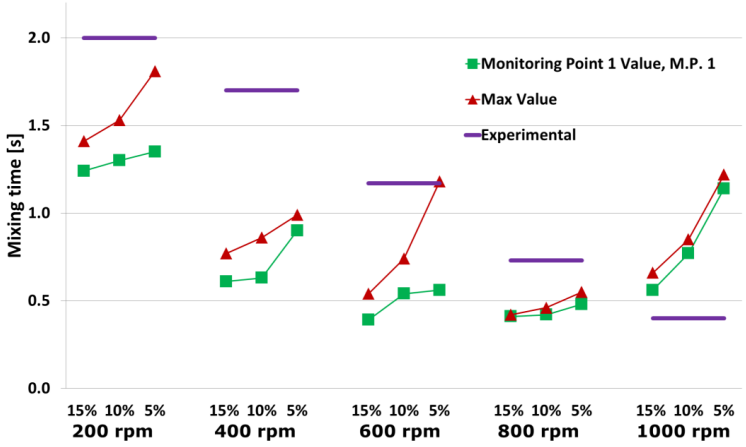

Figure 68. Simulated mixing times using the k-ε turbulence model, 'Mesh 2' and the time step 0.01 second compared with experimental data from Bolic et al. (2012).

The results in Figure 68 show that not all simulated data decrease with increasing rotational speeds as the experimental data did. The two perhaps most unexpected outcomes are that the mixing times for 1000 rpm appear slower than for 800 rpm, and that the 5% maximum mixing time for 600 rpm is very high compared to the corresponding value at 400 rpm. These two phenomena are investigated in more detail in the two following sections since investigating them demonstrates several possibilities and drawbacks related to performing mixing simulations using CFD.

4.1.5.3. Comparison between the 800 and 1000 rpm mixing time results

The 1000 rpm mixing time results in Figure 68 can be considered unexpected, as empirical results show mostly that the more a system is stirred the better is the mixing. From the previous sections, it is also known that the velocities and eddy viscosities, i.e. parameters that

should promote better mixing, were higher for 1000 rpm than 800 rpm on all investigated lines and polylines.

The maximum concentrations of the additional variable, as well as the concentrations of the additional variable in monitoring point 1 over time, are plotted in Figure 69 for the 800 and 100 rpm simulations. The ±10% interval from the final value is also shown and as explained in section 3.2.4.5 and the 10% mixing time is defined as the last time step the concentrations enter within this interval.

Figure 69 shows that the two curves corresponding to the 1000 rpm simulation enter the ±10% interval later than the 800 rpm curves do. This explains however not why the phenomenon occurred, but indications are seen by inspecting the 1000 rpm values around the time step 0.7 s. At 0.7 seconds the maximum value and the value at the monitoring point are the same for 1000 rpm, but they have still not reached their final concentration. They are both also located outside of the ±5% interval (not shown). This must be understood as if the additional variables are mixed to a homogenous concentration in almost the entire liquid region at 0.7 s, but that regions with lower concentrations are still present somewhere in the fluid. When the additional variables then manage to spread into the unmixed regions, the concentrations at the monitoring points also decrease into the ±5% interval.

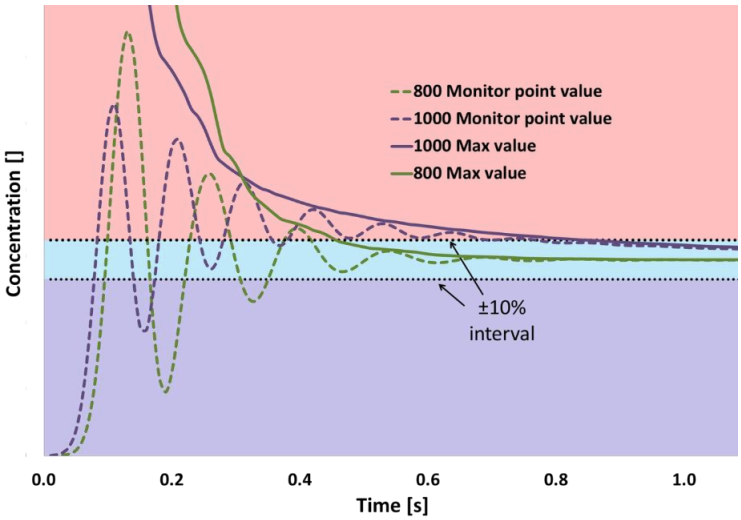

Figure 69. The concentrations of additional variable in the 800 and 1000 rpm mixing simulations related to Figure 68.

Figure 70 shows regions with concentrations of the additional variable higher than the ±10% interval in red and regions with concentrations lower than this threshold in blue. Volumes with concentrations of the additional variable within the ±10% interval are turquoise. The colouring scheme follows consequently the background colours in Figure 69.

In Figure 70, it is seen that there is a region with lower concentrations than the ±10% interval present at the time-step 1 second in the 1000 rpm simulation. This unmixed volume is therefore the reason behind the much longer mixing times for 1000 rpm.

A potential explanation for why this poorly mixed region only appears in the 1000 rpm is that the liquid strip in the top of the reactor is very narrow for this rotational rate. It is hard to see from the perspective in Figure 70, but the phenomenon appears clearer in Figure 48. Figure 48 also reveals that most of the gas-liquid interface for 800 rpm is not in contact with the top of the reactor but instead intersects with the outer static wall. For 1000 rpm, the gas-liquid interface is on the other hand in contact with the entire top wall. One explanation for why the liquid in this region was poorly mixed is therefore that it was farther away from the source points in the axial direction. Another explanation is that these regions had low axial velocities or eddy viscosities.

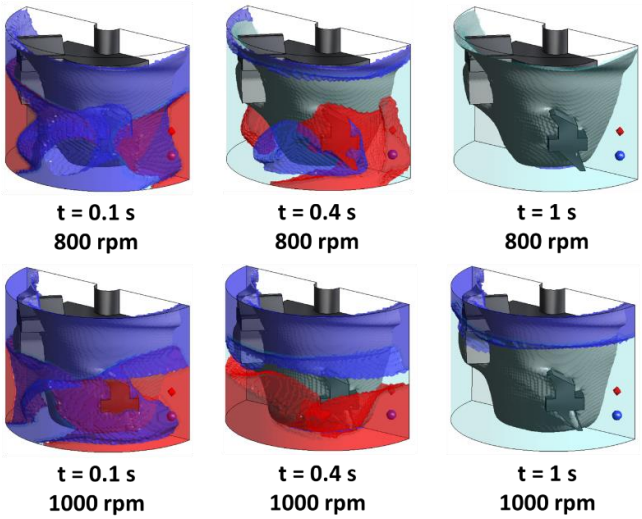

Figure 70. The distribution of concentrations of additional variables following the colour scheme in Figure 69 for 800 and 1000 rpm at three different points in time.

The conclusion is therefore that intensified stirring not always is better for the mixing simulations of a free-surface flow. It also shows the importance of investigating why different mixing phenomena occur for different methods, since both Figure 69 and Figure 70 were needed to draw the conclusions presented above.

It is also important to know that this phenomenon only occurred in the simulations and not in the experiments. This might be caused by the fact that the simulations were forced into a steady-state solution, which might only have been possible if the k-ε model exaggerated the eddy viscosities as previously discussed. In reality, this top volume might instead be oscillating with a high frequency.

4.1.5.4. Comparison between the 400 and 600 rpm mixing time results

The unexpected behaviour of the 5% mixing time for 600 rpm seen in Figure 68 is explained in Figure 71 and in Figure 72. Figure 71 is provided to investigate the reasons why the maximum levels of additional variable entered the ±5% interval later for 600 rpm than for 400 rpm while the ±10% and ±15% intervals were entered as expected, i.e. with 600 rpm first.

In the figure the concentrations of the additional variable at the monitoring point 1 (M.P.1) are plotted for 400 and 600 rpm together with the monitored maximum values. The +5% and +10% concentration lines are also plotted together with the final concentration value. The axes in the figure do not intersect in origo.

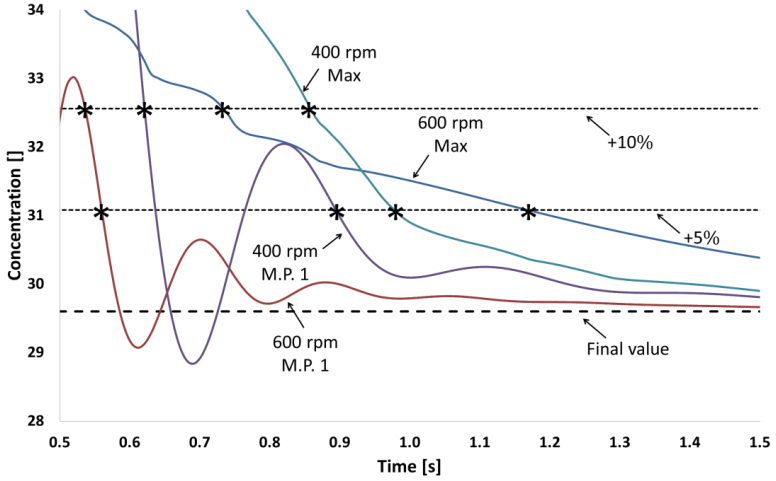

Figure 71. The concentrations of the additional variable for 400 and 600 rpm related to Figure 68.

The mixing times, i.e. when the concentrations enter within the respective intervals for the last time, are also indicated in Figure 71. The data from M.P.1 behave as expected and enter the interval first for 600 rpm and then for 400 rpm. For the maximum values the 600 rpm curve has however a much lower angle of inclination as it approaches the final value. Therefore, it reaches the ±5% interval later than the 400 rpm curve does.

This result suggests that the definition of 5% is probably too narrow in order to catch the correct behaviour of the system, and that the definitions 10% or 15% are possibly more suitable to determine the mixing time. This is however problematic, since it can be argued that homogenous mixing is actually not achieved until each point in a system has reached within the ±5% interval.

However, there is nothing in Figure 71 that explains why this behaviour occurs and for a better understanding Figure 72 is required. Figure 72 is similar to Figure 70 but the red volumes are symbolizing where the additional variable values are higher than the ±5% interval from the final value. The two columns to the left in Figure 72 show the liquid volumes only, i.e. those with a volume fraction of liquid above 0.5. The third column displays the highest additional variable values in the entire domain, i.e. both in regions where either the liquid or the gas phase dominates.

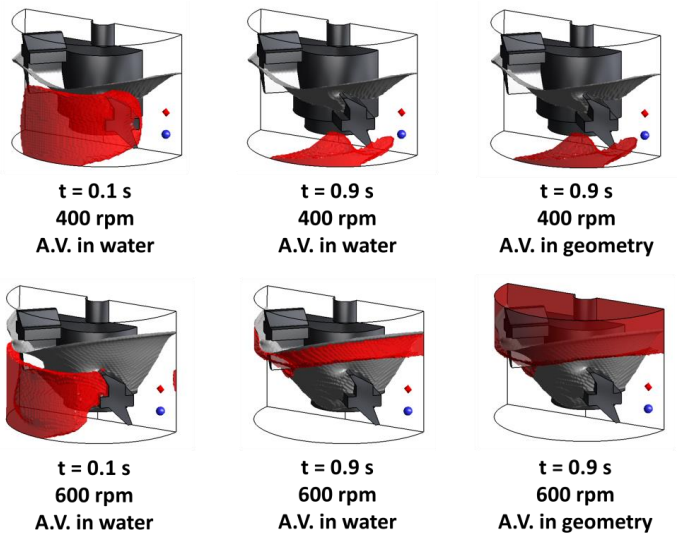

Figure 72. Concentrations of additional variables (A.V.) higher than the ±5% interval from the final value for the mixing times related to Figure 68.

The reason why the third column is different from the second is that even if the additional variable is only defined to be present in the liquid phase, the liquid phase is still present in the entire domain. This means that even if the volume fraction of water is only one in a million in a node the concentration of the additional variable in this node must still reach within the correct interval before mixing can be declared finished with the current mixing time definition.

After inspecting the mixing performance shown in Figure 72 it can be noted that the additional variables have behaved as expected after 0.1 seconds, i.e. the volume with high concentrations has moved further for the 600 rpm simulation than it has for 400 rpm. It is also important to note how the volumes have moved with respect to the paddles, since the additional variables are also located in the rotational frame of reference.

At 0.9 seconds, the highest concentrations are located in different regions for the two rotational speeds. For 400 rpm, the highest concentrations are at the bottom of the reactor and for 600 rpm, they are in the top of the liquid volume. This difference is important because shortly after 0.9 seconds the concentrations above 5% in the liquid volume vanish. Only the 400 rpm simulation will however have its maximum concentration decreased into the ± 5% interval since the 600 rpm simulation still has higher concentrations of additional variable in the air phase dominated regions. Disregarding the additional variable values in nodes where the air phase is dominant would solve this problem, but it was not possible with the current simulation setup.

One solution is however to create a second additional variable and define it as the product of the first variable and the step function in equation 87. The first additional variable will then be simulated as described previously, and the values of the second additional variable will be calculated in each node for each time step. In nodes where the step function is one, both additional variables will then have the same value. The transport equations will however only be solved for the first additional variable with the correct settings in ANSYS CFX 15.0. In

nodes where the step function takes the value zero, the second additional variable will be zero, which also eliminates its possibilities to define the highest value.

4.1.5.5. Mixing time comparisons between the different turbulence models

The mixing time comparisons between the laminar, SST and k-ε models are shown in Figure 73. For the results in the figure, Mesh 1 was used together with the time step 0.01 s. The reason why Mesh 1 was used for all turbulence models was for consistency, even if it was known from Figure 66 that the results for Mesh 1 were not fully mesh independent.

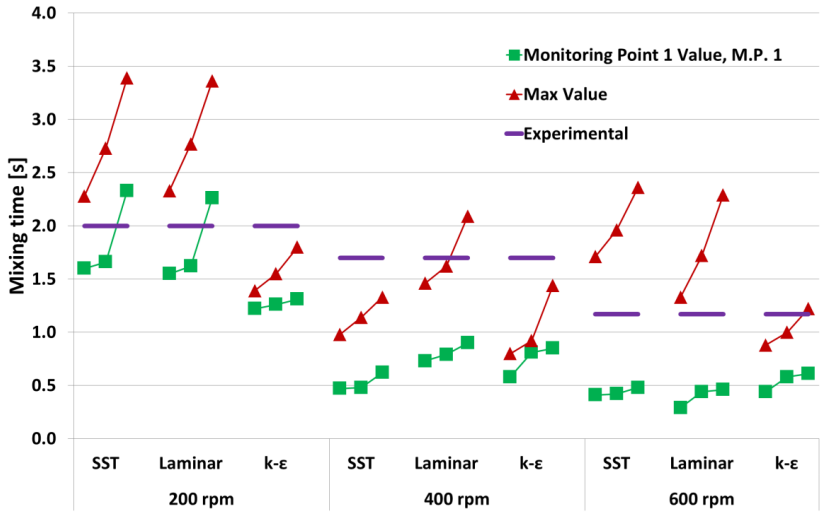

Figure 73. The mixing times for the SST, laminar and k-ε turbulence models. The connected sets of data represent the ±15%, ±10%, and ±5% mixing time values as in Figure 68.

Several observations can be made in Figure 73. For example, it can be seen that the mixing time results are very similar for the SST and the laminar model at 200 rpm. The reason for this is that the steady-state simulations for the mixing are based on very similar velocity lines as indicated in Figure 57 and Figure 58. The velocities for 400 and 600 rpm differ slightly more between the turbulence models, which explains why the trend was not persistent for these rotational speeds.

A second observation in Figure 73 is that the mixing time for the 400 rpm simulation is shorter for the SST than for the k-ε and laminar models evaluated at the monitoring point. The eddy viscosities are however much lower for the SST than the k-ε model, and shorter mixing times were therefore expected for the k-ε model since the eddy viscosity has an increasing impact on the diffusion terms in equation 43.

The concentrations of the additional variable at the monitoring point (M.P.1) over time for the different turbulence models are plotted in Figure 74. The figure also displays the ±5% interval as well as it highlights the positions where the concentration curves enter this region for the last time.

Figure 74 shows that the curves are different for the varying turbulence models. It also shows that the 10% mixing time is very similar between the laminar and the k-ε model even if their mixing behaviours appear very different. This is an important observation since Figure 73 alone, and if only the 10% interval is considered, suggests that there is no significant difference between the laminar and the k-ε model.

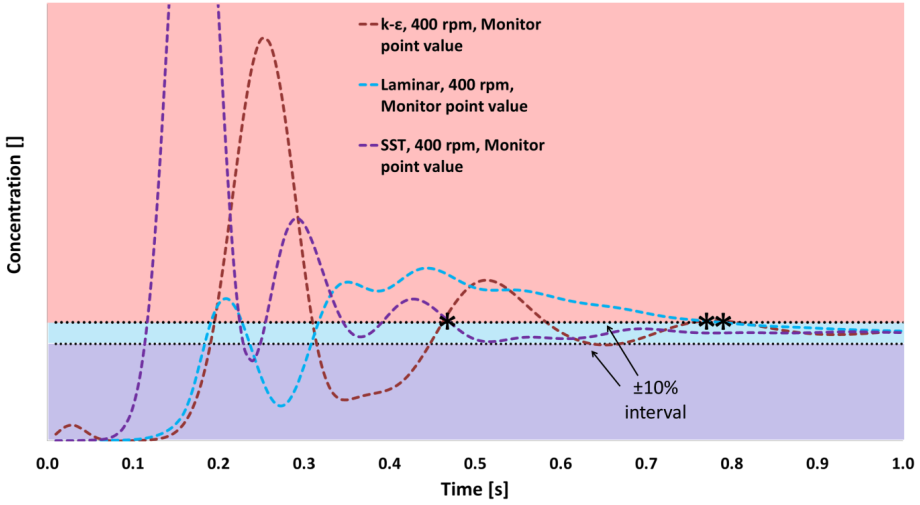

Figure 74. The concentrations of the additional variable in the monitoring point for 400 rpm and the three different turbulence models evaluated. The curves correlate with the mixing time data shown in Figure 73 and the 10% mixing time positions are highlighted with asterisks.

The spread of the additional variables over time for 400 rpm is displayed in Figure 75 and Figure 76. The red regions in the figures highlight liquid regions where the additional variable concentrations are higher than the ±10% interval and the turquoise regions indicate concentrations within the ±10% interval.

At 0.05 seconds in Figure 75 the SST and the laminar model have transported the additional variables further away from the source point in the circumferential direction than the k-ε model has. For the k-ε model the additional variable has on the other hand spread more in the axial direction.

Two pictures are used to illustrate the time step 0.15 seconds in Figure 75, which is also the time for the first SST-model peak in Figure 74. The laminar and the SST model appear very similar in Figure 75, but it can be seen that the monitoring point (blue) of the laminar flow is actually outside the red region while it is inside it for the SST model. This shows that the position of the monitoring points can be very important since the curves in Figure 74 appear so different.

For the time step 0.15 seconds it is seen that the additional variable is transported around the reactor as a concentrated region for the k-ε model while it is more spread out for the laminar and the SST model. The effect this has on the mixing, or the appearance of concentrations within the ±10% interval, is displayed in Figure 76.

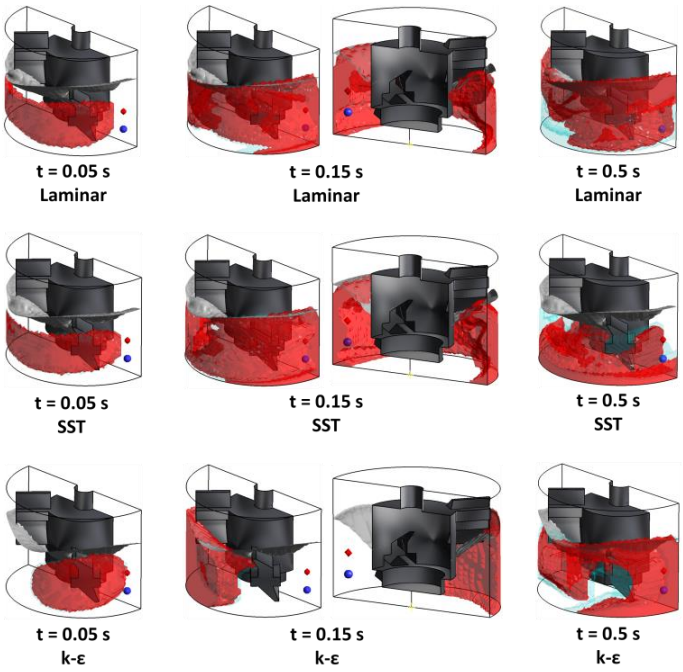

Figure 75. Transient mixing time simulations using Mesh 1, the time step 0.01 second and the rotational speed 400 rpm. The red regions have concentrations higher than the ±10% interval and the turquoise regions are within the interval.

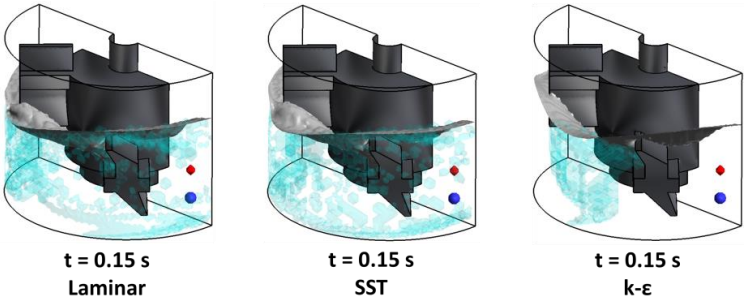

Figure 76. Detailed view on the turquoise regions in Figure 75 at 0.15 s.

In Figure 76 it can be seen that the well-mixed (turquoise) regions are spread relatively evenly in the liquid volume for the SST and the laminar model while the well-mixed region is centralized to one region for the k-ε model. Based on Figure 75 this is reasonable since well-mixed regions only can be initiated in the interface between regions of too high and too low concentrations. It also suggests that higher eddy viscosities do not always necessarily contribute to improved mixing in simulations on this scale. This is because high eddy viscosities do not only contribute to increased diffusion of the additional variables - they also decrease the velocity gradients and contribute therefore to a bulk flow.

At 0.5 seconds in Figure 75 the highest concentrations for the SST model have been relocated at the bottom and a layer of turquoise regions can be seen above it. From Figure 74 it can also be concluded that the monitoring point stayed within this well mixed region for the remaining part of the simulations. Based on Figure 75 it is however hard to argue that the SST model is better mixed than the other models. This makes it questionable if it is correct to determine mixing times on this scale based solely on monitoring points. If using monitoring points, it is recommended to use at least two of them in combination with a range of mixing time definitions, e.g. the 5, 10 and 15% intervals.

4.2. Magnetically stirred reactor

4.2.1. Experimental results

The k_La transfer coefficient results for the experiments performed in the magnetically stirred reactor are shown in Table 18. They are approximately 20 times smaller than the k_La values for the microbioreactor shown in Table 10. This is also an expected result since the microbioreactor is designed to support a growing cell culture with enough oxygen while the magnetically stirred reactor is not.

Table 18. The experimental k_La values for the magnetically stirred reactor.

Rotational speed	k_La [h^{-1}]	k_La [s^{-1}]
300 rpm	3.98	$1.11 \cdot 10^{-3}$
600 rpm	6.62	$1.84 \cdot 10^{-3}$
900 rpm	13.17	$3.65 \cdot 10^{-3}$

4.2.2. Reynolds number and the choice of turbulence model

The Reynolds numbers for the liquid phase in the magnetically stirred reactor are shown in Table 19. They were not calculated for the gas phase since the air was not in contact with the rotating magnet, which would have made the impeller Reynolds number inappropriate to use.

Table 19. The Reynolds numbers for the magnetically stirred reactor.

	300 rpm	600 rpm	900 rpm
Water	807	1613	2420

The Reynolds numbers for the magnetically stirred reactor are in the same range as the values for the microbioreactor which again makes the discussion regarding the choice of turbulence model from section 4.1.2 relevant. This is motivated by the experiences from the microbioreactor study, where the k-ε model was the only model that converged properly even though the SST model should be theoretically better.

However, both turbulence models converged well for the magnetically stirred reactor even if small oscillations in the monitoring points occurred for the SST model. The residuals of the SST model did not decrease towards zero for all meshes and rotational speeds, but based on the relatively stable values of the monitoring points it was not considered to be a serious concern. A general trend was also that the SST model had larger tendencies for convergence problems with the lower rotational speeds than for the higher.

There are many possible explanations why the magnetically stirred reactor was more successful with the SST model than the microbioreactor was. First of all the geometry of the magnetically stirred reactor was less complex which made it possible to create a hexahedral mesh consisting of good quality elements.

The geometry of the magnetically stirred reactor was also more simple in the sense that the gas-liquid interface never interfered with the rotating magnet. The gas-liquid interface was instead only present in the cylindrical region of the geometry, which contributed to a less complex flow pattern.

The three investigated rotational speeds were also selected based on the criterion that they did not cause any severe flow instabilities in the experimental setup. This was most likely not the

case when the five rotational speeds for the microbioreactor were selected. An unstable flow is often also not a drawback from an experimental point of view, and it can also be desired in order to increase the mixing in a system.

4.2.3. Steady-state results for the magnetically stirred reactor

4.2.3.1. Appearance and size of the gas-liquid interfaces

The appearance of the gas-liquid interfaces for 900 rpm and the three meshes with alternations in this region are shown in Figure 77. The specific interfacial areas for these, as well as the boundary refined mesh, are reported in Figure 78 together with data for 300 and 600 rpm.

In Figure 77 the SST model causes the vortex to reach deeper into the liquid, which is also reflected by the generally larger specific interfacial areas for the SST model in Figure 78.

It can also be seen that the interface for the coarsened mesh and the k-ε model both looks different and has a slightly increased calculated specific interfacial area. No noticeable differences can however be seen between the refined and the original meshes. The boundary refined mesh resulted also in a slightly larger calculated interfacial area for the SST/900 rpm case, but no differences could be seen for the visualised interfaces.

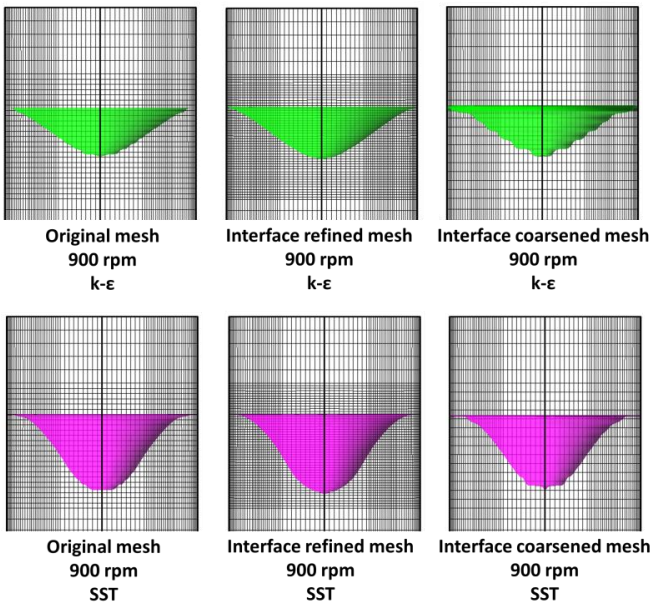

Figure 77. The appearances of the interfaces for 900 rpm and the SST and the k-ε turbulence model.

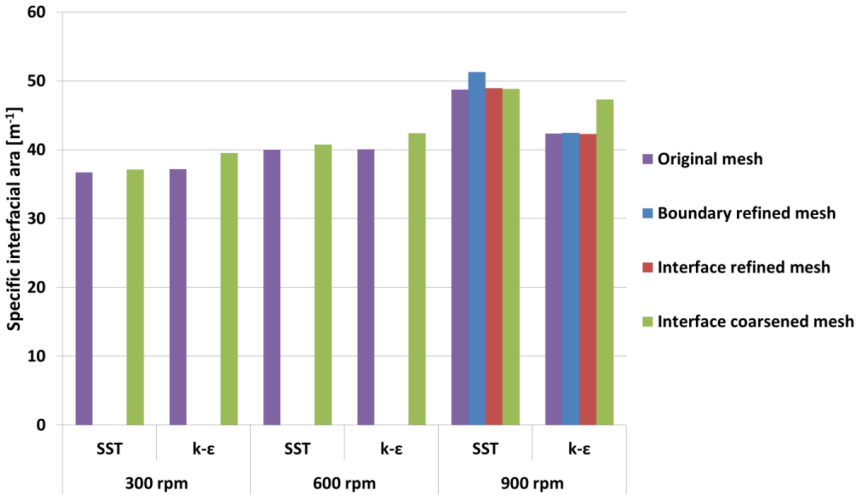

Figure 78. The sizes of the specific interfacial areas for the SST and the k-ε turbulence models.

The conclusion from this short preliminary investigation is that the coarsened interface mesh should not be used since it in one of the investigated cases (k-ε, 900 rpm) resulted in a relatively different specific interfacial area. The use of the refined interface mesh did however not add any extra value to the calculation of the specific interfacial area.

An additional observation from Figure 78 is that the specific interfacial areas do not differ substantially for the different rotational speeds. This is an interesting point to note, i.e. that 3-doubleling of the rotational speed and therefore the Reynolds number did not even increase the specific interfacial area with 15%. This is also further discussed in section 4.2.4.

4.2.3.2. Velocity profiles for the SST and the k-ε turbulence model

The velocity profiles and contour plots for the velocities are shown in Figure 79 for the SST turbulence model and in Figure 80 for the k-ε model. The velocity vectors in Figure 79 and Figure 80 are scaled in size in order to make them reasonably visible for the respective cases, and their magnitudes should therefore not be taken into consideration.

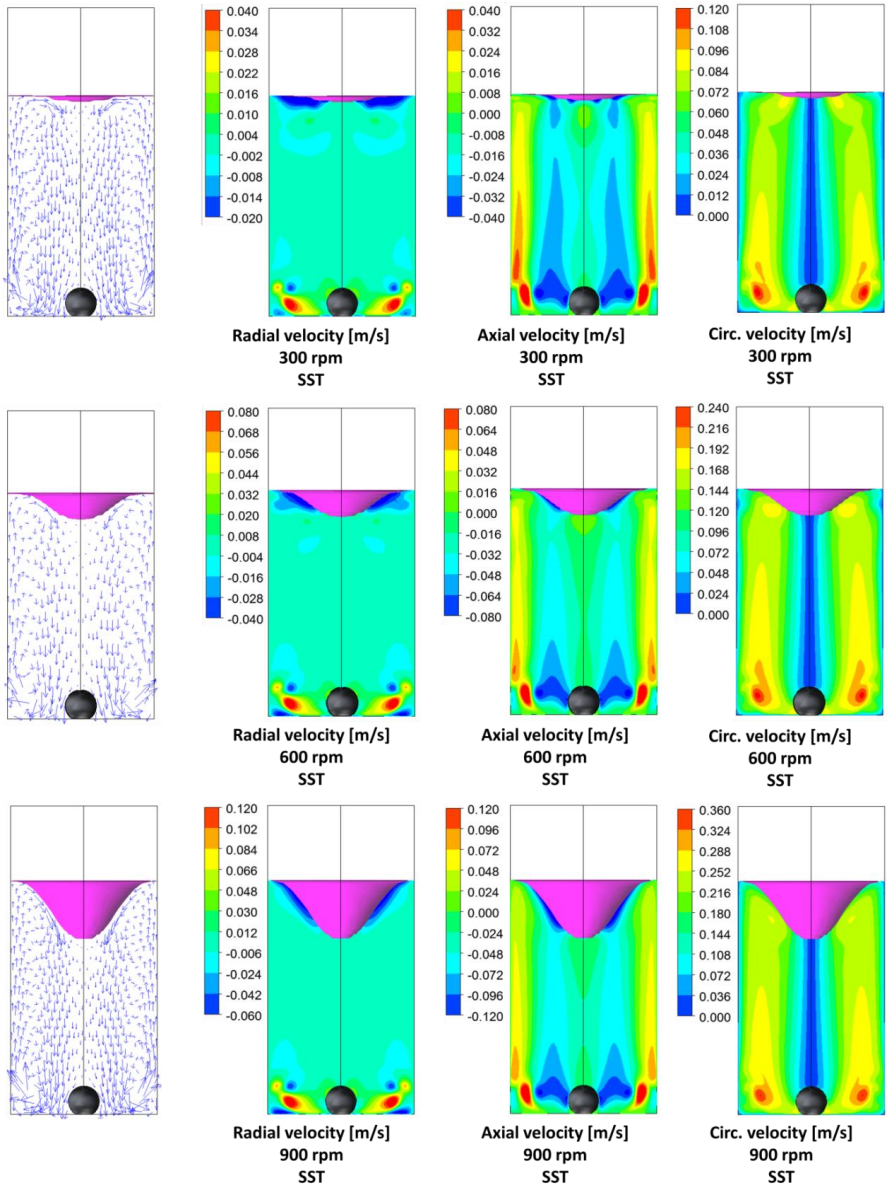

Figure 79. The velocity vectors and the radial, axial and circumferential velocity contour plots for the SST model applying the original mesh.

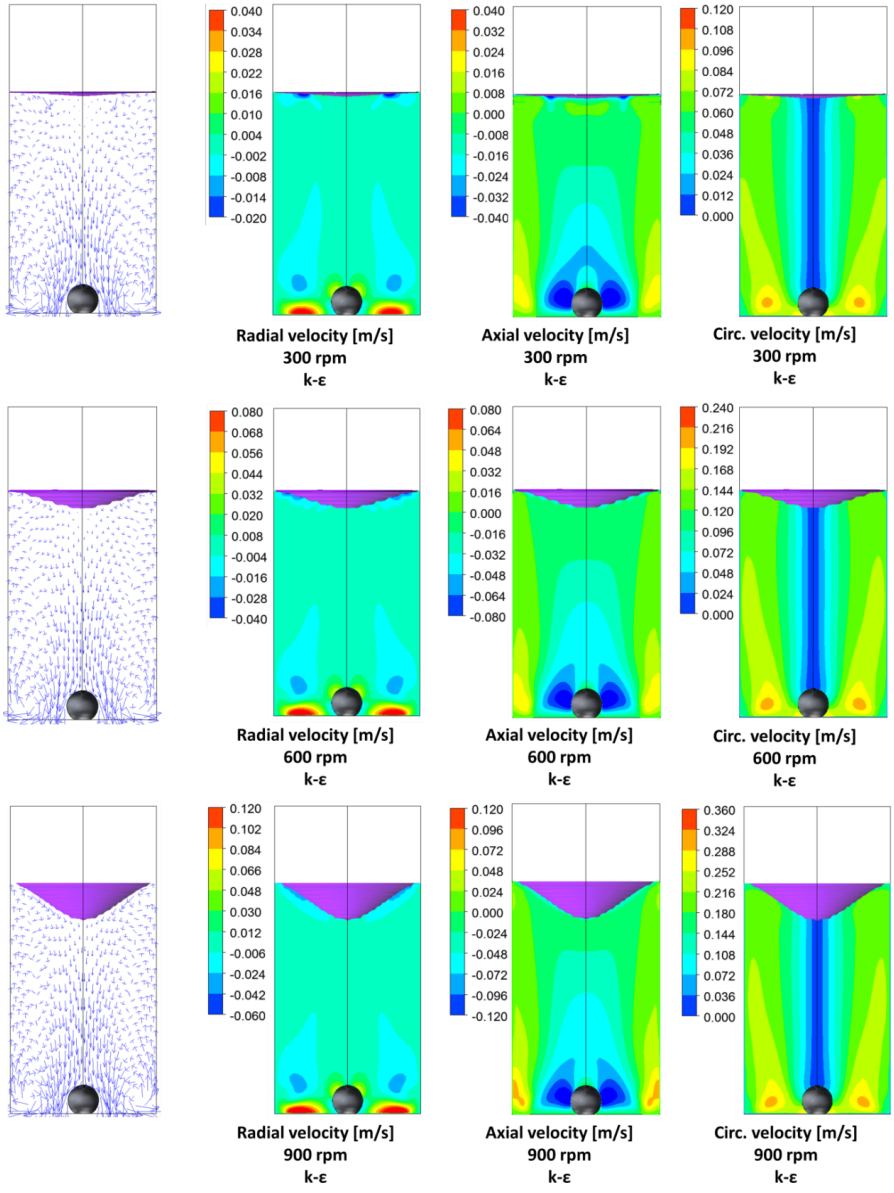

Figure 80. The velocity vectors and the radial, axial and circumferential velocity contour plots for the k-ε model applying the original mesh.

The general flow pattern for both turbulence models is created by the rotation of the magnet. The magnet accelerates the fluid in the outward direction, which means that new fluid needs to be provided to the parts of the magnet that are located more centrally, and this fluid must therefore be provided from above since the magnet is placed on the bottom.

Once the fluid is accelerated in the radial direction and reaches the cylindrical wall in the bottom of the reactor, it has to turn upwards. This has the effect that the liquid moves upwards close to the cylindrical walls and downwards in the centre of the vial. This means as well that the fluid needs to change the axial direction somewhere, which occurs at the top of the liquid volume.

The fluid is not only accelerated outward in the radial direction by the magnet, it is most of all also accelerated in the circumferential direction. The circumferential velocities decrease with an increasing distance in height to the magnet, but they are important throughout the vial since they cause the formation of the vortex and the deflection of the gas-liquid interface. This is because the circumferential velocities create an accelerating force outwards to the cylindrical walls. This force has no visible effect when only one fluid is present, but at the gas-liquid interface it forces the denser fluid (i.e. the liquid) more outwards while the less dense fluid (i.e. the air) is kept in the middle. The result is the deflection of the interface. The positive axial velocities close to the outer walls and their negative counterparts in the centre of the vial have also a minor effect on the creation of the deflected interface.

In Figure 79 and Figure 80 the legends of the contour plots are scaled with the rotational speeds. This means that the maximum and minimum values in the 900 rpm legends are three times larger than the corresponding values for 300 rpm. Visualising the velocities in this manner is interesting since it clearly shows commonalities between the flow structures. For example, the contour plots in the bottom parts of the reactors are very similar for the varying rotational speeds that have been tested.

A possible explanation for the differences between the depths of the vortexes between the turbulence models, i.e. that the SST model is better in creating a deeper deflection of the gas-liquid interface than the k-ε model, can also be found in the comparison between Figure 79 and Figure 80. As explained earlier the depth of the vortex is dependent on the magnitude of the accelerating forces moving the denser fluid outwards in the upper part of the reactor. The depth of the vortex is therefore also dependent on the magnitude of the circumferential velocities. It can also be seen in Figure 79 and Figure 80 that the SST model creates larger flows in the circumferential direction in the top of the reactors than the k-ε model does. This trend is evident throughout the reactor geometry and in the regions around the magnet are the circumferential velocities higher for the SST model than for the k-ε. This is interesting since the rotation of the magnets is the same for both turbulence models.

The velocities are however visualised at the surface perpendicular to the length of the magnet, which suggests that something in the fluid has dampened the velocities. One hypothesis is that the k-ε model achieved higher eddy viscosities in this region and this is therefore investigated in the following section.

There are also clear differences in the axial velocity components between the two turbulence models. The positive axial velocities are for example higher and more wall-bound for the SST model compared to the k-ε model.

The radial velocities differ also between the two turbulence models. For the k-ε model, the velocities leading outwards in the positive radial direction are located very close to the bottom of the reactor and there are small re-circulation areas present above the magnet where the liquid is transported inwards again. For the SST model, the outwards radial flows are

more concentrated to the middle of the magnet with two smaller but more pronounced re-circulation zones located above and underneath it.

4.2.3.3. Eddy viscosity profiles for the k-ε and the SST model

The velocity differences between the two discussed turbulence models in the previous section should be explained by differences in the distribution of the eddy viscosities. The eddy viscosities for Line 2 in Figure 27 are therefore displayed in Figure 81 and the values for the 'Outer Polyline 1' are displayed in Figure 82. In Figure 81 the values for both the original and the boundary refined mesh are displayed. It can however be seen that the boundary refinement had no significant effect.

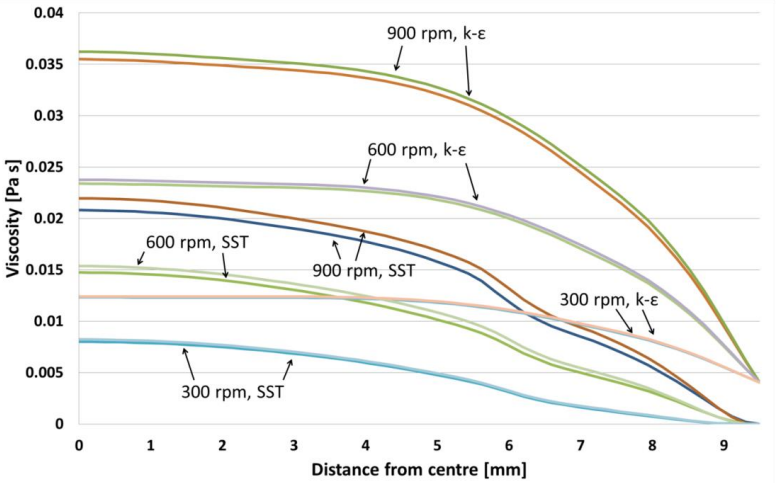

Figure 81. The eddy viscosities for Line 2 (Figure 27) using the original and the boundary refined mesh and the SST and the k-ε model.

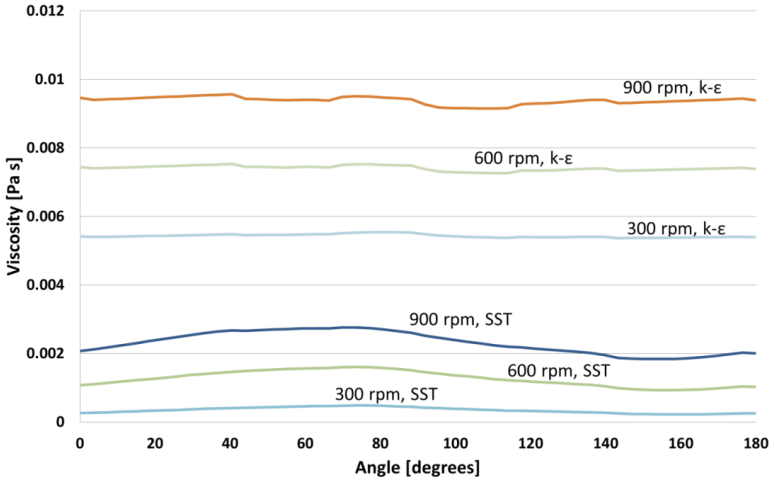

Figure 82. The eddy viscosities for the 'Outer Polyline 1' (Figure 27) using the original mesh and the SST and the k-ε model.

A first observation in Figure 81 and Figure 82 are that the produced eddy viscosities are in the same order of magnitude for both models. This can be compared to the result in section 4.1.3.4 where the eddy viscosities produced in the microbioreactor were much smaller for the SST model.

Another interesting phenomenon in Figure 81 is that the wall boundary values for the k-ε model are all the same, i.e. $4.04 \cdot 10^{-3}$ Pa s, which is identical to the boundary values in the microbioreactor case. That again suggests that the y^+ values at these walls as well are smaller than 11.06, and that the scalable wall function rounded the values to 11.06 as part of the wall treatment.

The boundary values for the SST model in Figure 81 are all very low, but they do not have the same numerical value. Instead, they are varying in the range between 10^{-6}-10^{-9} Pa s. This suggests also y^+ values smaller than 11.06, and that the laminar wall treatment has been applied for the automatic wall function.

The values of the eddy viscosities further away from the walls are also consistently higher for the k-ε model than for the SST model shown in Figure 81 and Figure 82. This means that there were increased eddy viscosities present in the k-ε model which slowed the velocities down.

4.2.3.4. Investigation of the y^+ values at the walls for the k-ε and the SST model

The y^+ values for 900 rpm are displayed in Figure 83 and the results from both the original and the boundary refined meshes are displayed in combination with the two turbulence models. The colour legends are also different between the meshes and it is noticeable that the original mesh results in values approximately three times higher than for the boundary-refined mesh. That is also fully reasonable knowing that the distances between the wall and their closest nodes are lowest in the refined mesh.

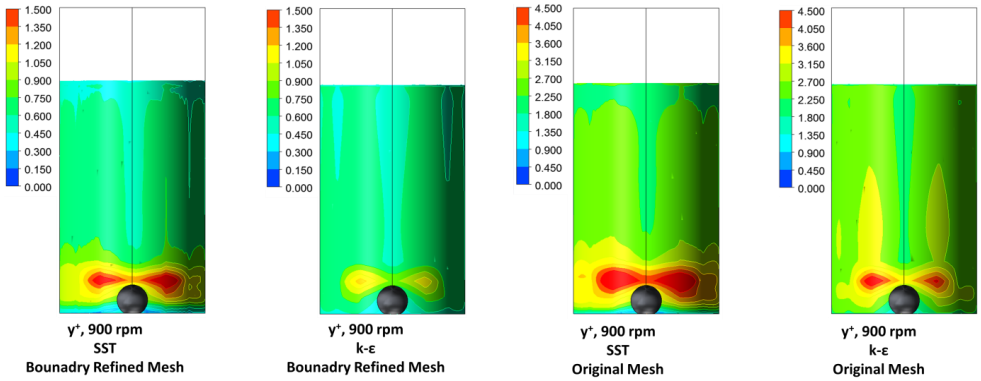

Figure 83. The y^+ values for the SST and k-ε model applied to the original and the boundary refined meshes.

In Figure 83 it can also be seen that the SST model has higher y^+ values especially in the region above the magnet, which is a consequence of higher velocities there. It must however be noted that Figure 83 displays the y^+ values at the cylindrical wall while Figure 79 and

Figure 80 show the velocities at the symmetry planes in the free stream. It is nevertheless possible to confirm by Figure 79 and Figure 80 that there are velocity differences in these regions between the turbulence models.

The final observation from Figure 83 is that the values are indeed lower than 11.06 for all investigated boundaries which confirms the wall treatment discussion of the previous sections.

4.2.3.5. Distribution of turbulent energy dissipation for the SST and the k-ε model

The turbulent energy dissipation rates (ε) in the simulations are interesting since they are one of two variable parameters in the eddy cell model. The turbulent eddy dissipation rates for Line 2 (in Figure 27) are displayed in Figure 84 for 900 rpm and the SST and the k-ε models. Three different meshes are evaluated, i.e. the original, the boundary refined one and the middle region coarsened one.

The figure is highly interesting since it reveals a completely different behaviour at the boundaries for the two turbulence models. It also shows that the choice of mesh has an impact for the SST model but not so much for k-ε. Regarding the SST model it shows that the mesh refinement in the direction parallel to the flow (i.e. the boundary refinement) had an impact while the mesh coarsening perpendicular to the flow (i.e. the middle coarsened mesh) did not have any effect. An explanation for this is that there are only low velocity gradients parallel to the flow direction while more pronounced gradients are present perpendicular to the flow due to the no slip conditions at the wall.

The difference between the two turbulence models is that the k-ε model results in relatively high ε values at the wall, which decline into the middle of the fluid while the SST model has lower values at the wall, which first increase and then decrease again once moving into the fluid. The diverging values at the walls can be explained by different wall treatments. However, for the behaviour in the bulk additional explanations are needed. To further investigate this behaviour Figure 85 is provided, which shows the values of ε for 300 and 600 rpm for the same line as in Figure 84. The coarse mesh is however excluded since it was very similar to the original mesh.

Figure 84 shows the same trend as Figure 85, i.e. that the values provided by the k-ε model are highest at the walls, and that the values for the SST model are relatively low by the walls and then first increase and then decrease towards the centre of the reactor. In order to explain this in more detail Figure 86 is provided.

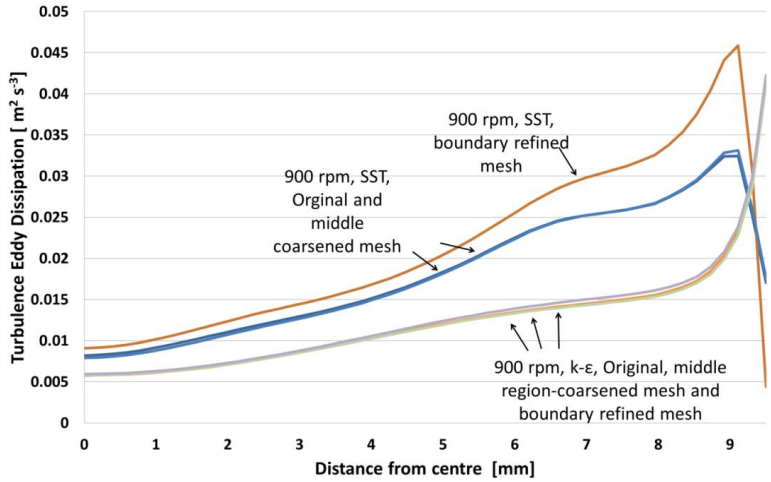

Figure 84. The turbulence energy dissipation rates for Line 2 (Figure 27) for the original, boundary refined and middle coarsened meshes for 900 rpm and the SST and the k-ε turbulence models.

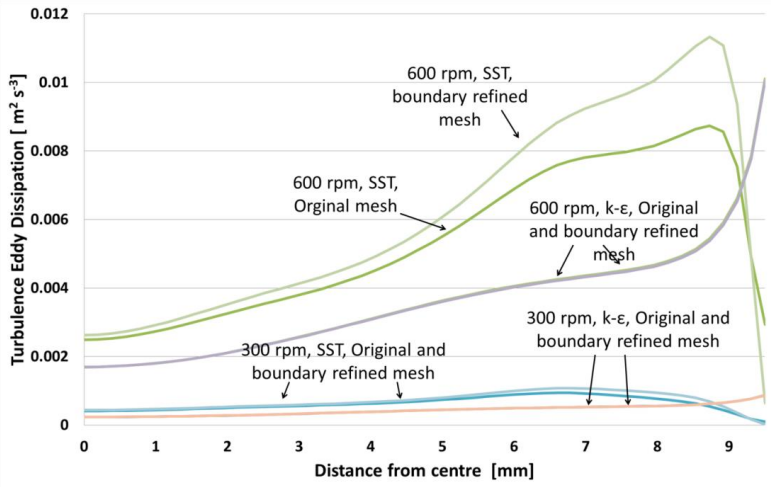

Figure 85. The turbulence energy dissipation rates for Line 2 (Figure 27) for the original and boundary refined meshes, 300 and 600 rpm, and the SST and the k-ε turbulence models.

Figure 86 shows the distributions of the turbulence energy dissipation (ε) in the fluid for the SST and the k-ε model and in the figure it can be seen that the highest values of ε are located at the bottom of the reactors. This is also reasonable since a lot of turbulence should be present in this region due to the stationary bottom and the rotating magnet. It appears also as if the ε produced in the bottom regions are transported upwards along the walls, but that this phenomenon is most successful for the SST simulation. This explains therefore the peak close to the walls for the SST model seen in Figure 84 and Figure 85.

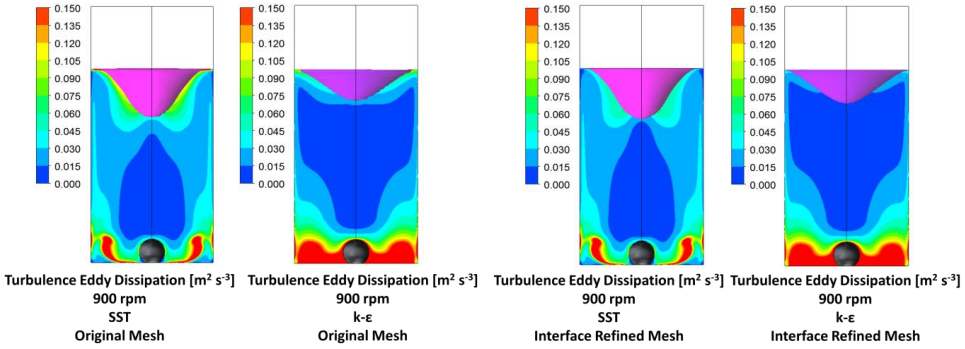

Figure 86. The distributions of ε at 900 rpm for the SST and the k-ε model and the original and the interface refined reactor.

The averaged and maximum values of ε will now be investigated for the two turbulence models and the most relevant meshes. The liquid volume averaged values of ε are therefore displayed in Figure 87 and the maximum values in Figure 88. The averaged values at the gas-liquid interface are presented in Figure 89.

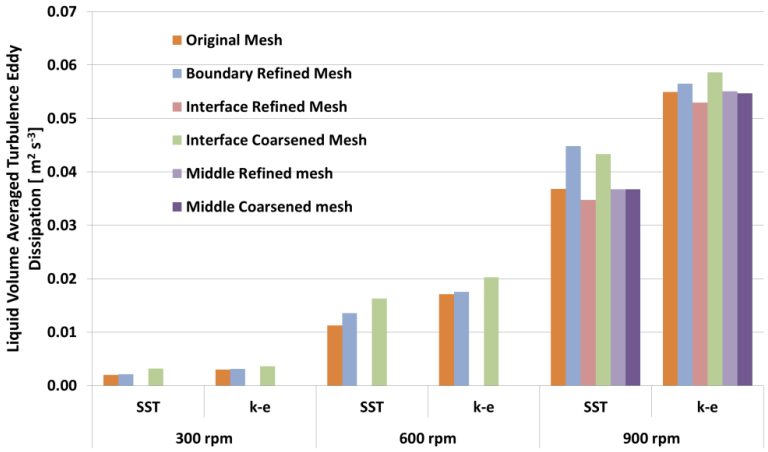

Figure 87. The liquid volume averaged turbulence eddy dissipation for the SST and the k-ε model.

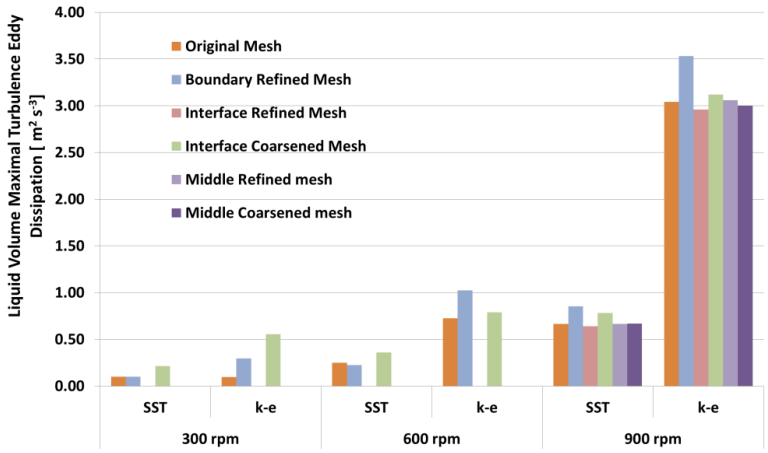

Figure 88. The maximum values in the liquid phase of the turbulence eddy dissipation for the SST and the k-ε model.

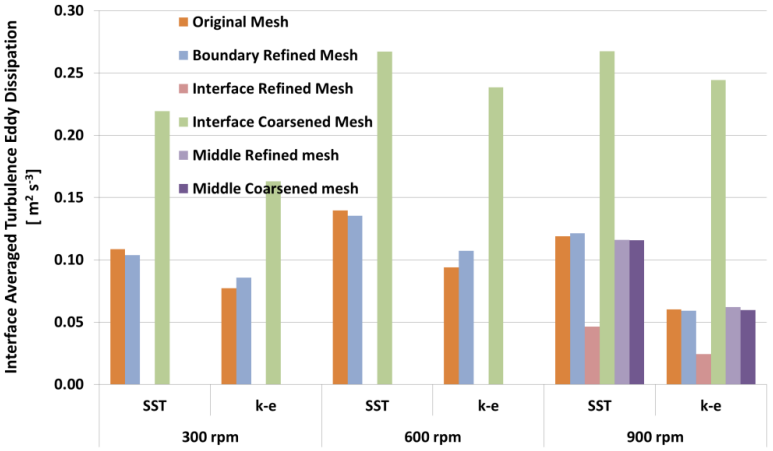

Figure 89. The gas-liquid interface averaged turbulence eddy dissipation for the SST and the k-ε model.

Many interesting conclusions can be made based on Figure 87, Figure 88 and Figure 89. In Figure 87 it can be seen that the averaged values are relatively similar for the different meshes and that there are distinct differences between the different rotational speeds. It also shows that the k-ε model predicts higher averaged values of ε than the SST model which is especially noticeable at 900 rpm. This is however problematic knowing where the quantities of ε actually are situated according to Figure 86.

In Figure 86, it can indeed be seen that most of the ε for the k-ε model are produced at the bottom of the reactor, i.e. not at the gas-liquid interface which is the only location where increased levels of ε should give meaning according to the eddy cell model. This highlights also an important shortcoming of the volume averaging of ε which should be an extra serious concern the larger the reactor is or the larger the distance from the regions with high values of ε to the interface responsible for the oxygen transfer.

As Figure 86 suggests the values of ε at the gas-liquid interface are higher for the SST model than for the k-ε model. This is also confirmed in Figure 89. A clear trend is also that the surface-averaged values are considerably higher than their corresponding volume averaged values. This result is different from the conclusions from the microbioreactor simulations where the two averaged quantities were approximately the same.

In Figure 89 it is also shown that the interface coarsened mesh, i.e. the one with a coarser distribution of nodes in the height direction in the gas-liquid interface area, produced noticeably higher values of ε. It is also seen in Figure 89 that the interface refined mesh produces considerably lower values of ε at the interface. One reasonable explanation is that the velocity gradients at the gas-liquid interfaces are larger the coarser the mesh since the fluid has only a limited space to turn from positive to negative axial velocities. The deeper vortexes created by the SST model also make this space smaller, and therefore also the gradients and production term for ε higher.

The maximum values of ε are highest for the k-ε model and these high values are most certainly located in the bottom of the reactor based on Figure 86. This again suggests therefore that the maximum values should be considered as not-representative for the entire system, especially since the maximum values by definition only appear in a single node.

4.2.3.6. The difference between the free slip wall and the entrainment top boundary condition

The differences in the velocity fields between using the top boundary conditions *free slip wall* and *entrainment* are displayed in Figure 90 and the results origin from simulations using the interface coarsened mesh, the SST turbulence model and the rotational speed 900 rpm. The red gas velocities are shown in the gas phase dominant region and the blue vectors are showing the liquid velocities in the liquid dominant region. The counts and magnitudes of the vectors are however adjusted between the phases.

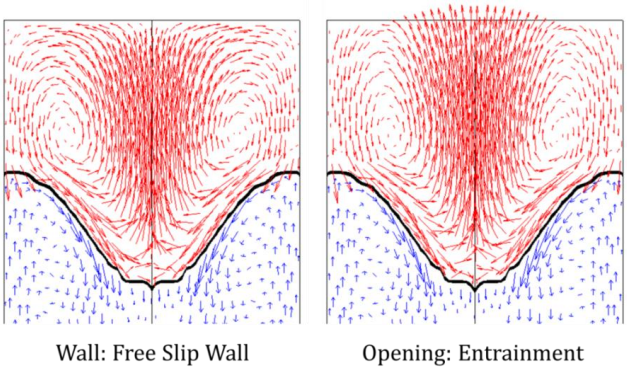

Figure 90. The gas (red) and liquid (blue) phase velocity vectors for the *free slip wall* and the *opening: entrainmen* top boundary conditions using the interface coarsened mesh, the SST turbulence model and the rotational speed 900 rpm.

As shown in Figure 90 no gas is allowed to exit or enter through the wall boundary condition while the opening has a visible outflow in the middle. Both simulations develop however the same general velocity pattern in the gas phase with two re-circulating vortexes. The velocity vectors in the liquid phase are also very similar, which suggests that the use of a free-slip wall

is fully reasonable even for a vessel not actually sealed on the top. One advantage using a *free slip wall* is that it simplifies mixing simulations involving additional variables since additional variables are allowed to leave and enter through openings. In systems with opening boundary conditions it is therefore problematic to define final concentrations since for example washout phenomena can occur. Similar situations can also arise with turbulent scalars, e.g. k and ε for the k-ε model, across an opening since the boundary conditions must be defined by the user. One solution to this problem is to use a zero-gradient boundary condition for the turbulent variables. Table 20 is provided in order to investigate if this option had any impact on the turbulent energy dissipation rates (ε) in the liquid. It can be seen that the resulting values of ε are very similar between the two top boundary conditions, and it was therefore decided that the free slip boundary condition was the best choice.

Table 20. Energy dissipation rate data for the SST model simulated at 900 rpm, comparing the *free slip wall* and the opening top boundary conditions.

	Wall: Free Slip Wall		**Opening: Entrainment**	
	Original mesh	**Interface coarsened mesh**	**Original mesh**	**Interface coarsened mesh**
Average ε in liquid volume [m^2s^{-3}]	$3.68 \cdot 10^{-2}$	$4.33 \cdot 10^{-2}$	$3.70 \cdot 10^{-2}$	$4.33 \cdot 10^{-2}$
Maximum ε in liquid volume [m^2s^{-3}]	$6.65 \cdot 10^{-1}$	$7.82 \cdot 10^{-1}$	$6.63 \cdot 10^{-1}$	$7.80 \cdot 10^{-1}$
Average ε at gas-liquid interface [m^2s^{-3}]	$1.19 \cdot 10^{-1}$	$2.67 \cdot 10^{-1}$	$1.17 \cdot 10^{-1}$	$2.66 \cdot 10^{-1}$

4.2.3.7. The difference between the homogenous and the inhomogeneous momentum equation

The inhomogeneous momentum equations were used for all two-phase simulations in this project with two exceptions. The reason for this is that the homogenous models did not manage to converge for the microbioreactor where it otherwise could have been considered an option. Using the homogenous momentum model for the flow in the magnetically stirred rector was however more successful, even if the general impression of the simulations was that they were slightly less stable than their inhomogeneous counterparts.

The comparison in this section is performed for the original mesh applying the SST turbulence model at a rotational speed of 900 rpm. The resulting cylindrical velocity contour plots for the homogenous model are displayed in Figure 91 where also the appearance of the gas-liquid interface and the velocity vectors are shown. Comparing Figure 91 with its inhomogeneous counterpart in Figure 79 it can be seen that the velocities are very similar for the two cases - especially in the lower parts of the reactor where the liquid phase volume fractions are almost 100%.

The appearance of the gas-liquid interface is however far from smooth in Figure 91, and the region where it is disrupted is also where the simulations had most difficulties to converge. A plausible justification for the difficulties with the homogenous model is that the gas velocities are directed upwards in the positive axial direction while the liquid velocities are directed downwards in this region according to Figure 90. In an unscientific language this should therefore has promoted a conflict over the choice of axial direction since the gas and liquid phase share the same velocity field with the homogenous momentum model.

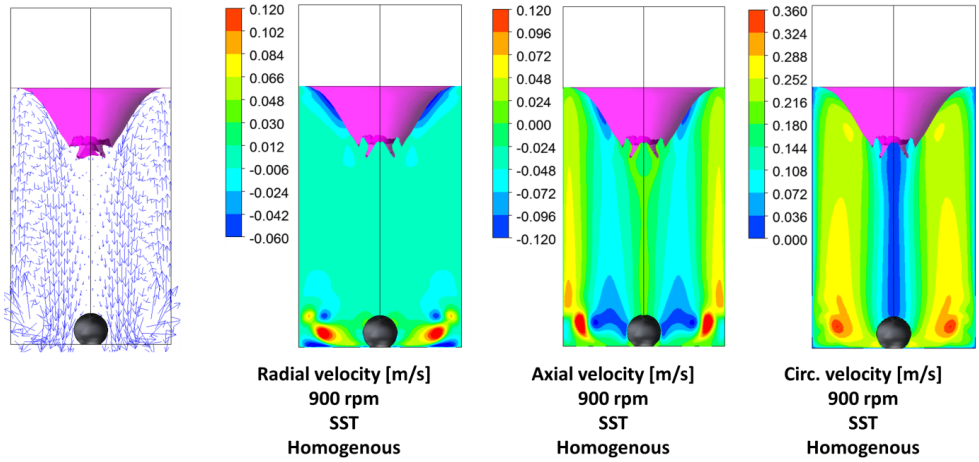

Figure 91. The radial, axial and circumferential velocities for the SST model, the original mesh, the rotational speed 900 rpm and the homogenous momentum model.

The choice between the homogenous and inhomogeneous momentum equation has not only an impact on the resulting velocity fields and volume fraction distributions. In Figure 92, the eddy viscosities and the turbulent energy dissipation rate contour plots are compared between the models and it can be seen that the inhomogeneous model has higher eddy viscosities in the region where the instabilities appeared for the homogenous model. These higher eddy viscosities can also have contributed to the stabilisation, i.e. the convergence, of the inhomogeneous model.

The differences between the turbulent energy dissipation rates in Figure 92 are also interesting since they clearly show that the values of ε are much higher at the gas-liquid interface for the inhomogeneous model. This is an important observation since it shows that either the inhomogeneous or the homogenous momentum model has severe shortcomings concerning the simulated values of ε in the interface region. It should also be considered especially important once using the eddy cell model where the software provided values of ε are the only variable influencing the modelling of the mass transfer coefficient.

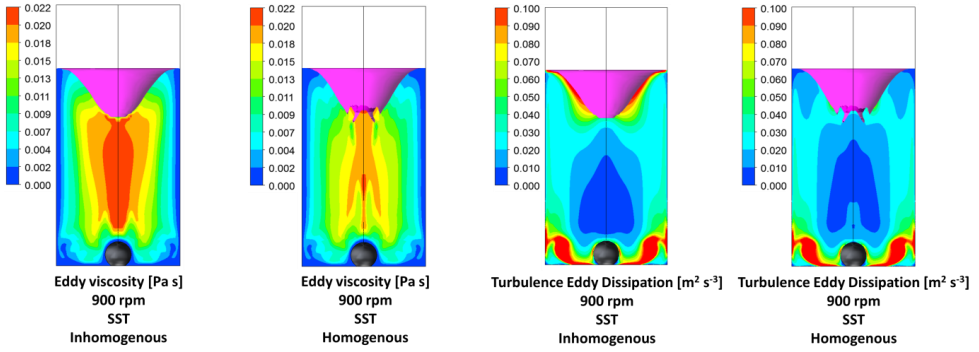

Figure 92. Comparison between the eddy viscosities and the turbulent energy dissipation rates between the inhomogeneous and homogenous momentum equations for the original mesh, the SST turbulence model and 900 rpm.

4.2.4. Oxygen transfer simulation results

The oxygen transfer simulations in the magnetically stirred reactor were performed in the same way as in the microbioreactor. The main difference between the microbioreactor and the magnetically stirred reactor was however that both the SST and the k-ε turbulence model converged for the latter.

4.2.4.1. Analysis of the experimental k_La values

The experimental k_La values from Table 18 and the corresponding Reynolds numbers from Table 19 are summarized in Table 21. Correlated to equation 90 the data result in equation 107 indicating that the Reynolds number and the experimental k_La are close to linearly proportional related. This means that the k_La values in the magnetically stirred reactor are more sensitive to the Reynolds number, i.e. the rotational speed, than they are in the microbioreactor.

Table 21. The experimental k_La values and the Reynolds numbers of the liquid phase in the microbioreactor

	300 rpm	**600 rpm**	**900 rpm**
Experimental k_La [s^{-1}]	$1.11 \cdot 10^{-3}$	$1.84 \cdot 10^{-3}$	$3.65 \cdot 10^{-3}$
Reynolds number	807	1613	2420

$$k_L a_{Exp.} \propto Re_{Impeller}^{1.05} \qquad R^2 \approx 0.95 \tag{107}$$

4.2.4.2. The simulated a, k_L and k_La values

The specific interfacial areas for the SST and the k-ε model for the magnetically stirred reactor are shown in Table 22. The original mesh was chosen to represent the system both for ε and the specific interfacial area even though it was not fully mesh independent as shown Figure 87. The volume averaged, liquid phase maximum and the interface averaged values of ε are shown in Table 23 for the original mesh, and the corresponding k_L and k_La values are displayed in Table 24 and Table 25.

Table 22. Specific interfacial area [m^{-1}] for the magnetically stirred reactor and the k-ε and SST turbulence models.

	SST			**k-ε**		
	300 rpm	**600 rpm**	**900 rpm**	**300 rpm**	**600 rpm**	**900 rpm**
Original Mesh	$3.67 \cdot 10^{1}$	$4.00 \cdot 10^{1}$	$4.87 \cdot 10^{1}$	$3.72 \cdot 10^{1}$	$4.01 \cdot 10^{1}$	$4.23 \cdot 10^{1}$
Boundary Refined Mesh	$3.68 \cdot 10^{1}$	$4.08 \cdot 10^{1}$	$5.13 \cdot 10^{1}$	$3.96 \cdot 10^{1}$	$4.26 \cdot 10^{1}$	$4.24 \cdot 10^{1}$
Interface Refined Mesh			$4.89 \cdot 10^{1}$			$4.23 \cdot 10^{1}$
Interface Coarsened Mesh	$3.71 \cdot 10^{1}$	$4.08 \cdot 10^{1}$	$4.89 \cdot 10^{1}$	$3.95 \cdot 10^{1}$	$4.24 \cdot 10^{1}$	$4.73 \cdot 10^{1}$
Middle refined mesh			$4.87 \cdot 10^{1}$			$4.24 \cdot 10^{1}$
Middle coarsened mesh			$4.88 \cdot 10^{1}$			$4.24 \cdot 10^{1}$

Table 23. Energy dissipation rate data for the k-ε and SST model and the original mesh.

	SST			k-ε		
	300 rpm	**600 rpm**	**900 rpm**	**300 rpm**	**600 rpm**	**900 rpm**
Average ε in liquid volume [m^2s^{-3}]	$2.00 \cdot 10^{-3}$	$1.13 \cdot 10^{-2}$	$3.68 \cdot 10^{-2}$	$3.00 \cdot 10^{-3}$	$1.71 \cdot 10^{-2}$	$5.50 \cdot 10^{-2}$
Maximum ε in liquid volume [m^2s^{-3}]	$1.01 \cdot 10^{-1}$	$2.48 \cdot 10^{-1}$	$6.65 \cdot 10^{-1}$	$9.82 \cdot 10^{-2}$	$7.25 \cdot 10^{-1}$	$3.04 \cdot 10^{0}$
Average ε at gas-liquid interface [m^2s^{-3}]	$1.08 \cdot 10^{-1}$	$1.40 \cdot 10^{-1}$	$1.19 \cdot 10^{-1}$	$7.72 \cdot 10^{-2}$	$9.93 \cdot 10^{-2}$	$6.01 \cdot 10^{-2}$

Table 24. Simulated k_L values based on the ε data in Table 24.

	SST			k-ε		
	300 rpm	**600 rpm**	**900 rpm**	**300 rpm**	**600 rpm**	**900 rpm**
Average k_L in liquid volume [m s^{-1}]	$3.06 \cdot 10^{-4}$	$4.72 \cdot 10^{-4}$	$6.34 \cdot 10^{-4}$	$3.39 \cdot 10^{-4}$	$5.24 \cdot 10^{-4}$	$7.01 \cdot 10^{-4}$
Maximum k_L in liquid volume [m s^{-1}]	$8.16 \cdot 10^{-4}$	$1.02 \cdot 10^{-3}$	$1.31 \cdot 10^{-3}$	$8.10 \cdot 10^{-4}$	$1.34 \cdot 10^{-3}$	$1.91 \cdot 10^{-3}$
Average k_L at gas-liquid interface [m s^{-1}]	$8.31 \cdot 10^{-4}$	$8.85 \cdot 10^{-4}$	$8.50 \cdot 10^{-4}$	$7.63 \cdot 10^{-4}$	$8.01 \cdot 10^{-4}$	$7.17 \cdot 10^{-4}$

Table 25. Simulated k_La values based on the products of the original mesh data in Table 22 and Table 24.

	SST			k-ε		
	300 rpm	**600 rpm**	**900 rpm**	**300 rpm**	**600 rpm**	**900 rpm**
Average k_La in liquid volume [s^{-1}]	$1.12 \cdot 10^{-2}$	$1.89 \cdot 10^{-2}$	$3.09 \cdot 10^{-2}$	$1.26 \cdot 10^{-2}$	$2.10 \cdot 10^{-2}$	$2.97 \cdot 10^{-2}$
Maximum k_La in liquid volume [s^{-1}]	$2.99 \cdot 10^{-2}$	$4.09 \cdot 10^{-2}$	$6.37 \cdot 10^{-2}$	$3.01 \cdot 10^{-2}$	$5.35 \cdot 10^{-2}$	$8.09 \cdot 10^{-2}$
Average k_La at gas-liquid interface [s^{-1}]	$3.05 \cdot 10^{-2}$	$3.54 \cdot 10^{-2}$	$4.14 \cdot 10^{-2}$	$2.84 \cdot 10^{-2}$	$3.21 \cdot 10^{-2}$	$3.03 \cdot 10^{-2}$

The k_L values in Table 24 are similar to those for the microbioreactor presented in Table 15 and match therefore also to the values described in Brüning and Weuster-Botz (2014). The differences between using the surface averaged and the volume-averaged definition of ε is however more pronounced in Table 24 than in Table 15.

The use of the volume-averaged value of ε for the magnetically stirred reactor can also be questioned since it was previously shown (Figure 86) that the highest values of ε are located at the bottom of the magnetically stirred reactor. The turbulent eddies located at the bottom of the reactor should not contribute to renewal of the gas-liquid interface, which is the main idea behind the eddy cell model. The use of the surface averaged values is however questionable as well after the observation that these values are highly dependent on the choice of momentum model, i.e. if the homogenous or inhomogeneous model is used, as described in section 4.2.3.7.

4.2.4.3. Correlation studies between experimental k_La and simulated ε and a

The turbulent energy dissipation rates in the magnetically stirred reactor are correlated to the experimental k_La data in equation 108-111. Equation 108 and 109 show that there is almost no difference between the SST and the k-ε turbulence model for the volume averaged values.

The average values are higher for the k-ε model in Table 24, but the relative increments appear similar for the two cases. The equations also show that the Reynolds number has a smaller impact on the eddy viscosities in the magnetically stirred reactor than in the microbioreactor where the exponent was 3.02 instead of 2.63 and 2.64.

Equation 110 and 111 reveal that the interface averages of ε are not well described by the model proposed in equation 91 since the R^2 values are very low. This is also confirmed in Figure 89 and Table 23 where it is demonstrated that the interface averaged value of ε not even increases with increasing rotational speeds. Table 15 shows however that the associated k_La values constantly are increasing using the interface averaged k_L. It also is not obvious that the surface averaged values of ε should increase for increasing rotational speeds in the physical system.

$$\varepsilon_{Sim,Volume\ Ave.,SST} \propto Re_{Impeller}{}^{2.64} \qquad R^2 \approx 1.00 \tag{108}$$

$$\varepsilon_{Sim,Volume\ Ave.,k-\varepsilon} \propto Re_{Impeller}{}^{2.63} \qquad R^2 \approx 1.00 \tag{109}$$

$$\varepsilon_{Sim,Interface\ Ave.,SST} \propto Re_{Impeller}{}^{0.11} \qquad R^2 \approx 0.24 \tag{110}$$

$$\varepsilon_{Sim,Interface\ Ave.,k-\varepsilon} \propto Re_{Impeller}{}^{-0.17} \qquad R^2 \approx 0.19 \tag{111}$$

The results of applying equation 92 to the simulated specific interfacial areas are shown in equation 112 and 113 for the two turbulence models. Compared with equation 102 it can be seen that the interfacial area in the microbioreactor is much more sensitive to the rotational speed than in the magnetically stirred reactor. This is also reasonable comparing the appearances and locations of the interfaces between Figure 48 and Figure 79 or Figure 80.

$$a_{Sim.,SST} \propto Re_{Impeller}{}^{0.24} \qquad R^2 \approx 0.87 \tag{112}$$

$$a_{Sim.,k-\varepsilon} \propto Re_{Impeller}{}^{0.12} \qquad R^2 \approx 1.00 \tag{113}$$

The results for correlating the data to equation 94 are displayed in equation 114 and 115. The volume-averaged values of ε are in proximity of the theoretically expected value of 0.25.

$$SST\text{:}\ \frac{k_L a_{Exp.}}{a^1_{Sim.}} \propto \varepsilon^{0.31}_{Sim,Volume\ Ave.} \qquad R^2 \approx 0.98 \tag{114}$$

$$k-\varepsilon\text{:}\ \frac{k_L a_{Exp.}}{a^1_{Sim.}} \propto \varepsilon^{0.35}_{Sim.Volume\ Ave} \qquad R^2 \approx 0.95 \tag{115}$$

The results of performing the same operation with equation 95 are shown in equation 116 and 117, where the exponents of the specific interfacial areas are not one as expected from theory. The results are nevertheless much more correct than the corresponding outcome for the microbioreactor displayed in equation 104. It is nevertheless important to remember that only three different rotational speeds were investigated for the magnetically stirred reactor, which makes data fitting both easier and less reliable. For example, if only two data points were

available it would be possible to find a perfect power law correlation between them, even if a power law would not be a suitable model to describe the data.

$$SST: \frac{k_L a_{Exp.}}{\varepsilon_{Sim,Volume\ Ave.}^{0.25}} \propto a_{Sim.}^{1.71} \qquad R^2 \approx 0.98 \tag{116}$$

$$k-\varepsilon: \frac{k_L a_{Exp.}}{\varepsilon_{Sim,Volume\ Ave.}^{0.25}} \propto a_{Sim.}^{3.48} \qquad R^2 \approx 0.81 \tag{117}$$

4.2.4.4. Correlation studies between experimental and simulated k_La

The experimental and simulated k_La data are plotted in Figure 93 for the SST model and in Figure 94 for the k-ε model. The proportionality constants for the volume-averaged k_La values are 0.1112 for the SST model and 0.1087 for k-ε. These are close to each other and also relatively similar to the corresponding value for the microbioreactor, i.e. 0.1304, presented in Figure 64.

The correlation constants for the surface averaged and liquid maximum values for the magnetically stirred reactor are in the approximate range 0.04-0.07. All correlation constants found in this project are therefore slightly smaller than those found in the literature. In order to achieve higher proportionality constants, the simulated values of k_La would have to be lower, assuming the experimental values and the eddy cell model are correct. If these are correct, it means that the simulations over-predict either the specific interfacial areas or the energy dissipation rates. Considering the appearance of the interfaces for the magnetically stirred reactor there is not much room for over-prediction. It is more reasonable that the energy dissipation rates were exaggerated since turbulence models were applied on flows which were not fully turbulent according to their Reynolds numbers.

Another explanation is that the eddy cell model or the underlying assumptions are not valid for the flow in the investigated cases. This must be considered a reasonable explanation, since the derivation in Lamont and Scott (1970) for example assumes two-dimensional flow and a fully developed turbulent field. Few sources in the literature have however been found which discuss the theory behind the model. The model is however questioned in Hung, Garbe, and Tsai (2010) for the application of mass transfer modelling at an air-sea interface. To determine if the arguments in Hung, Garbe, and Tsai (2010) are valid or not is however very difficult without a deep understanding of theoretical fluid dynamics and mathematics, and the same is true for the details in Lamont and Scott (1970). It must however be considered constructive for the field with a theoretical discussion about the basis of the model. This is especially important since Lamont and Scott (1970) are very modest about the model in their discussion, where it for example is stated that it is uncertain for which situations the model is applicable.

Despite this the data in Figure 93 and Figure 94 is correlated to their respective proportionality constants and the results are displayed in Figure 95. The data in the figure is very well fitted for the averaged and maximum values. It is not as good for the surface averaged value, which can even be considered an advantage of the model since these values also performed poor in equation 110 and 111. If these poor values resulted in simulated data close to the experimental values the credibility of the model should be questioned.

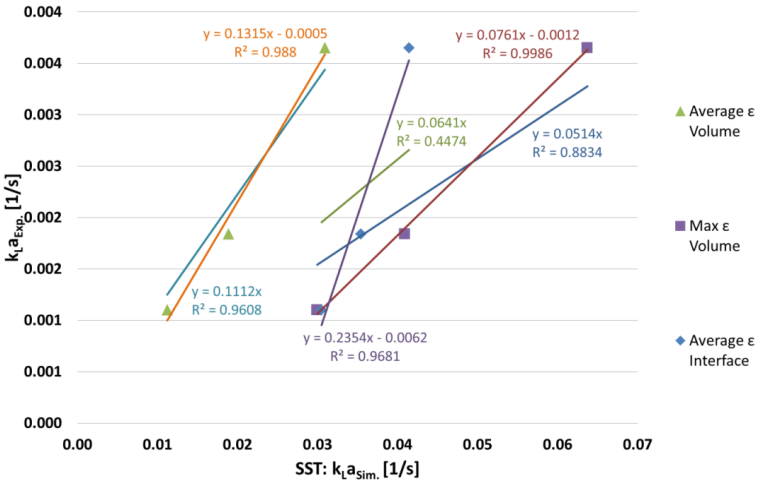

Figure 93. The simulated k_La data based on the liquid and surface averaged as well as the maximum ε plotted against the experimental values for the SST model. The linear trend lines and the corresponding equations are also displayed.

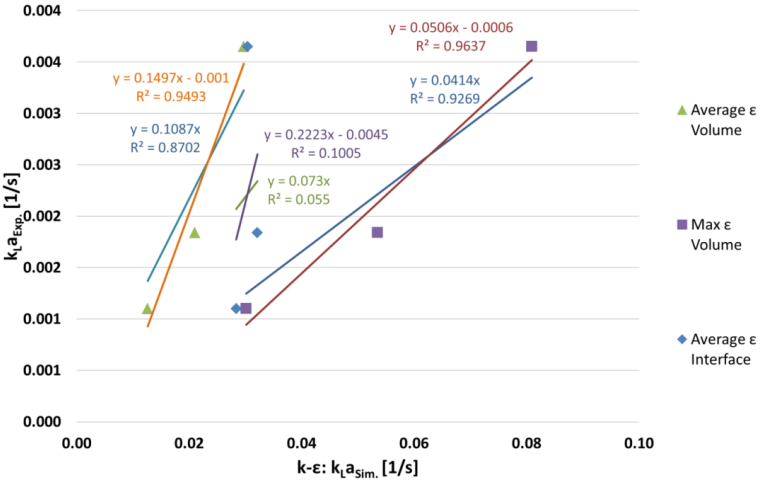

Figure 94. The simulated k_La data based on the liquid and surface averaged as well as the maximum ε plotted against the experimental values for the k-ε model. The linear trend lines and the corresponding equations are also displayed.

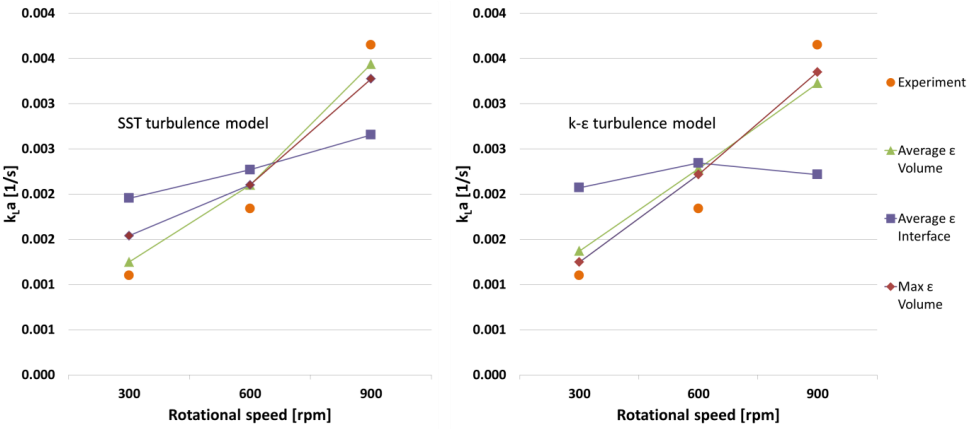

Figure 95. The experimental and simulated volume averaged and maximum $k_L a$ values plotted together for the SST (left) and the k-ε (right) model. The data sets are correlated with their respective proportionality constants from Figure 93 and Figure 94.

4.3. The pilot plant reactor

4.3.1. Reynolds number and the choice of turbulence model

The impeller Reynolds numbers for the liquid phase in the pilot plant reactor are displayed in Table 26. The values show that the flows are undoubtedly in the turbulent flow regime.

Table 26. The Reynolds numbers for the pilot plant reactor.

	174 rpm	230 rpm	286 rpm
Water	292 412	386 521	480 630

The fully turbulent flow implies that the k-ε turbulence model would be appropriate, but it was decided again to use also the SST model and compare the results for the two turbulence models. The reason for this is that the SST model appears to be the new industry standard for turbulence modelling while the k-ε model is the old standard according to LEAP CFD Team (2012). ANSYS Inc. states also that the SST model is the new industry standard two-equation model for separated flows (ANSYS Inc. (2011)).

For the one-phase simulations, the SST model had no convergence difficulties while the k-ε solutions oscillated slightly. For the two-phase simulations only the SST model was evaluated with the motivation that the differences between the results obtained with both approaches in the one-phase simulations was very small. The majority of the two-phase simulations converged well, but for the least stirred and most aerated simulation, i.e. the 174 rpm and 500 L/min, the solution was too unstable and thereby not considered to be converged. The simulations with a bubble diameter of 16 mm had also convergence difficulties. This was however not considered a shortcoming of the turbulence model.

4.3.2. One-phase steady-state results for the pilot plant reactor

4.3.2.1. Velocity profiles for one-phase flow and the SST and k-ε turbulence model

An overview of the velocity profiles for the one-phase flow in the pilot plant reactor is presented in Figure 96. The flow results displayed in the figure was calculated with the original mesh, 286 rpm and the SST model, but the velocity vectors for 174 and 230 rpm appeared very similar. In Figure 96 the velocity vectors are shown at the rotational symmetry planes and at the perpendicular plane. It displays the existence of one upper and one lower re-circulation zone.

The flow pattern is initiated by the rotational motion of the impeller that pushes the liquid outwards to the cylindrical wall where it is forced to move either upwards or downwards. New liquid is therefore drawn into the impeller which occurs from both above and underneath. This is very similar to the flow pattern presented for the magnetically stirred reactor in Figure 79 and Figure 80, but in this case new liquid can only approach the magnet from above due to its positioning at the reactor bottom.

After splitting at the outer cylindrical wall, the liquid streams follow the outer walls upwards or downwards until reaching either the top or the bottom wall. There they are re-directed into the centre of the reactor, and eventually back towards the impeller.

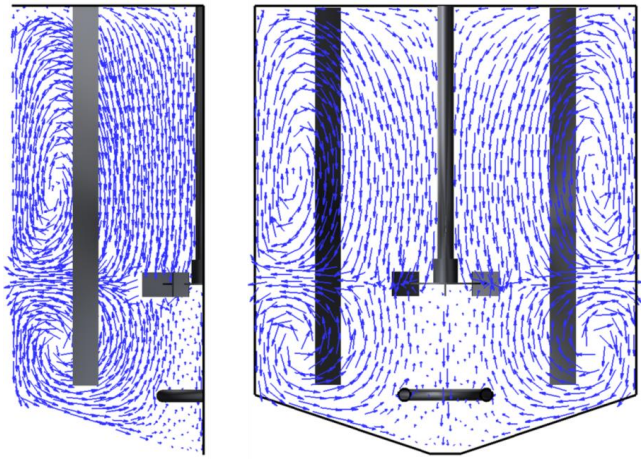

Figure 96. The velocity vectors in the pilot plant reactor obtained for two perpendicular planes.

Figure 97 shows the axial, radial and circumferential velocities for all investigated rotational speeds using the SST turbulence model and the original mesh. The colour legends are scaled with the rotational speeds, and the similarities between the cases indicate therefore that the magnitudes of the flow velocities are also scaled with the rotational speeds.

The flow pattern discussed above can also be recognized in Figure 97, where it can be seen that the radial velocities are considerably larger and positive close to the impeller. It is also shown that the highest radial velocities are centralized to a very thin region around the impellers compared to the negative radial velocities in the top and the bottom, which are spread over a larger region. It can also be seen that there are two large regions in between the impeller and the top and between the impeller and the bottom where the radial velocities are relatively low.

The axial velocities in Figure 97 show that the highest negative and positive magnitudes occur at the walls just above or underneath the region where the liquids from the impellers are directed. This is a reasonable result since all momentum contained in the radial velocities needs to be transferred into axial or circumferential velocities in this region unless it is transformed into turbulent kinetic energy. The regions of where the fluids are transported back to the impeller can also be detected in Figure 97 as negative and positive axial velocities above or underneath it.

The circumferential velocities in Figure 97 are highest around the impeller and it is observed that the circumferential velocities are relatively low in the remaining parts of the reactor. This behaviour is caused by the baffles and without them, the circumferential velocities should be similar to the flow in the magnetically stirred reactor in Figure 79 and Figure 80.

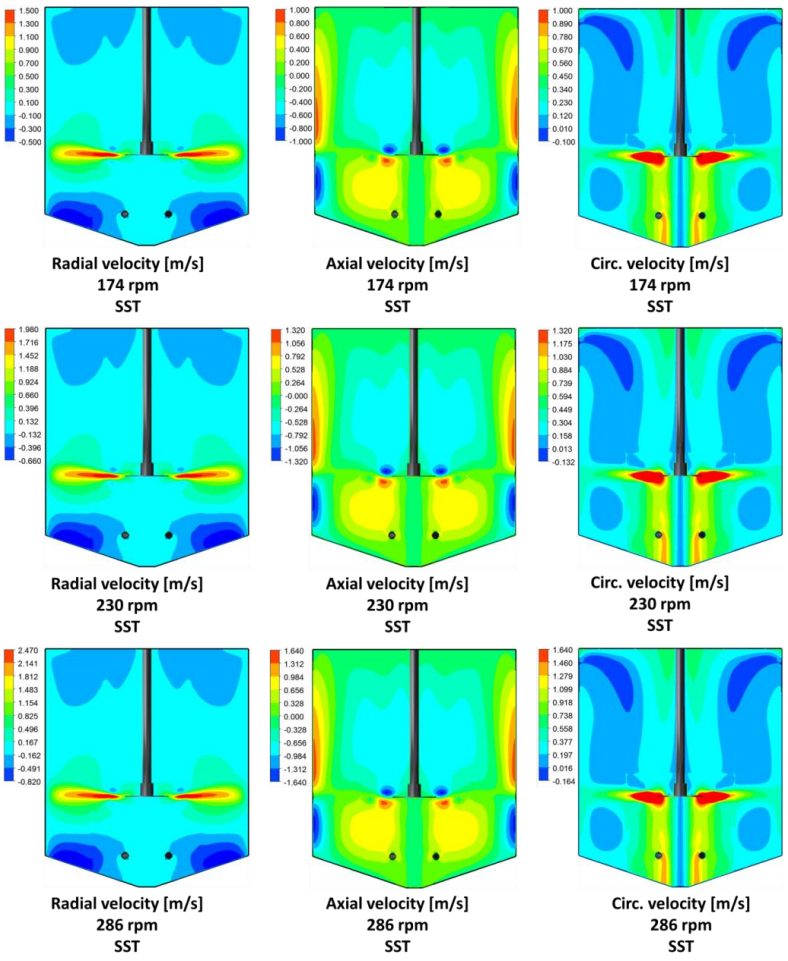

Figure 97. The radial, axial and circumferential velocity contour plots for the SST model for the original mesh. The maximum and minimum values are scaled with the rotational speed between the different cases.

The plots shown in Figure 98 and Figure 99 illustrate the differences between the rotational speeds for 174 and 286 rpm and the used two meshes. Figure 98 shows the axial velocities at the vertical line in Figure 33 and Figure 99 the circumferential velocities at the same location. Figure 98 and Figure 99 confirm what is described previously about the magnitudes of the velocities, i.e. that they are similar but scaled with each other for the different rotational speeds. They also suggest that the differences between the SST and the k-ε turbulence models are generally small for the pilot plant reactor.

Figure 98 shows furthermore that the velocities at the line are moving downwards above the impeller and upwards underneath it, which is as expected based on the previous discussion of the flow pattern. In Figure 99 it can also be seen that the circumferential velocities underneath the impeller are higher than above it, and that the velocity peaks closest to the impellers seems to be equally large for both meshes. Again, it is observed in Figure 99 that

the circumferential velocities are most concentrated in the regions around the impeller and that they are not as large in the rest of the reactor. The figure also confirms that the circumferential velocities are lower above the impeller than underneath it. This is reasonable since the baffles do not reach down to the bottom of the reactor, i.e. they are not present in the entire bottom region.

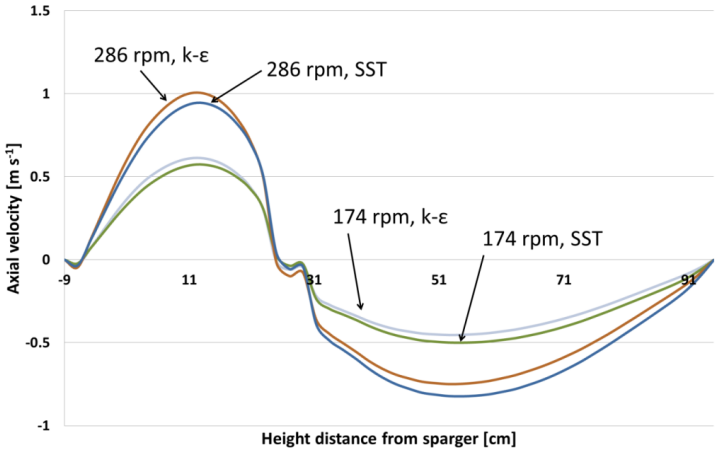

Figure 98. The axial velocities for the horizontal line in Figure 33 for 174 and 286 rpm and for the SST and k-ε turbulence models.

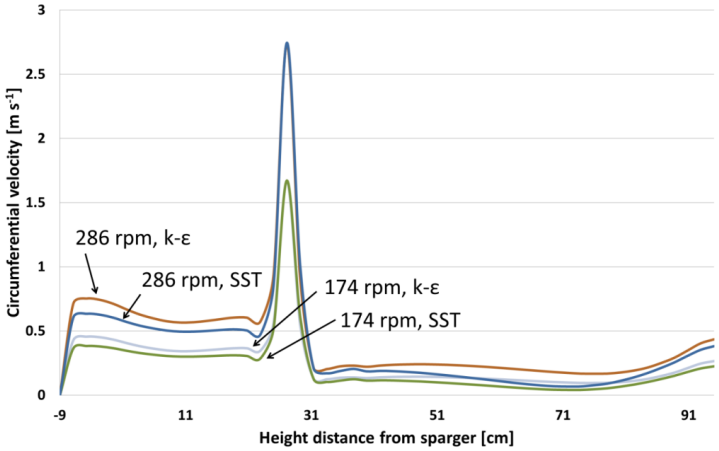

Figure 99. The circumferential velocities at the vertical line in Figure 33 for 174 and 286 rpm and for the SST and k-ε turbulence models.

Figure 100 illustrates yet another way to visualize the flow pattern from the pilot plant reactor. It shows 25 streamlines randomly initiated from four different planes, which are indicated as grey in the figure. The colours of the legends indicate the time. This means that all of the 25 streamlines initiated at Plane 1 and Plane 2, i.e. in the lower part of the reactor, stay in this region for at least 20 seconds. The figure also shows the same trend for the streamlines initiated in the top of the domain, i.e. that the streamlines initiated in the top region also stay there.

The streamlines indicate therefore the presence of two zones, one upper and one lower, with little exchange of fluid between them.

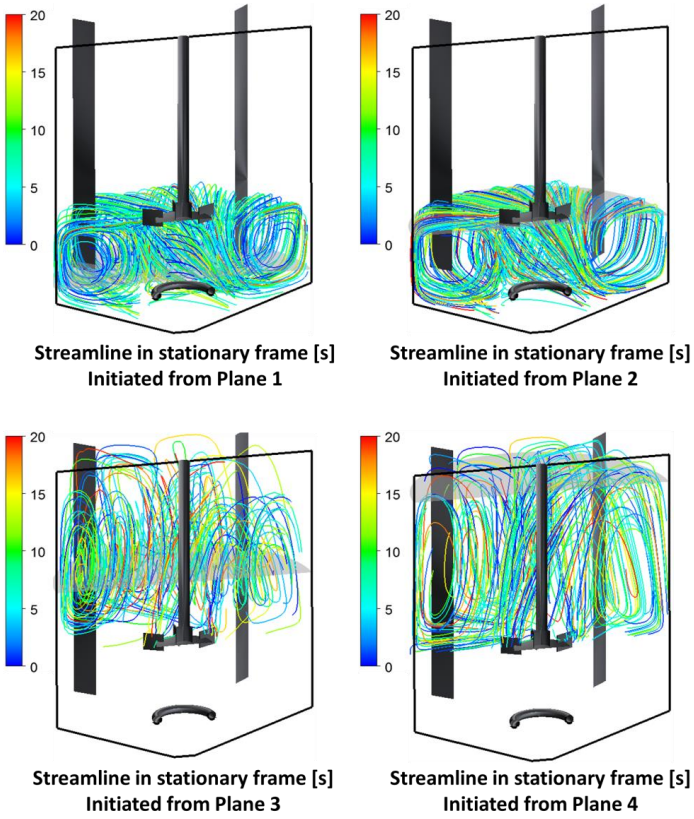

Figure 100. The streamlines initiated at four different planes in the pilot plant reactor.

4.3.2.2. Eddy viscosity profiles for one-phase flow and the SST and k-ε turbulence model

Since the velocity profiles for the SST and the k-ε model appeared very similar in the pilot plant reactor, it was suspected that the eddy viscosity profiles for the two turbulence models would be reasonably similar as well. The eddy viscosities at the horizontal line in Figure 33 are presented in Figure 101 for 286 rpm and the two turbulence models and meshes. The corresponding values at the vertical line are displayed in Figure 102.

The eddy viscosities are very similar between the two turbulence models, especially compared with the eddy viscosity values produced in the magnetically stirred reactor presented in Figure 81, or more extreme compared with the microbioreactor where eddy viscosities approached zero for the SST model. The eddy viscosities presented in Figure 101 and Figure 102 are also around 1000 times larger than the dynamic viscosity, which according to ANSYS® Academic Research (2013) suggests fully turbulent flow.

The eddy viscosity values at the walls in Figure 101 are all dissimilar from each other. This outcome is different from the microbioreactor and magnetically stirred reactor case studies where the eddy viscosities were exactly $4.04 \cdot 10^{-3}$ kg m^{-1} s^{-1} at the walls using the k-ε model. For these cases, it was explained with the y^+ values smaller than 11.06, which were then rounded up to 11.06. The varying wall bound eddy viscosity values in the pilot plant reactor suggest therefore y^+ values larger than 11.06.

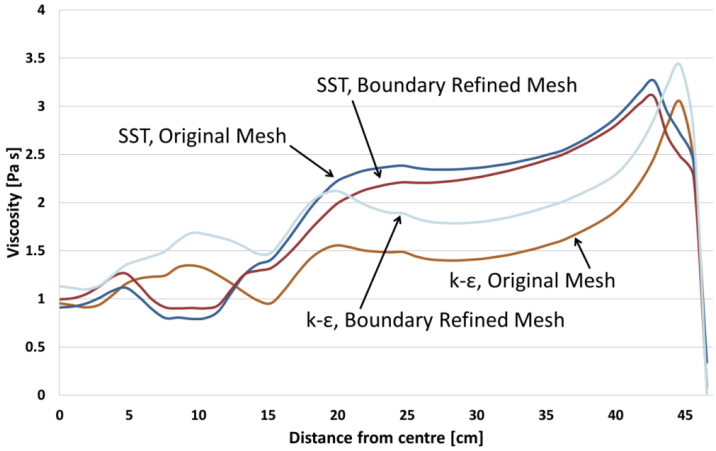

Figure 101. The eddy viscosities at the horizontal line in Figure 33 for 174 and 286 rpm and for the SST and k-ε turbulence models.

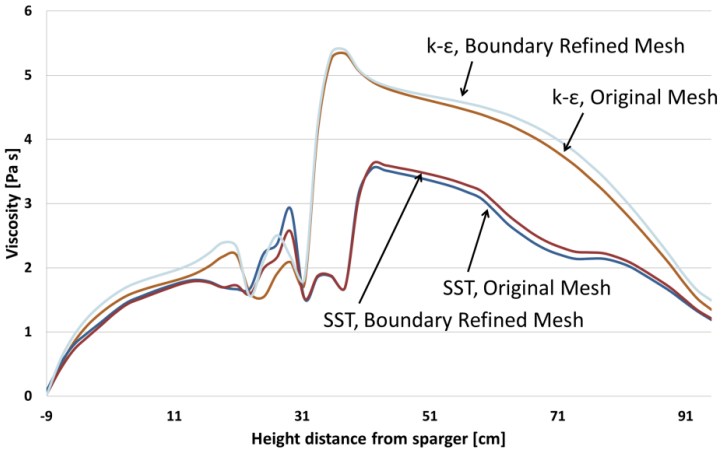

Figure 102. The eddy viscosities at the vertical line in Figure 33 for 174 and 286 rpm and for the SST and k-ε turbulence models.

There are however differences in the eddy viscosities between the SST and the k-ε model. For example, the eddy viscosities in the upper part of the reactor are higher for the k-ε model (Figure 102), while the SST model seems to result in higher eddy viscosities in the region around the impeller (Figure 101).

These observations are all confirmed in Figure 103, which visualises the eddy viscosities at the symmetry planes for both turbulence models and meshes. The advantage with a figure such as Figure 103 is that general trends can be seen that can be hard to detected in plots like Figure 101 and Figure 102. Curve plots can however detect details that contour plots cannot, for example trends in the behaviour close to walls, and they are also useful for comparing many different cases in the same figure.

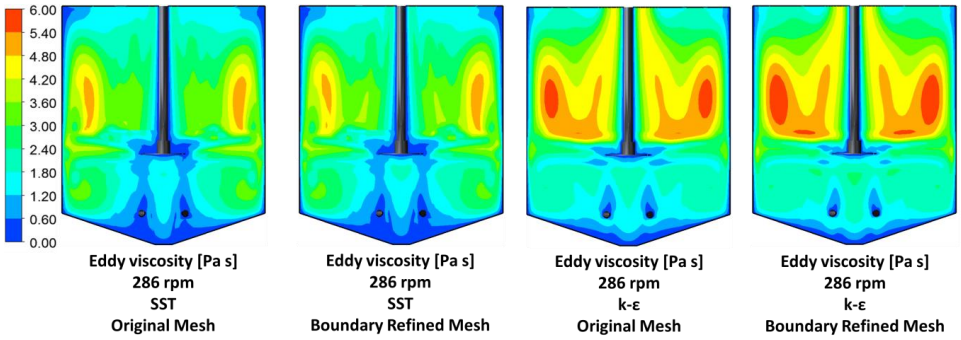

Figure 103. The contour plots of the eddy viscosity in the pilot plant reactor for the one-phase flow.

4.3.2.3. Investigation of the y^+ and the F_1 values for one-phase flow

In the previous section it was discussed that the y^+ values must be higher than 11.06 at the walls intersecting with the horizontal and vertical lines in Figure 33. Figure 104 shows the contour plots of y^+ for the SST turbulence model, 286 rpm and the boundary refined mesh. The contours are very similar for the k-ε model, and the original mesh (not shown) resulted in even higher y^+ values. All y^+ values were therefore higher than 11.06 for 286 rpm which means that the automatic wall function (associated with the SST model) never had to consider laminar boundary conditions, and that the scalable wall function (for the k-ε model) could use the calculated y^+ values directly without artificially increasing them to 11.06. The eddy viscosity differences between the turbulence models were therefore assumed more dependent on the behaviour of the bulk fluid than on the response of the turbulence models at the walls.

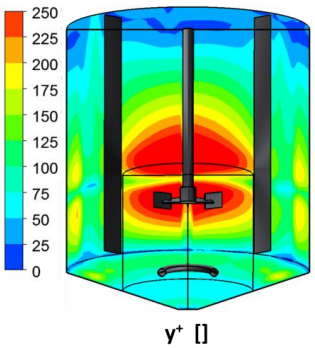

Figure 104. The contour plots of the y^+ values in the pilot plant reactor for the boundary refined mesh, the SST turbulence model and 286 rpm.

The behaviour of the SST model in the bulk fluid is partly a function of the blending factor F_1 as explained in section 2.2.5.5. If the blending function is close to unity it means for example that the parameters in the SST equation for ω are most similar to their corresponding value in the k-ω model, and if F_1 is closer to zero it means that the parameter values are more similar to those used in the k-ε model.

The F_1 values for the original mesh are visualised in Figure 105 where it is shown that the values are close to unity in the majority of the regions. The figure also reveals that the formula for calculating F_1 values is very complex and not only a function of the distance to the closest wall. If it was only dependent on the distance to the closest wall contours in the top of the reactor would for example appear differently. Understanding the F_1 formula was however considered beyond the objective of this project, but visualising the results is nevertheless interesting. For instance, it can be concluded from Figure 105 that most of the fluid was located in regions where the parameters in the ω-equation were more influenced by the k-ω model than they were by the k-ε model. This explains why the eddy viscosity distributions were different between the two turbulence models.

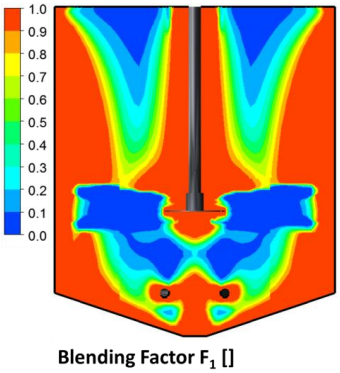

Figure 105. The F_1 values in the pilot plant reactor for 286 rpm and the original mesh.

4.3.2.4. Distribution of turbulent energy dissipation for one-phase flow and the SST and k-ε turbulence model

The distribution of turbulent energy dissipation (ε) in a reactor is as mentioned previously very important if the eddy cell model is applied for modelling of the oxygen transfer rates. The energy dissipation rates were therefore investigated also for the pilot plant reactor, and the outcomes are discussed in this section.

The energy dissipation rates at the horizontal line in Figure 33 are displayed in Figure 106 for the two meshes and turbulence models evaluated at 286 rpm. As displayed the magnitudes and patterns are very similar in all four cases.

Figure 106 shows that the values of ε are increasing towards the wall located around 46.5 cm from the centre of the reactor. This increase could either be the result of very high values of ε calculated by the wall functions, or by a large bulk production triggered by high velocity gradients. Large velocity gradients in this region are both expected and visualized in Figure 97.

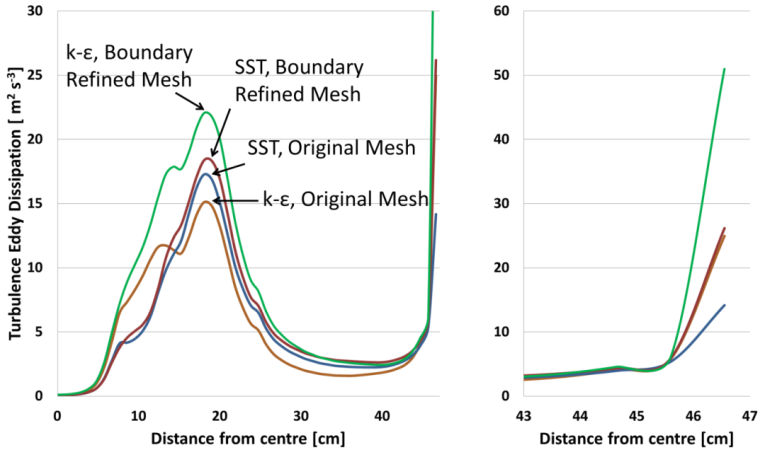

Figure 106. The turbulent energy dissipation rates for the horizontal line in Figure 33 for 174 and 286 rpm and for the SST and k-ε turbulence models. The figure to the right is a zoom-in for the picture to the left to show the details at the static wall.

The averaged and the maximum values of ε for the different rotational speeds and meshes are shown in Figure 107. A trend in the figure is that higher rotational speeds result in higher averaged energy dissipation rates. This is reasonable since a higher averaged value of ε also should correspond to a higher total energy input. There is also a weaker trend in Figure 107 suggesting that the original mesh results in slightly lower averages than the boundary refined meshes. One possible explanation for this is that a finer mesh structure resolves finer flow structures and consequently increases the velocity gradients and subsequently the turbulent production term.

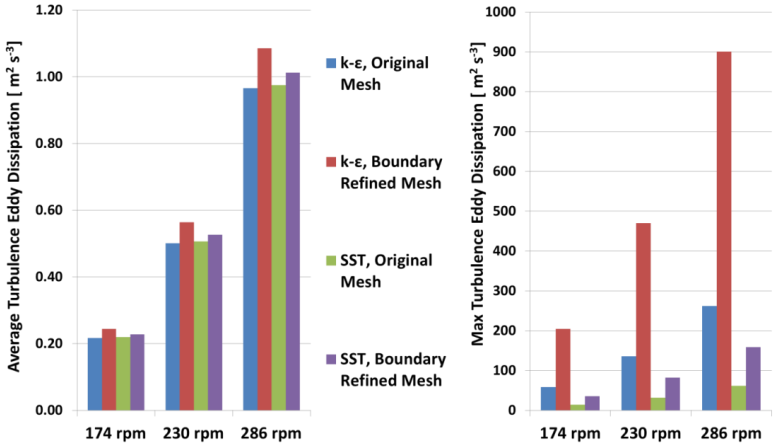

Figure 107. The averaged (left) and maximum (right) values of the turbulence eddy dissipation rate for the SST and k-ε model in combination with the original and boundary refined mesh.

Another important observation in Figure 107 is that the k-ε and the SST model display very similar averaged values, which suggests that the choice of the turbulence model is not very critical in this case study. The differences between the two turbulence models are however much more evident considering the maximum values, where the k-ε model predicts the

highest. The maximum values also appear to be more mesh sensitive since the boundary refined mesh results in significantly higher values of ε. This leads to the conclusion that the maximum values of ε are neither turbulence model nor mesh independent.

To investigate where the highest values of ε are created in the domains, and in order to gain a general understanding of the distribution Figure 108 is provided. Figure 108 reveals that the distributions of ε do not vary significantly between the different meshes and turbulence models which is again the opposite of the result from the magnetically stirred reactor in Figure 86. Figure 108 also confirms that most of the energy is dissipated around the impeller blades and in the region where the fluid hits the wall. It also shows that there are large regions above the impeller with very low energy dissipation rates.

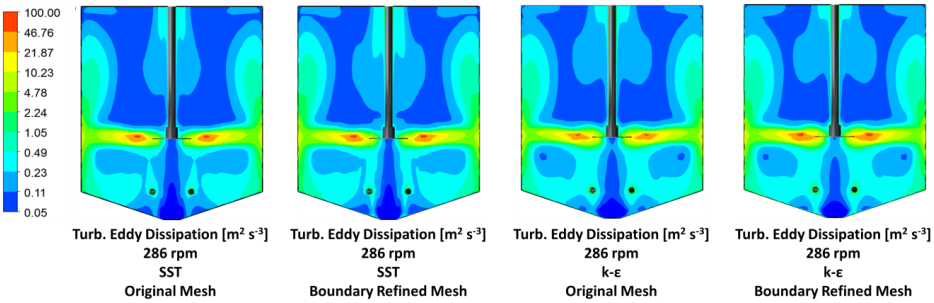

Figure 108. The contour plots of the turbulence eddy dissipation rates in the pilot plant reactor for the one-phase flow.

4.3.3. Two-phase steady-state results for the pilot plant reactor

4.3.3.1. Gas phase distributions in the reactor

Before examining the impacts of aeration (i.e. the introduction of two-phase flow) on the velocities and energy dissipation rates in the pilot plant reactor the distribution of air in it will be investigated for the varying rotational speeds and airflow rates. The air volume fractions for the different cases are therefore presented in Figure 109 where the colouring scheme is explained in the caption. The simulation with 174 rpm and the aeration rate 500 L/min did not converge properly, meaning that the monitoring points oscillated in an irregular manner, but its results are nevertheless displayed.

The trends in Figure 109 are similar to those described for a radial flow impeller for example in Kadic and Heindel (2014). Kadic and Heindel (2014) also report about the five flow regimes identified for this kind of system by Nienow, Wisdom, and Middleton (1977) and the gas holdups in Figure 109 are also consistent with some of these. Flooding phenomena, i.e. when little gas is dispersed in the lower re-circulation zone, are for example observed in Figure 109 when the aeration rates are too high in relation to the stirring. The general gas holdup pattern in Figure 109 is also similar to the pattern achieved by others e.g.Wang, Mao, and Yang (2006).

Several important and interesting conclusions can be made based on Figure 109. First of all the two re-circulation zones mentioned in section 4.3.2.1 are visible for 230 and 286 rpm since they have resulted in two toroid (doughnut) shaped regions of higher air volume fractions.

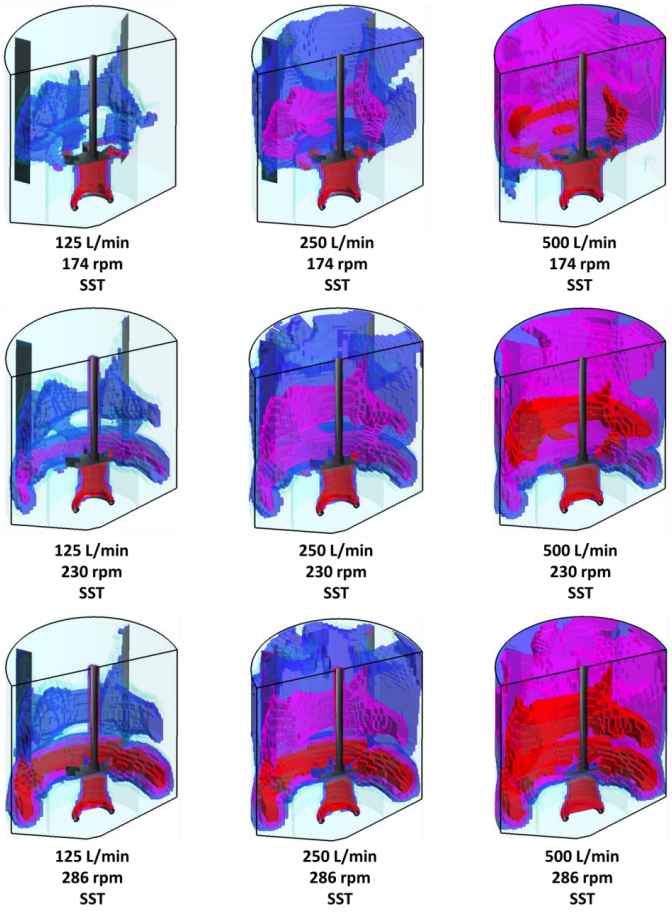

Figure 109. The distribution of the air volume fractions for the different agitation and aeration speeds for the SST turbulence model and the original mesh. Red regions have volume fractions of air larger than 0.1, purple larger than 0.05 and blue larger than 0.025. Regions with air volume fractions smaller than 0.025 are visualised as turquoise.

The 174 rpm simulations have no air volume fractions higher than 0.025 in their lower re-circulation zones. Air volume fractions larger than 0.025 under the impeller are only present around the sparger, but very little of this air phase is transported downwards again under the discharge zones. This is therefore an example of flooding of the reactor.

The air phase introduced by the sparger rises towards the top of the reactor but is hindered by the horizontal part of the impeller, i.e. the holder of the impeller blades. Very high gas volume fractions are therefore accumulated in this region in the simulations. This phenomenon however is most likely exaggerated in the simulations since perfect rotational symmetry is assumed and since the sparging is performed slightly different in the simulation compared with the experimental setup.

In the physical bioreactor the gas phase is introduced to the system via relatively small holes placed at the side of the sparger, which creates bubbles and instabilities in the system

instantaneously. In the simulations on the other hand larger inlets are created in which the gas volume fraction is set to one. This is because no liquid can be introduced in the simulation without also assigning it an outlet.

The gas holdup fractions for the cases in Figure 109 are displayed in Figure 110. The trends are same as discussed above, i.e. that higher rotational speeds and air flow rates increase the gas holdup in the reactor. The impact of the mesh on the gas holdup is show in Figure 11 for the most extreme cases, i.e. the highest and lowest rotational speeds in combination with the highest and lowest aeration rates. No significant difference is however seen between the two meshes.

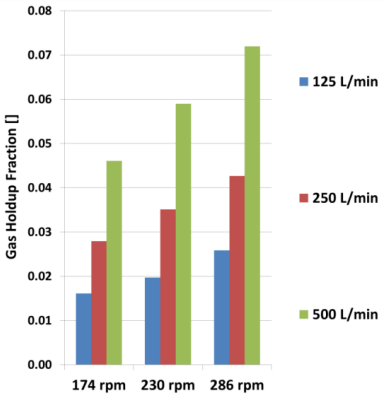

Figure 110. The gas holdup values for the different agitation and aeration rates simulated with the original mesh.

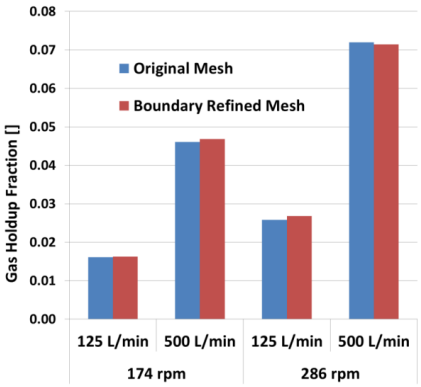

Figure 111. Comparison of the gas holdup values between the original and the boundary refined mesh.

The total volumes of liquid in the different simulated systems are displayed in Figure 112. At first varying liquid volumes in a simulation can appear strange when no liquid phase outlet is defined, but varying liquid volumes is an absolute requirement in order to simulate different gas holdups. The solver has also no defined constraint that the liquid volume should be constant over the course of the simulation, it only has the constraint (equation 48) that the volume fractions must sum up to unity in each node.

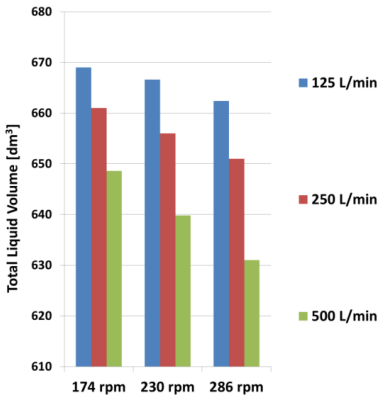

Figure 112. The liquid volumes in the simulations for different rotational speeds and aeration rates.

The average specific interfacial areas are shown in Figure 113 and have the same relative differences as the data presented in Figure 110. It is nevertheless important to show the specific interfacial areas individually since they are a function of both the air volume fractions in the individual nodes and the user defined bubble diameter.

The specific interfacial areas were calculated using both the formula used by ANSYS CFX 15.0 for the calculation of the drag force etc. (i.e. equation 56 in combination with equation 57) and the theoretical formula for the specific interfacial area (i.e. equation 56 only). The resulting specific interfacial areas are however very similar.

The average specific interfacial areas can also be compared with the previous case studies. They are considerably lower for the pilot plant reactor than for the microbioreactor where they were in the range 161-507 m^{-1}. For the magnetically stirred reactor the averaged specific interfacial areas were around 40 m^{-1}, i.e. slightly closer to the values in Figure 113. It is however important to remember that the averaged values are calculated in Figure 113 and that both considerably lower and higher values were present.

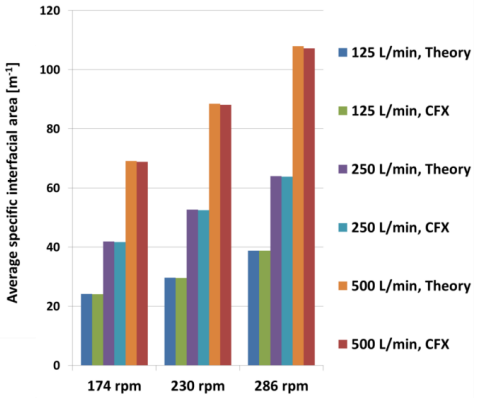

Figure 113. The averaged specific interfacial areas for the different rotational speeds and aeration rates using the two different formula *Theory* from equation 56 and *CFX* from equation 57.

4.3.3.2. Impact of air bubble size on the gas phase distributions

In the simulations presented above all gas bubble diameters were set to 4 mm. Variations of this user defined diameter were however simulated and the results for the 1, 2, and 8 mm bubble diameters are presented in Figure 114 for the rotational speed 286 rpm. The bubble diameter 16 mm was also evaluated for 286 rpm but did not converge.

The colouring scheme in Figure 114 is the same as in Figure 109, but orange volumes are also added to highlight regions with air volume fractions larger than 0.25. The orange volume at the top of the 8 mm bubble diameter reactor highlights also a shortcoming of the used top boundary condition, i.e. that it does not always seem to act as an opening for the gas phase. Exactly what went wrong could however not be investigated since the manual only states in words that the degassing boundary condition acts as an opening for the dispersed phase and as a free-slip wall for the continuous phase (ANSYS® Academic Research (2013)). This also highlights one of the disadvantages with using commercial software with a non-accessible code, i.e. that it is very difficult to troubleshoot cases where unexpected phenomena occur and occasionally also to find information about what is happening inside of the software. The

phenomena with very high gas volume fractions on the top of a similar rector is also seen in, but not discussed, in Jahoda, Tomášková, and Moštěk (2009).

Despite the obvious error at the top of the 8 mm simulation Figure 114 shows that air volume fractions higher than 0.25 are present only around the sparger for the 4 and 8 mm bubbles and also in the lower re-circulation loops for the 1 and 2 mm bubbles.

Figure 115 shows the same phenomena as Figure 114 but for 174 rpm and the aeration rate 125 L/min, i.e. for the lowest rotational speed and the lowest aeration rate investigated. A clear trend in Figure 114 and Figure 115 is that the smaller the bubble diameter the higher are the air-phase volume fractions. This means that the user defined bubble diameter is a very important parameter in the simulations. The main explanation for this is that smaller bubble diameters increase the specific interfacial areas, and larger specific interfacial areas mean that the drag coefficient between the two phases becomes bigger. The drag coefficient is responsible for the transfer of momentum between the phases, and a large momentum transfer between the phases decreases the dissimilarities between them. This means that small bubbles have larger tendencies to follow the liquid streams, while larger bubbles are less affected by the liquid velocities and therefore more prone to rise towards the top interface.

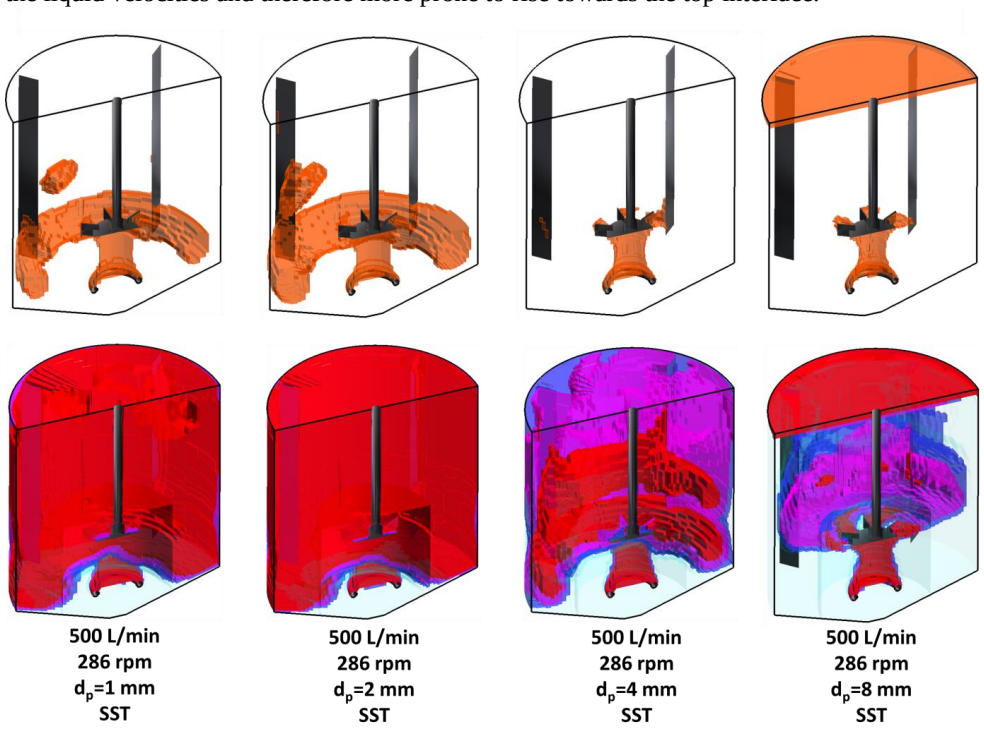

Figure 114. The distribution of air volume fraction for 286 rpm and 500 L/min for the SST turbulence model and the original mesh. In the top row the orange region volumes highlight air volume fractions larger than 0.25. Red regions have volume fractions of air larger than 0.1, purple larger than 0.05 and blue larger than 0.025. Regions with air volume fractions smaller than 0.025 are visualised as turquoise.

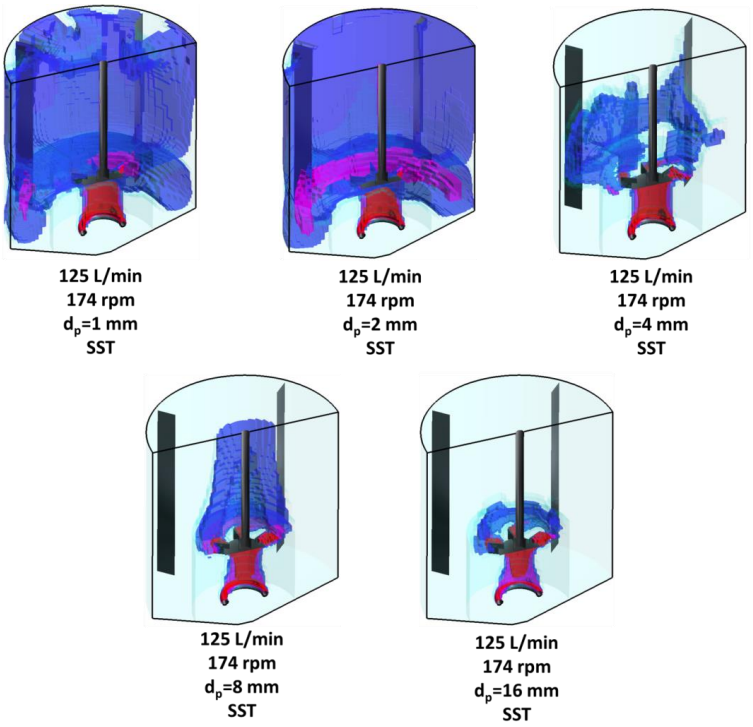

Figure 115. The distribution of air volume fractions for 174 rpm and 125 L/min for the SST turbulence model and the original mesh. The colouring scheme for the volumes is the same as in Figure 114.

The gas-holdups from Figure 114 and Figure 115 are summarized in Figure 116 where it is once again shown that the user defined bubble diameter has a very large impact on the gas holdup. This is however not necessarily a disadvantage since it for example opens up for the possibility to determine the correct bubble diameter or drag model based on experimental measurements of the gas holdup. It is also advantageous that the model simulates different gas-holdups for different bubble diameters since that is the expected behaviour of the experimental system. However, in reality a wide range of bubble diameters exist in the flow and ANSYS CFX 15.0 offers possibilities to model this including breakup and coalescence phenomena between the bubbles. These options have however not been considered within this project but are left for future work.

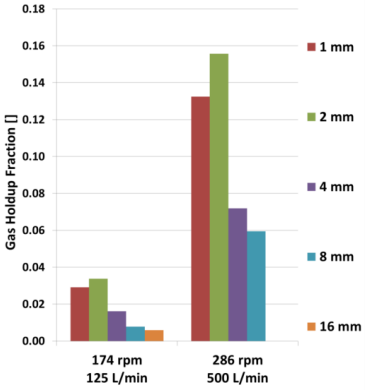

Figure 116. Comparison of the gas holdup values for varying bubble size diameters, the SST model and the original mesh.

In Figure 117 the specific interfacial areas are calculated based on the air volume fractions in the simulations and the user defined bubble diameters. It can be seen that the user defined bubble diameters have a much larger impact on the specific interfacial area than they have on the gas holdup. This is because the specific interfacial area is calculated as a function of both the air volume fraction in a node, which is dependent on the defined diameter and also directly proportional to the inverse diameter.

This is very important information to consider when modelling oxygen transfer in dispersed flows, especially since the specific interfacial area is one of two parameters applied in the calculations of the oxygen transfer rates $k_L a$.

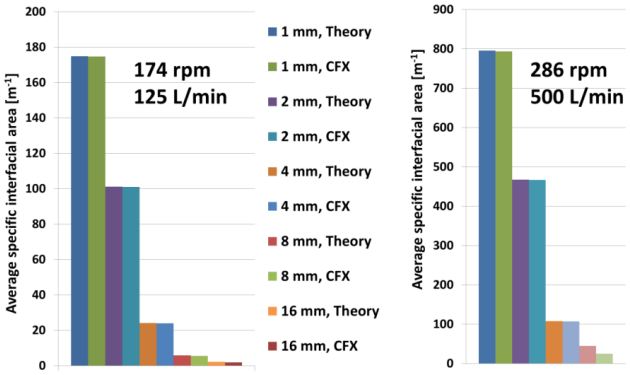

Figure 117. The averaged specific interfacial areas for varying bubble size diameters, the SST model and the original mesh. The data is calculated using the CFX formula, i.e. equation 57.

4.3.3.3. Velocity profiles for two phase flow and the SST turbulence model

After presenting the air volume distributions in the two previous sections the effects on the velocity fields caused by the introduction of two-phase flow will now be discussed. The flow velocities of the liquid and gas phases for 286 rpm are therefore initially displayed in Figure 118. It can be seen that the liquid phase velocity field (blue) still has the same major

characteristics as it had for the one-phases simulations, i.e. that the velocity field is quite similar to the one presented in Figure 96. There are however differences, for example the velocities moving upwards along the walls are bound to the walls for a longer distance in the single-phase flow. The figure also shows that the air phase velocities (red) are directed upwards leaving the domain through the top boundary wall.

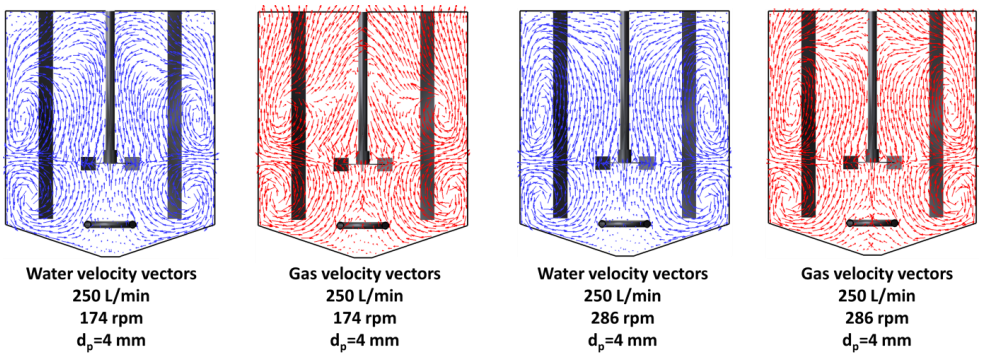

Figure 118. The velocity vectors for the liquid phase (blue) and for the air phase (red) for the aeration 250 L/min, the agitation 286 rpm, the SST model and the original mesh.

Figure 119 shows the liquid phase velocities for 286 rpm and the one-phase flow as well as the two-phase flows associated with the aeration rates 125, 250 and 500 L/min. The figure reveals that the liquid velocities in the radial and axial directions are more or less the same for all investigated aeration rates. The positive and negative axial velocities along the outer walls are however strongest in the one-phase simulation and decreases with increasing aeration rates. The appearances of the radial velocities at the top of the reactor changes also slightly the more the system is aerated.

For the one-phase flow the negative radial velocities occur close to the top of the reactor, and for the 500 L/min aerated simulations this occurs further from the top and closer to the shaft. This tendency can also be seen when comparing the velocity vectors in Figure 118 to the ones in Figure 96.

The circumferential velocities in the most aerated system are also differing a bit from the other cases displayed but it should be noted that the 500 L/min and 286 rpm-simulation was not fully stable. The general conclusion from the comparison between the liquid phases must therefore be that there were no fundamental differences between the different aeration rates. Some of the mentioned diversities had however consequences for the mixing simulations, which are further discussed in section 4.3.5.

The conclusion above is however only based on the liquid phase flows. In order to investigate the velocities in the gas phase the gas and liquid streamlines for the most aerated and agitated two-phase simulation (i.e. 286 rpm, 500 L/min) are shown in Figure 120.

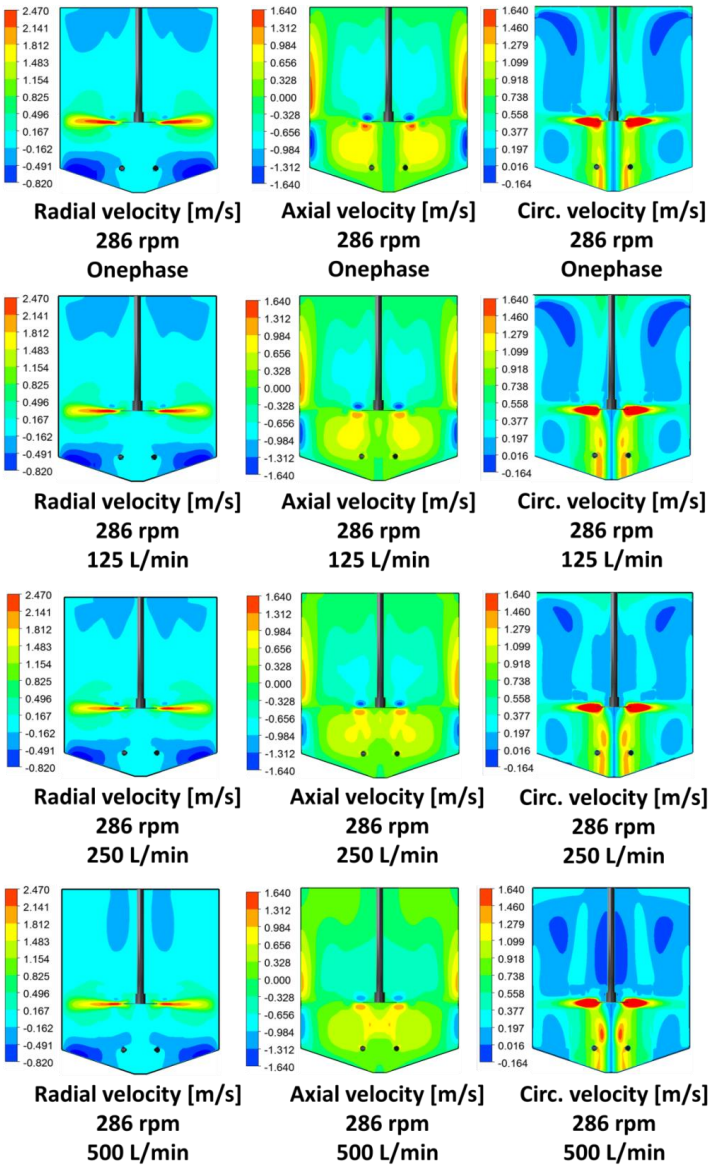

Figure 119. The radial, axial and circumferential velocities for 286 rpm, the SST model and varying aeration rates.

Comparing the liquid velocities in Figure 120 with their one-phase counterparts in Figure 100 it can be seen that the liquid streamlines released from Plane 2 are similar between the cases. The majority of the gas velocities released from Plane 2 are also retrieved in the lower re-circulation zone, but a few of them leave the zone immediately. For the velocity streamlines initiated at Plane 3 there are also differences between the one-and two-phase case. The two-phase streamlines do not seem to reach as high up in the reactor before turning downwards for example. This suggests that the liquids in the upper part of the aerated reactor are more stagnant compared to the velocities in the top of the one-phase reactor.

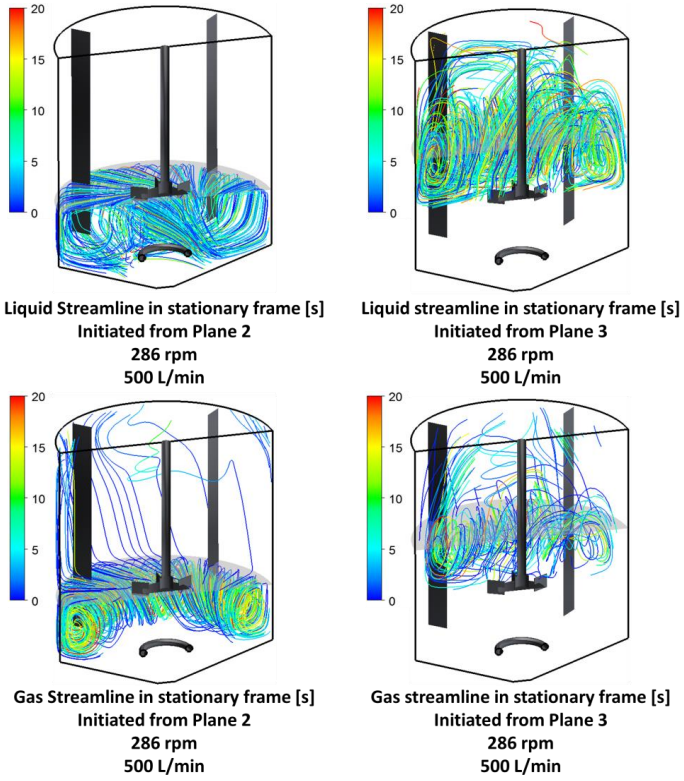

Figure 120. The gas and velocity streamlines in the 286 rpm, 500 L/min case with 4 mm large bubbles defined. The streamlines are initiated from two of the planes previously presented in Figure 100.

4.3.3.4. Impact of air bubble size on the velocity profiles

As discussed in section 4.3.3.2 the user defined bubble diameter has a large impact on the air distributions in the reactors, and it was therefore assumed that it would have an impact on the velocity fields as well. Figure 121 shows the gas velocity streamlines initiated from the two planes 'Plane 2' and 'Plane 3' for the rotational speed 286 rpm and the aeration rate 125 L/min. The planes are the same as those used in Figure 120, and in the figure the bubble diameter 4 mm is compared with the extreme cases 1 and 16 mm.

Figure 121 strongly confirms the impact of the user defined diameter on the gas velocity fields. The streamlines initiated from 'Plane 2' are for example kept in the lower re-circulation zone for all diameters but the 1 mm bubbles stay there much longer. This can be seen by the colour of the streamlines approaching the top boundary condition, which reveals how much time each streamline has spent in the re-circulation zone. Likewise it can be seen that the majority of the 16 mm bubbles leave the reactor fast. This is also a reasonable outcome considering Figure 115 which clearly shows that the 16 mm/174 rpm/125 L/min-case did not have any noticeable air volume fractions in the lower re-circulation zone.

A very similar trend is also revealed for the bubbles released from 'Plane 3', i.e. the smallest bubbles stay longer in the upper re-circulation zone while the largest aim straight for the top boundary without being noticeably affected by the velocity fields of the liquid phase.

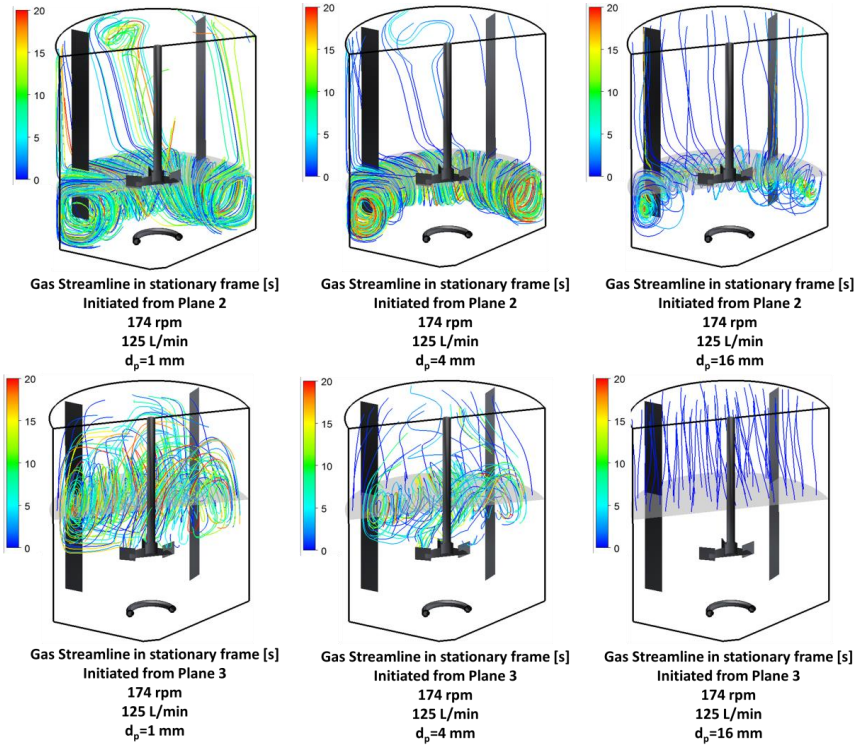

Figure 121. The gas phase streamlines initiated at two planes for the 1, 4, and 16 mm bubbles in the 174 rpm and 125 L/min simulations.

4.3.3.5. Energy dissipation rate profiles for two phase flow and the SST turbulence model

A correct estimation of the energy dissipation rates in a liquid is important if the eddy cell model is going to be used to calculate the oxygen transfer rates. In a larger system, it is also interesting for a correct estimation of the energy consumption of the motor since the turbulent energy dissipation rates and the power consumption of the motor are in theory directly correlated. All kinetic energy added to a fluid must namely be dissipated and this occurs when the kinetic energy of the smallest eddies in a turbulent flow is transformed to heat by the viscous forces. It must however be remembered that the quantities of ε are modelled in a CFD simulation, and that there is no inherited constraint in the software correlating the total sum of these to the torques around the impellers or similar.

The average turbulent energy dissipation rates in the liquid phase for all investigated rotational speeds and aeration rates (including the one-phase simulations) are summarized in Figure 122. The corresponding maximum values are displayed in Figure 123.

The trends in Figure 122 are the same as for the one-phase cases i.e. the higher the rotational speed the higher is also the average energy input in the fluid, as expected. The terms energy input and energy output can both be used here even if ε per definition describes the energy dissipation in a liquid, i.e. the transformation from kinetic to thermal energy. For a system at

steady-state, the energy input and output must however equalize which means that the terms occasionally are interchangeable.

It is also seen in Figure 122 that the average energy dissipation rates in the liquid are decreasing with increasing aeration rates. This phenomenon has been confirmed by others, i.e. Nienow (1998), and is caused by pockets of air created behind the impeller blades in an aerated system. These pockets decrease the power consumption compared with one-phase flows where vortexes instead occur in these regions as described in Nienow (1998). The pockets of air behind the impeller blades were also fully visible in the simulations of the pilot plant reactor, which adds credibility to the CFD model. Such air pockets have also been simulated by others, e.g. Deen, Solberg, and Hjertager (2002) and Scargiali et al. (2007).

The maximum values of the energy dissipation rates show however a different trend, i.e. that higher aeration rates also increase the maximum values of ε. When investigating exactly where these maximum values are located (data not shown) it could be seen that they appeared in the fluid closest to the impeller blades. The regions with the highest energy dissipation rates were however both small and isolated which again indicates that the maximum values should not be used as representative values for the entire domain.

The effects of the mesh on the averaged and maximum turbulent energy dissipation rates were also investigated (data not shown). It was observed that the mesh did not have any effect on the averaged values of ε, but that the refined mesh had much higher maximum values than the original mesh. These maximum values were also located adjacent to the impeller blades.

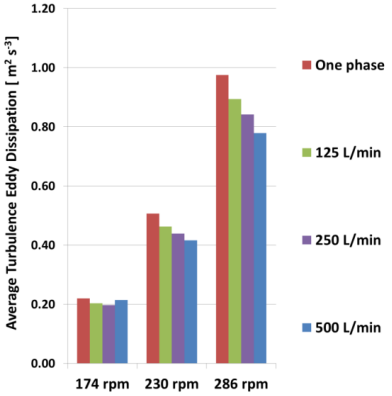

Figure 122. The average turbulent energy dissipation rates for all investigated rotational speeds and aeration rates simulated with the standard 4 mm gas bubbles.

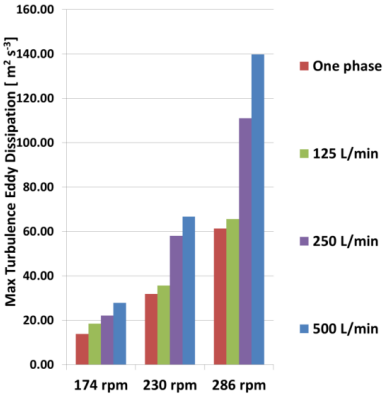

Figure 123. The maximum turbulent energy dissipation rates for all investigated rotational speeds and aeration rates simulated with the standard 4 mm gas bubbles.

The distributions of the energy dissipation rates are displayed in Figure 124 for the lowest and highest rotational speeds in combination with the highest and lowest aeration rates. The one-phase data is also displayed. The figure shows that the energy is dissipated in the same region as discussed for the one-phase flow, i.e. around the impellers and in the regions where the radial flow hits the cylindrical walls.

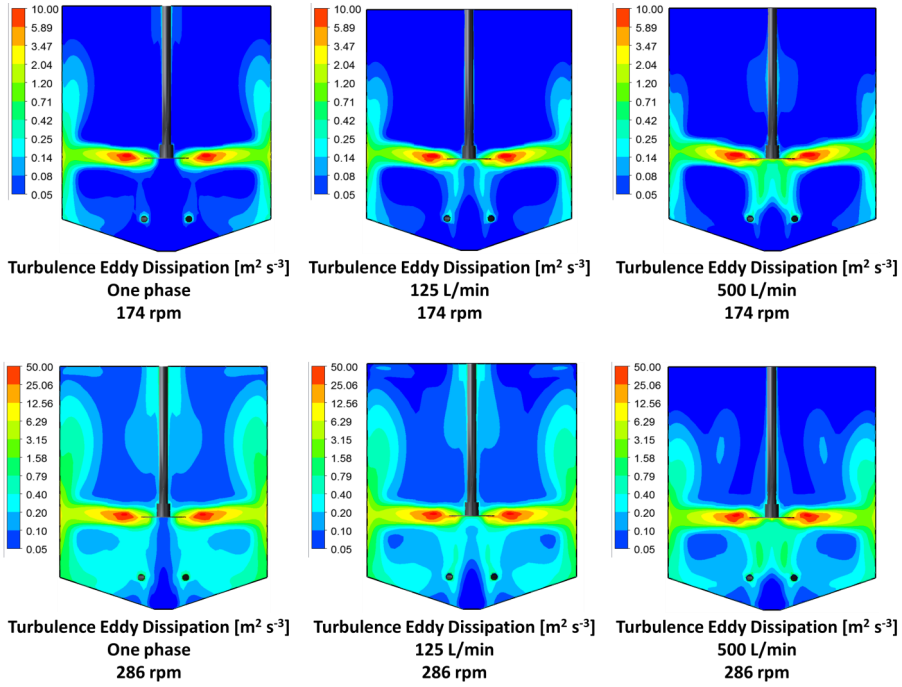

Figure 124. The distributions of turbulence eddy dissipation on the symmetry planes in the 174 and the 286 rpm cases for one-phase flow and the aeration rates 25 and 500 L/min.

The averaged and maximum ε-values presented in Figure 122 and Figure 123 should be compared with the results obtained in the microbioreactor and the magnetically stirred reactor cases. In Figure 122 it can be seen that the averaged values in the pilot plant reactor were between 0.2 and 1 $m^2\ s^{-3}$, which is not so far from the averaged value calculated for the microbioreactor stirred with 1000 rpm (approximately 0.3 $m^2\ s^{-3}$). It is also bigger than the largest averaged value for the magnetically stirred reactor, which was around 0.05 $m^2\ s^{-3}$ for 900 rpm. The maximum values in the pilot plant reactor were however considerably higher (up to 140 $m^2\ s^{-3}$) compared to the corresponding maximum values for the microbioreactor and the magnetically stirred reactor which were both around 3 $m^2\ s^{-3}$.

It is however hard to compare the case studies in this way since the average is presented in Figure 124 and regions with both much higher and lower values exist in the pilot plant reactor. It is therefore also questionable if the average can be seen as a representative value for the entire reactor. However, for the free-surface simulations the calculation of a global average was the best method available for the calculation of a representative ε value for the eddy cell model. For dispersed flows it is however possible to calculate local values of k_L using the eddy cell model as presented in section 4.3.4.

4.3.3.6. Impact of bubble size on the energy dissipation rate distribution

Figure 125 shows the effect of the different bubble sizes on the averaged energy dissipation rates for the most and least aerated and agitated flows. As can be seen the different bubble diameters have no substantial effects, which is interesting since the smaller bubble sizes lead

to considerably higher gas holdups which should have an effect on the energy input as discussed in the section above.

The gas inflow rates were however constant in between the two cases presented in Figure 125, which suggests that the amount of gas held in the entire reactor did not have an impact on the energy dissipation. It seems instead that only the amounts of transported gas towards the impellers is important for the averaged values of ε. This is also reasonable if only the gas volume fractions in between the impeller blades are important and not the gas holdups in the remaining part of the reactor.

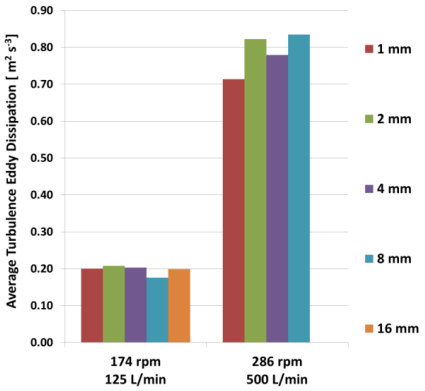

Figure 125. The average turbulence eddy dissipation rates for the varying bubble diameters for the 174 rpm + 125 L/min and the 284 rpm + 500 L/min-cases.

4.3.4. Oxygen transfer simulations

The oxygen transfer rates in the pilot plant reactor were calculated in each node in accordance with the description in section 3.5.3, and the proportionality constant C_P was set to one since no consistent value for it could be found in the literature. Future work includes however to find a case specific value of C_P for the pilot plant reactor.

The liquid volume averaged values of k_L in the reactor are displayed in Figure 126 for all aeration and agitation rates and the standard bubble diameter 4 mm. The values follow also the same relative trend as the corresponding volume averaged values of ε displayed in Figure 122 since k_L is directly proportional to $\varepsilon^{0.25}$. This correlation also explains why the distribution among the values is lower in Figure 126 than in Figure 122.

The k_L values in Figure 126 are approximately in the same order of magnitude as the values achieved in the previous case studies. For the magnetically stirred reactor (Table 24) and the microbioreactor (Table 15) the averaged values were around $3\text{-}7\cdot10^{-4}$ m s^{-1} and $3\cdot10^{-4}\text{-}1\cdot10^{-3}$ m s^{-1} respectively. This could be interpreted as a strength of the eddy cell model and the CFD models providing the values of ε, but without experimental and isolated k_L data it is very hard to conclude if the models are reliable or not.

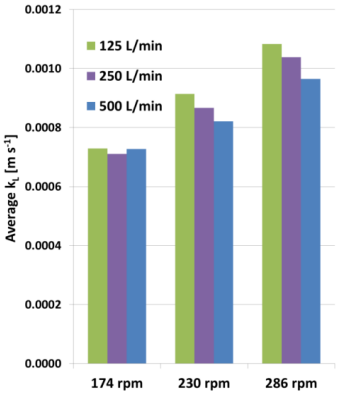

Figure 126. The average k_L values in the two-phase simulations.

The volume averaged k_La values are displayed in Figure 127. The trends in the figure are very similar to the ones displayed for the gas holdup in Figure 110, i.e. that the k_La values are higher for increasing air flow and agitation rates. This data can also be compared to the k_La data calculated for the microbioreactor and the magnetically stirred reactor from Table 16 and Table 25 respectively. The tables show that the average k_La values for the magnetically stirred reactor were in the interval $1{\cdot}10^{-2}$-$3{\cdot}10^{-2}$ s^{-1}, and for the microbioreactor the interval $5{\cdot}10^{-2}$-$5{\cdot}10^{-1}$ s^{-1} was found. The data in Figure 127 are in the range between $2{\cdot}10^{-2}$-$1{\cdot}10^{-1}$ s^{-1}, i.e. slightly lower than for the microbioreactor. However, it is once again important to remember that this is an average value for the entire reactor, and that there are regions with both higher and lower simulated values.

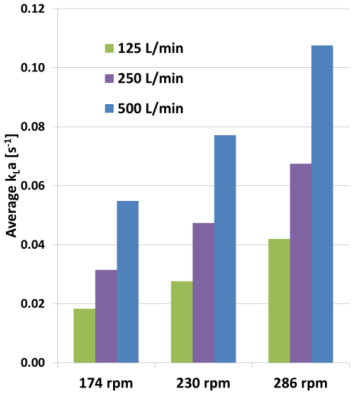

Figure 127. The average k_La values in the two-phase simulations.

The distribution of k_La in the sparged reactor for all varying rotational speeds and aeration rates are displayed in Figure 128. The colour scheme is presented in the legend, and it can be seen that the figure is similar to Figure 109 from which the specific interfacial areas are taken. Figure 128 and Figure 109 are however not only scaled versions of each other since also the distribution of turbulent eddy dissipation (i.e. Figure 124) has an impact.

Finally, the impacts of the user defined bubble size on the simulated k_La values are displayed in Figure 129. The differences are very large, and as discussed previously the major reason

for this is that the simulated interfacial areas are directly dependent on the user defined bubble diameter.

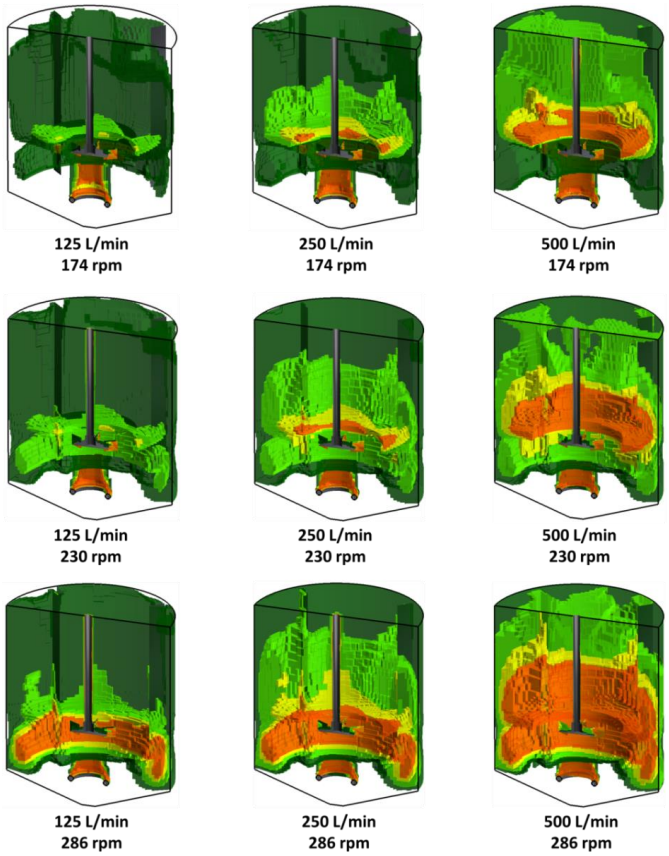

Figure 128. The k_La data for the two-phase simulations where the colours are as follows: Orange > 0.15 s^{-1}, 0.15 s^{-1} >Yellow > 0.1 s^{-1}, 0.1 s^{-1}> Lime Green > 0.05 s^{-1}, and 0.05 s^{-1} > Forest Green > 0.01 s^{-1}.

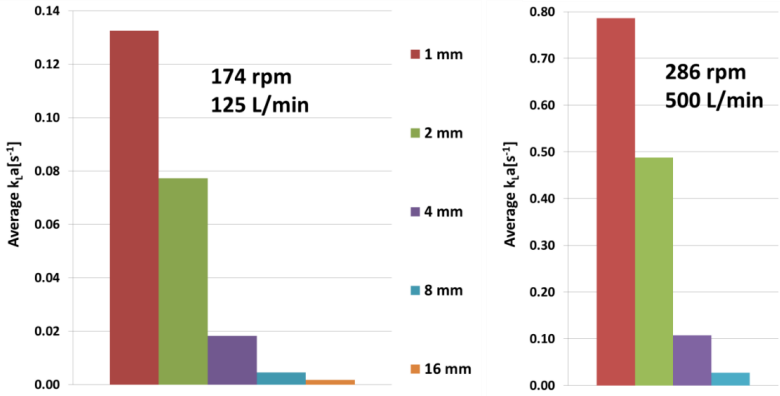

Figure 129. The impact of the bubble size on the average simulated k_La values.

4.3.5. Transient results for the pilot plant reactor

Similar as for the microbioreactor case the time step, mesh and turbulence model dependencies were investigated for the mixing times in the pilot plant reactor. These sensitivity studies were performed for the one-phase simulations. The conclusion was that all time steps smaller than 0.1 seconds were demonstrating time step independence, and that there was almost no difference between the original and the boundary refined mesh. The boundary refined mesh had only slightly longer mixing times when the definition was based on the minimum concentrations in the reactor. No major differences could be seen for the mixing times between the SST and the k-ε turbulence model.

4.3.5.1. One-phase mixing

The mixing time results for the one-phase mixing time simulations are displayed in Figure 130. The figure shows, as stated above, that the turbulence model choice was not critical. The choice of mixing time definition (5, 10 or 15%) appears however important, as well as how the additional variable value is defined, i.e. if it is the value in one of the monitoring points or the maximum or minimum value.

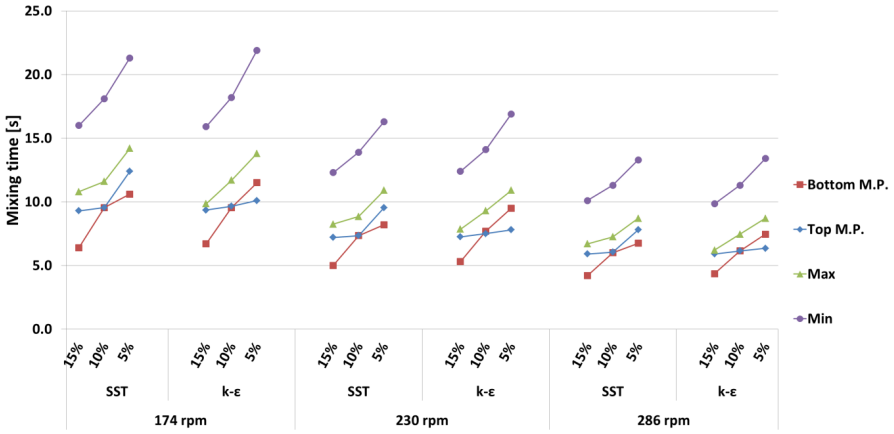

Figure 130. Comparison between the two turbulence models for all investigated rotational speeds. The original mesh and the time step 0.05 were used for the displayed data. The mixing times were defined based on either the top or bottom monitoring point (M.P.) value or the maximum or minimum value in the fluid.

The top and bottom monitoring point values for the transient additional variables for the SST model in Figure 130 are displayed in Figure 131. For the top monitoring point, the peak associated with 286 rpm occurs first, closely followed by the 230 and 174 rpm peaks. This is reasonable based on the knowledge from Figure 97 that the flow patterns are similar but scaled in magnitude for the varying rotational rates. The same trend is also apparent for the bottom monitoring point. The first peaks are presumably lowest because the eddy diffusion has the most impact on the highest rotational speeds.

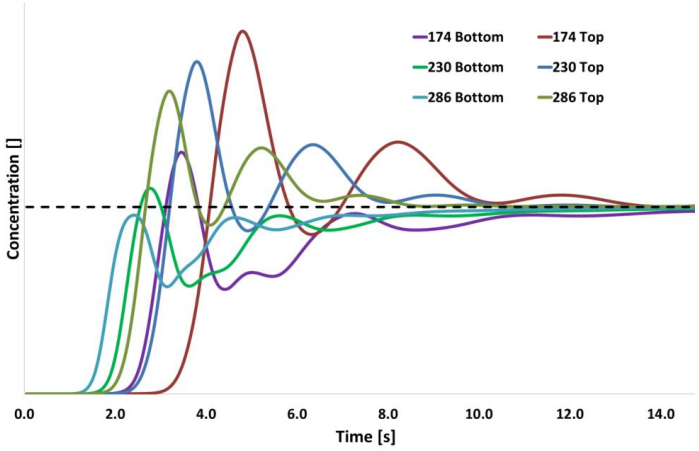

Figure 131. The transient additional variable concentrations for the top and bottom monitoring point for the SST data associated with the mixing times in Figure 130.

The one-phase flows are illustrated in Figure 132 for 174 rpm and in Figure 133 for 286 rpm. The used colouring schemes are consistent with the ones for the microbioreactor and are described in the figure legends. The general mixing pattern in the figures is similar to the pattern previously presented in Javed, Mahmud, and Zhu (2006) which also illustrates mixing in a Rushton impeller stirred reactor.

The first illustration in Figure 132 shows the spread of the additional variables after 1 second, which is also the time where the insertion of the additional variable from the source point is stopped. The source point is located on the left side of the reactor, but due to the rotational symmetry, the additional variables have also spread over to the right side. The additional variables have also been transported downwards in the reactor, which is fully consistent with the appearance of the flow field.

After two seconds the additional variables have been transported downwards even more and are also spread in the horizontal dimension. Fractions of the most concentrated, i.e. with the highest values of additional variable, fluid have also reached the impellers and been transported outwards to the vessel walls. This flow pattern is even more visible at 3 seconds, where also the regions with the lowest concentrations of additional variables are displayed.

After 4 seconds, the most concentrated volumes have left the discharge zones and instead they are located in the top or the bottom of the reactor. A second later the most concentrated fractions in the bottom have been diluted in the surrounding liquid. The fraction in the top part of the reactor is then approaching the impeller region for the second time. At 6 seconds this fluid has again reached the vessel walls and a fraction of it is transported downwards into the lower re-circulation zone. This time the downwards transported fluid is less concentrated, i.e. it is turquoise. The most concentrated fluid is for the second time transported through the top re-circulation zone, and this mixing behaviour is repeated until a homogenous concentration is achieved.

Figure 132 clarifies the appearance of the curves in Figure 131 and explains for example why the top monitoring point experiences the higher peaks and why the monitoring point in the bottom of the reactor seldom overshoots the final concentration.

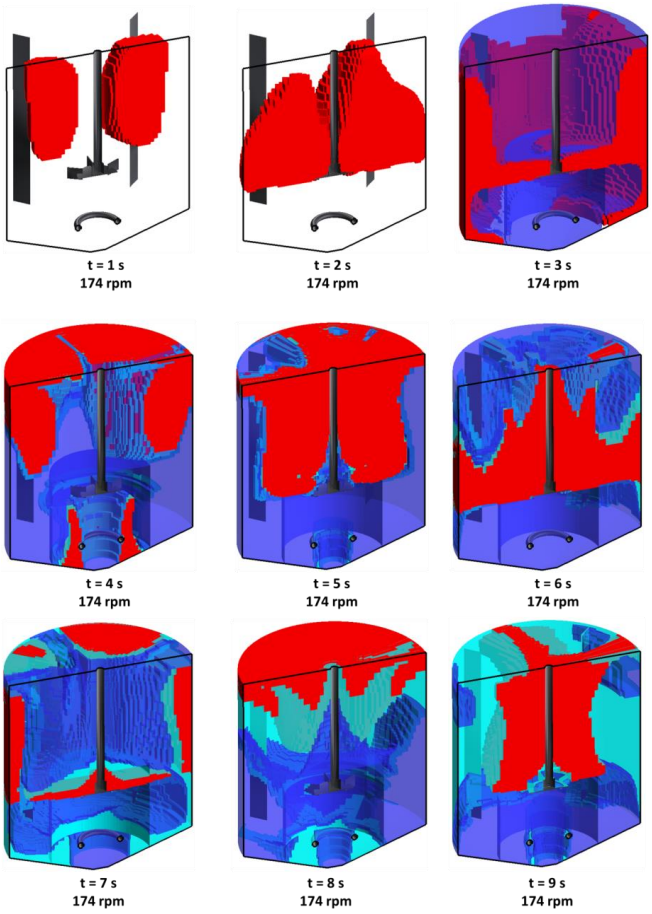

Figure 132. The transient mixing behaviour for 174 rpm. The red volumes have concentrations of the additional variable higher than +10% of the final concentrations and the blue regions have concentrations below 90%. The turquoise regions are within the ±10% interval from the final value.

The mixing pattern in Figure 133 shows that the mixing behaviour for 286 rpm is very similar to, but faster than, the pattern for 174 rpm. After 2 seconds for example, the additional variables have reached the outer walls and are already transported upwards or downwards.

The majority of the liquid in the upper re-circulation zone is also already within the correct ±10% interval after 6 seconds for 286 rpm, while the similar situation for 174 rpm not is reached until after 9 seconds.

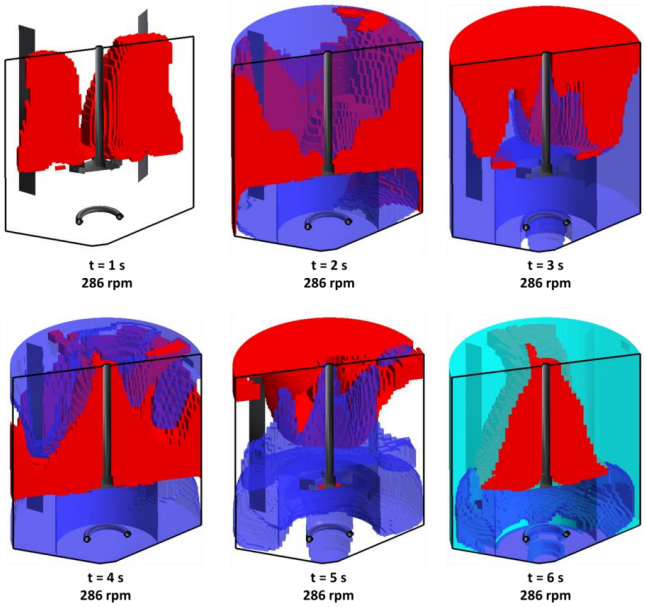

Figure 133. The mixing behaviour for 286 rpm following the colouring scheme presented in Figure 132.

4.3.5.2. Two-phase mixing

The results for the two-phase mixing simulations are displayed in Figure 134 and Figure 135. The simulations were performed with the time step 0.05 seconds and with the original mesh. In Figure 134 the air flow rate of 250 L/min is compared to the one-phase simulations for all investigated rotational speeds. There is no clear trend in the data, since the two-phase mixing time is higher for 174 rpm but lower for 230 and 286 rpm compared to the single-phase cases.

The results for 286 rpm and all investigated aeration rates are displayed in Figure 135. In the figure, it is observed that the mixing times are shorter for 125 and 250 L/min but considerably higher for 500 L/min. In order to explain these inconsistent phenomena Figure 136 and Figure 137 are provided.

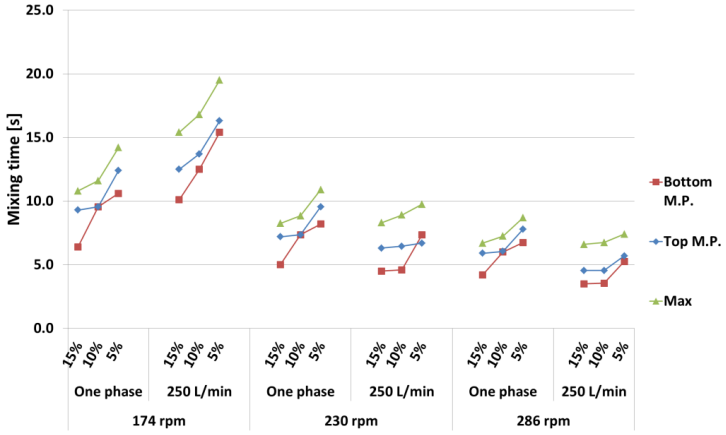

Figure 134. Mixing time results for all rotational speeds compared between one-phase flow and the simulations sparged with 250 L/min.

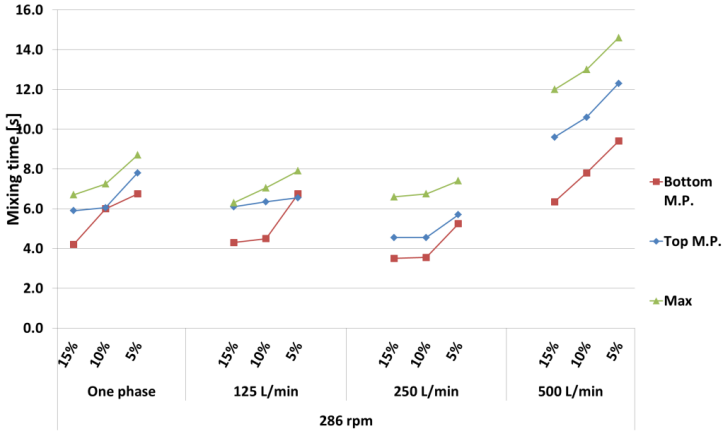

Figure 135. Mixing time results for all sparging speeds including the one-phase case for 286 rpm.

Figure 136 shows how the additional variable distributes in the 250 L/min and 174 rpm simulation. Comparing Figure 132 and Figure 136 it is seen that the most concentrated volume is directly transported towards the bottom in Figure 132 while it is more twisted in the circumferential direction in Figure 136. As a consequence the concentrated volumes do not reach the impeller before 4 seconds have passed in the two-phase simulation. At this point in time these volumes already reached the outer walls and are furthermore approaching the top of the reactor in the single-phase simulation. This explains therefore the delayed mixing times for the two-phase flow for 174 rpm displayed in Figure 134.

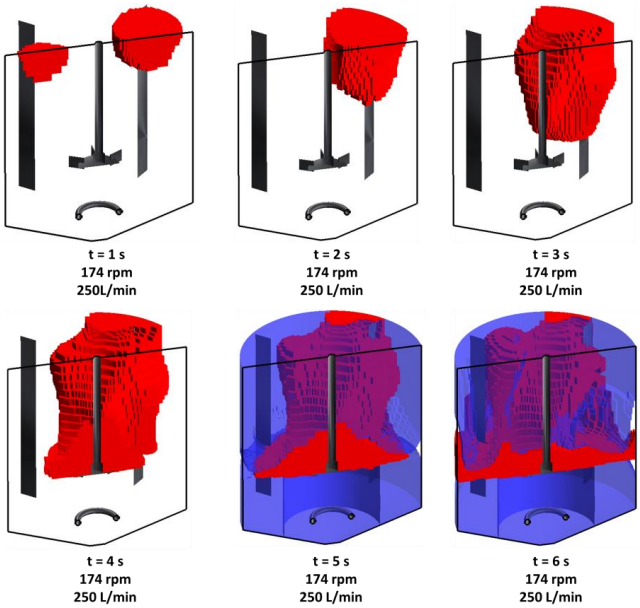

Figure 136. The mixing behaviour for 174 rpm and the aeration rate 250 L/min. The colouring scheme used is presented in Figure 132.

Figure 137 presents how the additional variable is distributed at 286 rpm in the one-phase simulation and for the aeration rates 250 and 500 L/min. The aim with the figure is to illustrate the results displayed in Figure 135, i.e. where 250 L/min mixes slightly faster and 500 L/min considerably slower than the one-phase simulation.

In Figure 137 the same phenomenon as in Figure 136 can be seen, i.e. that the concentrated volumes are not transported downwards as fast as in the two-phase flow. This behaviour is explained by the differences between the one-phase streamlines in Figure 100 and the two-phase streamlines in Figure 120.

This effect is apparent for both two-phase flows but most pronounced for the aeration rate 500 L/min, but it is not the only explanation for the longer mixing times obtained in Figure 135. The critical difference between the simulations is instead anticipated at 3 seconds where it shows that a larger fraction of the additional variables is transported into the lower re-circulation zone for 250 rpm. This has the effect that the lower re-circulation zone does not need to await the second round of additional variables being provided from the discharge zones in order to reach the final concentration interval. The level of additional variable in the upper re-circulation zone is also decreased which also reduces the mixing time for the top monitoring point. This is therewith beneficial for the mixing in both the upper and the lower re-circulation zones.

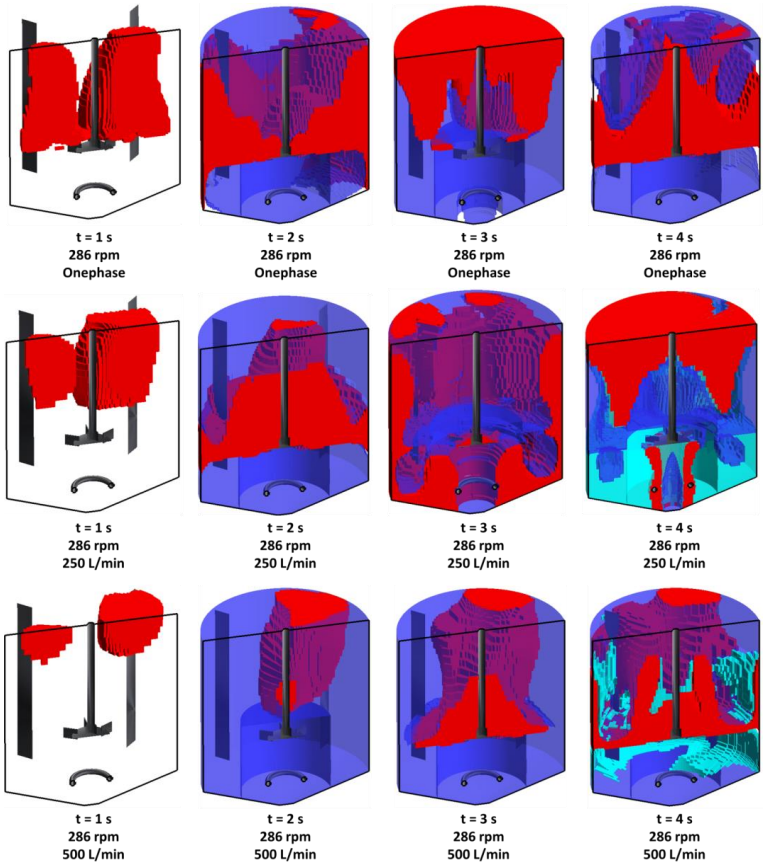

Figure 137. The mixing behaviour for 286 rpm for the single-phase flow and the aeration rates 250 and 500 L/min. The colouring scheme used is presented in Figure 132.

4.4. The rotating bed reactor

4.4.1. Experimental results

The experimental results for the rotating bed reactor (RBR) are displayed in Table 27 and as can be seen the reaction times are much longer for the lower rotational speeds compared to the higher. The experimental results are compared with the simulations in section 4.4.8.

Table 27. The experimental ion-exchange data for the RBR.

RPM	Time [s]	Standard Deviation	Number of data
70	816	-	1
100	367	0.71	2
200	104	5.3	6
300	58	0.56	3
400	38	1.73	3
500	29	2.63	15
600	26	0.71	2
700	21	0.71	2
800	19	0.71	2
900	16	1.41	2

4.4.2. Reynolds number and the choice of turbulence model

Defining the Reynolds numbers for the RBR is difficult since it is not obvious which equation to use due to its complex geometry. The impeller Reynolds number (equation 10) was however used since the four radial walls within the RBR act similarly to impeller blades. The impeller diameter was set to 45.5 mm, i.e. the same as the diameter of the device according to Figure 34, and the resulting Reynolds numbers are displayed in Table 28.

Table 28. The Reynolds number for the flow in the rotating bed reactor.

RPM	Reynolds number
70	2706
100	3866
500	19328
900	34791

According to the definition in Doran (1995) the Reynolds numbers in Table 28 are in the late transient or the fully turbulent regime. It was therefore decided to evaluate both the SST and the k-ε turbulence model and to compare the outcome.

Both turbulence models converged relatively well for the original meshes A, B and C. The SST model had however converging difficulties for Mesh C at 70 rpm. Mesh D converged poorly for both turbulence models at 500 rpm and 900 rpm. The simplified meshes α and β converged well for both turbulence models and all rotational speeds evaluated.

4.4.3. One-phase steady-state simulations of the original reactor

4.4.3.1. General flow pattern in the original mesh setup

The general flow pattern obtained for the RBR is displayed in Figure 138 which shows the velocity vectors at the purple plane indicated in Figure 36. The velocity vectors in the rotor and the stator are displayed as blue and the vectors inside in the porous domain are red.

The flow in the RBR is initiated when it rotates around its axis. The liquid inside of the porous material is then accelerated outwards through the small holes and new fluid must enter from underneath. The fluid leaving the porous material is discharged at the static walls of the vessel and is then directed either upwards or downwards. The fluid stream directed downwards reaches the bottom of the reactor where it is re-directed into the centre of it. A fraction of the fluid re-circulates then back towards the reactor wall while the remaining part is eventually drawn back into the porous material. A vortex is also formed underneath the RBR which creates downward directed velocities in the centre of the reactor.

The fraction of the liquid which is directed upwards after leaving the porous material also separates into two streams as visualised in Figure 138. One stream re-circulates downwards again while the other moves upwards to the top boundary. The top boundary is as explained in section 3.6.2.1 modelled as a free slip surface in order to simulate a gas-liquid interface. The upward directed flow then rotates in the top of the reactor before it returns to the region outside of the porous domain. The above presented flow pattern generates four visible re-circulation zones which are all indicated in Figure 138. The figure also shows the position of the discharge zone at the baffled wall.

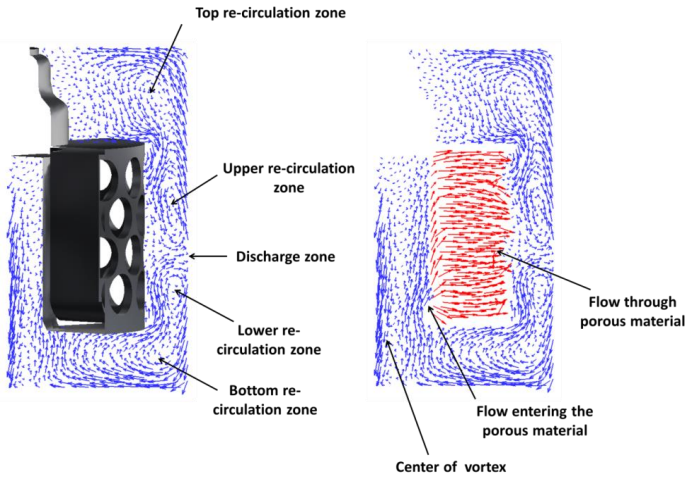

Figure 138. The general flow pattern achieved in the rotating bed reactor. The velocity vectors are blue in the stator and rotor domains and red in the porous domain.

The axial, radial and circumferential velocities for the meshes A, B and C are shown in Figure 139 for 500 rpm and the SST turbulence model. All meshes show the same general flow pattern but the re-circulation behaviour in the top of the geometry appears strongest in Mesh A and weakest in Mesh B. This can be seen on the radial velocity contours where it especially for Mesh A is observed that the radial velocities are negative closest to the top boundary condition and positive close to the top of the RBR. The same but opposite pattern is

displayed in the bottom of the reactor where the radial velocities are negative closest to the vessel bottom and positive at the bottom of the RBR.

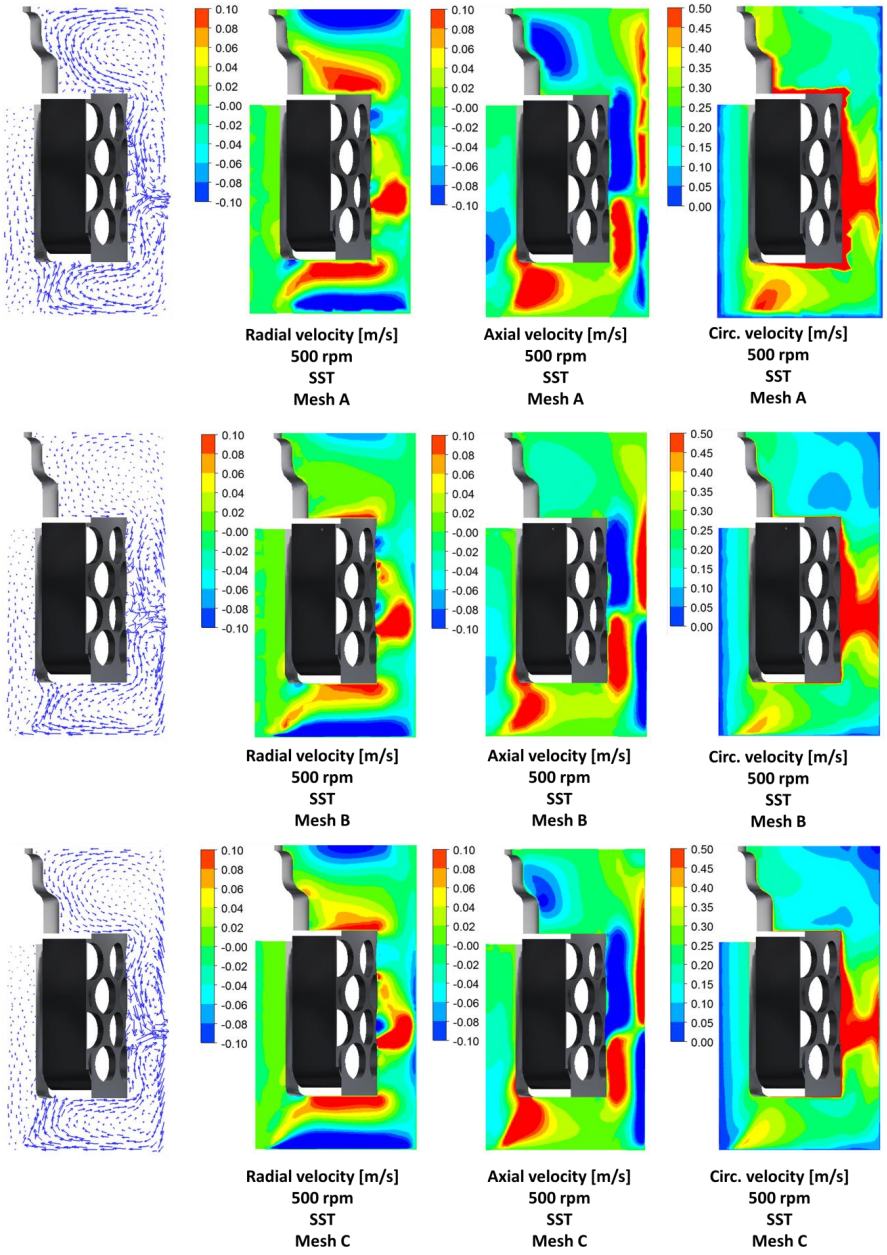

Figure 139. The radial, axial and circumferential velocity contour plots for the SST turbulence model on the three meshes A, B and C for the rotational speed 500 rpm.

The axial velocity contours in Figure 139 show how the flow is separated into one upward and one downward directed component after reaching the outer static wall. The upper and

lower re-circulation zones are also visible. The regions where the liquids are drawn upwards to enter the porous domain underneath the BRB are also detectable as well as the downwards directed inner cores of the central vortexes.

The circumferential velocities presented in Figure 139 demonstrate that the fluids leaving the porous material have the highest velocities. This is an expected outcome since the fluid in the porous material should have the same rotational speeds as the RBR itself. The circumferential velocities are however rapidly slowed down after leaving the porous domain.

Figure 140 shows the velocity contours for 900 rpm, Mesh A, and the SST model. The colour legends are therefore scaled with the increase in rotational speed from 500 to 900 rpm, i.e. with a factor 9/5 compared to the legends in Figure 139. The general flow patterns are very similar, but there are a few differences between 500 and 900 rpm. The negative axial velocities in the centre of the reactor for example are more pronounced for 900 rpm.

The fluid in the vortex under the RBR, i.e. in the region where it is pumped upwards into the porous material, has also a much more pronounced circumferential velocity in the 900 rpm case compared to 500 rpm. It also appears in Figure 140 that the fluid is accelerated both in the axial and in the circumferential direction in this region. This justifies the existence of the vortex, i.e. that it helps to accelerate the liquid in the circumferential direction so that it can enter the porous material again.

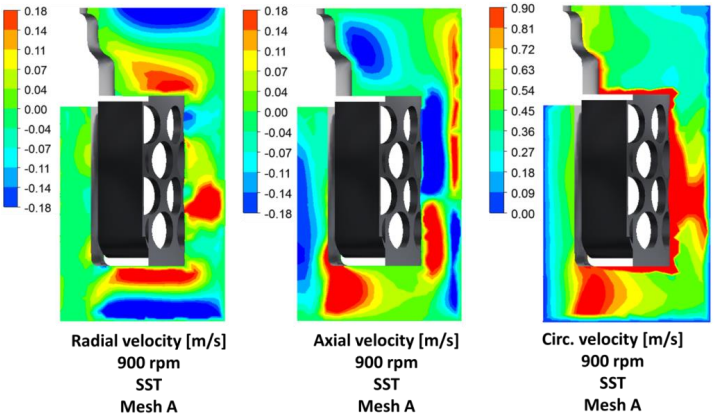

Figure 140. The radial, axial and circumferential velocity contour plots for the SST turbulence model on Meshes A for 900 rpm. The maximum and minimum values on the colour legends are the ones used in Figure 139 scaled with the fraction 9/5.

The velocity contour plots for the k-ε model, Mesh A and 500 rpm are displayed in Figure 141. Once compared to their SST model counterparts in Figure 139 it can be seen that the flow patterns appear very similar between the two turbulence models.

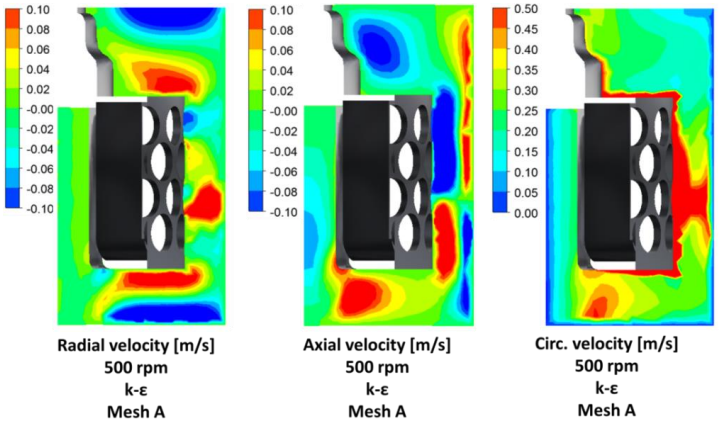

Figure 141. The radial, axial and circumferential velocity contour plots for the k-ε turbulence model on Meshes A for 500 rpm.

The velocity streamlines in the original geometry will now be presented. The streamlines are shown in Figure 142, Figure 143 and Figure 144 and are all initiated from the green dots in the respective figures.

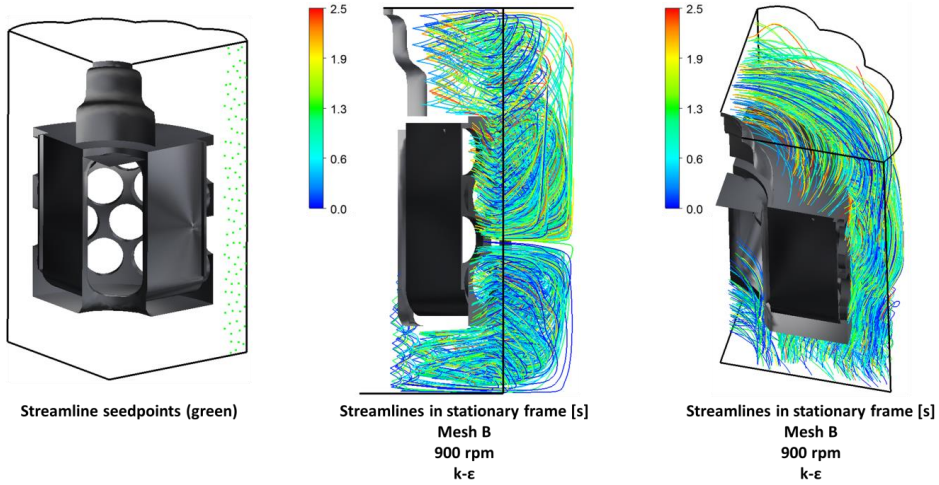

Figure 142. The streamlines in the rotating bed rector initiated in the outer section of the stationary domain.

In Figure 142 it can be seen that the flow is separated into one upper and one lower part at the height of the discharge zone. This flow pattern is similar to the flow in the pilot plant rector presented in Figure 100, and there is also no apparent exchange between the two zones. Streamlines however only show the time averaged velocities which means that turbulence can still promote mixing between the zones.

The streamlines in Figure 142 are all based on the velocities in the stationary frame, but especially for streamlines initiated in a rotating reference frame it is important to verify if the streamlines are following the stationary or the rotating velocities. Figure 143 shows an example of the difference between visualizing the rotational and the stationary streamlines. In

the figure the rotating frame streamlines are transported through the porous material while the stationary frame streamlines are kept in the vortex region.

This difference can be understood by the fact that the reactor basket is standing still once visualised but that it actually is located in the rotating domain. This means that the streamlines visualized in the rotating domain are rotating as well and it therefore appears as if they are transported straight into the porous material.

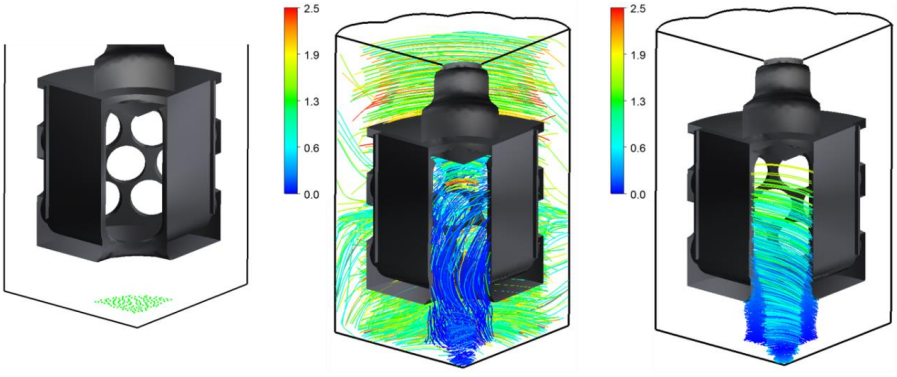

Figure 143. The rotating and stationary streamlines in the rotating bed rector initiated in the vortex region.

Figure 144 shows the difference between how the two turbulence models handle the vortex underneath the rotor. The streamlines released closest to the centre of the reactor are moving downwards while the ones initiated farther out are transported upwards. It can be seen that the streamlines associated with the k-ε model contain a slightly larger fraction of streamlines transported upwards directly, which suggests a thinner vortex with the k-ε model.

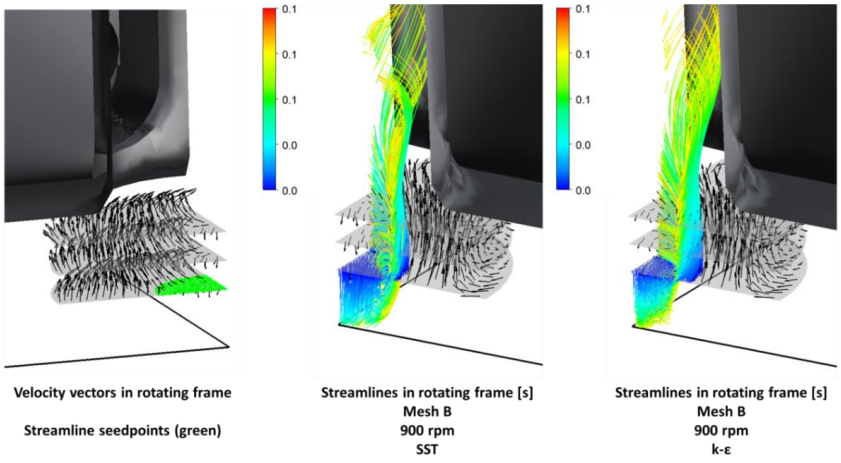

Figure 144. A comparison of the rotating streamlines initiated in the vortex region between the k-ε and the SST turbulence models.

4.4.3.2. Flow through the rotating bed reactor

The flows through the porous material in the RBR for the different evaluated meshes and turbulence models (k-ε and SST) are shown in Figure 145. The flows are calculated for the full (360°) reactor even if only 90° sections were simulated. The same is true for all reported flows in this section, i.e. every flow is converted to its full reactor equivalent.

Only small differences between the SST and the k-ε model are observed Figure 145 and for 500 and 900 rpm there is a vague trend with slightly higher flows for the SST model. Shifting from Mesh A (coarse with no prism elements) to Mesh B (coarse with prism elements) and to Mesh C (fine with prism elements) there is also an increase in predicted flow through the porous material. The conclusion must therefore be that the flow through the porous material is not mesh independent for the investigated meshes. The flows are nevertheless significantly different for the varying rotational speeds.

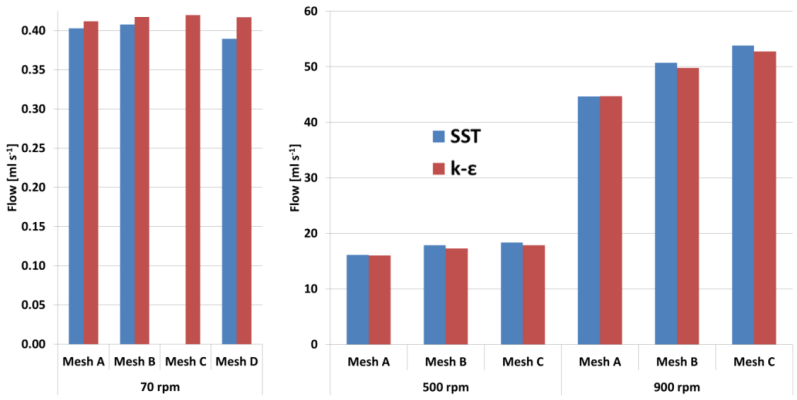

Figure 145. The flows through the porous materials for the SST and k-ε turbulence models, the meshes A, B and C and the rotational speeds 70, 500 and 900 rpm.

4.4.3.3. Eddy viscosity profiles for the k-ε and the SST model

The eddy viscosity contours for 500 rpm and the meshes A, B and C are displayed in Figure 146 for the SST and k-ε turbulence model. The distributions of eddy viscosities are highly mesh dependent and the eddy viscosities are generally higher the finer the mesh. There are also differences between the two turbulence model especially in the vortex-regions where the k-ε model computes considerably higher values.

In the figure it also looks as if the high eddy viscosity values in the vortex-region are transported into the porous material for the k-ε model. If this observation is correct it highlights a severe shortcoming of the model since turbulent flow is not expected in the porous material at all.

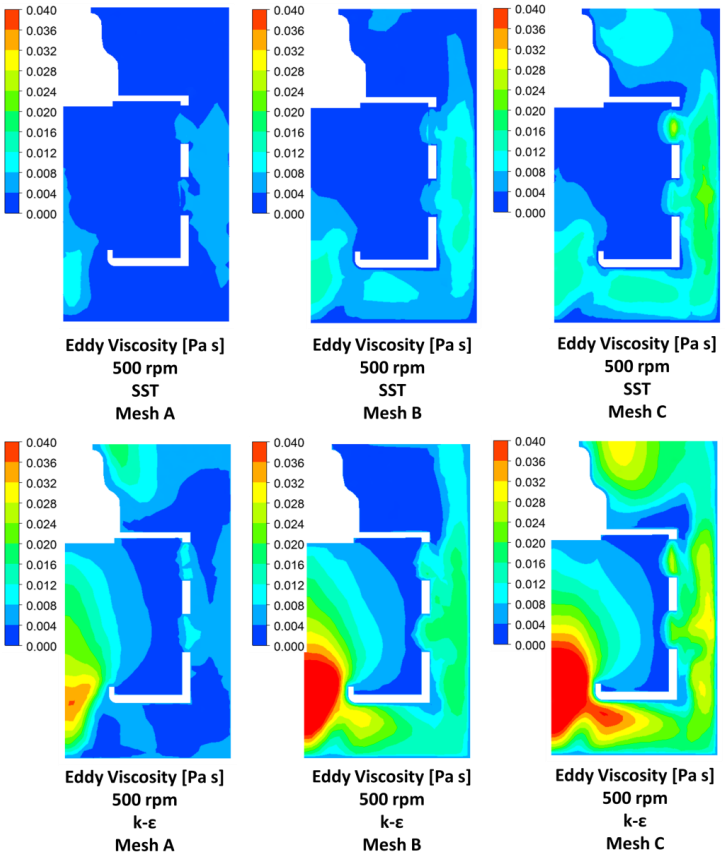

Figure 146. The eddy viscosities for 500 rpm for the SST and k-ε turbulence models on the meshes A, B and C.

The eddy viscosities for the lower horizontal line in Figure 45 are displayed in Figure 147. A small subfigure also displays the position of the line. It can be seen that the eddy viscosities for 70 rpm in combination the SST model are very low which might be caused by the same mechanism as described in section 4.1.3.4 for the microbioreactor, i.e. that the eddy viscosities decrease towards zero due to a lack of kinetic turbulent energy.

The range of the eddy viscosities in Figure 147 for 500 and 900 rpm, i.e. 0.01 to 0.1, can also be compared with the eddy viscosities developed in the other case studies. For the pilot plant reactor, they were for example about ten times larger and for the magnetically stirred reactor they were approximately 5 to 10 times smaller.

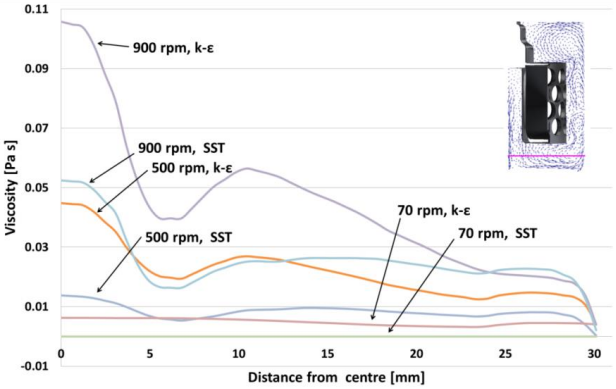

Figure 147. The eddy viscosities for Mesh B, the SST and the k-ε turbulence model and the rotational speeds 70, 500 and 900 rpm.

4.4.3.4. Investigation of the y^+ and F_1 values

The differences in the eddy viscosity values between the SST and the k-ε model in Figure 147 suggest that there might be a difference in the wall treatment between the two models. Another alternative is the influence of differences in the turbulence modelling in the bulk flow. The y^+ values at the walls are displayed in Figure 148 for the SST model, 900 rpm for the three meshes A, B and C. It can be seen that the y^+ values are smaller than 11.06 in several regions, which means that the SST model calculates the wall boundary conditions as laminar in accordance with the automatic wall function described in section 2.2.5.7. Varying wall treatments between the turbulence models contributed therefore most likely to the observed eddy viscosity differences.

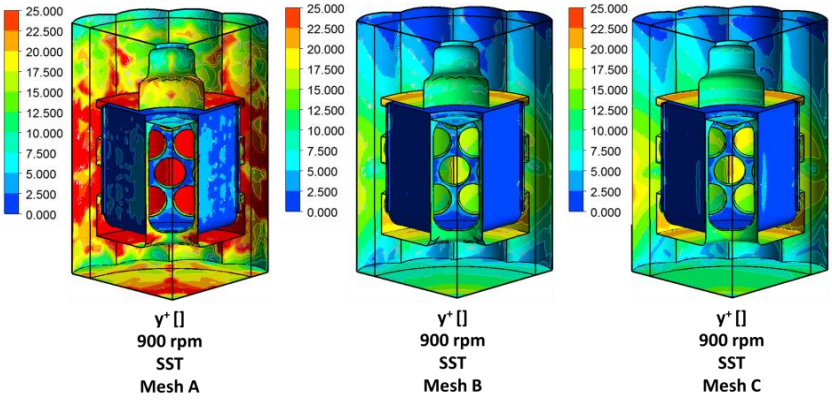

Figure 148. The contour plots of the y^+ values in the original geometry for 900 rpm and the SST turbulence model.

Figure 149 shows the F_1 values for the SST model and 500 rpm. The figure shows, as expected, that F_1 values are not all zero and therefore that the parameters associated with the SST model must be influenced by the k-ω model values. This might therefore also explain why the SST model differed from the k-ε model. Figure 149 also shows that the F_1 values are

highly mesh dependent, i.e. that they are not only a function of the absolute distance to walls. This could be interesting knowledge if specified F_1 values are desired.

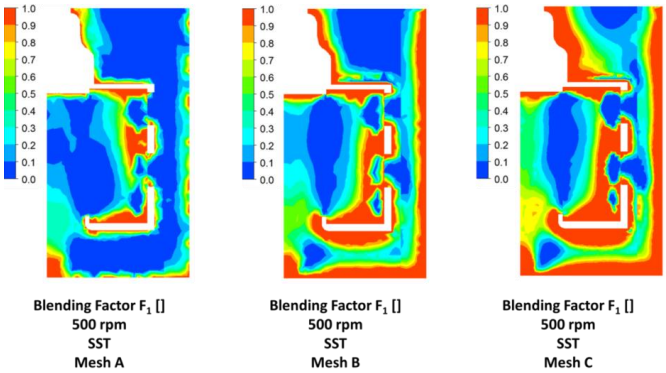

Figure 149. The F_1 values for the SST model at 500 rpm.

4.4.3.5. Distribution of turbulent energy dissipation for the SST and k-ε turbulence model

The turbulent energy dissipation rates for 500 rpm and the SST and k-ε turbulence model are displayed in Figure 150. The figure shows that most energy is dissipated where the fluid leaves the outlet holes and where it reaches the outer walls. The distributions of ε are thereby similar to the distributions in the pilot plant reactor. Figure 150 also shows that the ε values are higher underneath the RBR than above it. This could be because of the free slip top boundary condition or the presence of the vortex under the reactor.

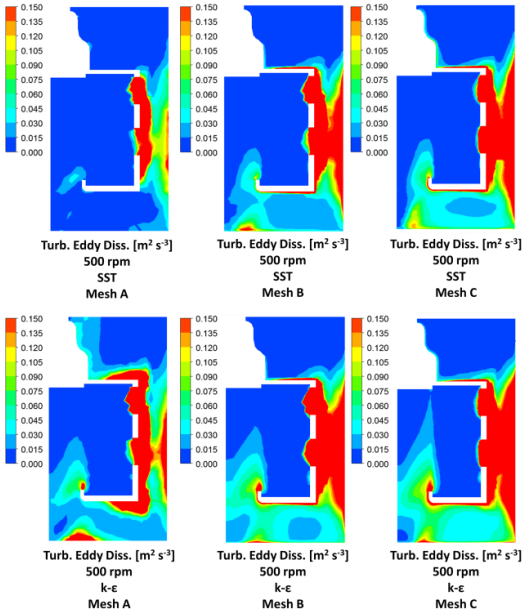

Figure 150. The turbulent energy dissipation rates for 500 and 900 rpm for the SST and k-ε turbulence models applied to mesh A, B and C.

4.4.4. Evaluation of the reactor simplifications

Two fundamentally different simplifications were performed for the original reactor design and both are evaluated in this section. First a 90° segment of the original 360° geometry was created by taking advantage of the rotational symmetry of its design, and secondly a simplified reactor was designed and evaluated. The simplified reactor design was originally presented in Schjøtt Andersen (2015) and the purpose of it was mainly to reduce the complexity of the geometry and to enable high quality hexahedral meshes.

4.4.4.1. The simplification of simulating a 90° section of the original reactor

In order to investigate if the 90° setup gave any different results compared to the full geometry they were both simulated and compared. The resulting velocities and flows through the porous material were very similar for the two setups. The eddy viscosities for the SST and the k-ε turbulence model are displayed in Figure 151 for the 90° and 360° geometries. Since no major differences are seen for the otherwise mesh sensitive eddy viscosity it was concluded that the 90° geometry could be used instead of the full geometry.

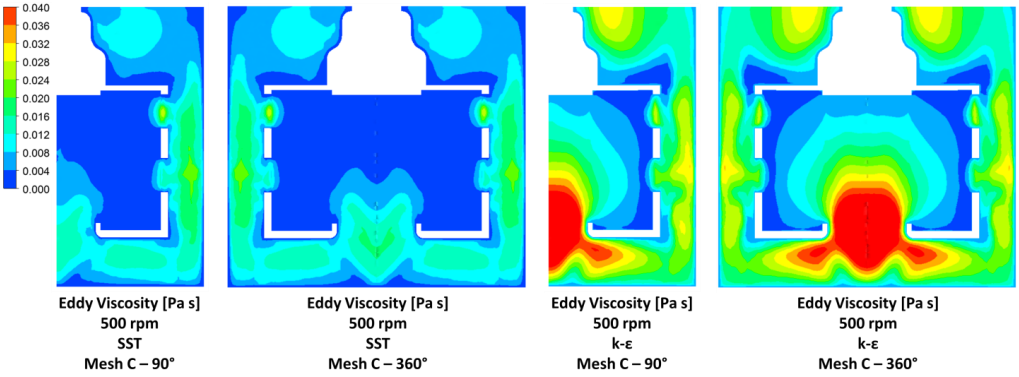

Figure 151. Comparison of the eddy viscosities between the 90° and 360° reactor setups for the SST and the k-ε turbulence model.

4.4.4.2. The simplified reactor design

Replacing the original reactor design with the simplified is highly preferred. One of the motivations for this is that the simplified reactor can be reduced down to 22.5° segments since the geometric bottleneck for rotational symmetry in the simplified reactor are the 16 petals. The lack of small outer holes made it also considerably easier to create hexahedral meshes for the simplified reactor. In order to use the results from the simplified reactor design it was however first necessary to confirm that the model was reproducing the flow characteristics of the original reactor.

The velocity profiles for 500 rpm and the SST turbulence model are compared between the original Mesh A and the simplified Mesh α and Mesh β in Figure 152. In Figure 152 both reactor designs show the same general flow features, but the flows at the top of the reactor are more pronounced in Mesh A than in Mesh α and Mesh β. The flows in the top of Mesh α and Mesh β are however very similar to the one displayed for Mesh B in Figure 139. The differences should therefore not necessarily be considered as consequence of the design simplification. The radial flows below the RBR are also more pronounced for Mesh A.

The velocity contours also appear smoother in the simplified mesh. This can be explained by differences in mesh quality between the designs and by the more complex flow pattern in the original reactor due to the small outlet holes.

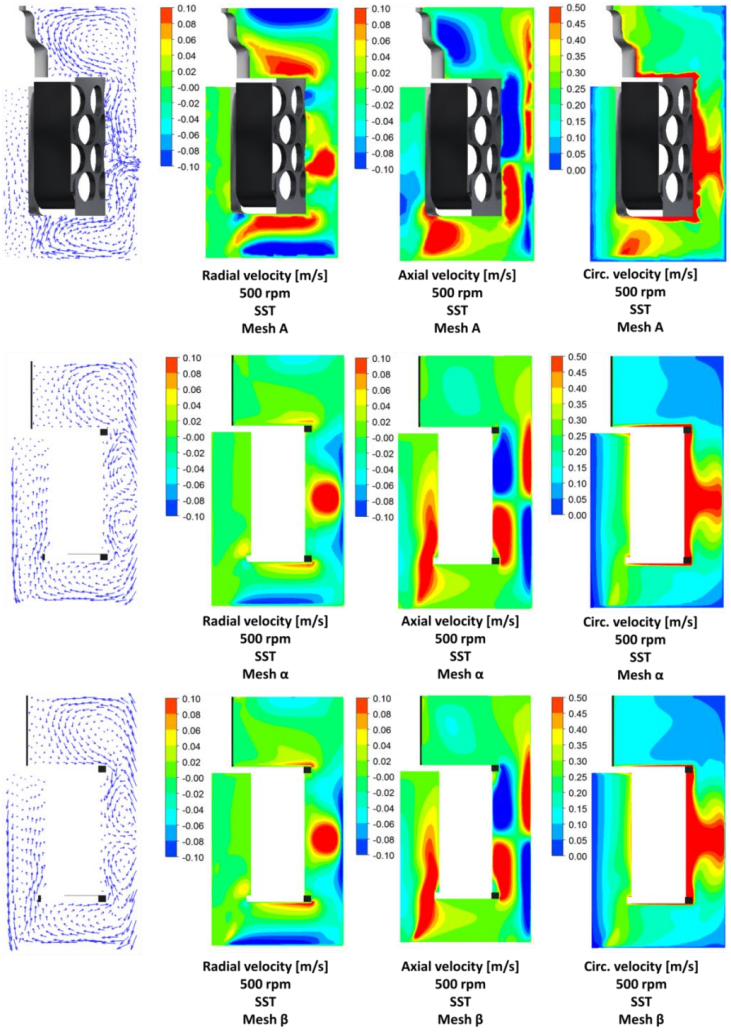

Figure 152. The velocity profiles for 500 rpm and the SST models for Mesh A (i.e. the original design from Figure 155) and for Mesh α and Mesh β (i.e. the simplified design from Figure 156)

Among the similarities between the reactor types, it should first be noted that all recirculation zones displayed in Figure 138 are also present in the simplified reactors, and likewise for the discharge zone. The behaviour of the liquid leaving the reactor is also very similar between the original and the simplified design, which is interesting especially since the flow through the porous domain is relatively uniform. The uniformity of the flow in the porous domain is discussed in section 4.4.8.1. Figure 152 also shows that the vortex appear in the simplified reactor and this is further investigated in Figure 153.

Figure 153 shows the streamlines in the simplified reactor (Mesh β) and is therefore the corresponding illustration of the phenomena presented in Figure 144. The behaviour of the different vortexes is very similar, which adds credibility to the use of the simplified design. Both Figure 153 and Figure 144 demonstrate for example that the vortex created by the k-ε model is the most narrow.

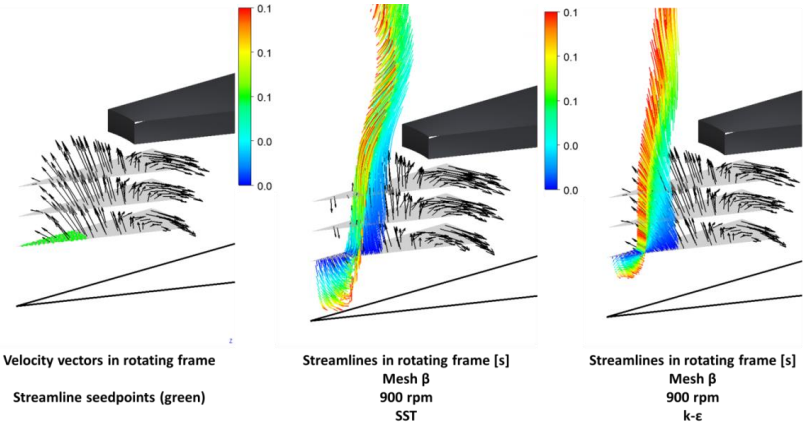

Figure 153. The streamlines in the vortex region of Mesh β for 900 rpm and the SST turbulence model.

The total flows for the simplified reactor are compared with the flows through the original meshes in Figure 154 for 70, 500 and 900 rpm. The flows are larger for the simplified geometries (i.e. Mesh α and Mesh β) but they are all still within the same order of magnitude. One possible explanation for the larger flows in the simplified reactors is the lack of outlet holes which decreases the average distance through the porous material.

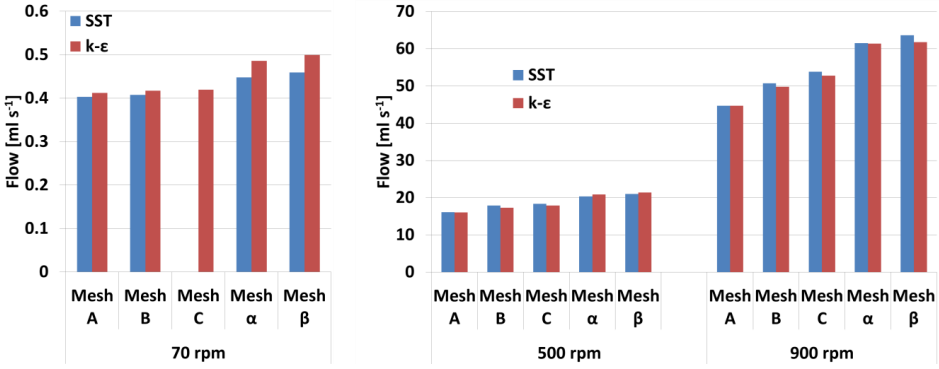

Figure 154. The flows through the rotating materials for the SST and k-ε turbulence models, the meshes A, B, C, α and β and the rotational speeds 70, 500 and 900 rpm.

The simulated flows through the porous materials for Mesh α for an extended set of rotational speeds are summarized in Figure 155. It is, as expected, observed that the rotational speed has a large impact on the flow. This is in alignment with the data in Table 27, where it is shown that the rotational speed also has a considerable impact on the completion times of the experimental ion-exchange reaction times. Very little flow through the catalytic porous material at 70 rpm would also explain its very long reaction times.

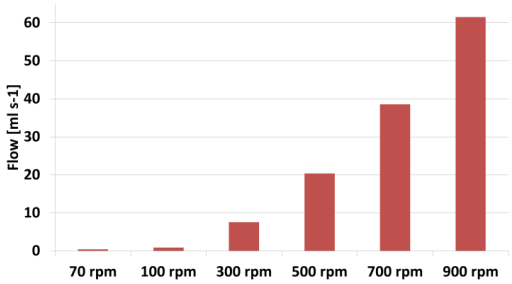

Figure 155. The flows through the porous material for Mesh α, the SST turbulence model and the rotational speeds 70, 100, 300, 500, 700 and 900 rpm.

The average residence times in the porous materials for the varying rotational speeds are displayed in Table 29. It can be seen that the fluids spend about 0.5 seconds in the porous domain at 900 rpm. This raises the question if 0.5 seconds is time enough for the ion-exchange to occur or if unreacted (i.e. not exchanged) hydrogen ions also leave the porous domain at the porous outlet. This is therefore further explored in section 4.4.8.

Table 29. The average residence time in the porous material calculated based on Mesh α.

RPM	Average residence time [s]
70 rpm	72.85
100 rpm	36.41
300 rpm	4.31
500 rpm	1.60
700 rpm	0.84
900 rpm	0.53

In Figure 156 the produced eddy viscosities for the simplified meshes α and β are compared to the data of Mesh C for 500 rpm and the figure shows that the eddy viscosities are considerably higher for the simplified meshes. These differences cannot be explained without further investigations, but it is nevertheless important to acknowledge their existence since it might have a large effect on mixing simulations or similar involving additional variables.

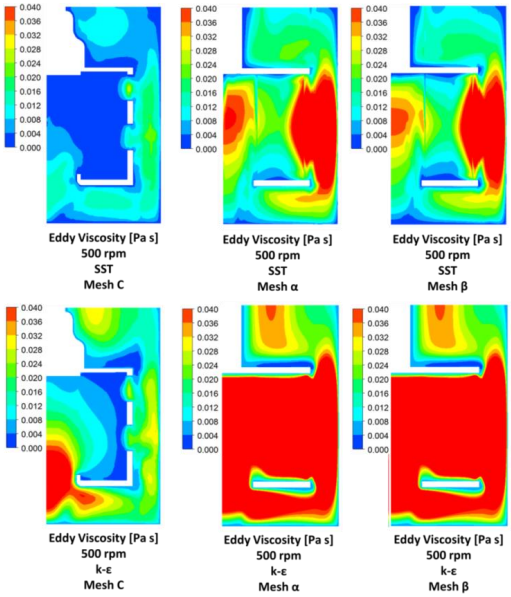

Figure 156. Eddy viscosity comparison between Mesh C and Mesh α and Mesh β for 500 rpm and the SST and the k-ε turbulence model.

The turbulent energy dissipation rates corresponding to Figure 156 are shown in Figure 157. It is surprising that the energy dissipation rates are more similar between the different meshes than the eddy viscosities are, and this suggests that it is actually the values of the turbulent kinetic energy (*k*) which varies between the meshes.

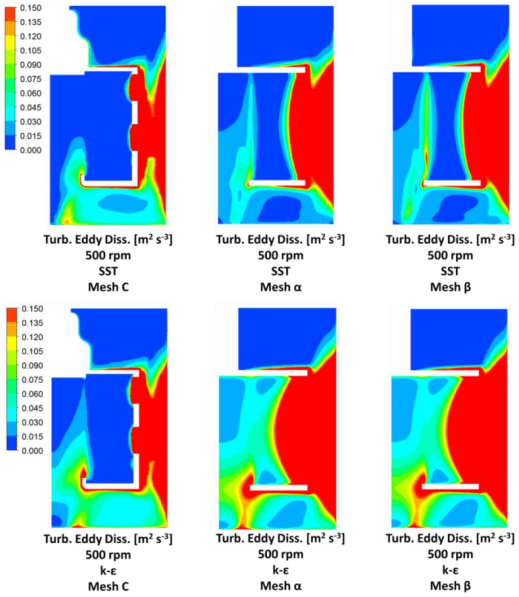

Figure 157. Turbulence eddy dissipation rate comparison between Mesh C and Mesh α and Mesh β for 500 rpm and the SST and the k-ε turbulence model.

The y^+ values in the simplified reactor designs were investigated for 500 rpm, the SST model and the simplified mesh and the outcome was similar as for the original reactor, i.e. that the values were both higher and lower than 11.06. In addition to this the F_1 values were investigated and the results are compared to the original mesh values in Figure 158. The differences displayed in Figure 158 might be part of the explanation for the different flow behaviours between the original and the simplified meshes.

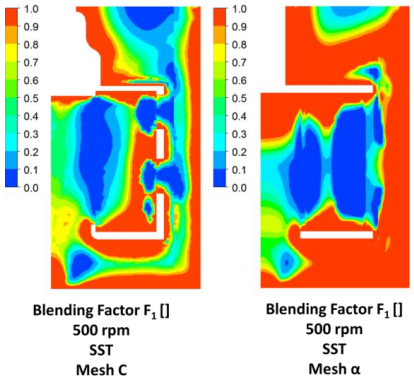

Figure 158. Comparison of the F_1 values for the SST model at 500 rpm between Mesh C and Mesh α.

4.4.5. Sensitivity analysis of the porous model

4.4.5.1. Sensitivity analysis of the linear loss coefficient C_1

The effects of the evaluated changes in the linear flow resistance coefficient C_1 on the flows through the simplified reactor are shown in Figure 159. In the figure it can be seen that the user defined value C_1 has a large impact on the results, and that a lower pressure loss coefficient increases the flows through the porous material. The simulations were performed with Mesh α at 500 rpm and with the SST turbulence model and the results are compared to the original C_1 value, i.e. $5.4 \cdot 10^6$ kg m^{-3} s^{-1}.

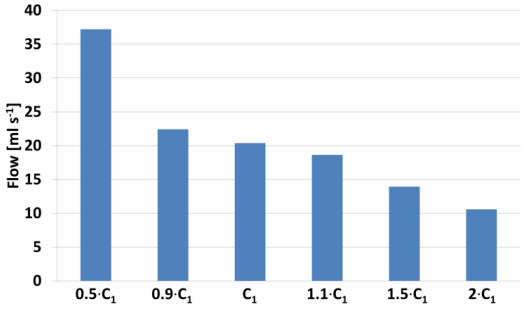

Figure 159. The flows through the porous materials in the Mesh α, 500 rpm and SST setup for a range of multiples of the linear flow resistance coefficient C_1.

The experimental data from the material data sheet was also directly modelled by simulating the pressure drop in a porous pipe using C_1, and it was confirmed that the pressure loss model worked very well. There are no guarantees however that the porous material in the RBR had

exactly the same pressure loss characteristics as the provided pressure loss data. The particles could for example be packed with different density in the different setups.

4.4.5.2. Sensitivity analysis of the porosity coefficient γ

The volume fraction coefficient γ (from equation 44) was set to 1 for the majority of the flow simulations since it was experienced in preliminary simulations that the coefficient did not have any effect on the superficial velocities. The effect of alternating γ was nevertheless investigated and the values 0.1 and 0.5 were compared with the reference case $\gamma = 1$ using Mesh α at 500 rpm in combination with the SST turbulence model.

Setting γ to one means that the porous domain fully consists of liquid, i.e. that no solid is modelled to contribute to the volume. This parameter is modelled such that no effects on the pressure loss coefficients C_1 and C_2 are considered, and this also means that the modelled pressure drop is the same independently if the volume is modelled to consist of 90% or 0% solid particles. If, however, the porous domain consists of 50% stationary particles the velocities around them must be twice as high compared to a case without porous material. This has nevertheless no direct effect on the superficial velocities.

The flow results for the varying γ values are displayed in Figure 160 and it can be seen that the differences are small, but nevertheless present, between the different porosities. These differences prove however that the γ values have an impact on the flow, which therefore also reveals overseen details of the porous model.

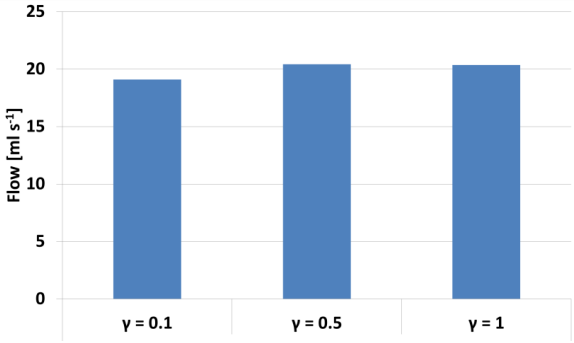

Figure 160. The flows through the porous materials in the Mesh α, 500 rpm and SST setup for varying values of γ.

The first step in investigating the differences in Figure 160 was to visualize the velocities throughout the porous material. The velocities are displayed in Figure 161 and it can be seen that the flow patterns are very similar, but not identical, for the different cases. It must also be noted that the colour legends are scaled with the reciprocal porosities. This means that even if the superficial velocities through the porous material were more or less the same for the different cases the simulated actual velocities through it varied.

The differences in Figure 161 are especially evident at the outlet and Figure 162 is therefore provided in order to display the circumferential velocities in the full reactor. The figure shows that varying values of γ only have small effects on the outer circumferential velocities, and the same is true for the radial and axial velocities (not shown).

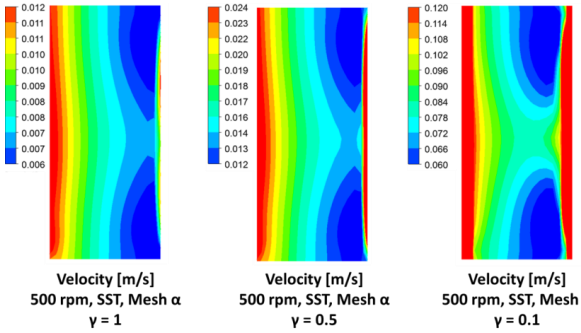

Figure 161. The true velocities through the porous materials corresponding to the flows displayed in Figure 160.

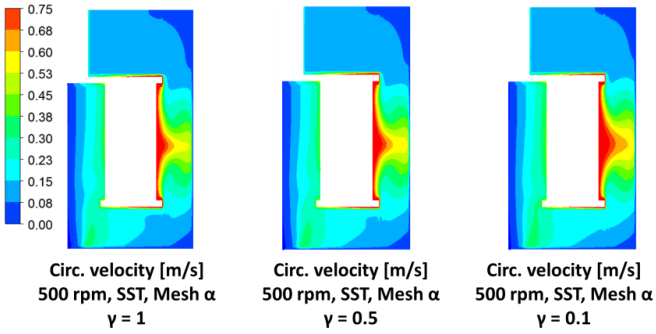

Figure 162. The circumferential velocities in the stator and rotor for the flows corresponding to Figure 161.

The differences in Figure 161 and Figure 162 are nevertheless considered to be important since they reveal the existence of overseen modelling features in the simulation setup. In order to find an explanation for these differences Figure 163 is provided which shows the eddy viscosities and turbulent energy dissipation rates for the varying values of γ.

Figure 163 reveals interesting features at the inlets and outlets of the porous material since the turbulent energy dissipation rates seems to be higher there the lower the values of γ. The eddy viscosities follow also the same trend which should be a direct consequence of the increased turbulence in the regions. Increased turbulence in these regions makes sense from a simulation point of view since the velocities are higher the lower the γ. This should induce increased gradients in the velocity field, and consequently increased production of ε.

This offers a possible explanation for why the eddy viscosities, and therefore also the velocities, differed between the different values of γ. It also reveals that the behaviour of the porous model is somewhat unphysical. It is more reasonable to assume that a lower value of γ, i.e. a higher fraction of fixed solid particles, should have a dampening effect on the turbulence and that the flow through a porous domain should be closer to a laminar regime.

As explained in section 2.4.6 others have solved this problem by modelling the porous domain as laminar or pseudo-laminar while the remaining domains have been simulated with a turbulence model. This was however not possible in ANSYS CFX 15.0 without activating the unsupported beta-features of the software. Variations of alternating eddy viscosities in the

isolated porous domain were therefore instead investigated and is further discussed in section 4.4.8.

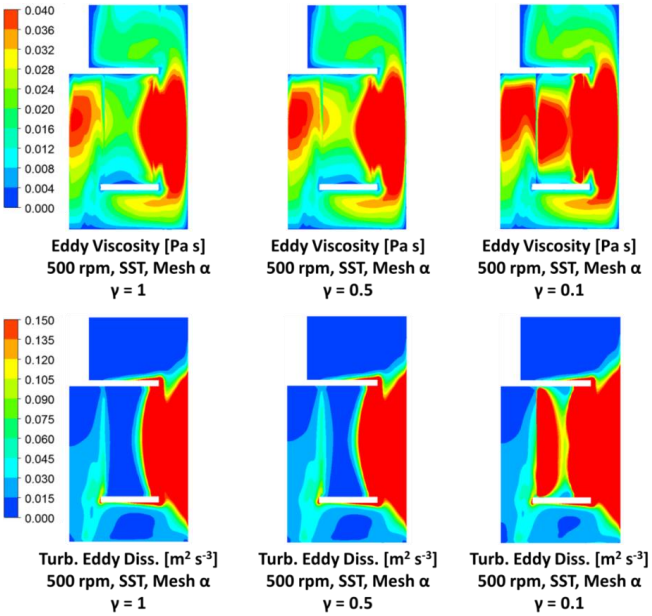

Figure 163. The eddy viscosities and the turbulent energy dissipation rates for the varying *γ* values.

4.4.6. Geometry optimization studies of the simplified geometry

The shape and size of the outer glass vessel was varied in order to investigate if this could have an impact on the flow through the reactor. The flow through the porous material was selected as the most important parameter affecting the ion-exchange reaction rate and was therefore investigated.

Two fundamentally different alternations were performed on the glass vessel. First it was made deeper, meaning that the distances from the bottom of the RBR to the bottom of the vessel were increased. The vessel was furthermore studied with alternating diameters and baffle depths as displayed in Figure 40.

Additionally two-phase simulations were performed to see if the simulated gas-liquid interfaces would be flat for the baffled reactors and curved for the cylindrical vial as reported for the experimental interfaces by SpinChem AB.

4.4.6.1. Impact of depth of the reactor

The cylindrical velocity contours for the vessel depths 1, 2, 3, 5, and 10 cm are displayed in Figure 164. The 1 cm deep reactor is equivalent to the simplified reactor Mesh α from previous sections, and the SST turbulence model and the rotational rate 500 rpm were used for all simulations in the figure. The corresponding flow results, with an addition of the 1.5 and 2.5 cm reactors, are also displayed in Figure 165 where it can be seen that the depth of the reactor had only minor effects on the flow rates through the porous material. In Figure

164 it can nevertheless be seen that the reactors developed different flow patterns, which for example could influence the mixing times. The flows in the upper parts of the reactors in Figure 165 are however, as expected, unaffected by the alternations. Differences in the flow pattern can only be seen in the extended volumes and the vortex region.

The visualised flows in the 5 cm reactor show also a previously overseen detail in the flow. It appears that the lower part of the positive axial velocities in the vortex region is the result of the negative radial velocities approaching the rotationally symmetric axis along the bottom wall of the reactor. Approaching the centre, the negative radial velocities must change direction, and the only option is to change to positive axial velocities. This should be the cause of the most centralized negative axial velocities. The theory is supported by the fact that no centralized negative axial velocities are present in the 10 cm reactor, which also does not have any negative radial velocities along its bottom wall.

It can also be seen in both Figure 164 and Figure 165 that positive axial velocities in the central part of the reactor and flow through the porous material are created regardless if there is a vortex connecting to the bottom of the reactor or not. This means that the porous material has the possibility to drag fluid into it by its own, and that the vortex formed at the bottom is not necessary to create a flow through the RBR.

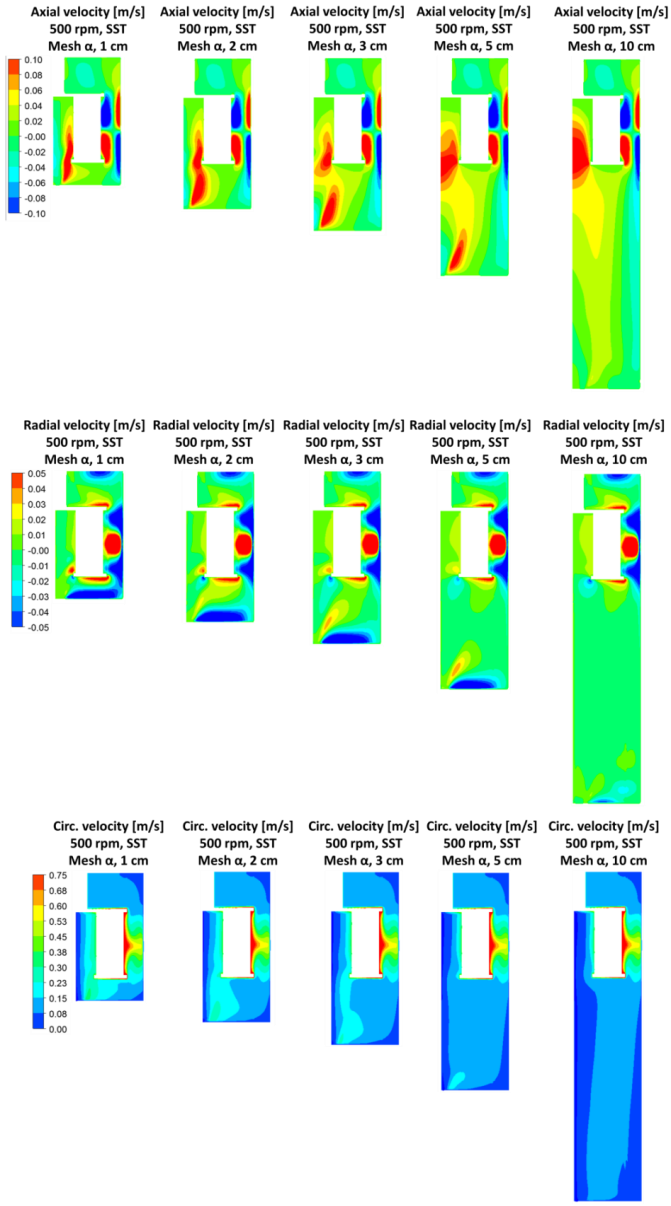

Figure 164. The axial, radial and circumferential velocities for the original Mesh α and the 2, 3, 5 and 10 cm deep reactor designs. The simulations were performed with the SST turbulence model and the rotational speed 500 rpm.

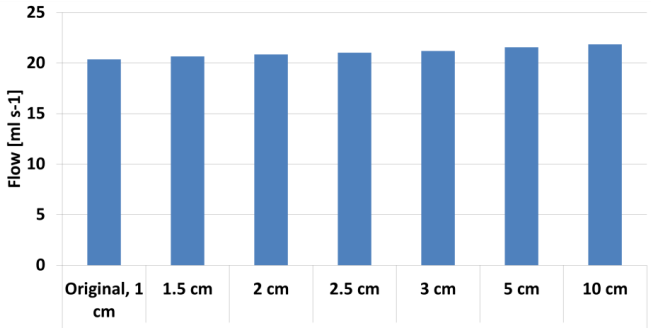

Figure 165. The flow through the reactor for 500 rpm and the SST model and the reactors with varying depths.

A detailed view of the flow streamlines initiated in the vortex region in the original reactor and five of the alternated designs are displayed in Figure 166. The figure confirms that there are no negative axial velocities in the central part of the reactor in the 3, 5 and 10 cm deep designs.

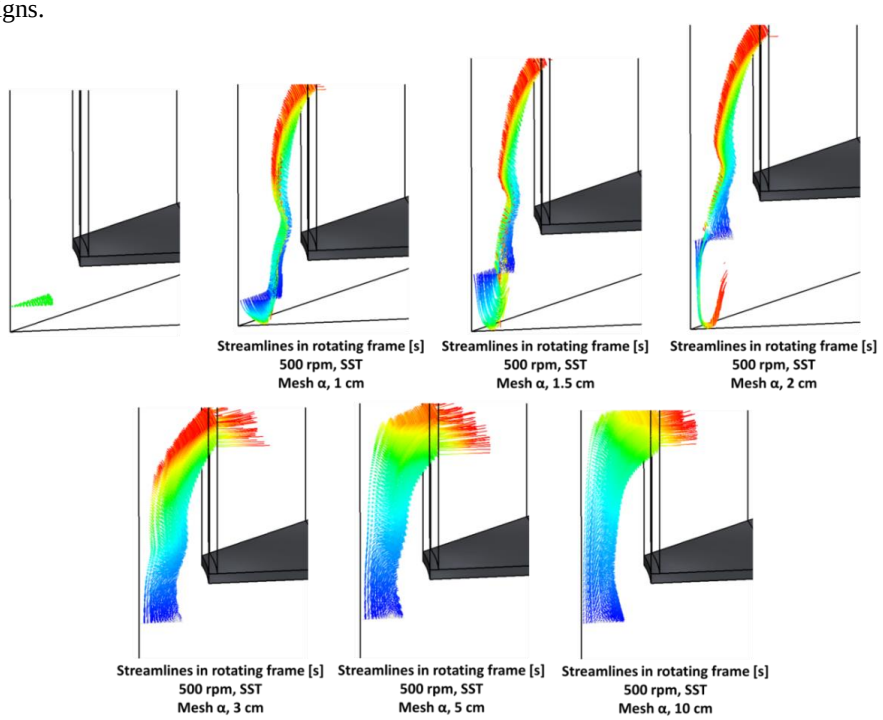

Figure 166. A comparison of the rotating streamlines initiated in the vortex region for reactors with varying depths using the SST turbulence model and the rotational speed 500 rpm.

4.4.6.2. Impact of the reactor width and baffle depth

Two kinds of alternations were applied for changing the width of the reactor designs. One option was to increase the inner radius of the glass vial wall, which was originally 31.1 mm as seen in Figure 34. The other alternative was to change the depth of the baffles, which were

originally 2.1 mm deep. The final designs are summarized in Figure 40 and the corresponding results of the flows through the porous materials are displayed in Figure 167.

The geometry alternations had a substantial effect on the flow through the porous material and the general trend in Figure 167 is that removal of the baffles decreased the flow while making the baffles deeper increased it. This is a very interesting result, especially since the geometrical alternations were not very big, and it suggests that a lot of improvements (or deteriorations) can be achieved by using different vessel designs.

According to Figure 167 a closer distance to the outer wall is also beneficial for the flow through the reactor. This suggests that if there is an aspiration to increase the total fluid volume in the system it is better to add additional volume underneath the RBR rather than around it. The suggestion takes however not into account that the mixing in the bottom of the deepest reactors in Figure 164 probably is quite poor.

In Figure 167 it is also indicated that the presence or absence of baffles in the 75.1 mm design did not matter much but that the baffled wall still performed slightly better than the cylindrical walls at this distance.

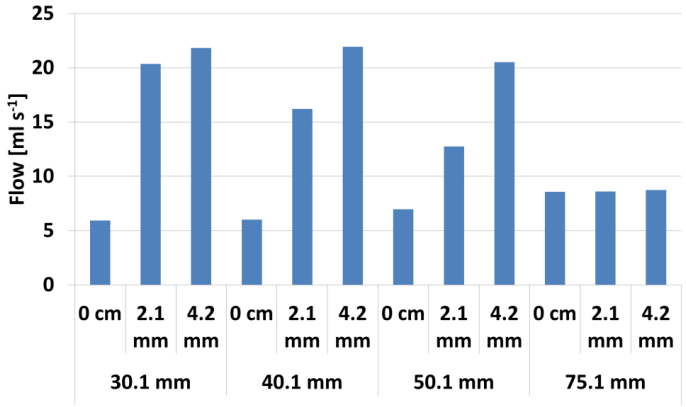

Figure 167. The flows through the porous materials in the reactor designs presented in Figure 40. The original reactor design is the one with the 30.1 mm inner radius and the 2.1 mm deep baffle. The simulations were performed with the SST turbulence model at 500 rpm.

The unbaffled simulation results are however questionable since the very purpose of the baffles is to avoid vortex formation and to keep the top gas-liquid interface flat. Performing one-phase simulations in an unbaffled system with an enforced flat top boundary condition could therefore give misleading results. This topic is further investigated in section 4.4.7, but before this the developed flow patterns in the baffled system will be discussed based on the velocity contours presented in Figure 168 and Figure 169.

Comparing the baffle depths in Figure 168 and Figure 169 it can be seen that the deeper the baffle the more effective the outer wall is in slowing down the circumferential velocities rising from the rotation of the reactor. It can also be seen that the closer the outer wall the more effective is its deceleration effect on the circumferential velocities. This suggests also that the decelerated circumferential velocities are beneficial for the flow through the reactor. The mechanisms can however not be explained at this point, but one potential explanation

could be that the circumferential velocities of the porous outlet are more than twice the ones at the inlet which means that the fluid would need to slow down in order to be able to enter the porous material again.

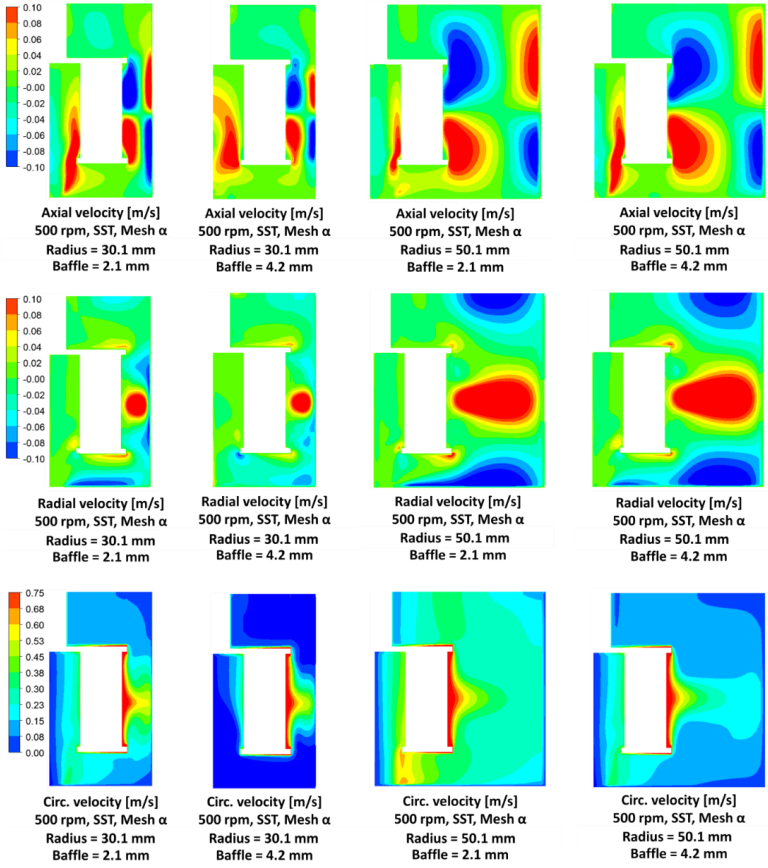

Figure 168. The axial, radial and circumferential velocities for the 30.1 and 50.1 mm radius reactors with the 2.1 and 4.2 mm deep baffles, respectively. The simulations were performed at 500 rpm with the SST turbulence model.

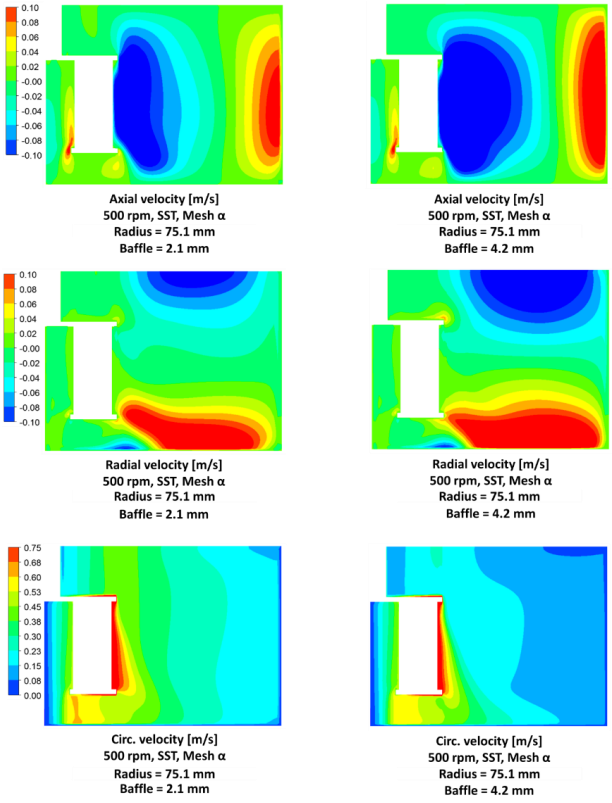

Figure 169. The axial, radial and circumferential velocities for the 75.1 mm radius reactor with the 2.1 and 4.2 mm deep baffles, respectively. The simulations were performed at 500 rpm with the SST turbulence model.

In Figure 169, it can also be seen that a single counter rotating recirculation zone is developed outside of the porous domain. This can be noted via the positive radial velocities in the bottom of the reactor and the negative one at the top in combination with the positive axial velocities at the outer walls and their negative counterparts close to the porous outlet. This pattern differs also from the ones in Figure 168 where two such zones can be seen.

Finally, the developed turbulent energy dissipation fields are displayed for the alternated reactor designs in Figure 170. Most energy is dissipated in the discharge zone as discussed before, but the figure also highlights that the regions just outside the porous domain and at the outer wall have the highest values for the 30.1 and 50.1 mm reactors. For the 75.1 mm reactor most dissipated energy is at the bottom wall, which is fully reasonable since the flow is directed that way.

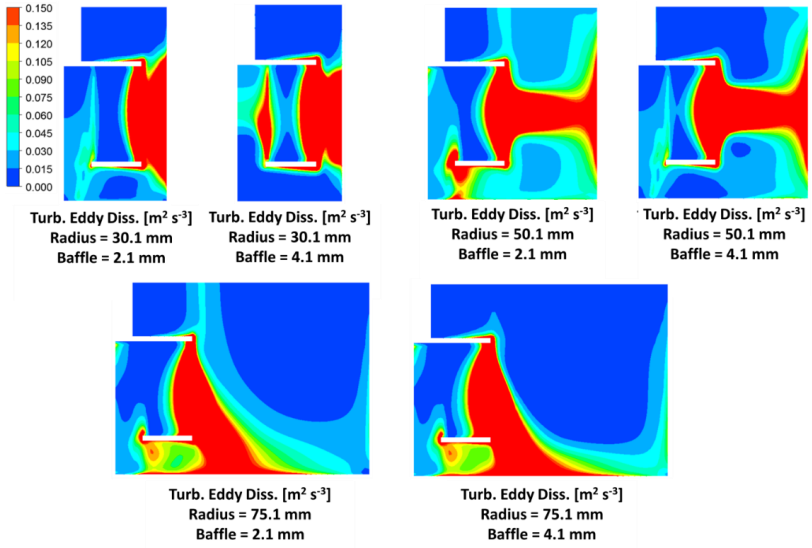

Figure 170. The turbulent energy dissipation rates for the 30.1, 50.1 and 75.1 mm radius reactors with the 2.1 and 4.2 mm deep baffles, respectively. The simulations were performed at 500 rpm with the SST turbulence model.

4.4.7. Two-phase simulations of the rotating bed reactor

Two-phase simulations were as mentioned previously performed in order to see how the gas-liquid interface would be positioned, and to investigate if the one-phase simulations had any overseen disadvantages.

The resulting flows through the porous reactor for the baffled and unbaffled systems are displayed in Figure 171 where shifting from one-phase to two-phase did not have any noticeable effect. This is a promising result since the one-phase simulations are preferred, but the velocity profiles (Figure 172) as well as the eddy viscosity and turbulent energy dissipation rate profiles (Figure 173) were nevertheless investigated.

The appearances of the gas-liquid interfaces are also seen in the two-phase figures since they only display the liquid dominated regions. The interface for the baffled system is almost completely horizontal while the one in the cylindrical reactor has an interface curved similarly as the surface in the magnetically stirred reactor case (section 4.2.3). The principal appearance of the gas-liquid interfaces is also in accordance with experimental observations reported by SpinChem AB. It is also interesting to see that the developed velocity patterns are almost identical between the one and two-phase simulations in Figure 172 except for the top region of the cylindrical reactor.

The eddy viscosity and turbulent energy dissipation rates in Figure 173 are also very similar for the compared cases. However, one important difference are the increased turbulent energy dissipation rates at the gas-liquid interfaces. This phenomenon has been discussed in section 4.2.3.7 and the reappearance of it in this case study implies that it is common in inhomogeneous free-surface simulations.

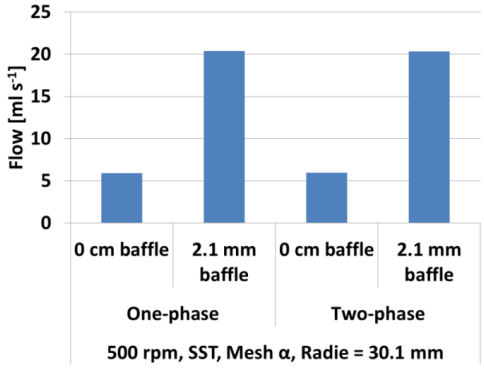

Figure 171. The flows through the porous material for the one and two-phase simulations with the baffled and unbaffled reactors. The simulations were performed at 500 rpm with the SST turbulence model.

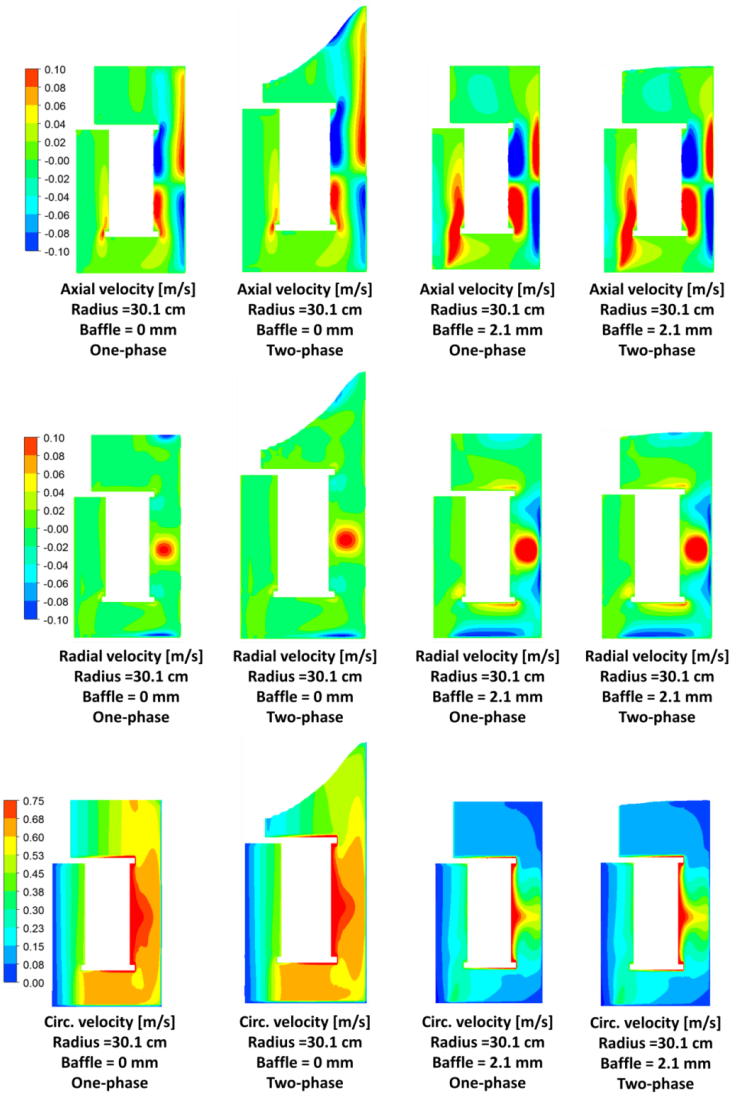

Figure 172. The liquid phase axial, radial and circumferential velocities for the one and two-phase simulations with the baffled and unbaffled reactors. The simulations were performed at 500 rpm with the SST turbulence model.

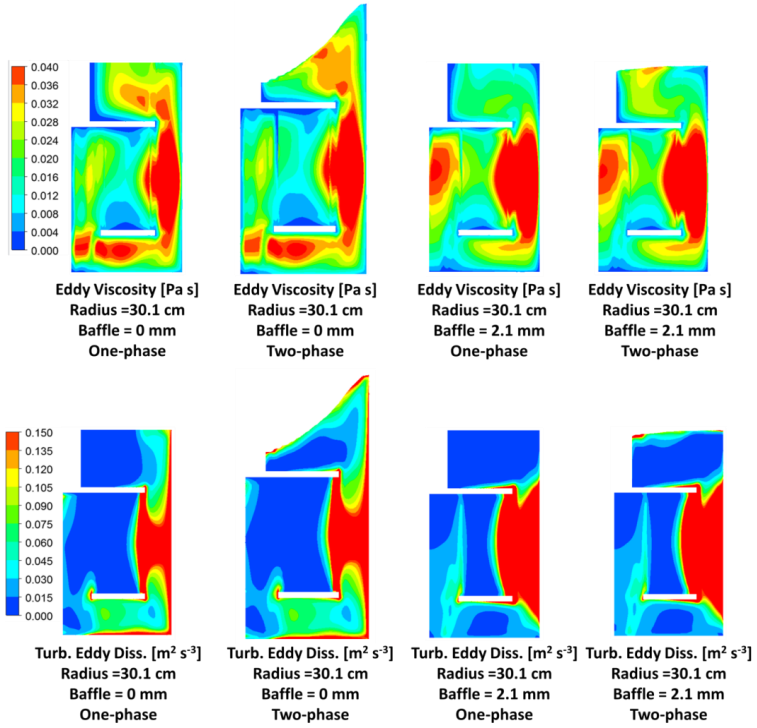

Figure 173. The eddy viscosity and turbulent eddy dissipation rates in the liquid phase for the one and two-phase simulations with the baffled and unbaffled reactors. The simulations were performed at 500 rpm with the SST turbulence model.

4.4.8. Flow and chemical reactions in the isolated porous domain

In the simulations with the isolated porous material, as explained in 3.6.2.2, the inlet velocities were set to match the corresponding flow rates through the porous material taken from the simulations with the simplified reactor. The flow data used for this was the one with Mesh α and the SST model previously displayed in Figure 155. No rotational speeds were therefore used in the simulations of the isolated porous material. The displayed results in this section are however named after their corresponding rotational speed.

4.4.8.1. Steady-state flow pattern and transient mixing time studies

The velocity profiles through the isolated material for 500 rpm, i.e. the simulation with the pre-defined flow rates taken from the 500 rpm simulation, are displayed in Figure 174. The velocities are highest at the inlet and lowest at the outlet, which is explained by increasing cross sectional areas along the geometry.

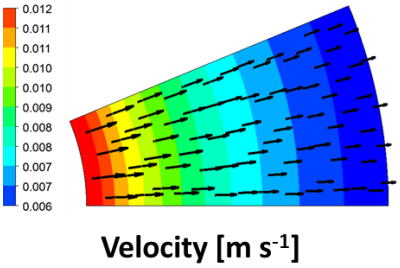

Figure 174. Velocity profiles in the isolated porous domain for 500 rpm, Mesh iii and the SST turbulence model.

Before any chemical reaction in the porous domain was implemented, a few initial mixing time studies (results not shown) were performed. These studies revealed that the turbulence model had an effect on how fast the additional variables were transported through the isolated porous material and that the transport was noticeably higher for the SST model than for the laminar model. This was suspected due to the effect of the eddy viscosities associated with the SST model and this effect was therefore further investigated.

The initial transient studies also revealed that there was almost no difference in how fast the additional variables were transported in the different meshes (Mesh i, ii and iii) using the SST turbulence model and a time-step smaller than or equal to 0.01 s.

The impact of the eddy viscosities was investigated in transient simulations where they were artificially set to various constant values, which means that they were not calculated based on the turbulent quantities. For this, the time-step 0.01 second was used and the results are displayed in Figure 175 and Figure 176. In Figure 175 the distributions of the additional variable after 0.5 seconds are shown for the simulations initiated with no additional variables in the domains and unity concentrations in the inlet flow.

In Figure 175 the fronts between the zero and unity concentrations are more pronounced the lower the eddy viscosities. For the highest evaluated eddy viscosity ($5 \cdot 10^{-1}$ Pa s) the front line is even not detectable. That suggests that the additional variable diffuses faster through the porous domain than it is transported by advection. This is problematic since it most certainly does not happen in reality. The figure also suggests that the simulations with the lowest eddy viscosities (0 and $5 \cdot 10^{-5}$ Pa s) have some numerical difficulties and therefore a lower time step or a finer mesh should have been used.

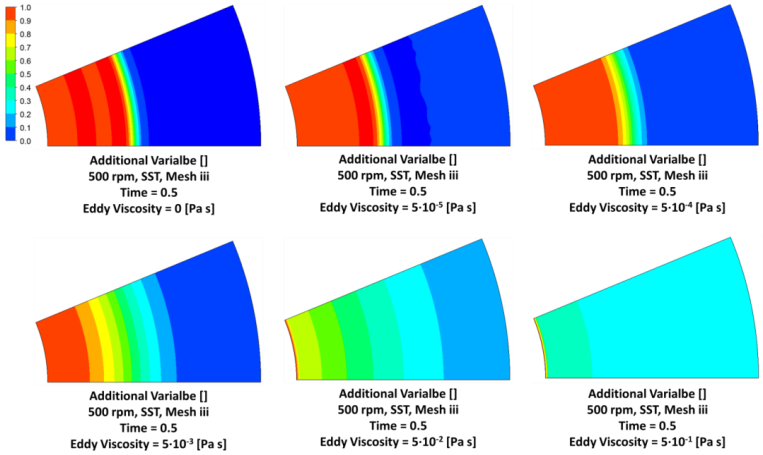

Figure 175. The distribution of the additional variable entering with the concentration 1 from the inlet side for the case corresponding to the rotational speed 500 rpm. The transient simulations were performed on Mesh iii using the time step 0.01 second and the SST turbulence model.

The corresponding mixing times for Figure 175 are displayed in Figure 176, which shows the effect of the different eddy viscosities on the mixing times. The figure shows still how long it took the two monitoring points to reach within the ±10% interval, which in this case is equivalent to the time it took them to reach the value 0.9. The results in Figure 176 complement the results in Figure 175 in showing that higher eddy viscosities decrease the transport times through the porous material.

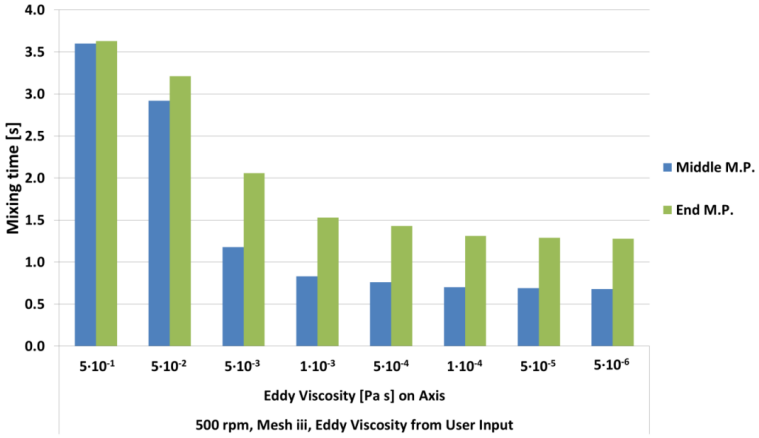

Figure 176. The mixing times corresponding to the setup in Figure 175 but for an altered set of eddy viscosities. The positions of the monitoring points (M.P.) are displayed in Figure 46.

Figure 176 reveals that too high eddy viscosities had an impact on the transport of additional variables through the isolated porous domain. It was therefore interesting to investigate the ranges developed by the SST turbulence model. The developed eddy viscosities in the isolated porous domain are therefore compared in Figure 177 with the values in the porous domain of the simplified geometry. The corresponding velocities are displayed in Figure 178.

Figure 177 exhibits that the eddy viscosities in the isolated porous domain are considerably lower than their counterparts in the porous part of the simplified geometry. This is problematic as discussed before, especially since the values in the simplified geometry most likely are exaggerated. Defining the eddy viscosity values in the isolated porous material to correspond to the values in the porous material in the simplified geometry would therefore be a poor solution. It was therefore instead decided to fix the eddy viscosity value in the isolated porous domains to $5 \cdot 10^{-4}$ Pa s and to investigate the impact of this choice later. The value $5 \cdot 10^{-4}$ Pa s was chosen as a trade-off since it did not have a too big effect on the additional variable transport in Figure 176 compared to the lower values, and since it appeared to be more numerically stable than the lower alternatives in Figure 175.

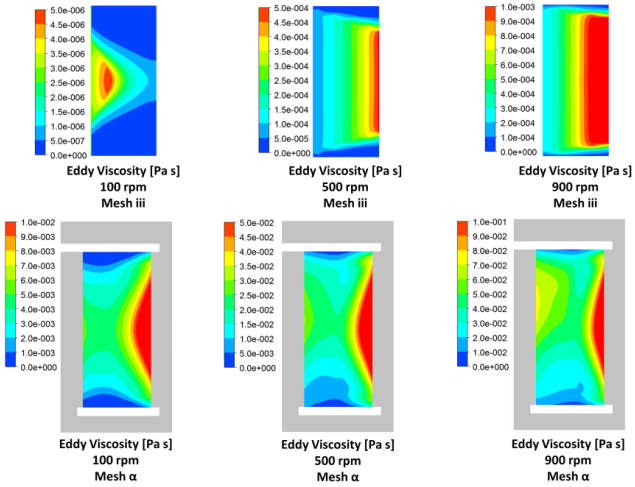

Figure 177. The eddy viscosities developed in the isolated porous material (top row) with the automatic inlet conditions for the turbulent quantities, and the eddy viscosities in the porous material in the simplified reactor (bottom row). In both cases the SST turbulence model were used.

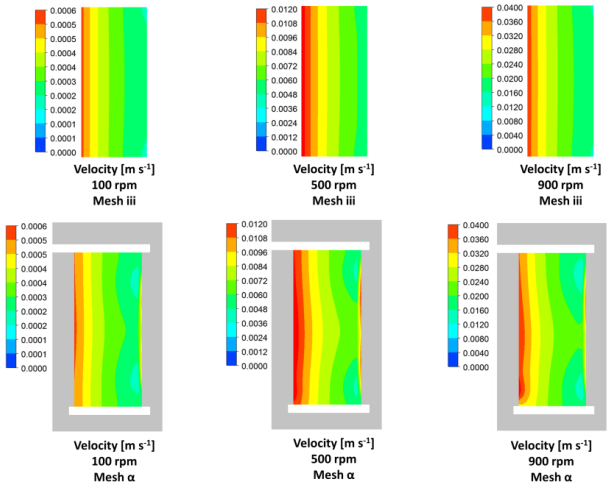

Figure 178. The velocities corresponding to the eddy viscosities in Figure 177.

Despite the varying eddy viscosities, Figure 178 demonstrates that the flow profiles are very similar between the cases. This is probably a consequence of the fact that the inlet rates in the simplified geometry are relatively uniform over the inner interface between the rotating and porous domain. Uniform velocities across the cross-sectional area should also minimize the pressure drops induced by the porous material and were therefore an expected simulation result.

The velocities in the porous domain are important since they dictate the residence time in the catalytic material. They also have a direct effect on the particle Reynolds number, and thereby the Sherwood number, and eventually also the reaction rate constant. The resulting particle Reynolds numbers for the different flows are displayed in Figure 179 and these are also the values used to calculate the varying Sherwood numbers according to the correlations in equation 97 and Figure 44.

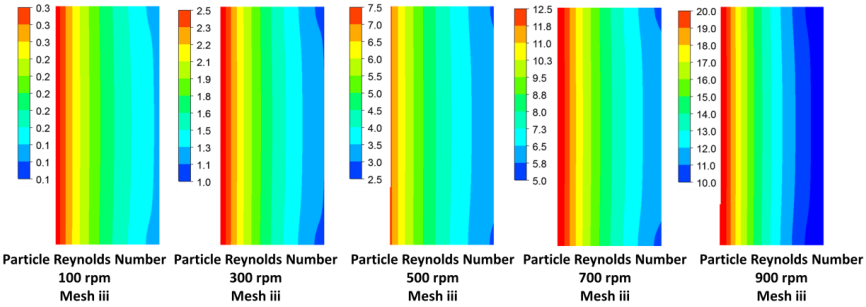

Figure 179. The particle Reynolds numbers developed in the isolated porous domain.

The resulting Sherwood number for the rotational speeds 100, 500 and 900 rpm are displayed in Figure 180. They are calculated based on the correlations in equation 97, but the exponent 0.42 was used instead of 0.41 for *Magnico*. The effect of this error was however considered insignificant for the results. As expected, the Sherwood numbers achieved for *Magnico* are generally lower than those calculated with the *Santos-Moreau* approach, and they have a lower variance. The effect of these Sherwood numbers, in addition to the fixed values 5 and 50, on the resulting chemical reactions is investigated in the two following sections.

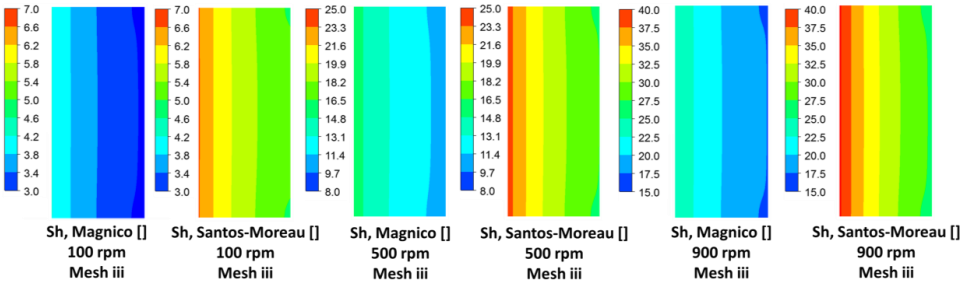

Figure 180. The Sherwood numbers in the isolated porous domain based on the *Magnico* and *Santos-Moreau* correlations from equation 97.

4.4.8.2. Steady-state ion-exchange results

The results from the steady-state ion-exchange simulations for the different rotational speeds and Sherwood number correlations are displayed in Figure 181. Again, the inlet concentrations of the additional variable were set to one, and since the additional variables were reacted inside of the domain, it was actually possible to achieve interesting steady-state simulations.

In Figure 181 all additional variables managed to fully react, i.e. disappear before reaching the outlet, for all Sherwood number correlations for 70, 100 and 300 rpm. This is a direct consequence of the higher residence times in these simulations, since the reaction rates were relatively low due to low particle Reynolds numbers as displayed in Figure 179. For 500 rpm it can however be seen that the concentration of additional variables at the outlet is not zero when the Sherwood number is set to 5, and the same can be seen for the higher rotational speeds where even more of the additional variable is leaving the porous domain unreacted.

It must however be recalled from Table 29 that the residence times are lower the higher the rotational rates are. This means that still more of the additional variable might have reacted per time unit for the higher rotational speeds. This is investigated in Figure 182 and Figure 183, where the flow of reactants (i.e. the additional variables) is calculated at the outlet. The reactants are divided into one reacted and one not reacted fraction, which can be thought of as the Na^+ (i.e. the reacted chemical, or the "product" of the ion-exchange reaction) and H^+ (i.e. the "substrate" in the reaction) in the experiments described in section 3.1.2. In the figures, it can clearly be seen that 900 rpm is the most effective rotational speed, even if it has the lowest fraction of reacted additional variables at the outlet. This outcome also confirms the experimental data in section 4.4.1.

The steady-state solutions are useful in order to compare different Sherwood number correlations and rotational speeds, but they cannot be used to regenerate data similar to the experimental ones in section 4.4.1. This is explained by the additional variable concentrations at the inlet, which are set to one in the steady-state simulations but in reality decrease over time. This is important since the reaction rate is dependent on the substrate concentration in accordance with equation 96, and therefore the transient simulation results are presented in the next section. But first, the eddy viscosity dependence on the reaction rates will be investigated in Figure 184 and Figure 185, which is also a good example of a situation where steady-state simulations were both sufficient and preferred.

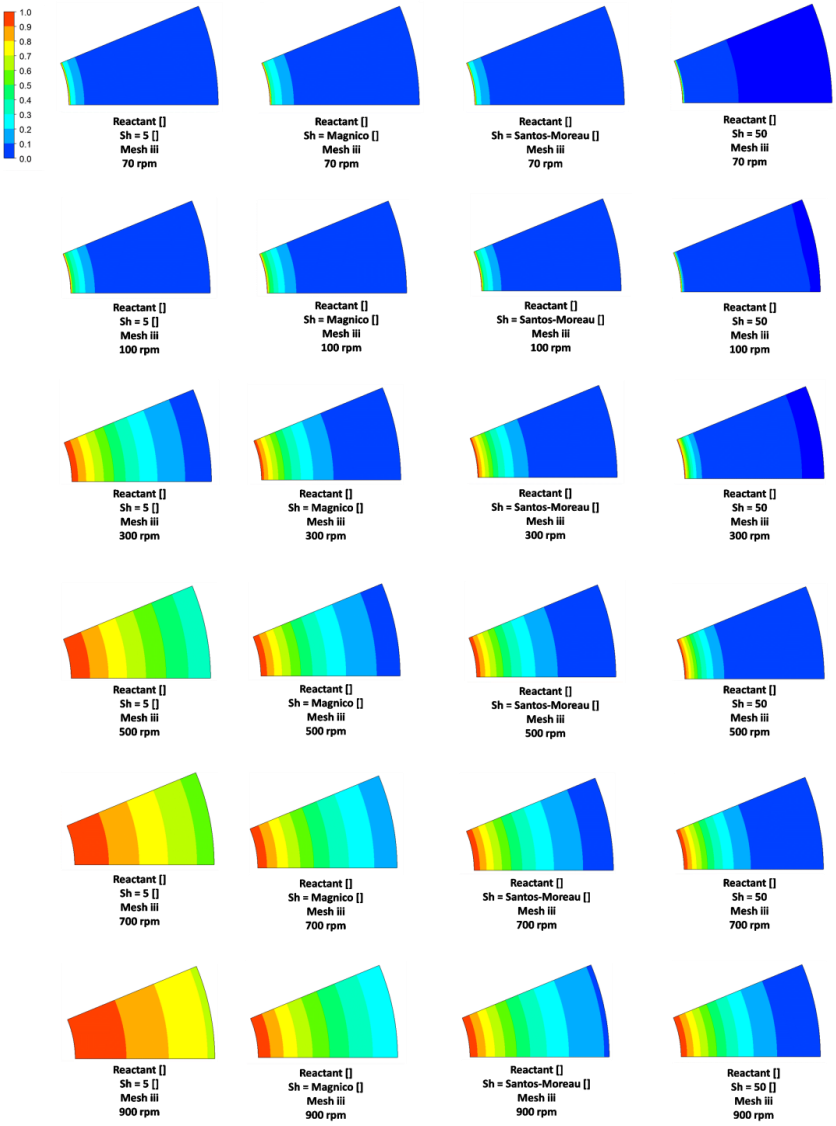

Figure 181. The distributions of reacting additional variables for the investigated varying rotational speeds and Sherwood number correlations. The steady-state simulations were performed with Mesh iii, the SST turbulence model and the eddy viscosity fixed to $5 \cdot 10^{-4}$ Pa s.

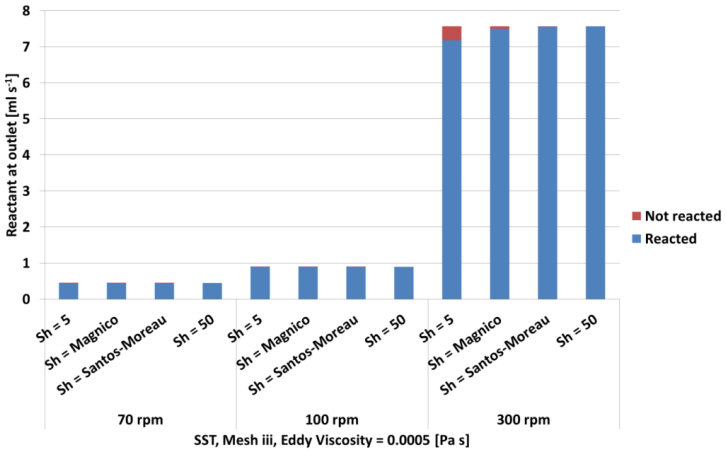

Figure 182. The flow rates of reacted and not reacted additional variables at the outlet in the 70, 100 and 300 rpm cases shown in Figure 181.

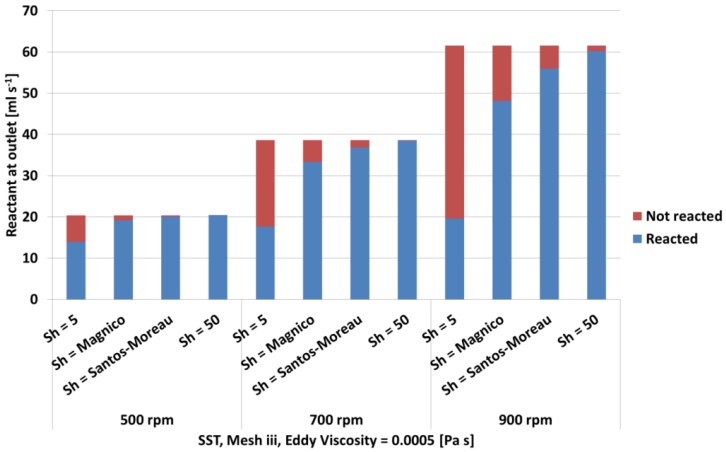

Figure 183. The flow rates of reacted and not reacted additional variables at the outlet in the 500, 700 and 900 rpm cases shown in Figure 181.

In Figure 184 and in Figure 185 the result of setting the eddy viscosity equal to $5 \cdot 10^{-4}$ Pa s was visually the same as if a lower value of the eddy viscosity had been chosen. That is a positive outcome since no turbulence was expected in the porous domain. The figures also show the risk of simulating with a too high eddy viscosity value since the additional variables then diffuse so fast through the domain that they do not have time to react before leaving it.

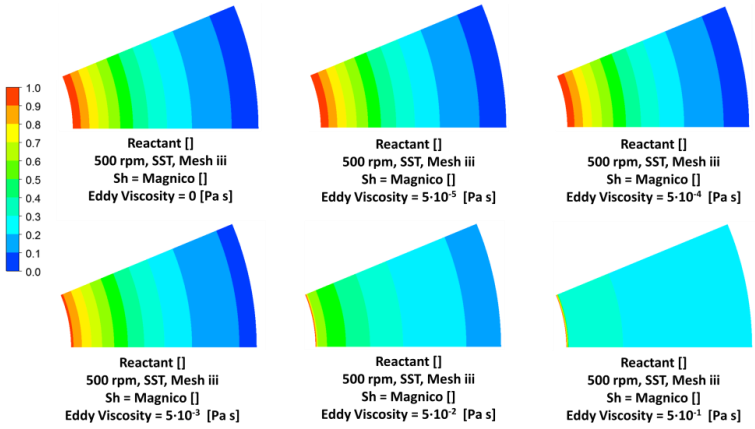

Figure 184. The distributions of reacting additional variables with different constant eddy viscosity values. The steady-state simulations were performed with Mesh iii, the SST turbulence model, 500 rpm and the *Magnico* Sherwood number correlation.

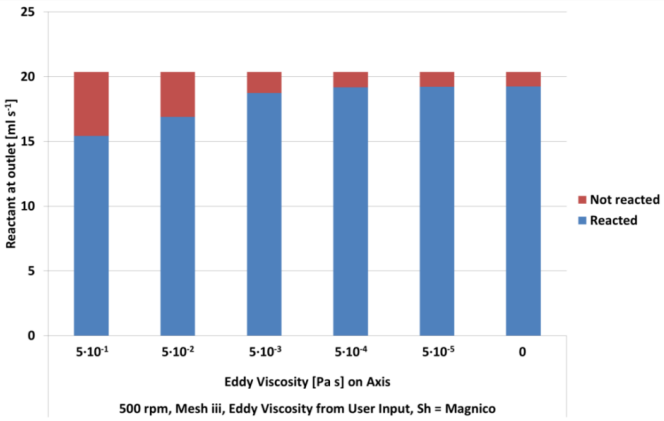

Figure 185. The flow rates of reacted and not reacted additional variables at the outlet in the cases visualised in Figure 184.

4.4.8.3. Transient ion-exchange results

The results for the transient ion-exchange results are displayed in Figure 186 and Figure 187. In these figures, the simulated results are compared to the experimental data previously displayed in Table 27. In the simulated results *85% reacted* means that the concentrations of additional variables had reached down to 0.15 since they were initiated with a dimensionless value of one. It can be seen that the simulations and the experimental data are in good agreement for all simulated rotational velocities. However, it can also be seen that the threshold definition of when a reaction is finished plays a somewhat larger role than the reaction model itself.

The different Sherwood number correlations are performing differently for the varying rotational speeds. For the 900 rpm simulations, it can be seen that the Sherwood number 5 is representing the experimental data best, while the value 50 predicts the overall ion-exchange reaction to be almost twice as fast. For 70 rpm on the other hand, it seems that the reaction

model is not of importance, which is also reasonable based on Figure 181 which shows that all additional variables react in the 70 rpm simulation no matter which reaction model is used.

The proposed model does not take mixing in the outer liquid into account, but it seems from the figures that the perfect mixing assumption was sufficiently precise to represent the general characteristics of the system. This means that the mixing in the free liquid volume of the reactor is fast compared to the material transport and reaction kinetics in the porous material. This result confirms that it is sufficient to model the porous material only, which is much easier than modelling the entire simplified reactor volume.

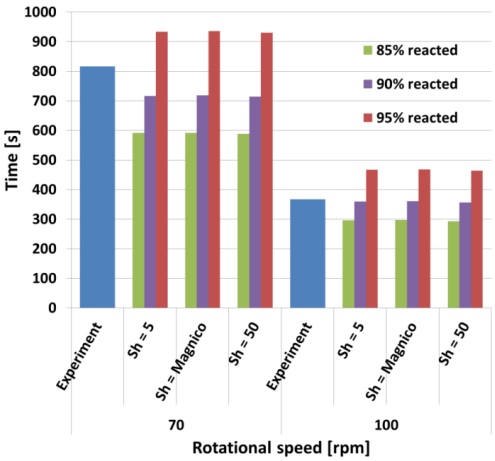

Figure 186. The experimental ion-exchange data for 70 and 100 rpm compared to simulated data for the four Sherwood number correlations. The simulated reaction times were defined as when 85, 90 or 95% of the additional variables had reacted. Mesh iii and the SST turbulence model were used and the eddy viscosity was fixed to $5 \cdot 10^{-4}$ Pa s.

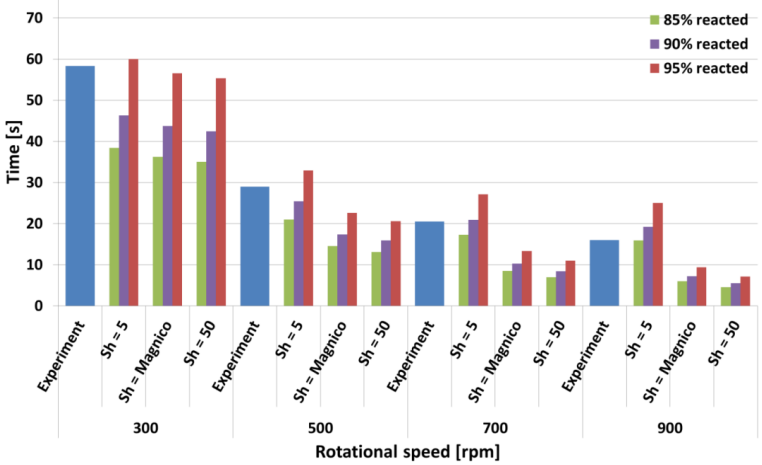

Figure 187. The experimental ion-exchange data for 300, 500, 700 and 900 rpm compared to simulated data for the four Sherwood number correlations. The simulated reaction times were defined as when 85, 90 or 95% of the additional variables had reacted. Mesh iii and the SST turbulence model were used and the eddy viscosity y was fixed to $5 \cdot 10^{-4}$ Pa s.

5. Conclusions and Outlook

5.1. Summary and conclusions

5.1.1. The microbioreactor and the magnetically stirred reactor

For the microbioreactor it was very challenging to achieve converging solutions for most combinations of meshes and tested turbulence models. The k-ε model was the only one which resulted in converged solutions for all evaluated meshes, so this turbulence model was therefore applied despite theoretical concerns that it was not suitable for a flow with such low Reynolds numbers.

The magnetically stirred reactor, which used the same principal modelling setup as the microbioreactor, converged for both the SST and the k-ε model when the inhomogeneous momentum model was used. The main reason for this difference should be the considerably less complex flow pattern in the magnetically stirred reactor. The gas-liquid interface is for example located at a distance from the rotating magnet, and the majority of the rotating magnet reactor geometry is a cylinder with static walls and high quality mesh elements.

The differences between using the homogenous and the inhomogeneous momentum equations were investigated for the magnetically stirred reactor. The homogenous model did not manage to converge and resulted also in an unrealistic appearance of the gas-liquid interface as well as an alternative distribution of turbulent energy dissipation rate compared to the inhomogeneous model. This was an interesting discovery, since the homogenous momentum model is theoretically applicable and since it also has been applied by others e.g. Mahmud et al. (2009) for similar systems.

The eddy cell model combined with the simulated specific areas predicts k_La values close to experimental data both for the microbioreactor and the magnetically stirred reactor. Several theoretical drawbacks of this method are however presented in section 4.1.4 and 4.2.4 and summarized in section 5.1.6. The conclusion for the mixing time simulations for the microbioreactor is similar, i.e. the simulated and experimental mixing times are in the same order of magnitude despite the in section 5.1.4 summarized modelling challenges.

5.1.2. The pilot plant reactor

Both one and two-phase simulations were performed for the pilot plant reactor. For the one-phase flow it was concluded that the choice between the SST and the k-ε model was not critical neither for the velocity fields nor for the volume average energy dissipation rates. For the two-phase simulations the user defined bubble size appeared to have large both direct and indirect impact on the gas holdup and the simulated specific interfacial areas. The direct effect is seen in equation 56 where the specific interfacial area is proportional to the inverse of the user defined bubble diameter. The indirect effect is the impact of the diameter on the drag force, i.e. the momentum transfer between the gas bubbles and the continuous liquid phase, as described by equation 53.

The Grace model was selected to model the parameter C_{Drag} in equation 53. This parameter might also have had an effect on the drag force but this was not investigated. The Grace model as well as the s*ato enhanced eddy viscosity* model were applied in this case study since they were used in a similar case in ANSYS® Academic Research (2013). The Grace model is

however very complex as it appears in the documentation, and regarding the *sato enhanced eddy viscosity* model no mathematical description is provided in the documentation.

This is a general disadvantage with the commercial software used, i.e. that the models often are selected by their name and that no explicit mathematical description of them is given directly in the software. Many models are however explained in the manual, but not all. One advantage with this is that it makes the software more user friendly and easy to learn. Certainly it also decreases the amount of errors the user is allowed to make compared to software where all equations can be manipulated manually.

In the *sato enhanced eddy viscosity* case this information deficiency not only caused a lack of understanding of the model, but it also had consequences for the use of the degassing boundary condition as discussed in section 4.3.3.2. The boundary condition appeared not to function properly for the larger bubble diameters, but since the equations behind it were inaccessible it was not possible to troubleshoot the problem.

Despite the above-mentioned shortcomings in the understanding of the modelling details, the simulations of the pilot plant reactor were overall successful. The expected flow pattern was achieved with upper and lower re-circulation zones, and gas-filled cavities behind the impeller blades were formed in the model. In addition to this the gas holdup trends shown in Figure 109 are comparable to those in Kadic and Heindel (2014) for a radial impeller stirred tank reactor. It was also shown that the simulated average energy dissipation rates decreased with increasing aeration rates which is a behavior explained for example in Nienow (1998). In addition to this the highest energy dissipation rates were also situated around the impeller blades which is also consistent with the work of others, e.g. Ranganathan and Sivaraman (2011).

The mixing simulations for the pilot scale reactor should also be considered successful. The mixing patterns are for example similar to Javed, Mahmud, and Zhu (2006) which visualised the spread of an additional variable on a two dimensional surface for a Rushton impeller stirred reactor. The mixing simulations also explain how the introduction of gas can both facilitate and prolong mixing in a simulation. The simulation also shows that relatively fast mixing can be achieved in the system despite the presence of the two re-circulation zones.

5.1.3. The rotating bed reactor

The use of the simplified reactor design showed that several geometry simplifications can be performed and still the general flow characteristics of the system are captured. This is a considerable result, since it can save a lot of time both computational and for the mesh generation. The simplified reactor design was also much easier to vary for the geometry optimization studies.

The two-phase simulations for the RBR showed that the gas-liquid interface was kept relatively horizontal for the baffled vessel, and that a vortex was formed for the cylindrically shaped vessel. This induced confidence for the use of the free-surface model since the interfaces behaved accordingly during experimental studies. The close similarities for the flow fields in the one and two-phase simulations for the baffled reactor confirmed furthermore that it was reasonable to simulate only the liquid phase, which simplified the simulations significantly. Furthermore, the geometry optimisation studies showed that the design of the reactor vessel is a very important issue for the rotating bed reactor, and that a

narrow and baffled design is preferred in order to optimize the flow throughout the porous material.

The implementation of the isolated porous domain and the kinetic model was successful such that the simulated and experimental data correlated well as shown in Figure 186 and Figure 187. However, the figures also illustrate shortcomings of the modelling approach. The definition of the simulated finishing time, i.e. 85, 90 or 95% completed reaction, is for example very important for the result. It is also meaningful to remember that the values of the reactive additional variables in the simulation range from one to zero, while experimental H^+ concentrations are calculated to start at $3.27 \cdot 10^{-3}$ mol/l and to cause a colour shift at $1.6 \cdot 10^{-6}$ mol/l. The final H^+ concentration in the experimental liquid is also not zero, which is also a complicating factor in the modelling of the reaction.

Figure 186 and Figure 187 demonstrate that the modelled Sherwood numbers have a large impact on the reaction times, especially for the higher rotational rates. This is important to acknowledge since the Sherwood numbers were modelled differently in all literature sources presented in section 2.4.6. The Sherwood number is also only one of several parameters in equation 96 which describes the chemical reaction rate implemented in the model. The remaining parameters, i.e. the mass diffusion coefficient, the porous particle diameter and the specific interfacial area of the porous particles were kept constant throughout the simulations in this project. It must nevertheless be remembered that the particle diameter was estimated based on relatively scarce information from the resin product data sheet. The particle diameter is also a parameter in equation 67, which is used for the calculation of the specific interfacial areas. This equation uses furthermore an estimated void volume fraction. The equation also assumes solid, spherical particles with their entire outer surface available for ion-exchange.

The simulation of the rotating bed reactor was the most novel of the four case studies since the simultaneous modelling of chemical reactions and fluid transport in a rotating bed reactor has not been published before to the best of my knowledge. The case study, as presented in this thesis and in Schjøtt Andersen (2015), is therefore a fundament on which further studies can build.

5.1.4. The mixing simulations

The literature review in section 2.4.5 exemplifies the wide range of possibilities available for CFD modelling of mixing times. The diversity could be interpreted as an absence of consistency within the CFD community, but it is also important to realize that standardizing mixing simulations is not reasonable. Mixing experiments are for example performed in a similar variety and in order to mimic such investigations also the simulation approaches must differ. How additional variables are introduced in a system and monitored must also be unique for each specific geometry.

The choice to use monitoring surfaces rather than monitoring points in mixing simulation as implemented in Johnson, Natarajan, and Antoniou (2014) is an interesting suggestion which should be considered in future work. The benefit of this approach should result in more consistent and less location dependent mixing times. In section 4.1.5.5 it was for example noticed that the exact position of the monitoring point was important for the virtual measurements of the concentrations of an additional variable for the laminar and the SST simulations.

The drawback of using monitoring surfaces is that they cannot be defined directly in ANSYS CFX 15.0. Monitoring surfaces can however be implemented if the surfaces are created in the geometry and mesh generation step, but this makes their positioning less flexible and more time consuming to change. Monitoring surfaces can also be defined in the post-processing unit of the software but that requires more data to be saved in each transient simulation step compared to the monitoring point method applied in this project.

The conclusion for the mixing simulations for the microbioreactor case study is that the simulated mixing times were all close to the experimental values. It was however discovered that it was necessary to visualize the mixing in several different ways in order to understand the flow characteristics and to explain unexpected phenomena. It was also useful that the mixing times were defined in several different ways, i.e. as 5, 10, and 15% and not only as one of these options.

One example of this the is 5% mixing time for the monitoring point at 400 and 600 rpm displayed in Figure 68. If the 10% and 15% definitions would not have been included, and if intuition and experimental data would not have indicated that the 600 rpm simulation should mix faster, it could easily have been concluded that the 400 rpm simulation had lower mixing times without further considerations. Now this phenomenon was instead investigated in detail, and the obstacle with too high additional variable concentrations in regions not dominated by the liquid phase was discovered. This conclusion would also have been very hard to settle without Figure 72, which stresses the importance and usefulness of the visualization tools available in the software.

The same is true for the 800 and 1000 rpm simulated mixing times in Figure 68, which could have been interpreted as that 1000 rpm mixes much slower than 800 rpm. This conclusion was however disregarded after visualizing the distribution of the additional variables over time in Figure 70. The conclusion was consequently that the behavior most likely was a simulation artefact caused by the frozen velocity fields.

A final example of why it is not enough to only determine the mixing time based on single monitoring point values is presented in section 4.1.5.5. In Figure 73 it can be interpreted that the mixing behaviours in the laminar and the k-ε model are almost identical at 400 rpm if only the monitoring point values for 5% and 10% are considered. Figure 74 and Figure 75 reveal however that their similarities are only a coincidence. This demonstrates again the danger of only reporting the mixing time from one defined monitoring point without further investigation of the mixing patterns.

5.1.5. Choice and impact of the turbulence model

One major conclusion regarding the choice of turbulence model in this project is that it was not equally important in the different case studies. In the microbioreactor, the k-ε model was for example the only evaluated turbulence model which converged. For the magnetically stirred reactor both the SST and the k-ε model had converging solutions with similar velocity fields, but the depths of the developed vortexes and the distributions of ε differed. This is for example illustrated in Figure 84 and Figure 86.

For the pilot plant reactor the choice between the SST and the k-ε model had only a minor effect on the distributions of ε (Figure 106 and Figure 108). The average values of ε were also very similar between the two models (Figure 107). No major impact could neither be seen for

the velocity fields (Figure 98 and Figure 99) even if the simulated eddy viscosity values (Figure 101 and Figure 102) differed slightly for the two turbulence models. For the rotating bed reactor the choice of turbulence model had an impact on the vortex formation underneath the reactor (Figure 144) and on the developed eddy viscosities (Figure 146) but not on the mass flow rates through the porous material (Figure 145).

It was also noted that the choice between using the homogenous and the inhomogeneous momentum model had an impact on the distribution of ε at the gas-liquid interface as displayed in Figure 92. This is an important discovery, since it unfortunately prooves that at least one of the models miscalculates ε. The choice between the RNG k-ε model and the k-ε model also gave different results for ε in Magnico and Fongarland (2006). This is problematic if calculating correct ε values is of interest, for instance when they are used directly in the eddy cell model.

Another conclusion from the literature review is that there is no clear consistency regarding which turbulence models are applied for different flows and applications. The free-surface flow in 50-150 ml shake flasks were for example modelled with the RNG k-ε turbulence model in Li et al. (2013) while 25-100 ml filling volume shake flasks were modelled in Zhang et al. (2005) without any turbulence model mentioned. Lamping et al. (2003) also presented a 6 ml dispersed system which is simulated with the k-ε turbulence model, and Allonneau et al. (2015) evaluated the laminar, SST and k-ε models for a 10 ml magnetically stirred reactor. This means that using the k-ε turbulence model is not completely uncommon for flows that are most likely not fully turbulent.

5.1.6. Considerations using the eddy cell model

The eddy cell model has, as presented in the literature review section, been extensively used in the scientific literature for the estimation of the mass transfer coefficient k_L. The energy dissipation rate ε has most often been taken directly from the applied turbulence model, and k_La has been calculated by multiplication of the simulated specific interfacial area a. The proportionality constant in the eddy cell model is occasionally defined as a fixed value, often 0.4 or $2/\sqrt{\pi}$, or set to a case specific constant value in order to provide the best fit between experimental and simulated data. With the latter approach, the methodology was also able to simulate k_La values close to experimental data for the microbioreactor and magnetically stirred reactor in this project.

The use of the eddy cell model is however not straight-forward since the values of ε are dependent on which turbulence model is used. For free-surface simulations it is also dependent on if ε is defined as the gas-liquid interface average or the liquid-phase averaged value. In addition to this the value for the proportionality constant C_P is also dependent on the simulated specific interfacial areas, which are just as ε seldom verified with experimental data. A harsh interpretation of the eddy cell model is therefore that it is the multiplication of two not experimentally verified parameters that are correlated with a user defined proportionality constant in order to provide the best match to experimental data.

A similar thought is presented in the literature review, where Wang and Wang (2007) state that Sheng, Meng, and Fox (2000) claim that the reasons for inconsistencies in the determination of the proportionality constant between different cases is explained by the difficulties to determine the turbulent energy dissipation rates.

Disqualifying the use of the eddy cell model with the motivation that the turbulence models might miscalculate the energy dissipation rates is however problematic, especially if it is done without suggesting an alternative model. Also, even if the use of the model suffers from severe shortcomings it must be weighed against not having a model at all.

5.2. Outlook and Further Work

The most important future work related to this thesis should be to disseminate awareness of the possibilities and challenges with CFD modelling within the chemical engineering community. The reason for this is that CFD offers many interesting opportunities but that the users must be aware of its limitations.

One example of this is the energy dissipation rate in a fluid, which is a mutual interest between turbulence modelling experts and chemical reactor engineers. All mechanical energy added to a fluid, for example by an impeller, must be dissipated somewhere in the fluid and for a turbulent system most is dissipated in the smallest turbulent eddies. The turbulent energy dissipation rate ε is also what is simulated for example in the commonly used k-ε turbulence model. It is however important to know that there is no inherent connection between the simulated values of ε and the actual energy dissipation in the liquid – especially not if an inappropriate turbulence model is applied. This is especially important when the eddy cell model is applied where ε is a direct input variable.

One important part of the suggested future work is therefore to bring attention to the potential shortcomings of the use of the eddy cell model in CFD. This should however be conducted with care in order not to underestimate the power of CFD modelling. The challenge is to balance the wide range of valuable potential for CFD modelling of chemical and biochemical reactors without creating an overestimation of the limited potential.

The impact of modelling decisions made by the user must also be properly communicated, and examples of this were found in each investigated case study. In the pilot plant reactor, it was for example seen that the simulated specific interfacial areas were highly dependent on the user defined bubble diameters. The equivalent was true for the rotating bed reactor where the user defined particle diameter had a large impact on the modelled reaction rates. For the magnetically stirred reactor the choice between the inhomogeneous and homogenous momentum model also appeared to be important for the value of ε at the gas-liquid interface. The user defined classifications for completed mixing and ion-exchange were also important, e.g. if the limits should be the 5, 10, or 15% from the final values.

The benefits of CFD should also be highlighted. It was for example possible to model, visualise, and calculate the area of the gas-liquid interfaces in the microbioreactor and magnetically stirred reactor case studies. Achieving this with any method other than CFD is hard to imagine. The same is true for the gas holdup and specific interfacial areas in the pilot plant reactor, i.e. that even if the CFD model is sensitive to the user defined bubble diameter it should be considered as the most reliable available tool for simulating and visualising gas distributions in stirred tank reactors.

For the microbioreactor and the magnetically stirred reactor the model proposed in equation 106 should be validated by extending the range and number of investigated agitation rates. The purpose of this would be to a gain a larger set of experimental and simulated data to correlate the two new model parameters. The proposed equation 106 is however still based on the eddy cell model for modelling of the turbulence dependent part of k_L. The challenges discussed in this thesis concerning the use of the eddy cell model should therefore first be carefully considered.

The work for the magnetically stirred reactor should also be extended to other magnet shapes and vessel sizes and a wider range of volumes in a fixed setup could also be investigated. The

focus of this extended study could be a wider range of specific interfacial areas and varying expected values of ε at the interfaces. It is for example likely that interfaces located closer to the rotating magnet have higher averaged values of ε.

If the work with the microbioreactor is extended, for example in order to investigate a wider range of turbulence models, it is advisable to simplify the geometry of the paddles to an easier design to allow the use of a high quality mesh for the simulation. This advice should actually be applied to most complicated geometries if it is not clear which models to include. A large amount of alternatives can then be evaluated for the simpler mesh and only a few selected candidates need to be simulated for the more complicated geometry.

Future work regarding the pilot scale reactor is to compare the simulated mixing times and oxygen transfer rates to experimental data. This includes also to find a case specific value of the proportionality constant C_{P1} in equation 78. The total gas holdup in the reactor can also be experimentally investigated by monitoring the height of the aerated liquid. Likewise, the simulated values of ε can be compared with the experimental estimations of the power input. Alternative methods of evaluating k_L could also be considered for the pilot scale reactor, for example by applying equation 79 which takes the bubble slip velocity into account rather than ε.

The implementation of a population balance model could also be considered for the pilot plant reactor. Options for this are already available in ANSYS CFX 15.0 where modelling of breakup and coalescence phenomena between bubbles can be simulated. Modelling of a non-Newtonian liquid in the pilot scale reactor should also be considered.

For the rotating bed reactor, it would be interesting to validate the simulated kinetic model for a controlled flow through a packed bed. It could also be valuable to validate the pressure drop profile from the material data sheet. An experimentally confirmed pressure drop coefficient and a validated kinetic model would increase the confidence in the simulated flows through the porous material of the rotating bed reactor which is otherwise hard to validate experimentally.

Additional ion-exchange experiments should be performed for a wider range of vessels in order to seek validation of the geometry optimization studies stating that a narrow vessel is beneficial for the flow through the porous material. Alternative setups could also be considered, for example by fixing the porous material to an inner or outer region inside the packed bed rector or by using resins with different diameters or pressure drop characteristics.

6. References

Allonneau, Charline, Eric Olmos, Stéphane Guyot, Eric Ferret, Patrick Gervais, and Rémy Cachon, 2015, Hydrodynamic characterization of a new small-scale reactor mixed by a magnetic bar, *Biochemical Engineering Journal* 96, 29–37.

Alves, S. S., C. I. Maia, and J. M T Vasconcelos, 2004, Gas-liquid mass transfer coefficient in stirred tanks interpreted through bubble contamination kinetics, *Chemical Engineering and Processing: Process Intensification* 43, 823–830.

ANSYS Inc., 2011, *Turbulence Modeling* (http://www.ansys.com/staticassets/ANSYS/staticassets/resourcelibrary/brochure/ANSYS-Turbulence.pdf).

ANSYS® Academic Research, 2013, Release 15.0, Help System, CFX: CFX-Solver Manager User's guide, *ANSYS, Inc*.

ANSYS® Academic Research, 2013, Release 15.0, Help System, CFX: Theory Guide, *ANSYS, Inc*.

ANSYS® Academic Research, 2013, Release 15.0, Help System, Fluent: Theory Guide, *ANSYS, Inc*.

ANSYS® Academic Research, 2013, Release 15.0, Help System, CFX: Modeling Guide, *ANSYS, Inc*.

ANSYS® Academic Research, 2013, Release 15.0, Help System, CFX: Tutorials: Free Surface Flow Over a Bump, *ANSYS, Inc*.

ANSYS® Academic Research, 2013, Release 15.0, Help System, CFX: Tutorials: Multiphase Flow in a Mixing Vessel, *ANSYS, Inc*.

ANSYS® Academic Research, 2013, Release 15.0, Help System, CFX: Modeling Guide, *ANSYS, Inc*.

ANSYS-bloggen, *ANSYS Tutorial: Time Operations in CFX* (http://www.edr.no/blogg/ansys_bloggen/ansys_tutorial_time_operations_in_cfx).

Appa, H., D. a. Deglon, and C. J. Meyer, 2013, Numerical modelling of mass transfer in an autoclave, *Hydrometallurgy* 147-148, 234–240.

Bolic, Andrijana, Ulrich Krühne, Rasmus A Prior, Tobias Vilby, Siewert Hugelier, Anna Eliasson Lantz, and Krist V Gernaey, 2012, One-Millilitre Microbioreactor with Impeller for Improved Mixing, *One-Millilitre Microbioreactor with Impeller for Improved Mixing*.

Brüning, Stefanie, 2012, *Strömungssimulation Als Werkzeug Zur Bioreaktorcharakterisierung*.

Brüning, Stefanie, and Dirk Weuster-Botz, 2014, CFD analysis of interphase mass transfer and energy dissipation in a milliliter-scale stirred-tank reactor for filamentous microorganisms, *Chemical Engineering Research and Design* 92, 240–248.

Carberry, J J, 1964, Designing Laboratory Catalytic Reactors, *Industrial & Engineering Chemistry* 56, 39–46.

Coroneo, M., G. Montante, A. Paglianti, and F. Magelli, 2011, CFD prediction of fluid flow and mixing in stirred tanks: Numerical issues about the RANS simulations, *Computers & Chemical Engineering* 35, 1959–1968.

Danckwerts, P V, 1951, Significance of liquid-film coefficients in gas absorption, *Industrial & Engineering Chemistry* 43, 1460–1467.

Deen, Niels G, Tron Solberg, and Bjørn H Hjertager, 2002, Flow generated by an aerated Rushton impeller: two-phase PIV experiments and numerical simulations, *The Canadian Journal of Chemical Engineering* 80, 1–15.

Doran, P M, 1995, *Bioprocess Engineering Principles* (Elsevier Science).

Dwivedi, P Nfffe, and S N Upadhyay, 1977, Particle-fluid mass transfer in fixed and fluidized beds,

Industrial & Engineering Chemistry Process Design and Development 16, 157–165.

Eibl, Regine, Sören Werner, and Dieter Eibl, 2009, Bag bioreactor based on wave-induced motion: Characteristics and applications, *Disposable bioreactors* (Springer).

Elqotbi, M., S.D. Vlaev, L. Montastruc, and I. Nikov, 2013, CFD modelling of two-phase stirred bioreaction systems by segregated solution of the Euler–Euler model, *Computers & Chemical Engineering* 48, 113–120.

Garcia-Ochoa, Félix, and Emilio Gomez, 2004, Theoretical prediction of gas–liquid mass transfer coefficient, specific area and hold-up in sparged stirred tanks, *Chemical engineering science* 59, 2489–2501.

Gimbun, J., C. D. Rielly, and Z. K. Nagy, 2009, Modelling of mass transfer in gas-liquid stirred tanks agitated by Rushton turbine and CD-6 impeller: A scale-up study, *Chemical Engineering Research and Design* 87, 437–451.

Haque, J. N., T. Mahmud, K. J. Roberts, J. K. Liang, G. White, D. Wilkinson, and D. Rhodes, 2011, Free-surface turbulent flow induced by a Rushton turbine in an unbaffled dish-bottom stirred tank reactor: LDV measurements and CFD simulations, *The Canadian Journal of Chemical Engineering* 89, 745–753.

Haque, Jennifer N, Tariq Mahmud, Kevin J Roberts, and Dominic Rhodes, 2006, Modeling Turbulent Flows with Free-Surface in Unbaffled Agitated Vessels, *Industrial & Engineering Chemistry Research* 45, 2881–2891.

Hartmann, H., J.J. Derksen, C. Montavon, J. Pearson, I.S. Hamill, and H.E.A. van den Akker, 2004, Assessment of large eddy and RANS stirred tank simulations by means of LDA, *Chemical Engineering Science* 59, 2419–2432.

Hennig, T., J. Grän-Heedfeld, and G. Deerberg, 2007, Simulation der Strömung in Fermentern von Biogasanlagen, *Chemie Ingenieur Technik* 79, 643–650.

Higbie, R, 1935, The rate of absorption of a pure gas into a still liquid during short period of exposure, *Trans. Am. Inst. Chem. Eng* 31, 365–389.

Hinze, J O, 1959, *Turbulence New York* (McGraw-Hill).

Hung, LP, CS Garbe, and WT Tsai, 2010, Validation of Eddy-renewal model by numerical simulation, in Satoru Komori, in Wade McGillis, and in Ryoichi Kurose ed.: *Gas transfer at water surfaces* (Kyoto University Press).

Jahoda, M., L. Tomášková, and M. Moštěk, 2009, CFD prediction of liquid homogenisation in a gas-liquid stirred tank, *Chemical Engineering Research and Design* 87, 460–467.

Javed, K.H., T. Mahmud, and J.M. Zhu, 2006, Numerical simulation of turbulent batch mixing in a vessel agitated by a Rushton turbine, *Chemical Engineering and Processing: Process Intensification* 45, 99–112.

Johnson, Chris, Venkatesh Natarajan, and Chris Antoniou, 2014, Verification of energy dissipation rate scalability in pilot and production scale bioreactors using computational fluid dynamics., *Biotechnology progress* 30, 760–4.

Kadic, Enes, and Theodore J Heindel, 2014, *An Introduction to Bioreactor Hydrodynamics and Gas-Liquid Mass Transfer* (John Wiley & Sons).

Kaiser, Stephan C., Christian Löffelholz, Sören Werner, and Dieter Eibl, 2011, CFD for characterizing standard and single-use stirred cell culture bioreactors, in Igor Minin ed.: *Computational Fluid Dynamics Technologies and Applications* (InTech - Open Access Publisher).

Kaiser, Stephan Christian, 2014, *Characterization and Optimization of Single-Use Bioreactors and Biopharmaceutical Production Processes Using Computational Fluid Dynamics*.

Kawase, Y, B Halard, and M Moo-Young, 1992, Liquid-phase mass transfer coefficients in bioreactors., *Biotechnology and bioengineering* 39, 1133–1140.

Kerdouss, F., a. Bannari, P. Proulx, R. Bannari, M. Skrga, and Y. Labrecque, 2008, Two-phase mass transfer coefficient prediction in stirred vessel with a CFD model, *Computers & Chemical Engineering* 32, 1943–1955.

Khopkar, Avinash R., and Vivek V. Ranade, 2006, CFD simulation of gas–liquid stirred vessel: VC, S33, and L33 flow regimes, *AIChE Journal* 52, 1654–1672.

Kolmogorov, Andrey Nikolaevich, 1941, The local structure of turbulence in incompressible viscous fluid for very large Reynolds numbers, *Dokl. Akad. Nauk SSSR*.

Kumaresan, T., and Jyeshtharaj B. Joshi, 2006, Effect of impeller design on the flow pattern and mixing in stirred tanks, *Chemical Engineering Journal* 115, 173–193.

Laakkonen, M., P. Moilanen, V. Alopaeus, and J. Aittamaa, 2007, Modelling Local Gas–Liquid Mass Transfer in Agitated Vessels, *Chemical Engineering Research and Design* 85, 665–675.

Laakkonen, Marko, Ville Alopaeus, and Juhani Aittamaa, 2006, Validation of bubble breakage, coalescence and mass transfer models for gas–liquid dispersion in agitated vessel, *Chemical Engineering Science* 61, 218–228.

Laakkonen, Marko, Pasi Moilanen, Ville Alopaeus, and Juhani Aittamaa, 2006, Dynamic Modeling of Local Reaction Conditions in an Agitated Aerobic Fermenter, *AIChE Journal* 52.

Lamont, J. C., and D. S. Scott, 1966, Mass transfer from bubbles in cocurrent flow, *The Canadian Journal of Chemical Engineering* 44, 201–208.

Lamont, John C., and D. S. Scott, 1970, An eddy cell model of mass transfer into the surface of a turbulent liquid, *AIChE Journal* 16, 513–519.

Lamont, John Craig, 1966, *Gas Absorption in Cocurrent Turbulent Bubble Flow*.

Lamping, S.R, H Zhang, B Allen, and P Ayazi Shamlou, 2003, Design of a prototype miniature bioreactor for high throughput automated bioprocessing, *Chemical Engineering Science* 58, 747–758.

LEAP CFD Team, 2012, *Tips & Tricks: Convergence and Mesh Independence Study* (http://www.computationalfluiddynamics.com.au/convergence-and-mesh-independent-study/).

LEAP CFD Team, 2012, *Tips & Tricks: Turbulence Part 1 - Introduction to Turbulence Modelling* (http://www.computationalfluiddynamics.com.au/turbulence-modelling/).

Lee, B H, 2014, *Fundamentals of Food Biotechnology* (Wiley).

Li, Chao, Jian-Ye Xia, Ju Chu, Yong-Hong Wang, Ying-Ping Zhuang, and Si-Liang Zhang, 2013, CFD analysis of the turbulent flow in baffled shake flasks, *Biochemical Engineering Journal* 70, 140–150.

Magnico, P., and P. Fongarland, 2006, CFD simulations of two stirred tank reactors with stationary catalytic basket, *Chemical Engineering Science* 61, 1217–1236.

Mahmud, Tariq, Jennifer N. Haque, Kevin J. Roberts, Dominic Rhodes, and Derek Wilkinson, 2009, Measurements and modelling of free-surface turbulent flows induced by a magnetic stirrer in an unbaffled stirred tank reactor, *Chemical Engineering Science* 64, 4197–4209.

Martínez, Edgar L., Ronald Jaimes, Jose L. Gomez, and Rubens Maciel Filho, 2012, CFD simulation of three-dimensional multiphase flow in a rotating packed bed, in Ian David Bogle and in Michael Fairweather ed.: *Proceedings of the 22nd European Symposium on Computer Aided Process Engineering*. Vol. 30 (Elsevier).

Moilanen, Pasi, Marko Laakkonen, and Juhani Aittamaa, 2006, Modeling Aerated Fermenters with Computational Fluid Dynamics, *Industrial & engineering chemistry research* 45, 8656–8663.

Moilanen, Pasi, Marko Laakkonen, Olli Visuri, Ville Alopaeus, and Juhani Aittamaa, 2008, Modelling mass transfer in an aerated 0.2 m3 vessel agitated by Rushton, Phasejet and Combijet impellers, *Chemical Engineering Journal* 142, 95–108.

Nienow, A W, 1998, Hydrodynamics of stirred bioreactors, *Applied Mechanics Reviews* 51, 3–32.

Nienow, A W, D J Wisdom, and J C Middleton, 1977, The effect of scale and geometry on flooding, recirculation and power in gassed stirred vessels, *Proceedings of the 2nd European Conference on Mixing*.

Ranganathan, Panneerselvam, and Savithri Sivaraman, 2011, Investigations on hydrodynamics and mass transfer in gas-liquid stirred reactor using computational fluid dynamics, *Chemical Engineering Science* 66, 3108–3124.

Santos-Moreau, Vania, Lena Brunet-Errard, and Matthieu Rolland, 2012, Numerical CFD simulation of a batch stirred tank reactor with stationary catalytic basket, *Chemical Engineering Journal* 207-208, 596–606.

Scargiali, F, a D'Orazio, F Grisafi, and a Brucato, 2007, Modelling and Simulation of Gas–Liquid Hydrodynamics in Mechanically Stirred Tanks, *Chemical Engineering Research and Design* 85, 637–646.

Schjøtt Andersen, Patrick Alexander, 2015, *Computational Fluid Dynamic Modeling of a Novel Rotating Bed Reactor*.

Serowy, Steffen, Sapar M. Saparov, Yuri N. Antonenko, Wladas Kozlovsky, Volker Hagen, and Peter Pohl, 2003, Structural Proton Diffusion along Lipid Bilayers, *Biophysical Journal* 84, 1031–1037.

Sheng, J., H. Meng, and R.O. Fox, 2000, A large eddy PIV method for turbulence dissipation rate estimation, *Chemical Engineering Science* 55, 4423–4434.

Shi, Xin, Yang Xiang, Li-Xiong Wen, and Jian-Feng Chen, 2013, CFD analysis of liquid phase flow in a rotating packed bed reactor, *Chemical Engineering Journal* 228, 1040–1049.

Sun, Haiyan, Zai-Sha Mao, and Gengzhi Yu, 2006, Experimental and numerical study of gas hold-up in surface aerated stirred tanks, *Chemical Engineering Science* 61, 4098–4110.

Svendsen, Lene, 2013, *Evaluation of Novel Reactor Technology for Biodiesel Production*.

Talvy, Samuel, Arnaud Cockx, and Alain Line, 2007, Modeling of Oxygen Mass Transfer in a Gas – Liquid Airlift Reactor, *AIChE Journal* 53, 316–326.

Taniguchi, Shoji, Seiji Kawaguchi, and Atsushi Kikuchi, 2002, Fluid flow and gas – liquid mass transfer in gas-injected vessels, *Applied Mathematical Modelling* 26, 249–262.

The Dow Chemical Company, AMBERLITE ™ IRN99 Resin, (http://msdssearch.dow.com/PublishedLiteratureDOWCOM/dh_06b2/0901b803806b2d60.pdf?filepath=liquidseps/pdfs/noreg/177-02232.pdf&fromPage=GetDoc).

Thompson, Jennifer, Diane McBride, Benjamin P Wilson, Oubay Hassan, Sue Plummer, David Bould, Sam Rolland, Nick Lavery, and Hans Sienz, 2014, An experimental and CFD investigation into the mixing in a closed system stirred vessel, in R Setchi, in R.J. Howlett, in M. Naim, and in H. Seinz ed.: *Sustainable Design and Manufacturing 2014 Part 2* (Future Technology Press).

Torré, Jean-Philippe, David F. Fletcher, Thierry Lasuye, and Catherine Xuereb, 2007, Single and multiphase CFD approaches for modelling partially baffled stirred vessels: Comparison of experimental data with numerical predictions, *Chemical Engineering Science* 62, 6246–6262.

Versteeg, H. K., 2007, *An Introduction to Computational Fluid Dynamics : The Fintie Volume Method* (Pearson Education).

Wang, Tiefeng, and Jinfu Wang, 2007, Numerical simulations of gas–liquid mass transfer in bubble columns with a CFD–PBM coupled model, *Chemical Engineering Science* 62, 7107–7118.

Wang, Weijing, Zai Sha Mao, and Chao Yang, 2006, Experimental and numerical investigation on gas holdup and flooding in an aerated stirred tank with Rushton impeller, *Industrial and Engineering Chemistry Research*, 1141–1151.

Warna, J, M Ronnholm, T Salmi, and K Keikko, 2002, Application of CFD on a Catalytic Rotating Basket Reactor, in Johan Grievink and in Jan van Schijnde ed.: *European Symposium on Computer Aided Process Engineering-1235th European Symposium of the Working Party on Computer Aided Process Engineering* (Elsevier).

Werner, Sören, Stephan C Kaiser, Matthias Kraume, and Dieter Eibl, 2014, Computational fluid dynamics as a modern tool for engineering characterization of bioreactors, *Pharmaceutical Bioprocessing* 2, 85–99.

Wutz, Johannes, Alexey Lapin, Martina Berger, and Ralf Takors, 2015, Modelling of local behaviour of the gas phase in stirred tank bioreactors with CFD: An Euler-Langrange approach for scale-up predictions, *Scale-up and scale-down of bioprocesses*.

Xia, Jian-Ye, Yong-Hong Wang, Si-Liang Zhang, Ning Chen, Peng Yin, Ying-Ping Zhuang, and Ju Chu, 2009, Fluid dynamics investigation of variant impeller combinations by simulation and fermentation experiment, *Biochemical Engineering Journal* 43, 252–260.

Yang, Wenjing, Yundong Wang, Jianfeng Chen, and Weiyang Fei, 2010, Computational fluid dynamic simulation of fluid flow in a rotating packed bed, *Chemical Engineering Journal* 156, 582–587.

Yeoh, S.L., G. Papadakis, and M. Yianneskis, 2005, Determination of mixing time and degree of homogeneity in stirred vessels with large eddy simulation, *Chemical Engineering Science* 60, 2293–2302.

Zhang, Hu, Sally R. Lamping, Samuel C.R. Pickering, Gary J. Lye, and Parviz Ayazi Shamlou, 2008, Engineering characterisation of a single well from 24-well and 96-well microtitre plates, *Biochemical Engineering Journal* 40, 138–149.

Zhang, Hu, Wellae Williams-Dalson, Eli Keshavarz-Moore, and Parviz Ayazi Shamlou, 2005, Computational-fluid-dynamics (CFD) analysis of mixing and gas-liquid mass transfer in shake flasks., *Biotechnology and applied biochemistry* 41, 1–8.

CAPEC-PROCESS Research Center
Department of Chemical and Biochemical Engineering
Technical University of Denmark
Building 229
DK – 2800 Kgs. Lyngby
Denmark

Phone: +45 45 25 28 00
Web: capec-process.kt.dtu.dk